RL-TR-91-156, Vol I (of two)
In-House Report
April 1991

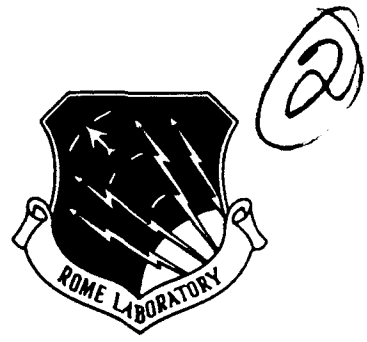

PROCEEDINGS OF THE 1990 ANTENNA APPLICATIONS SYMPOSIUM

Paul Mayes, et al.

Sponsored by
DIRECTORATE OF ELECTROMAGNETICS
ROME LABORATORY
HANSCOM AIR FORCE BASE
AIR FORCE SYSTEMS COMMAND

APPROVED FOR PUBLIC RELEASE; DISTRIBUTION UNLIMITED.

Rome Laboratory
Air Force Systems Command
Griffiss Air Force Base, NY 13441-5700

This report has been reviewed by the Rome Laboratory Public Affairs Division (PA) and is releasable to the National Technical Information Service (NTIS). At NTIS it will be releasable to the general public, including foreign nations.

RL-TR-91-156, Volume I (of two) has been reviewed and is approved for publication.

APPROVED: Robert J. Mailloux

ROBERT J. MAILLOUX
Chief, Antennas & Components Division
Directorate of Electromagnetics

APPROVED: John K. Schindler

JOHN K. SCHINDLER
Director of Electromagnetics

FOR THE COMMANDER: James W. Hyde III

JAMES W. HYDE III
Directorate of Plans & Programs

If your address has changed or if you wish to be removed from the Rome Laboratory mailing list, or if the addressee is no longer employed by your organization, please notify Rome Laboratory (EEAS) Hanscom AFB MA 01731-5000. This will assist us in maintaining a current mailing list.

Do not return copies of this report unless contractual obligations or notices on a specific document require that it be returned.

REPORT DOCUMENTATION PAGE

Form Approved
OMB No 0704-0188

1. AGENCY USE ONLY *(Leave blank)*	2. REPORT DATE	3. REPORT TYPE AND DATES COVERED
	April 1991	Scientific Interim Volume I

4. TITLE AND SUBTITLE
Proceedings of the 1990 Antenna Applications Symposium

5. FUNDING NUMBERS
PE 62702F
PR 4600 TA 14 WU PE

6. AUTHOR(S)
Paul Mayes, et al

7. PERFORMING ORGANIZATION NAME(S) AND ADDRESS(ES)
Rome Laboratory
Hanscom AFB, MA 01731-5000

Project Engineer: John Antonucci/EEAS

8. PERFORMING ORGANIZATION REPORT NUMBER
RL-TR-91-156 (I)

9. SPONSORING/MONITORING AGENCY NAME(S) AND ADDRESS(ES)

10. SPONSORING/MONITORING AGENCY REPORT NUMBER

11. SUPPLEMENTARY NOTES
Volume I consists of pages 1 - 296; Volume II consists of pages 297 - 573

12a. DISTRIBUTION/AVAILABILITY STATEMENT
Approved for public release; distribution unlimited

12b. DISTRIBUTION CODE

13. ABSTRACT *(Maximum 200 words)*
The Proceedings of the 1990 Antenna Applications Symposium is a collection of state-of-the-art papers relating to phased array antennas, multibeam antennas, satellite antennas, microstrip antennas, reflector antennas, HF, VHF, UHF and various other antennas.

14. SUBJECT TERMS			15. NUMBER OF PAGES
Antennas	Microstrip	Multibeam antennas	302
Satellite antennas	Reflector	Array antennas	16. PRICE CODE
Broadband antennas	HF, VHF, UHF		

17. SECURITY CLASSIFICATION OF REPORT	18. SECURITY CLASSIFICATION OF THIS PAGE	19. SECURITY CLASSIFICATION OF ABSTRACT	20. LIMITATION OF ABSTRACT
Unclassified	Unclassified	Unclassified	SAR

Contents

WEDNESDAY, SEPTEMBER 26, 1990

OVER-THE-HORIZON RADAR

* Keynote: "HF Antennas: Application to OTH Radars," J. Leon Poirier

1. "A Thinned High Frequency Linear Antenna Array to Study Ionospheric Structure" by Anthony J. Gould, Capt, USAF 1

2. "Coherence of HF Skywave Propagation Wavefronts," by John B. Morris and James R. Barnum 41

3. "Adaptive Nulling of Transient Atmospheric Noise Received by an HF Antenna Array," by Dean O. Carhoun 61

4. "Near End Fire Effects in a Large, Planar, Random Array of Monopoles," by R. J. Richards 77

5. "Antenna Designs for the AN/FPS-118 OTH Radar," by K. John Scott 107

Contents

ARRAYS

6. "Phased Array Calibration by Adaptive Nulling," by Herbert M. Aumann and Frank G. Willwerth 131

7. "Applications of Self-Steered Phased Arrays," by Dean A. Paschen 153

8. "Array Thinning Using the Image Element Antenna," by Joe Kobus, Robert Shillingburg and Ron Kielmeyer 172

9. "Distributed Beamsteering Control of Monolithic Phased Arrays," by S. F. Nati, G. T. Cokinos and D. K. Lewis 202

10. "Analysis of Edge Effects in Finite Phased Array Antennas," by Steven M. Wright 217

11. "Multimode Performance From a Single Slotted Array Antenna," by John Cross, Don Collier and Len Goldstone 244

12. "An Adaptive Array Using Reference Signal Extraction," by Jian-Ren E. Hang and Donald R. Ucci 261

THURSDAY, SEPTEMBER 27, 1990

SHF/EHF ANTENNAS

13. "Optically Linked SHF Antenna Array," by Salvatore L. Carollo, Anthony M. Greci and Richard N. Smith 275

14. "A Modularized Antenna Concept for a Ku-Band Ferrite Phased Array," by F. Lauriente, A. Evenson and M. J. Kiss 297

15. "A Matrix Feed Beam Steering Controller for Monolithic EHF Phased Array Systems," by G. T. Wells, S. T. Salvage and S. R. Oliver 322

16. "Omnidirectional Ku-Band Data Link Antenna Design," by F. Hsu and A. J. Lockyer 353

17. "A Retrospective on Antenna Design via Waveguide Modes," by K. C. Kelly 372

* 18. "Conformal Microstrip Antennas," by M. Oberhart and Y. T. Lo

19. "A Dual Polarized Horn With a Scanning Bean," by Zvi Frank 396

* NOT INCLUDED IN THIS VOLUME

ANTENNA ELEMENTS

20. "Multi-Octave Microstrip Antennas," by Victor K. Tripp and Johnson J. H. Wang 414

21. "External Lens Loading of Cavity-Backed Spiral Antennas for Improved Performance," by George J. Monser 444

22. "A Compact Broadband Antenna," by Sam C. Kuo and Warren Shelton 457

23. "Reduced Profile Log Periodic Dipole Antenna Designed for Compact Storage and Self Deployment," by G. D. Fenner, J. Rivera and P. G. Ingerson 486

24. "A Printed Circuit Log Periodic Dipole Antenna With an Improved Stripline Feed Technique," by Jeffrey A. Johnson 504

25. "Half Wave "V" Dipole Antenna," by Valentin Trainotti 512

FRIDAY, SEPTEMBER 28, 1990

ANALYSIS AND PROCESSING

26. "Compact Highly Integrated Dual Linear Antenna Feed," by Joseph A. Smolko, Daniel M. Earley, Daniel J. Lawrence and Michael J. Virostko 538

27. "Shaped Beam Design With a Limited Sized Aperture," by F. Rahman 552

28. "Adaptive Algorithms for Energy Density Antennas in Scattering Environments," by James P. Phillips and Donald Ucci 558

* 29. "Finding the Sources of Momentary HF Signals From a Single Site," by A. F. L. Rocke

* NOT INCLUDED IN THIS VOLUME

A Thinned High Frequency Linear Antenna Array to Study Ionospheric Structure

Capt Anthony J. Gould

RADC/EECP

A Thinned High Frequency Linear Antenna Array to Study Ionospheric Structure

ABSTRACT

This study reports on the design, modeling and performance measurements of a high frequency (HF) linear antenna array with 36 sensors. The array was designed to achieve a narrow azimuthal beamwidth while maintaining grating lobes 10 dB below the main beam during a +/-30° scan in azimuth. The configuration chosen utilizes two active vertical monopole elements and two parasitic backpoles to form a subarray. The subarrays, or sensors, are spaced at distances greater than half a wavelength to provide a large effective array aperture while the elemental radiation pattern, provided by the subarrays, suppresses the grating lobe as the array is scanned. Radiation patterns for the array were determined using three independent techniques; theoretical calculation, computer modeling using the Numerical Electromagnetics Code (NEC), and measurement of the fielded antenna. Results showed close agreement in antenna performance among the three methods of pattern determination. The three step process of theory, numerical modeling and measurement appears to be an optimum approach to antenna design.

Table of Contents

1. Introduction
   1.1 RADC High Frequency Test Facility

2. Linear Array Antenna
   2.1 Design objectives
   2.2 Verona array description

3. Theoretical Methods and Considerations
   3.1 Calculation of theoretical radiation patterns
      3.1.1 Simple vertical monopole element.

   3.2 Two Element Subarray.
      3.2.1 Two active elements phased broadside
      3.2.2 Active element and backpole phased endfire

   3.3 Design of Subarray Dimensions.
   3.4 Calculation of the array factor.
   3.5 Pattern multiplication of array factor and subarray pattern.
   3.6 Reducing grating lobes.

4. Calculations using Numerical Electromagnetics Code (NEC)
   4.1 Introduction to NEC.

   4.2 Far-field Patterns Calculated with NEC.
      4.2.1 Vertical monopole over perfect ground
      4.2.2 Two active elements.
      4.2.3 Monopole with backpole.
      4.2.4 Full subarray
      4.2.5 Model of the full array.

5. Field Measurements
   5.1 Introduction and techniques
   5.2 Measurement of the subarray pattern
   5.3 Measurement of the array pattern

6. Array Description

7. Discussion

References

Illustrations:

1. Verona linear array coverage
2. Subarray configuration for the Verona linear array
3. Verona linear antenna array setup
4. Theoretical elevation patterns for a vertical monopole.
5. Theoretical azimuthal far-field pattern for two vertical monopoles phased broad-side.
6. Theoretical pattern for one active element and one backpole phased end-fire.
7. Theoretical azimuthal far-field pattern for a subarray with two active elements and two backpoles.
8. Array factor, subarray pattern, and resultant radiation pattern from pattern multiplication of array factor with the subarray pattern.
9. Array factor, subarray pattern, and resultant radiation pattern for linear array scanned 20 deg. off broadside.
10. Elevation radiation pattern for a simple vertical monopole over perfect and finite ground planes calculated with the NEC modeling program.
11. Azimuthal pattern for a two element subarray phased broadside calculated with NEC.
12. Azimuthal radiation pattern for a two element subarray phased end-fire calculated using the NEC routine.
13. NEC azimuthal radiation pattern for a four element subarray including two active elements and two backpoles.
14. NEC radiation pattern for a linear array of 15 subarrays, including two active elements and two backpoles. Zero degree scan angle.
15. NEC radiation pattern for a linear array of 15 subarrays, with a 32 dB cosine squared weighting taper.
16. Measured azimuthal radiation pattern for the fielded four element subarray.
17. Measured 36 element linear array radiation pattern using the Ava Tx. site as a source with a 32 dB cosine square weighting
18. Schematic of one active element.
19. Subarray schematic.

1. INTRODUCTION

1.1 RADC High Frequency Test Facility

RADC/EECP has assembled a high frequency (HF) radar and communication test facility at the RADC Verona Test Annex, Verona NY. The system consists of a set of 36 digital HF radio receivers controlled by a DEC Micro-Vax II computer and an extended aperture linear antenna array. The mission of the facility is two-fold. First, investigate propagation mechanisms and limits imposed on HF systems by the ionosphere. Second, explore digital processing techniques such as adaptive sidelobe cancellation, narrowband noise excision, and time domain noise excision that could lead to improvement of current and future Air Force surveillance and communications systems which use the HF frequency band.

The radar system at Verona converts the RF signals from the 36 antenna sensors of the linear array to a digital format using A/D converters in each of 36 receivers. Antenna calibration, beamforming, and all radar processing is carried out by the system computer during post processing. This paper details only the linear antenna array. Information concerning the receivers, operational methods, and data processing will be presented in a separate paper.

The purpose of equipping the test facility with an extended aperture linear array was to create a high resolution probe to study ionospheric structure and use this knowledge to improve backscatter radar techniques.

2. LINEAR ANTENNA ARRAY

2.1 Design Objectives

The objective of the HF test facility at Verona is to measure ionospheric backscatter signals with high resolution and record the receiver baseband digitally. There are many sources of ionospheric clutter; radio aurora, f-region irregularities, equatorial irregularities and others. All these mechanisms contribute interference that is known to degrade HF propagation performance. Measurements using the linear antenna array will help provide the data needed to evaluate the effectiveness of digital processing techniques to reduce interference caused by the irregularities at the high latitudes. The backscatter data will also be used to characterize or map ionospheric phenomena in the high latitudes. This mapping will help determine the spatial and temporal extent of ionospheric irregularities.

The frequency range of the receiver system is 5-30 MHz which encompasses most of the HF band. However, high intensity phenomena are usually present during nighttime operation when the ionosphere dictates that the most effective operating frequencies are at the low end of the HF band. Therefore, 6-12 MHz was used as the design operating band for the linear array. While the array will certainly work to some extent over a much larger frequency band, the array was tuned to perform best in the 6-12 MHz region. With this criterion in mind, the 36 element linear array was configured to obtain maximum resolution in azimuth while still maintaining low sidelobe control over the operating frequency band of 6-12 MHz.

A random array of elements spaced over a large aperture is one way to approach this problem. However, it was decided not to use this method for several reasons. First, increased signal

processing is necessary to reduce the sidelobes to levels comparable to a periodic array. Secondly, the mainbeam pattern and sidelobe levels are difficult to predict during all operating situations and finally the array was to retain as much commonality as possible with other existing HF antenna systems.

A linear array of widely spaced (greater than half wavelength) directional elements was chosen as a practical solution to the problem. Such an array provides a wide aperture that results in a narrow beamwidth in azimuth and also provides good sidelobe control. A wider aperture is possible using subarrays of monopole elements that control grating lobes as the array is scanned. Backpoles placed a quarter wavelength behind each active element provide increased directivity of the array in the forward direction. While a backscreen is more effective, environmental concerns and colocation with other experiments on the selected site currently prohibit use of a large backscreen. The geographic coverage area of the array is shown in Figure 1. Note that the coverage area includes a large overlap of the area associated with the nighttime auroral oval.

2.2 Verona Array Description

The linear HF antenna array at Verona NY is composed of 36 subarrays with a spacing of 20 meters between centers of each subarray. This elemental spacing corresponds to 0.8 wavelengths at the upper design frequency of 12 MHz. The dimensions and components of the subarrays are shown in Figure 2. The main idea in the subarray design process was to use a given number of monopoles as the basic components to create a directional element. Two monopole elements, placed a half wavelength apart (D2=12.5 m),

in a broadside configuration provided forward directivity and reduced the energy received from signals arriving from the direction parallel to the array. The 6 meter height of these two elements was chosen to keep the element length near a quarter wavelength of the operating frequencies. A 12 meter backpole was placed a quarter wavelength (D1 = 6.25 m) behind each of the 6 meter elements. A height of 12 meters was chosen to keep the backpoles greater than a quarter wavelength even at the low end of the operating band. The four monopoles acting together as a subarray provide forward directivity and wide nulls at angles of ±90° and 180°. The spacing between the subarrays (D3) was determined from the constraint of reducing the grating lobe by 10 dB when the array is scanned 30° at a frequency of 12 MHz.

A schematic of the linear array setup is shown in Figure 3. Several parameters are included in this figure to point out the major features of the array including its length, spatial orientation, operating frequency band, scan limits, and minimum beamwidth.

3. THEORETICAL METHODS AND CONSIDERATIONS

3.1 Calculation of Theoretical Radiation Patterns

Far-field azimuthal radiation patterns were calculated at several stages of the antenna array development. These stages included a simple monopole element, two elements phased broadside, two elements phased endfire, a four element subarray, and the 36 element linear array.

A great deal of consideration was given to the effect of the ground upon the vertical field patterns. While a finite ground might have little effect on the input impedance of a vertical monopole, the field pattern can be greatly influenced by the ground conductivity. Fortunately for the antenna, (and unfortunately for the experimenters), the land at Verona is for all intents and purposes a swamp. Ground conductivity for this area is very high. A conductivity value of σ = 0.1 mhos/meter and a relative dielectric constant of ϵ = 30 were used for all calculations. These values were chosen from literature as being consistent for a marshy ground[1]. While this is by no means a perfectly reflective ground it improves the antenna performance at receive angles close to the horizon. In addition, a ground screen was installed in front of the array to ensure a stable impedance for the antenna. The ground screen consisted of two 22 gauge aluminum clad wires extending 75 meters in front of each element. Field calculations were made with the assumption of an infinite and perfect ground plane.

3.2 Simple vertical monopole element.

The first antenna structure investigated was a vertical monopole over a perfect ground plane. This antenna has a radiation

pattern similar to a vertical dipole in free space and is therefore omnidirectional in the azimuthal plane. The elevation field pattern for a vertical monopole has been extensively calculated in the past and verified for nearly all situations[2]. Parameters that influence the pattern are ground conductivity, element length, element radius, and operating frequency. Elevation patterns are shown in Figure 4. for a thin, 6 meter monopole over a perfect ground plane and also with $\sigma = 0.1$ and $\epsilon = 30$. Note that the loss in gain for the antenna over a finite conducting ground becomes critical only at angles close to the horizon, (greater than 85°). This strongly suggests good low angle performance for the Verona linear antenna, which allows for long range OTH radar operation.

3.3 Two Element Subarrays

3.3.1 Two Active Elements Phased Broadside

The next step in the pattern shaping process was to add a second monopole and phase the resultant pair to increase the gain broadside (0°) while placing a null in the endfire (90°,270°) direction. The azimuth pattern for a two element broadside array of point sources with D2 = 0.5 \ is described by Eq. 1.

$$E(\phi) = 2 \cdot \sin\left(\frac{k \cdot D_2 \cdot \cos(\phi)}{2}\right) \qquad \text{EQ: 1}$$

$$k = \frac{2\pi}{\lambda}$$

The pattern resulting from Eq. 1 is shown in Figure 5. Note the nulls in the ±90° directions and maximum directivity to the front and rear of the array.

3.3.2 Active Element and Backpole Phased Endfire

The next step in the pattern shaping process was the addition of parasitic backpoles placed a quarter wavelength (D1 = 6.25 m) behind each active element. One active element and one parasitic backpole were considered as an endfire array. A backscreen greater than a quarter wavelength in height (at 6 MHz) and placed one quarter wavelength behind the active radiators acts as a reflector. This reflector increases gain in the forward direction by several decibels and provides nulling of any signals arriving from behind the array. Such a backscreen would be over 12 meters in height and 700 meters long. Environmental constraints and other on-going experiments conducted at the Verona test site prevented building such a structure. However, the antenna gained significant benefit by placing a passive or parasitic element one quarter wavelength behind each active element. These "backpole" elements are connected only to the ground screen and to a copper grounding stake driven 1.2 meters deep into the earth beside each backpole. The increase in electric field intensity as a function of azimuth angle ϕ, of one active monopole with a parasitic backpole, is derived by Kraus[3] and shown by Eq. 2.

$$G(\phi) = \sqrt{\frac{R_{11} + R_{1L}}{R_{11} + R_{1L} - \left| Z^2_{12}/Z_{22} \right| \cos(2 \cdot \tau_m - \tau_2)}} \quad \text{EQ: 2}$$

$$\times \left[1 + \left| \frac{Z_{12}}{Z_{22}} \right| \cdot \underline{/\epsilon} \pm \underline{dr \cdot \cos(\phi)} \right]$$

R11 = self-resistance of a vertical antenna element

R1L = effective loss resistance of a single element

$R_{12} + jX_{12} = Z_{12}$ = Mutual impedance, elements 1 and 2.

$R_{22} + jX_{22} = Z_{22}$ = Backpoles self-impedance.

$$\tau_m = \arctan \frac{X_{12}}{R_{12}}, \quad \tau_2 = \arctan \frac{X_{22}}{R_{22}}$$

d_r = spacing between elements

Note in Eq. 2, that as the impedance of the back pole element (Z22) is increased the effect of the backpole decreases and the gain approaches that of a single active element ($G(\phi)=1$). The effectiveness of the backpole therefore depends to a large extent upon its length. Also, it can be shown from Eq. 2 that when the backpole is made longer than $\lambda/4$ it acts as a reflector, and when it is shorter than $\lambda/4$ it becomes capacitive and behaves as a director. Changing frequency will alter the performance of the array since this corresponds to changing the dimensions of the array in terms of wavelength. Complete cancellation of the signal arriving from 180° is possible only if dimensions and physical orientation of the array are perfect. Signals arriving from angles not exactly 180° are never completely cancelled. This arrangement does

however, predict a significant increase in the forward (0°) directivity and a decrease in directivity to the rear (180°). The field pattern for one active element and one backpole in a two element endfire configuration array of point sources with (D1 = $\lambda/4$) is described by Eq. 3 and illustrated in Figure 6. The pattern shows the largest gain in the forward direction and indicates a null in the ±180° direction.

$$E_1(\phi) = 2 \cdot Eo \cdot Cos\left(\frac{k \cdot D_1}{2} \cdot Sin(\phi)\right) \qquad \text{EQ: 3}$$

D_1 = Distance in wavelength between elements.

ϕ = Azimuthal scan angle from broadside.

$$k = \frac{2 \cdot \pi}{\lambda}$$

3.4 Design of Subarray Dimensions

The last step in elemental beam shaping is to combine the broad-side and end-fire configurations to create the final subarray. Combination of the broadside and end-fire patterns through pattern multiplication results in the subarray pattern formed by the two active elements and the two passive backpoles. The pattern for this setup is shown in Figure 7. The main element gain is shown to be in the forward direction. Nulls are located in the ± 90° and 180° directions. This pattern is considered to be the theoretical element pattern.

3.5 Calculation of the Array Factor

The far-field array factor for a linear array of 36 isotropic point sources is described by the square of Eq. 4. The field pattern for the array factor with N = 36, D3 = 0.8 λ, and ϕ_o = 0 is shown by the plot in Figure 8. This pattern is for a uniform array where all 36 elements are weighted equally. The peak of the first side-lobe is 13.2 dB below the main beam. The 3 dB beamwidth is approximately 2.5°.

$$E_{array} = \frac{\mathrm{Sin}[\pi \cdot N \cdot D3[\mathrm{Sin}(\phi) - \mathrm{Sin}(\phi_o)]}{N \cdot \mathrm{Sin}[\pi \cdot D3 \cdot [\mathrm{Sin}(\phi) - \mathrm{Sin}(\phi_o)]} \qquad \text{EQ: 4}$$

N = Total number of elements.

D_3 = Distance between array sensors in wavelengths.

3.6 Pattern Multiplication of Array Factor and Subarray Pattern

A broadside (0° scan) far-field array pattern for the thinned linear antenna array is also shown in Figure 8. It was calculated by multiplying the subarray (element) pattern (also shown in Figure 8.) by the array factor. Uniform amplitude weighting was used in calculating this pattern. Characteristic 13 dB sidelobes are seen on either side of the main beam. However, now a broad subarray pattern has been placed over the array factor. This results in higher directivity in the forward direction and nulls at angles of ±90°,and 180°.

3.7 Grating Lobe Reductions

A plot of the array factor when the array is scanned off broadside by 20° is shown in Figure 9. Note the grating lobes that have moved into the pattern. They are located at -120°, -80° and 160° and are equal in amplitude to the main beam of the pattern now at 20°. Another plot in Figure 9 shows the total array pattern. Notice that the amplitude of the grating lobes relative to the main beam has been lowered significantly by the element pattern with the nearest one at -80° now lower by 16 dB. This reduction in grating lobes of the array by using directive subarrays has permitted the aperture of the array to be increased from 437.5 meters for the usual $\lambda/2$ spacing between elements to 700 meters or 0.8 wavelengths between elements. This corresponds to a decrease in beamwidth from 4° to 2.5° at the 12 MHz design frequency.

4. Calculations Using Numerical Electromagnetics Code (NEC)

4.1 Introduction to NEC

The Numerical Electromagnetics Code (NEC)[4] is a computer program that uses the Method of Moments technique to predict the electromagnetic response of antennas and other metal structures. The physical structure to be analyzed is modeled using wire segments to approximate the correct shape and electrical characteristics. The required integral equations are then solved to determine the currents on an electromagnetically excited wire or structure. Similar to the theoretical calculations a step by step process using NEC was employed to model various monopole combinations. These structures were then combined to obtain the subarray and finally the complete array. All computations were carried out on a Digital Equipment Corp. Micro-Vax II computer.

4.2 Far-field Patterns Calculated with NEC

4.2.1 Vertical Monopole Over perfect Ground

A simple vertical monopole antenna was modeled first using NEC. The height of the antenna is 6 meters and the element is driven by a 1 volt source close to the ground. A calculation assuming a perfect ground plane was made to create a baseline and verify that the model is accurate. Next an element over a finite ground plane was modeled using NEC. An option available with the NEC program to use Sommerfeld Integrals was employed. This method allows simulation of a structure very close to the ground. Various ground plane configurations and different frequencies were

examined. Resultant patterns are shown in Figure 10. for both the perfectly conducting ground and a ground with finite conductivity representative of the earth at the Verona test site (σ=0.1 mhos/meter, ϵ=30).

4.2.2 Two Active Elements

A simulation of two active elements phased for a broad-side configuration was computed and the field patterns calculated. This arrangement generates the common "figure-eight" pattern with nulls at ±90° in relation to broadside. The resultant azimuth pattern is shown in Figure 11.

4.2.3 Monopole with Backpole

Similar to the process using theoretical methods, a backpole was paired with an active element to reduce the gain in the back half plane. The backpole in the NEC model is again located a quarter wavelength behind the active element. Ground wires are connected from the front element to the backpole. The backpole is not driven with a voltage but purely reacts in the passive manner as described earlier in Section 3.3.2. This setup as in the earlier theoretical case results in an endfire configuration. The resultant pattern is shown in Figure 12. Note that nulls approximately 6 dB below the forward direction are formed at 180°. In this and the following simulations the a perfectly conducting ground plane model was used since only the azimuthal variation is under consideration.

4.2.4 Full Subarray

The full subarray of two active elements and two backpoles was modeled next. Both active elements are driven in phase by 1 volt sources. The resultant pattern for azimuthal scan is shown in Figure 13. This is the element pattern for the array. It is this

pattern that can be multiplied by the array factor to create the full array pattern. The subarray pattern calculated using NEC shows nearly 15 dB of increased directivity in the forward direction (0°) compared to behind the array (180°).

4.2.5 Model of the Full Array

The final modeling effort is naturally the full array of 36 subarrays and calculation of the composite element-array far-field patterns. Unfortunately, our version of the NEC code cannot accommodate structures as large as the full array of 36 elements. The largest array that could be handled in the program was 15 subarrays. The limitation of 15 subarrays should only decrease the gain, beamwidth, and number of lobes in the patterns. The overall response of the 15 element linear array model should still be a good representation of the 36 element array.

All active elements were fed with a one volt source with no phase difference between elements causing the main beam of the pattern to occur in the broadside direction. The result is identical to a plane wave arriving that is oriented parallel to the array. The resultant azimuthal radiation pattern is shown in Figure 14. In order to determine the expected side lobe behavior of the array, an amplitude weighting taper was used during calculation of the field pattern. This is done by factoring each of the voltage sources with a 32 dB Cosine Squared amplitude weight. The cosine squared function is only one of many possible weightings and was chosen because it does not broaden the main beam as much as other comparable weighting functions. The pattern for this simulation is shown in Figure 15. Notice that the sidelobe levels have been reduced from the uniform level of 13.2 dB shown in Figure 14 to 32 dB below the main beam. The main beam

has broadened by 1 degree and about 3 dB of main beam amplitude loss has occurred. This loss and beam spread will cause a reduction in array resolution but it does not prevent adequate system performance.

5. Field Measurements

5.1 Introduction and Techniques

The HF test facility using the linear antenna array at Verona NY is currently in operation. Calibration and testing are complete and some preliminary clutter data have been collected. The pertinent pattern measurements made were the subarray pattern and the full 36 subarray, linear antenna pattern. The essential antenna information gained from these measurements includes the gain, average sidelobe level, beamwidth, grating lobe response, front to back ratio and scan direction accuracy.

5.2 Measurement of the Subarray Pattern

The subarray pattern was determined by moving a continuous wave probe across the subarray aperture and plotting the received signal strength as a function of azimuth. Measurements were also made behind the array to determine the element directivity to the rear (180°). Figure 16 shows the azimuthal element pattern for all the elements at a frequency of 10.205 MHz. Although not shown on this plot the front to back ratio was also measured and is approximately 12 dB. Note that the subarray or element gain falls off rapidly for signals arriving at angles greater than 25° from broadside. This is the mechanism that permits the array to scan ±30° with the grating lobes reduced to at least 10 dB below the main beam.

5.3 Measurement of the Array Pattern

The field pattern for the full array was measured by scanning the array main beam past a CW signal transmitted from Ava NY. Ava is located 21 miles away at a bearing from Verona of 31° east of true north which corresponds to 21° east of the array boresight. The power of the transmitted signal was ten kilowatts and the antenna used was a horizontal log periodic. The resultant full array pattern is shown in Figure 17. This pattern was obtained using measured data and applying a 32 dB cosine squared amplitude weighting function. Sidelobe response to the test signal is less than 32 dB RMS. Note that the beamwidth is greater than the 2.5 degrees available without the weighting taper but is still only approximately 4 degrees. This method of course does not account for the response of the subarray pattern but only the subarray pattern at a single bearing. Therefore, the actual gain will fall off as the scan angles become greater than 20° as shown in Figure 16 by the subarray pattern.

6. Array Description

The elements and pre-amplifiers for the linear antenna array were designed and built at RADC "in-house". The elements are constructed from electrical supply house materials including, 1 inch diameter rigid aluminum conduit, pvc pipe, pvc flanges, and pvc junction boxes. A diagram of the element is shown in Figure 18.

The signal output of each active monopole element is fed to a power combiner located halfway between the elements. The combined output is then band-pass filtered and sent to the pre-amplifier. Pre-amplifiers were deemed essential to overcome the sum of losses from cables, filters, and power combiners, which was calculated to be 15-20 dB. The gain of the pre-amps was chosen to be 20 dB. The

output of the pre-amplifier is carried through RG/215 coaxial cable to the receivers located in a central receive building. The building is located slightly off the middle of the array and 30 meters behind the array. The RG/215-U used for the co-axial feed cable is low loss double shielded cable with an outside armor sheath. A unique aspect of this array is that eacn one of the cables, connecting a subarray back to one of the receivers, are of different length. The longest cable is approximately 1600 feet, while the shortest is 150 feet. Phase and amplitude differences for all channels are accounted for and adjusted digitally during the beamforming process. Figure 19 details the subarray configuration including the elements, power combiners, filters, and pre-amplifiers.

7. Discussion

Once the required operating properties of the antenna ie. gain, beamwidth, frequency band, etc. were specified, the antenna design effort and testing for this system consisted of a three stage process. First, antenna theory was used to design an antenna that would meet these specifications. Second, numerical methods were used to test the theoretical designs and ensure that the designs met the performance specifications. Finally, pattern measurements of the fielded antenna were made to verify that the array performed as designed. Table 1. contains some of the major required specifications and the results obtained from each of the three techniques used. Although there are some minor differences, in general, the agreement between the numbers is quite good and shows that the use of theory and modeling techniques leads to the fabrication of an antenna with the properties needed for conducting meaningful experiments.

Table 1. Parameter Values from Each of Three Techniques

Parameter	Theoretical Calculations	NEC Calculations	FIELD Measurements
Gain (dB)	26	24	23
BW (dB)	2.5	2	≈ 2.5
AVE. SLL (dB)	32	≈ 30	32
F/B ratio (dB)	> 20	15	12-14

References:

1. E. Jordan, Editor, "Reference Data for Radio Engineers", Howard W. Sams & Co., 1986

2. J. D. Kraus, "Electromagnetics", 3rd ed., McGraw Hill, 1984, p. 518.

3. John D. Kraus, "Antennas", McGraw-Hill Book Company, 1988

4. G. J. Burke and A.J. Poggio, "Numerical Electromagnetics Code (NEC)", Tech. Doc. 116, Naval Oceans System Center, 1980.

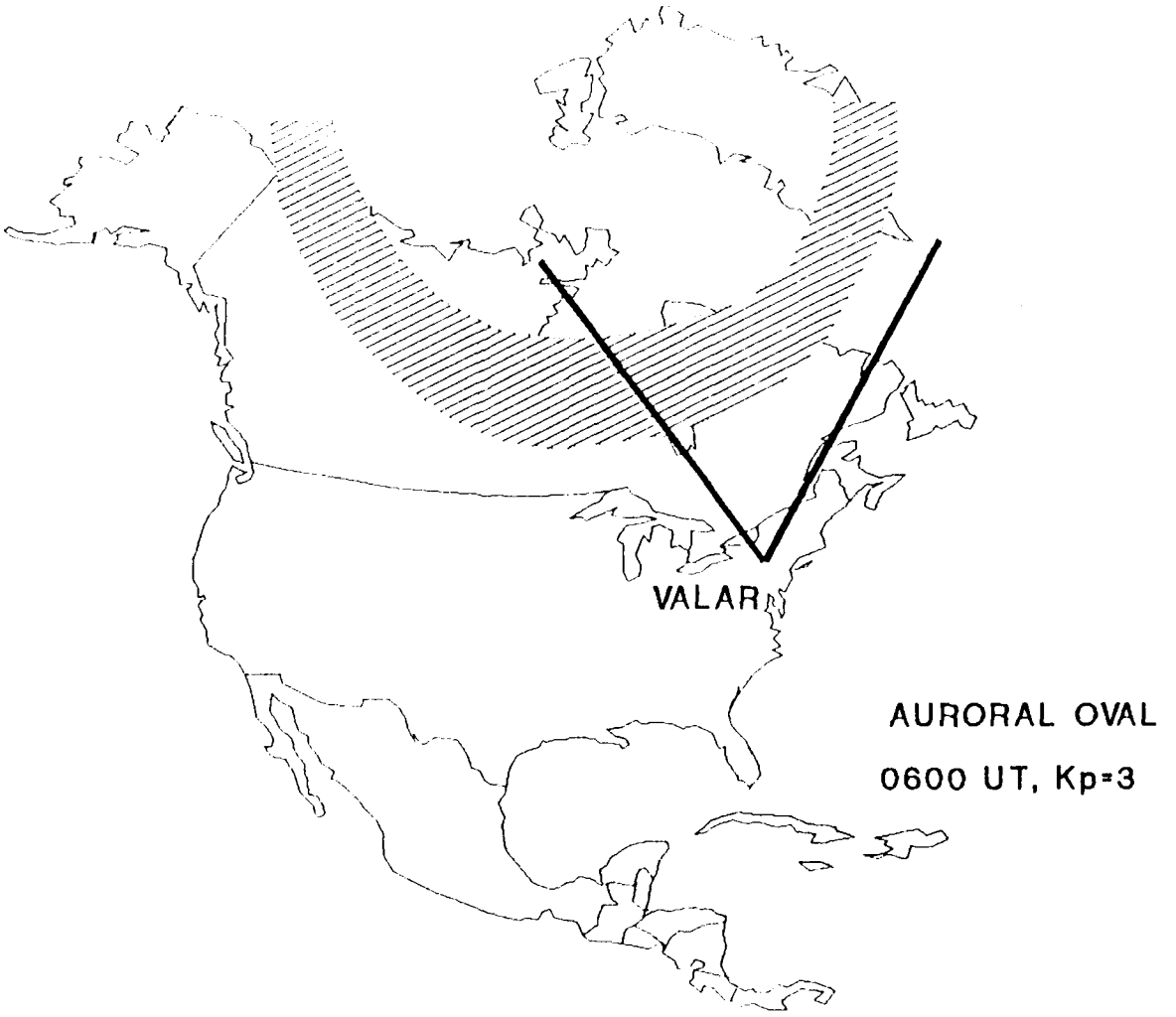

MEP20

Figure 1. Verona linear array coverage.

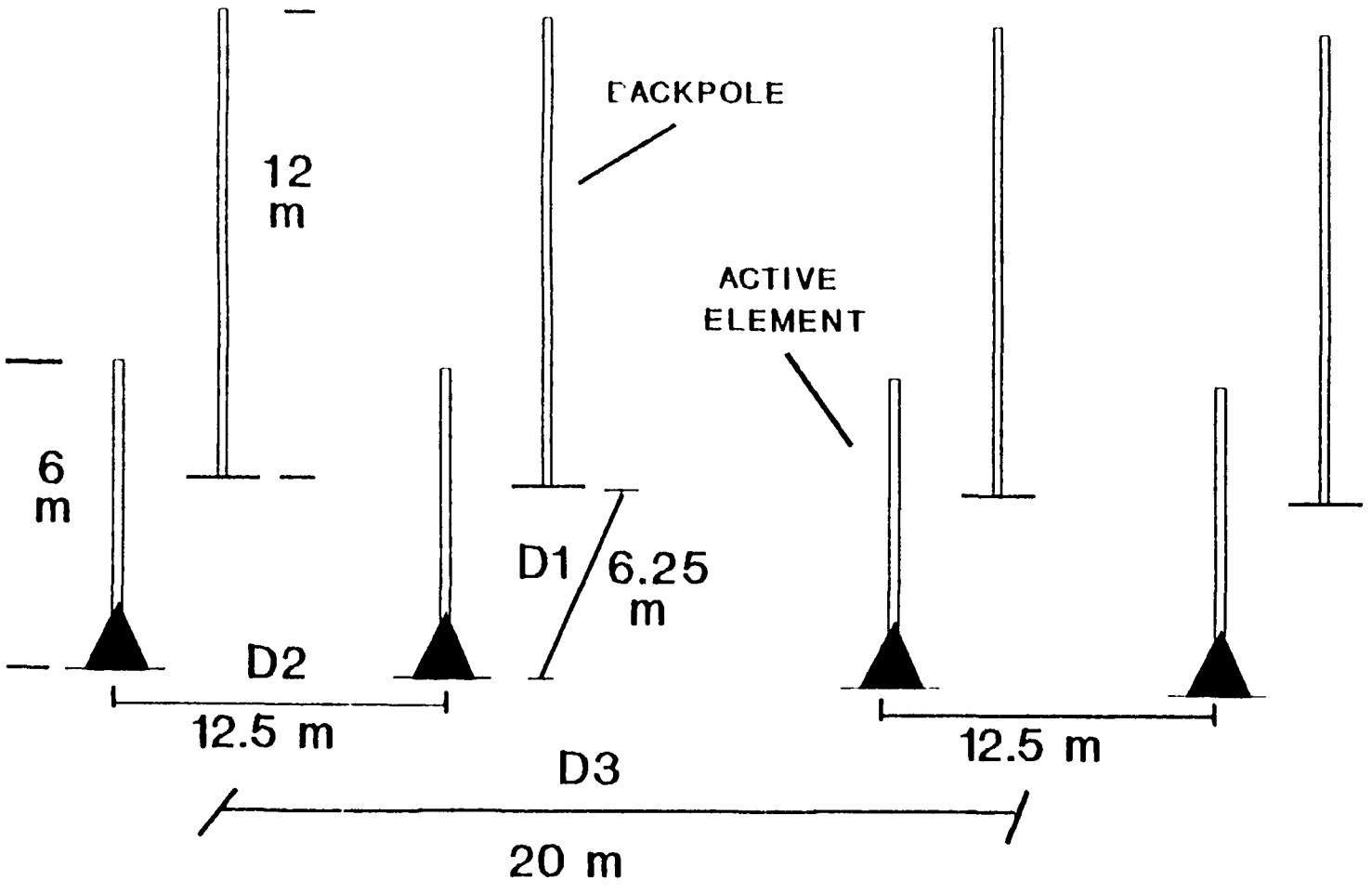

Figure 2. Subarray configuration for the Verona linear array.

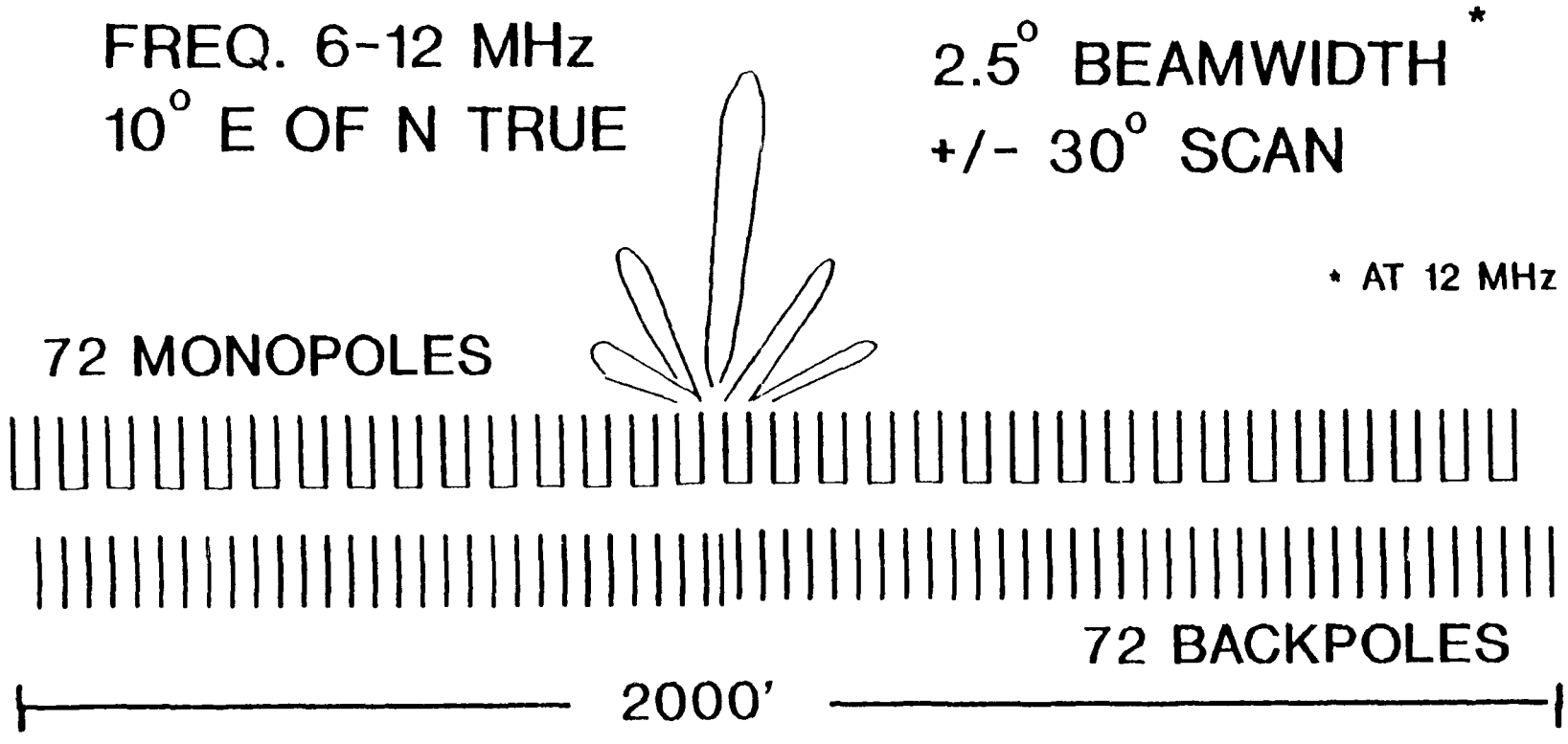

Figure 3. Verona linear antenna array setup

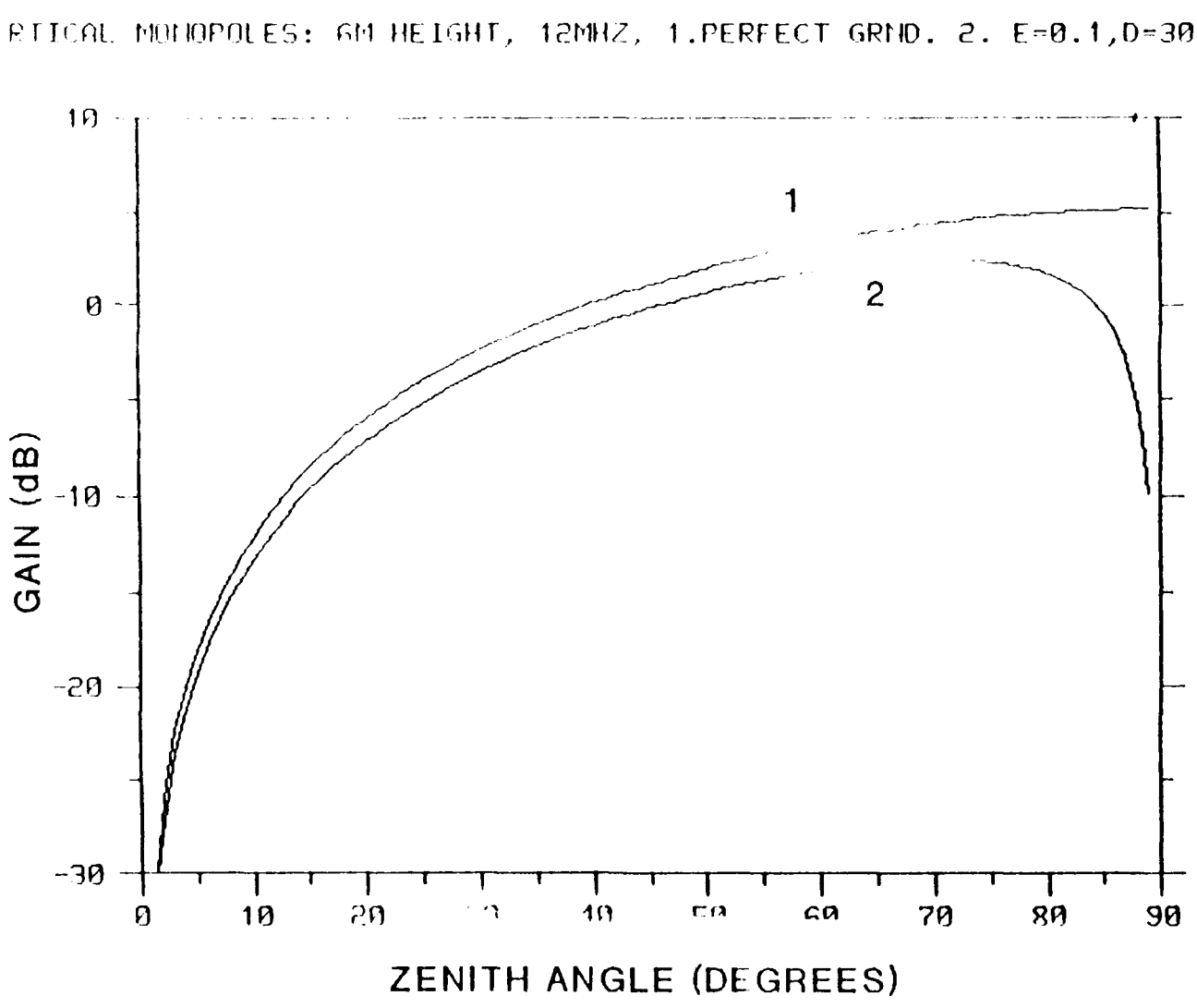

Figure 4. Theoretical elevation patterns for a vertical monopole.

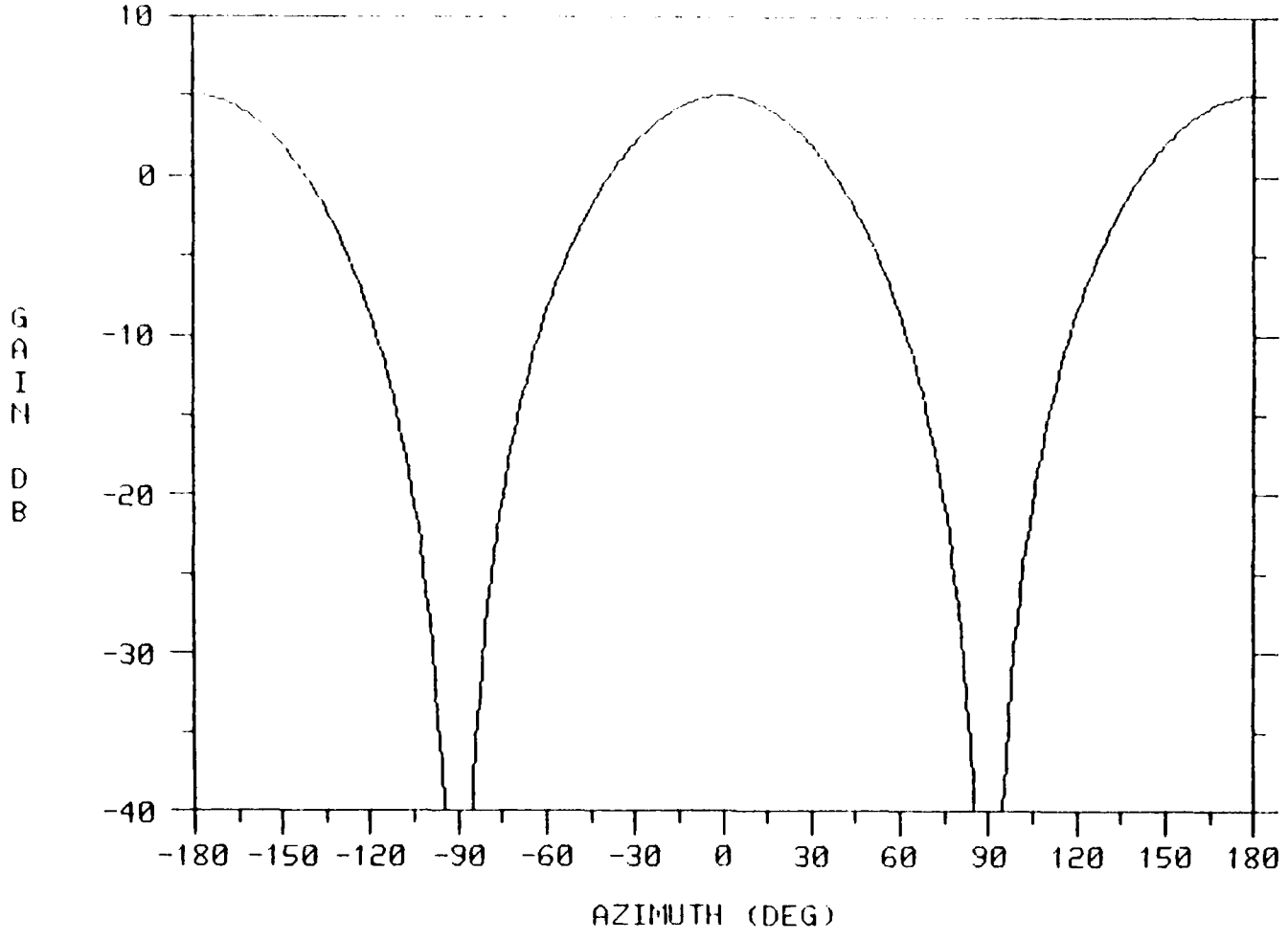

Figure 5. Theoretical azimuthal far-field pattern for two vertical monopoles phased broadside.

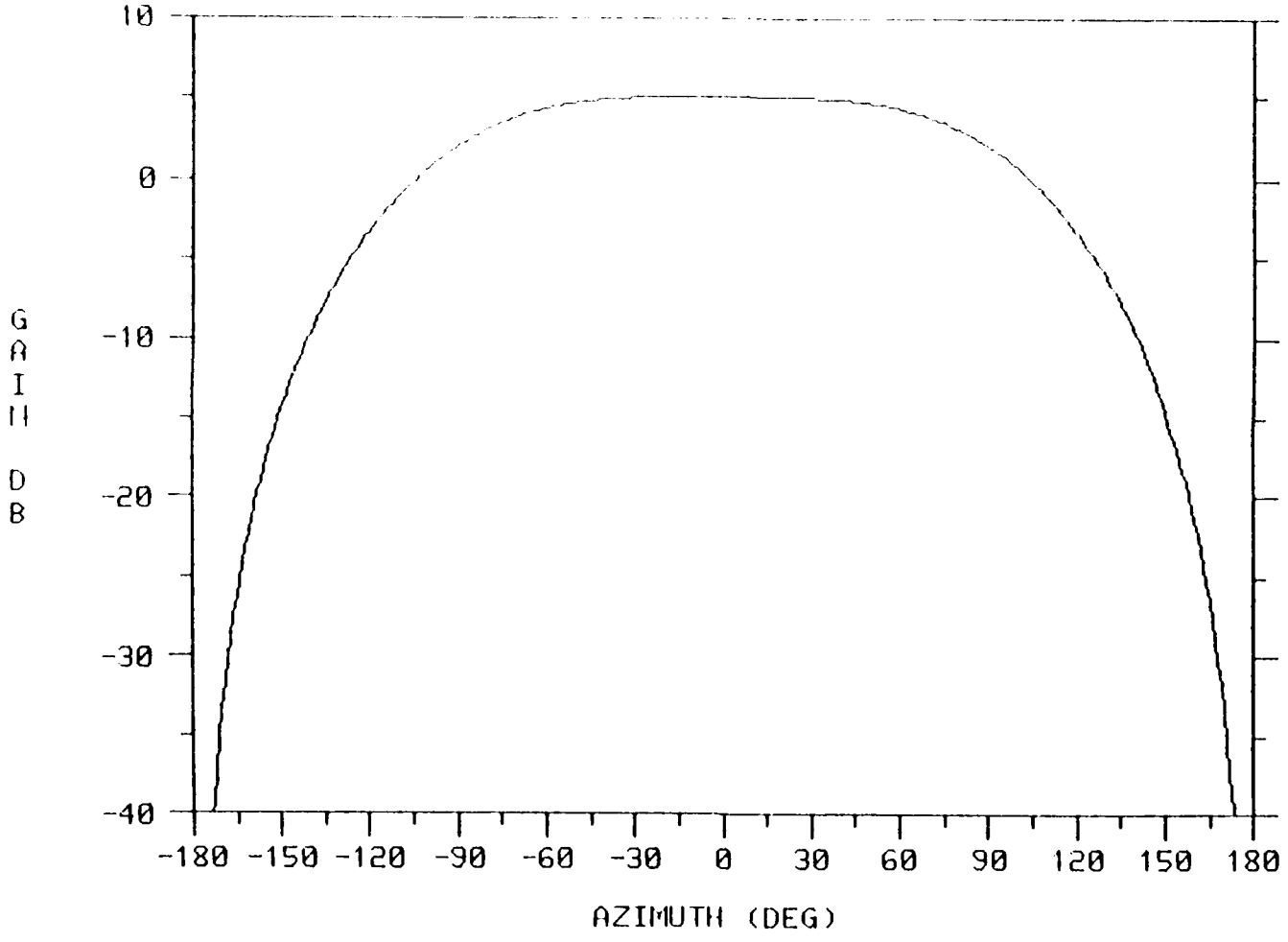

Figure 6. Theoretical pattern for one active element and one backpole phased end-fire.

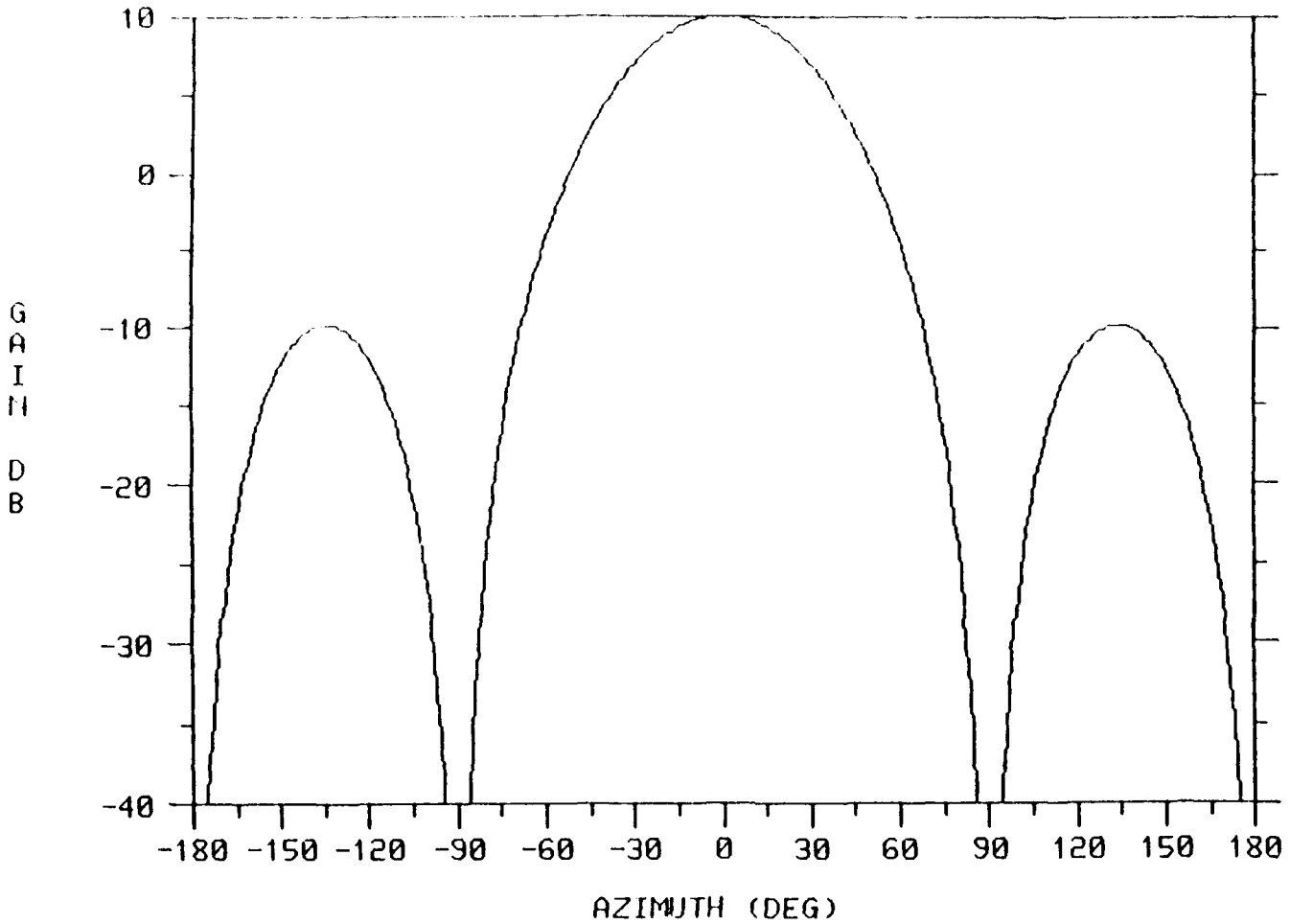

Figure 7. Theoretical azimuthal far-field pattern for a subarray with two active elements and two backpoles.

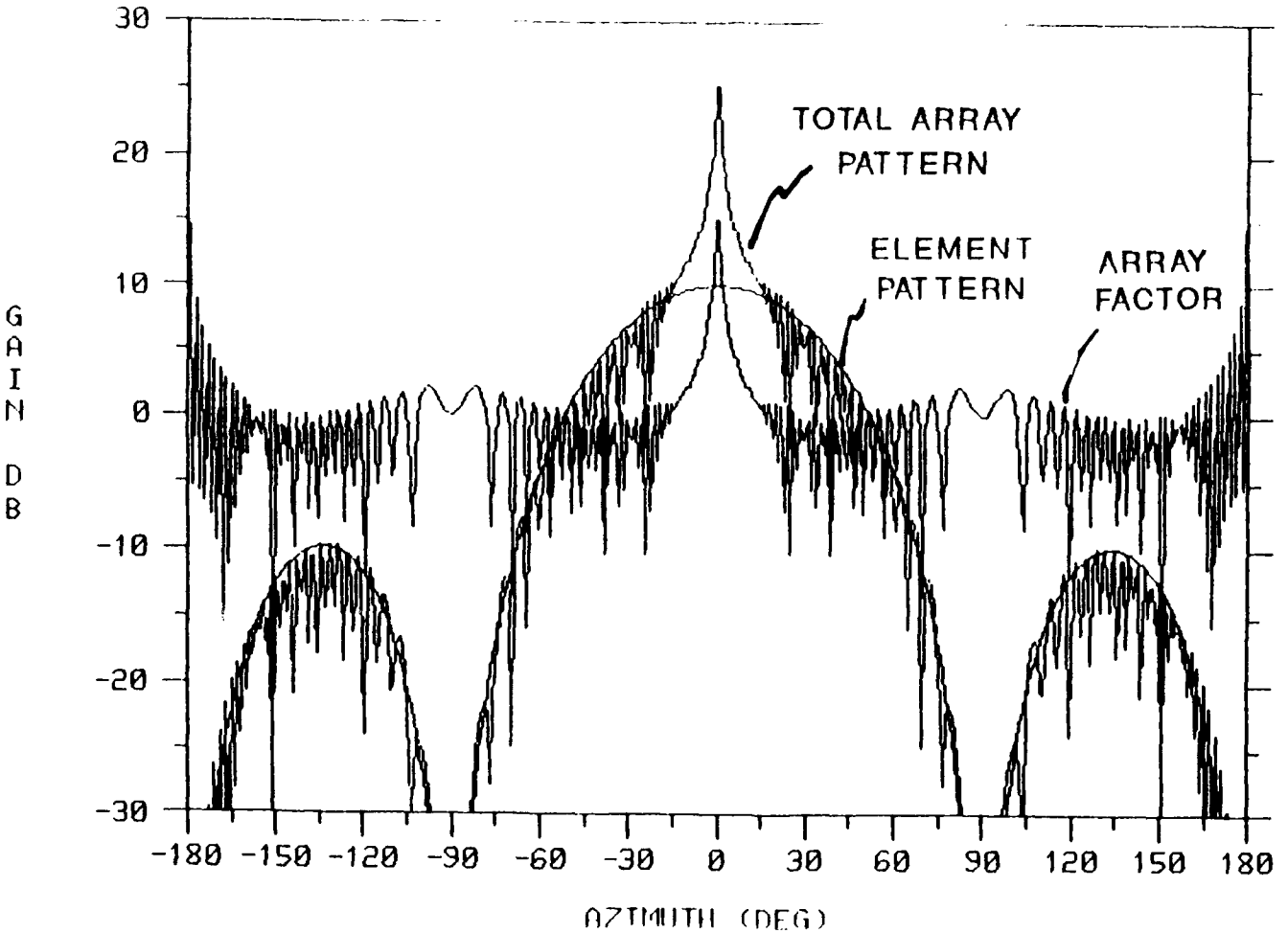

Figure 8. Array factor, subarray pattern, and resultant radiation pattern from pattern multiplication of array factor with the subarray pattern.

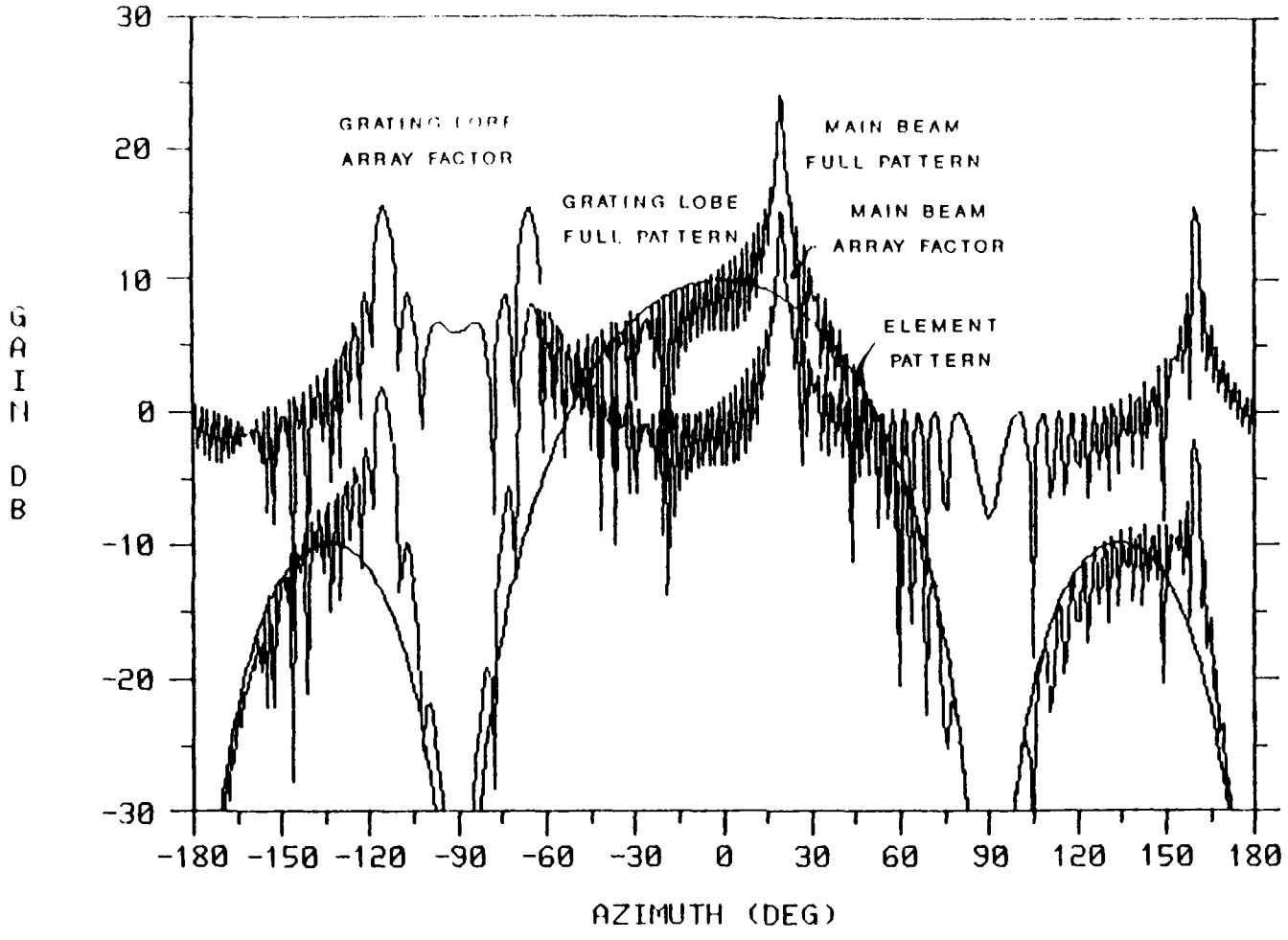

Figure 9. Array factor, subarray pattern, and resultant radiation pattern for linear array scanned 20 degrees off broadside.

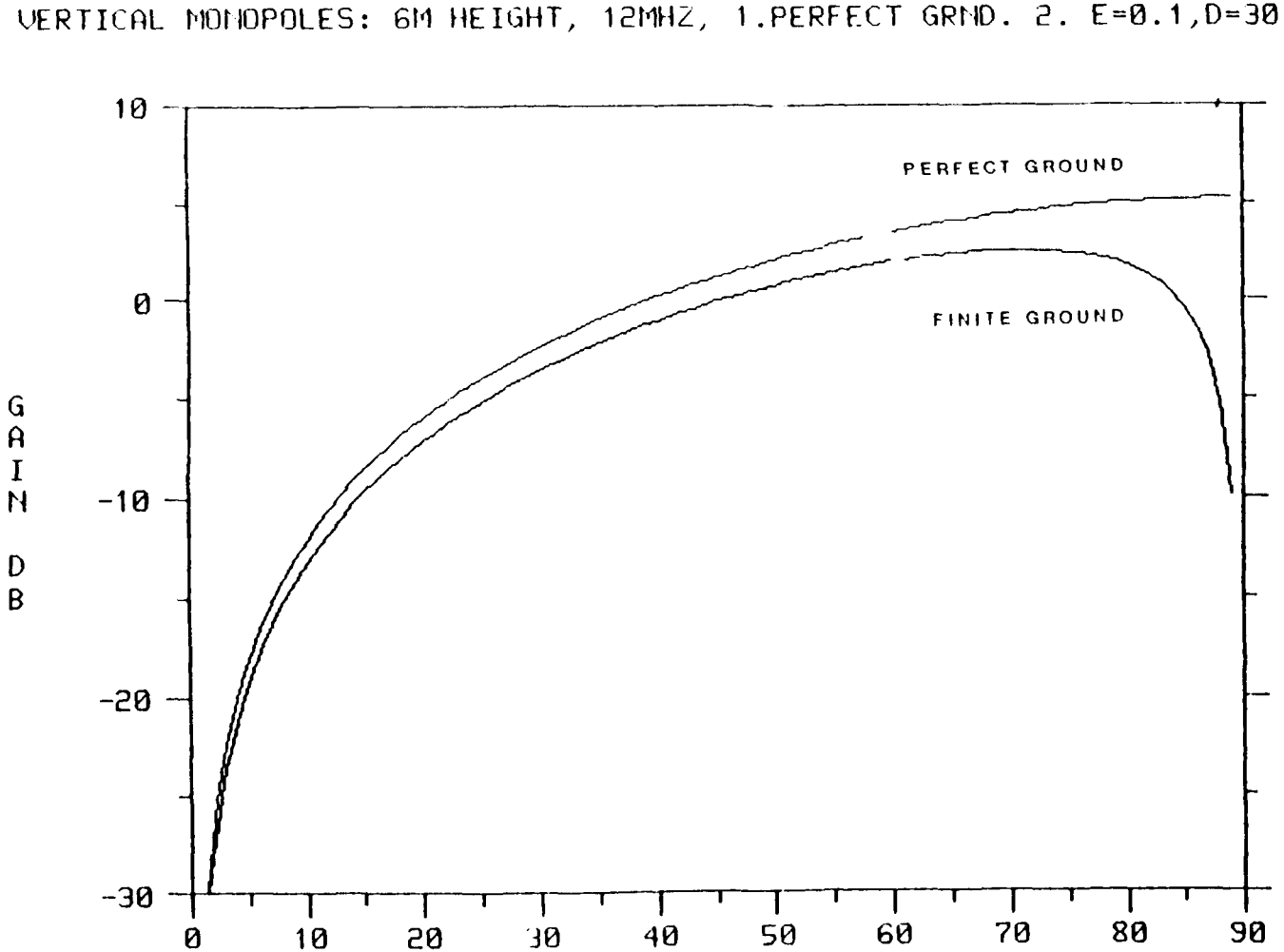

Figure 10. Elevation radiation for a simple vertical monopole over perfect and finite ground planes calculated with the NEC modeling program.

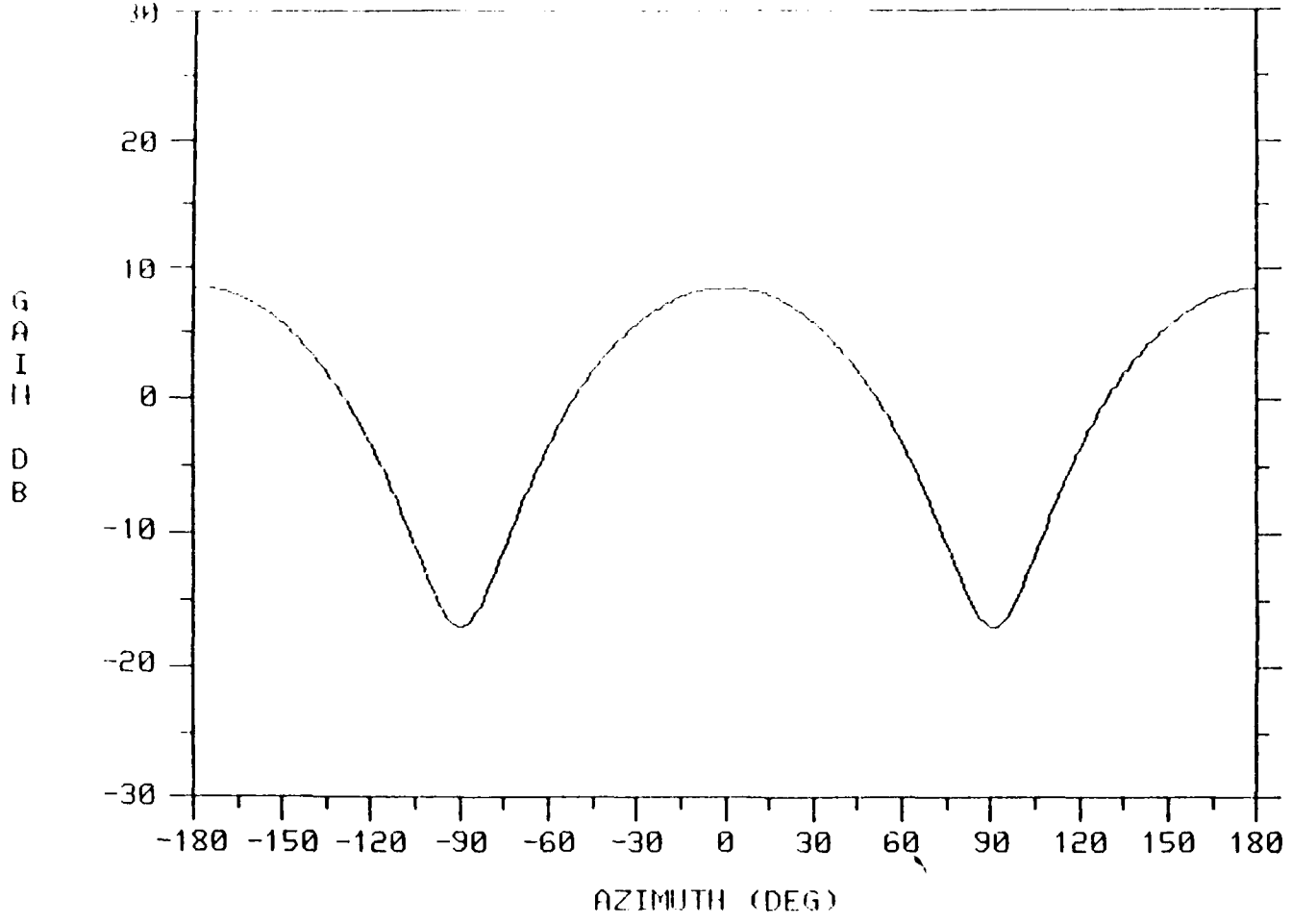

Figure 11. Azimuth pattern for a two element subarray phased broadside calculated with NEC.

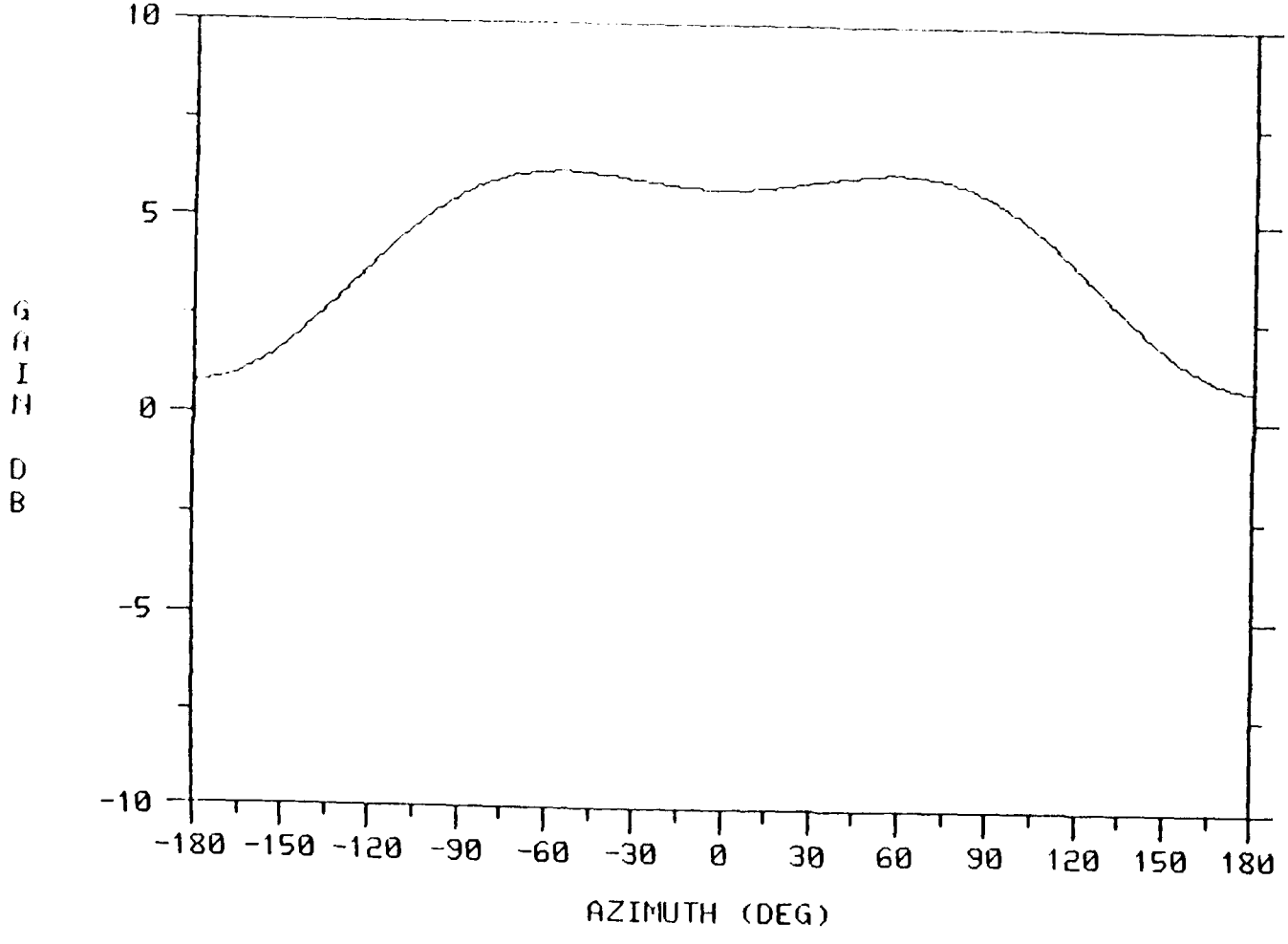

Figure 12. Azimuthal radiation pattern for a two element subarray phased end-fire calculated using the NEC routine.

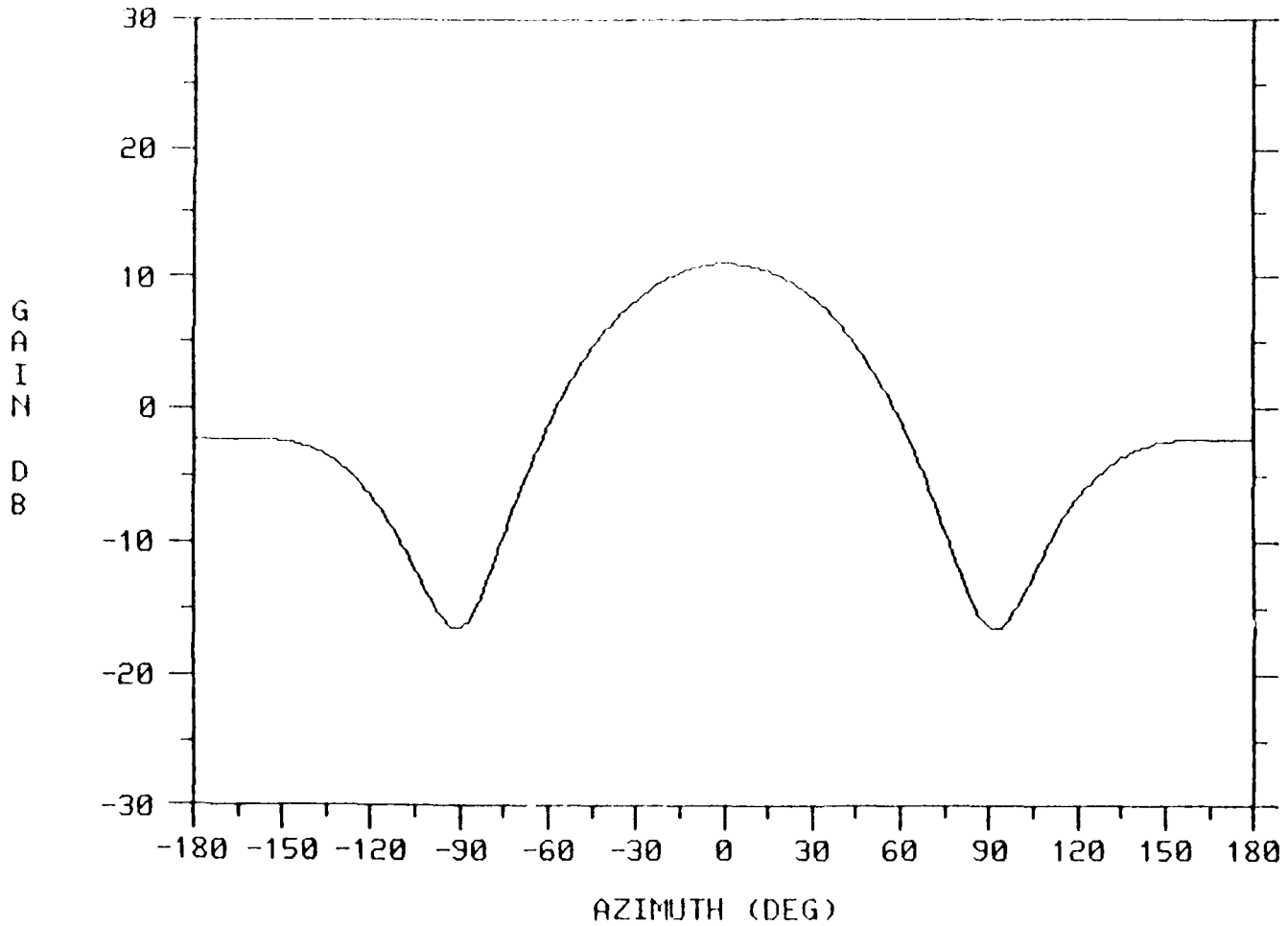

Figure 13. NEC azimuthal radiation pattern for a four element subarray including two active elements and two backpoles.

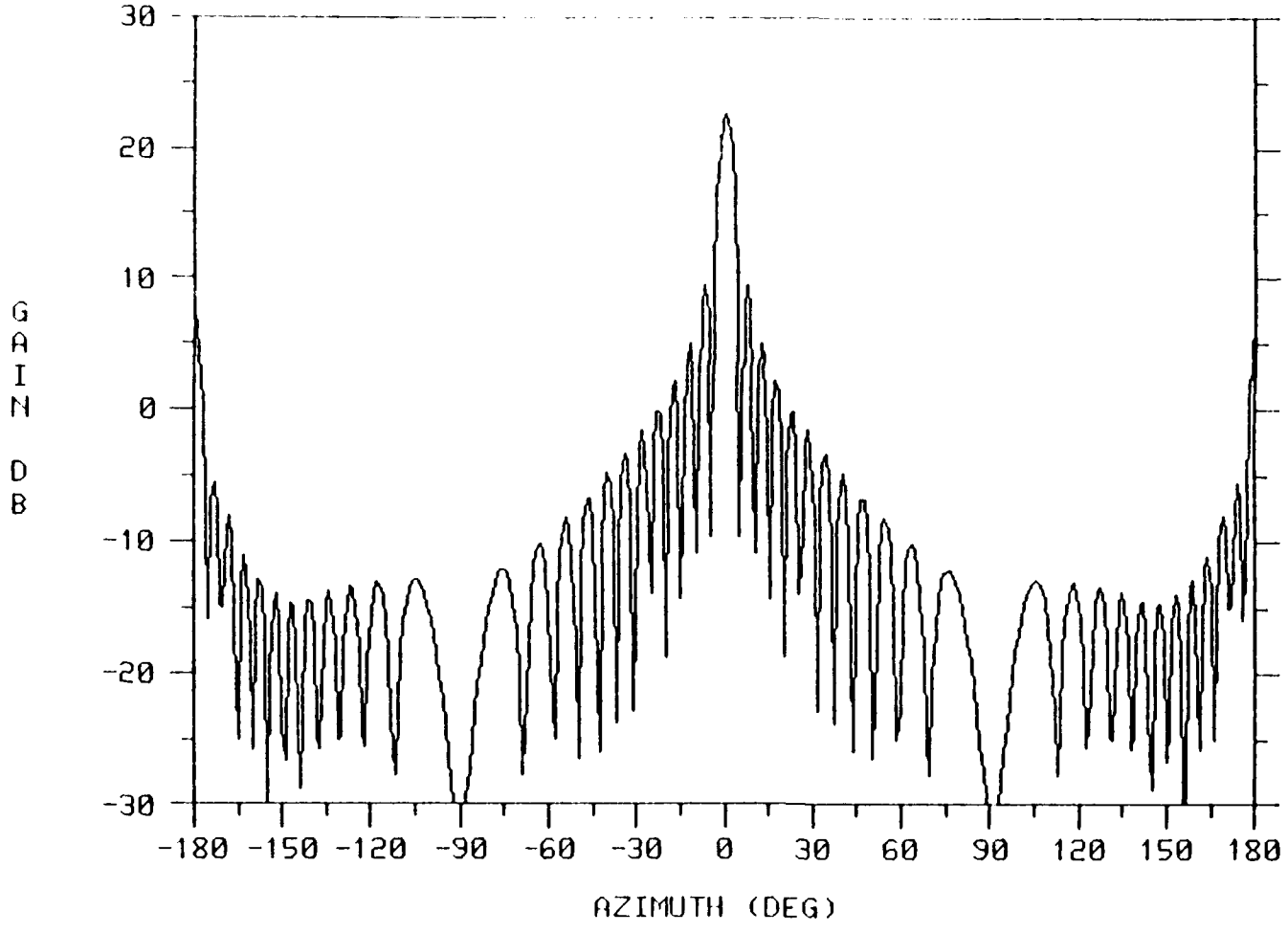

Figure 14. NEC radiation pattern for a linear array of 15 subarrays, including two active elements and two backpoles. Zero degree scan angle.

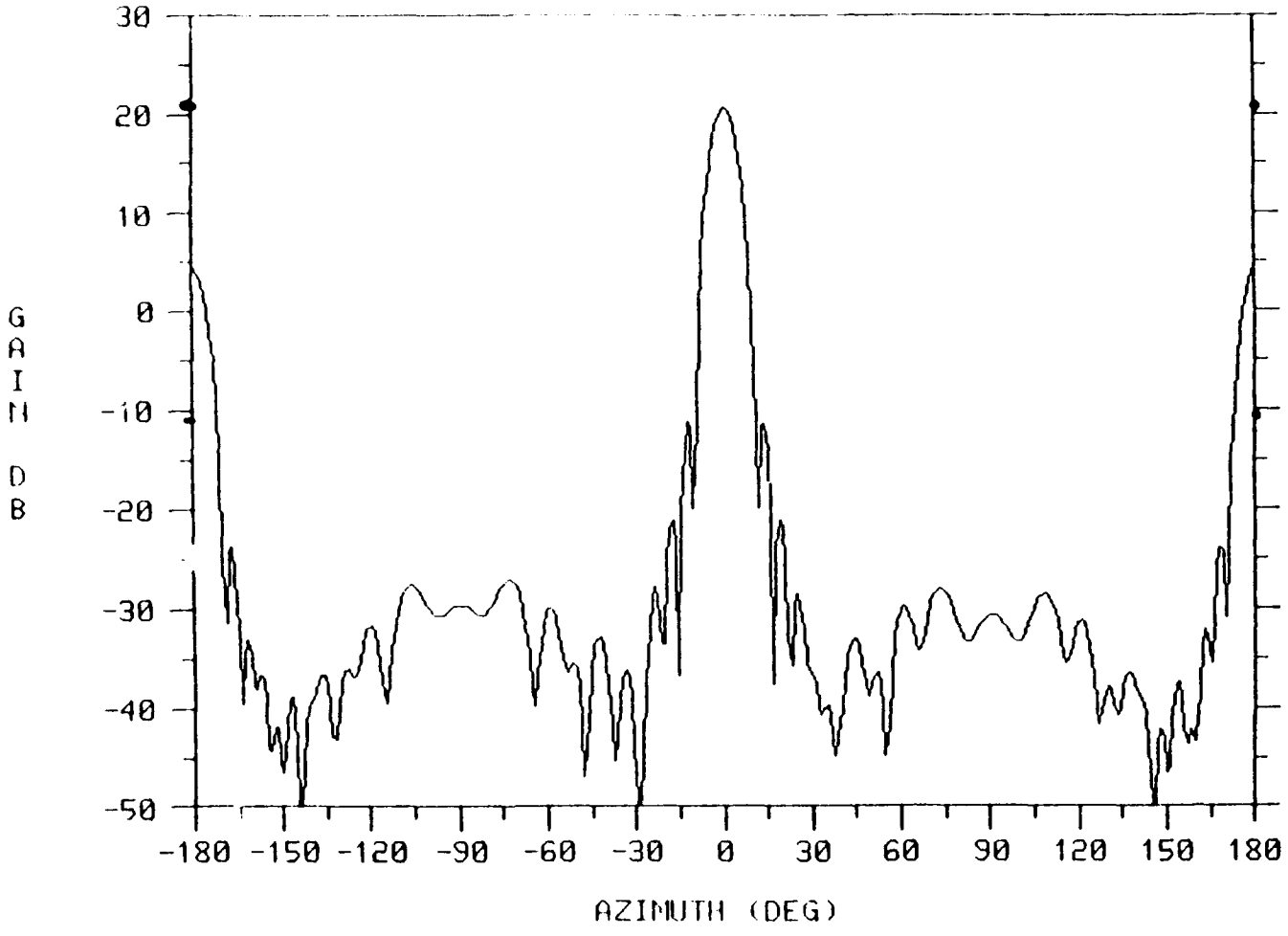

Figure 15. NEC radiation pattern for a linear array of 15 subarrays, with a 32 Db cosine squared weigthing taper.

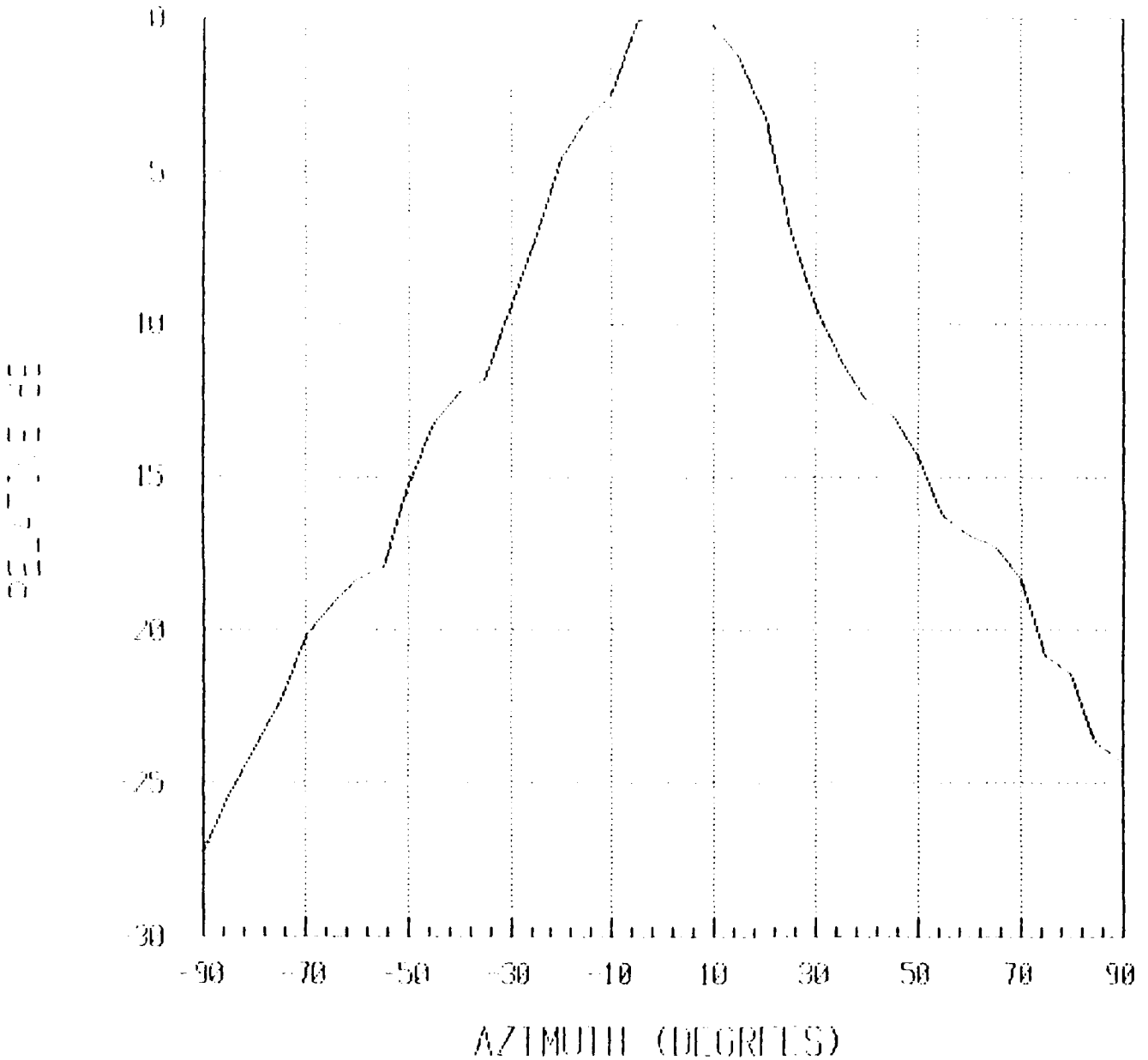

Figure 16. Measured azimuthal radiation pattern for the fielded four element subarray.

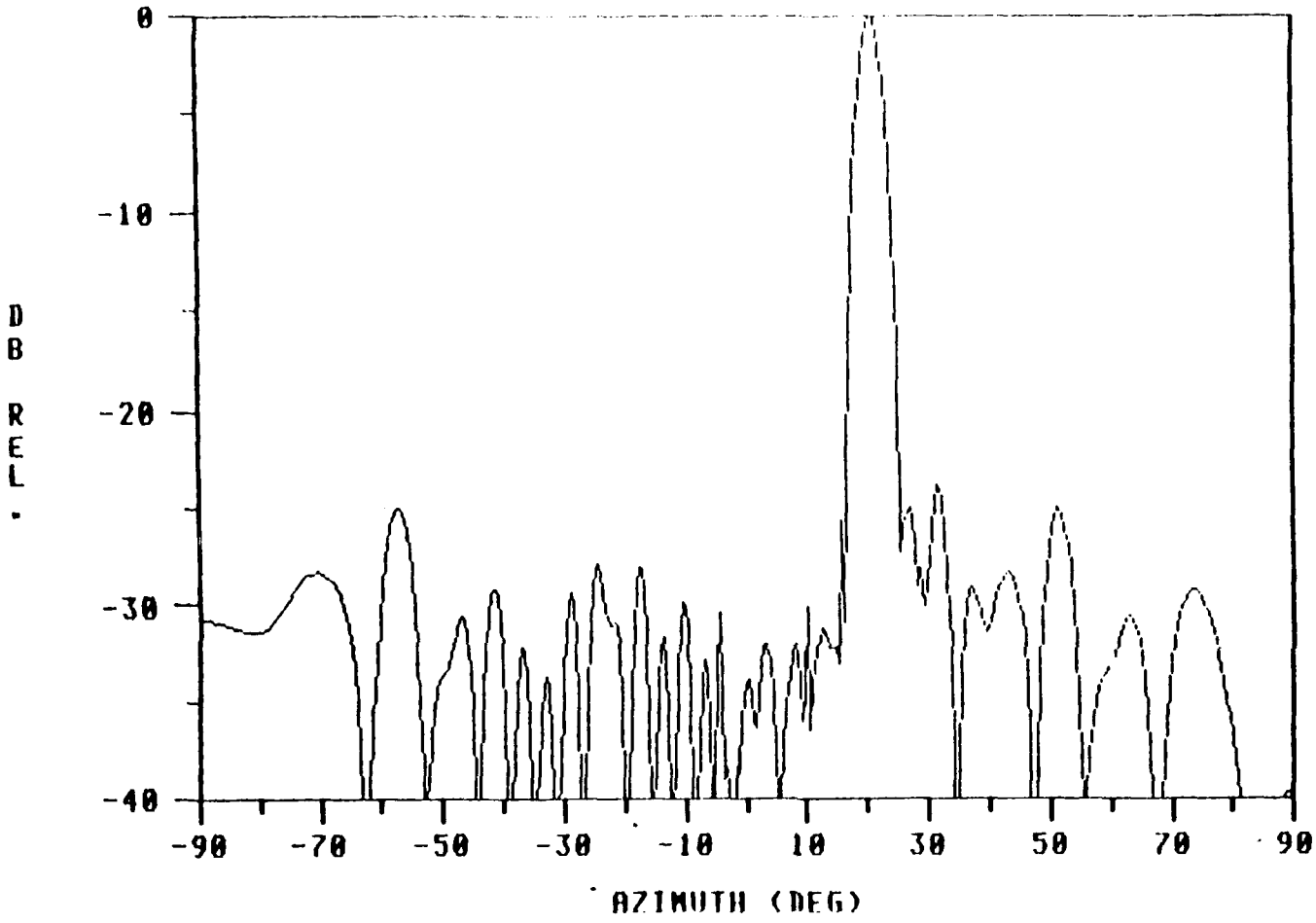

Figure 17. Measured 36 element linear array radiation pattern using the Ava transmit site as a source with a 32 db cosine squared weighing taper.

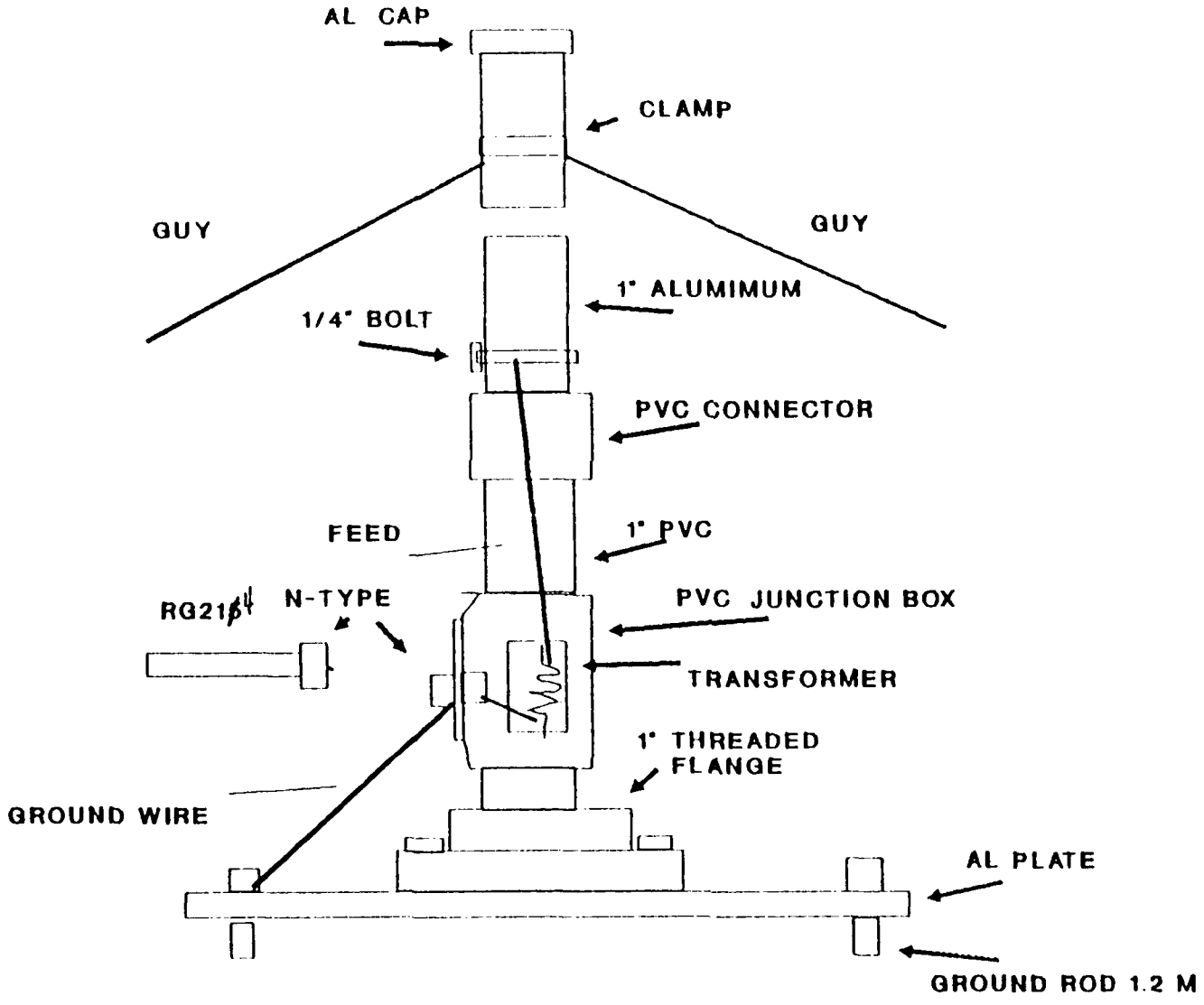

Figure 18. Schematic of one active element.

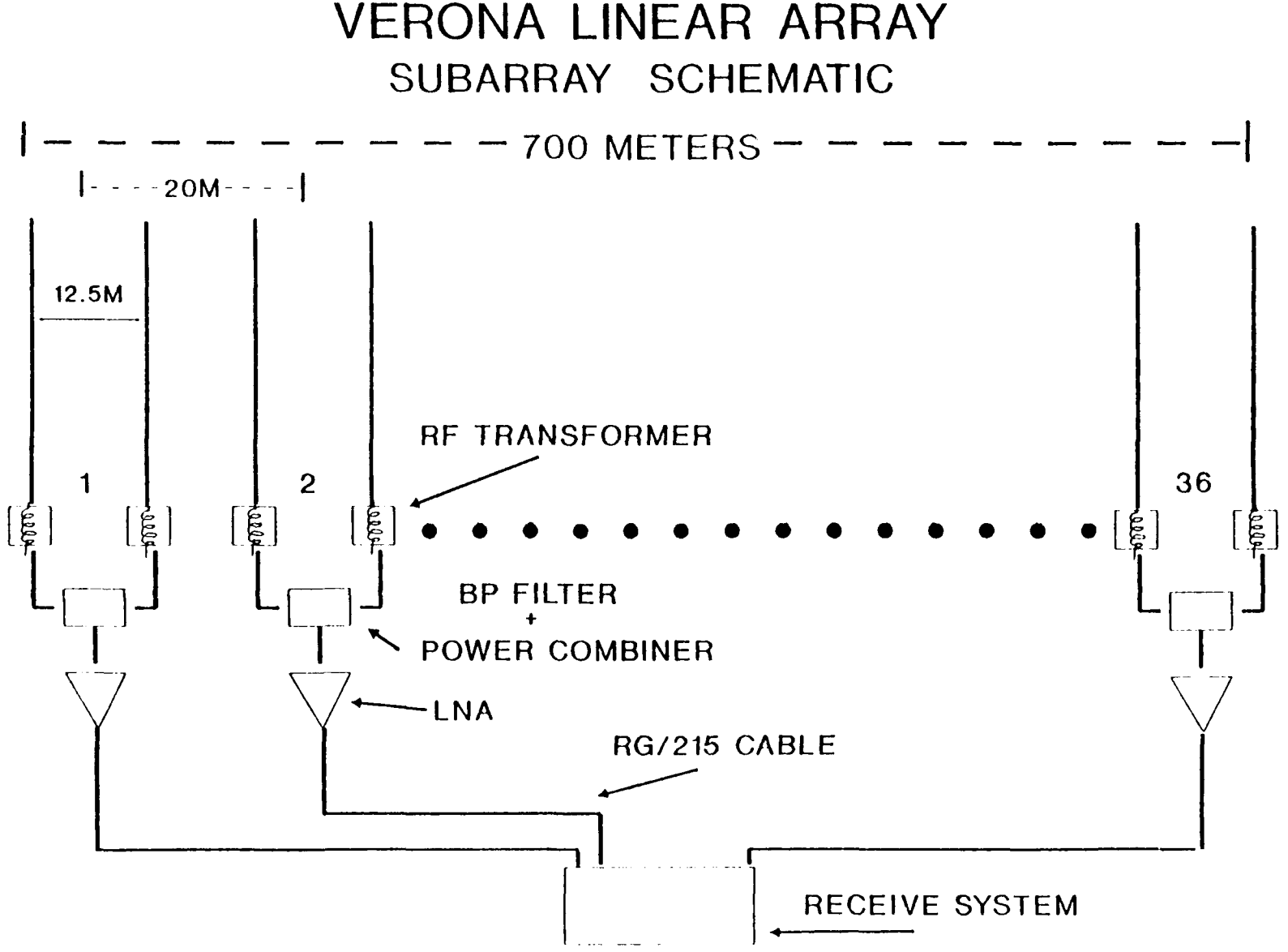

Figure 19. Subarray schematic.

COHERENCE OF HF SKYWAVE PROPAGATED WAVEFRONTS

John B. Morris
Rome Air Development Center
Hanscom AFB, MA 01731

James R. Barnum
SRI International
Menlo Park, CA 94025

Abstract

HF skywave signals are propagated beyond the Earth's curvature by refraction within the ionosphere. As a result, over-the-horizon radars have an advantage in providing advanced notice of targets of interest as well as a much enhanced surveillance area when compared to conventional line of sight radars.

After passing through the ionosphere signal wavefronts may experience perturbations in both amplitude and phase. The corrupted wavefront propagates and impinges on an antenna aperture. If we consider the ionosphere and antenna as a system, these ionospherically induced errors will negatively influence the antenna's response and consequently affect radar performance.

We have begun a measurement program to quantify statistically the effects of ionospherically induced errors on apertures up to 10 km in length. A complex correlation of the signals received along spaced coherent receivers is used to form a mutual coherence function which is useful in evaluating antenna performance. We examine limitations on the mutual coherence function in two dimensions (laterally in space, and time) for four different propagation paths. The various propagation modes are easily separated using a 12.5 KHz bandwidth

swept frequency continuous waveform (SFCW); emphasis is placed on F_2 low ray propagation.

1. Introduction

Temporal coherence affects the spectral width of a signal source and spatial coherence affects the apparent size of a signal source. In our experiment, the source, which simulates a target return, is coherent in both these domains during a measurement period. The intervening medium, namely the ionosphere, is responsible for degrading the image of the source as seen by a six element 10-km receive aperture. Ideally, the ionosphere would reflect an exact image of this perfect source. However, variations in the spatial distribution of electron density cause the image to appear to have come from and extended source. Also, the time variability of this medium produces effects similar to those produced by a source of finite spectral width.

If the errors induced by the ionosphere are considered as antenna errors, the aperture becomes only partially coherent. Techniques developed earlier[1] may be used to analyze the performance of antennas with partially coherent illumination. The corrupted wavefront is then described in terms of a mutual coherence function. Several authors, for example, Altshuler et. al.[2] and

Mitchell[3], have shown the degradation in the performance of antennas with such illumination.

In figure 1, a computer simulation shows the ideal and corrupted antenna patterns of a 100 element 10-km linear array of isotropic radiators. Interelement spacing is 2 wavelenghts at 6 MHz, and a Hamming amplitude taper is applied. The ideal pattern shows the expected 0.3-degree beamwidth and -43 dB side lobe level. In the case of the corrupted pattern, a 0.7-radian rms phase deviation and a 1 km phase error correlation length were used. These errors are assumed to have originated in the ionosphere, however we consider the effective antenna performance as though they were truely antenna errors. The averaged power pattern of this antenna/ionosphere system experiences gain loss, beam broadening, and an increase in side lobe level.

Data have been recorded to quantify the spatial and temporal variability of the ionosphere with diurnal, seasonal, and latitude changes. This ongoing experimental program is known as the Extended Coherent Aperture Project (ECAP). In this paper, we present four measured normalized mutual coherence functions for winter nighttime conditions using F_2 low ray propagation. These data are considered typical for the conditions stated, although they are snapshots or samples of this function.

2. Mutual Coherence Function

The mutual coherence function is a complex correlation of the signals across an aperture, which can be written after Born and Wolf[4] as:

$$\Gamma(x_1, x_2, \tau) = \Gamma_{12}(\tau) = \langle V_1(t+\tau)\, V_2^*(t) \rangle \qquad (1)$$

where V refers to a scalar field component, x_1 and x_2 refer to position, t refers to time, and τ represents a time delay. The sharp brackets indicate an infinite time average and * denotes complex conjugation. A time stationary ergodic process is assumed. In optics, it is convenient to define a time average since practical devices can only measure such an average. However, at HF, measurements of the instantaneous fields are easily made so that an ensemble average can be computed. We choose to rewrite (1) as

$$\Gamma(\delta, \tau) = \langle V(x+\delta, t+\tau)\, V^*(x, t) \rangle \qquad (2)$$

where δ refers to a spatial delay and the sharp brackets now indicate an ensemble average. That is, the average is performed over a group of measured wavefronts. Spatial and temporal stationarity are implied in (2) since $\Gamma(\delta, \tau)$ does not depend on space or time origin.

Each computed value of $\Gamma(\delta,\tau)$ is normalized by the average value of $\Gamma(0,0)$ for six individual receiving elements.

Spatial coherence effects are described by $\Gamma(\delta,0)$ and may be measured perpendicular to the direction of propagation with an array of antennas. $\Gamma(\delta,0)$ is also called the lateral coherence function[5] and can be related to the angular spectrum of incident plane waves. Temporal coherence effects are described by $\Gamma(0,\tau)$ and can be related to the power spectrum of the fluctuations (Weiner-Khinchine theorem). We are primarily interested in the lateral coherence function $\Gamma(\delta,0)$ because it is used to predict the average pattern of an arbitrary antenna[1]. However, the two dimensional mutual coherence function $\Gamma(\delta,\tau)$ is useful in revealing limitations on coherent integration time for operational radars.

Figure 2 shows how the various quantities of interest are interrelated. The heavy two-way arrow represents a Fourier transform pair and the one-way arrow represents a nonreversible path. Nonreversible implies, for example, that the aperture field A(x) cannot be uniquely determined from knowledge of the autocorrelation alone.

With no wavefront perturbation, $\Gamma(\delta,0)$ is unity and the effective antenna transfer function $\tau(x)$ is the unaltered autocorrelation of the field distribution. The average power pattern $P(\theta)$ (θ being the azimuthal

angle) is then simply the Fourier transform of the coherent transfer function. Alternately, the Fourier transform of the lateral coherence function $\hat{\Gamma}(\nu,0)$ (ν is an angular coordinate and the $\hat{}$ denotes a Fourier transform) is a dirac delta function which must be convolved with $|E(\theta)|^2$ to produce the average power pattern. In this case, the average power pattern is the expected coherent power pattern.

With wavefront perturbation, $P(\theta)$ can also be considered in two ways. First, the average power pattern is the Fourier transform of the product of $\Gamma(\delta,0)$ and $\langle A(x)A^*(x+\delta)\rangle$. Or equivalently, the average power pattern is the convolution of the ideal power pattern with $\hat{\Gamma}(\nu,0)$. Knowledge of $\Gamma(\delta,0)$ and its statistical variation is necessary to predict average antenna performance.

To determine the mutual coherence function for an ionospheric propagation path, one can transmit a known coherent (space, time) signal and directly measure the complex correlation of the reflected skywave signal along a series of spaced aerials. We then assign these measured errors to the aperture, and treat the aperture as being partially coherent. One could, in principle, measure the angular power spectrum directly and Fourier transform this spectrum to arrive at the lateral coherence function. For an aperture approaching 10 km in

size, the former represents a more tractable approach and is the one used here.

3. Experiment

As shown in Figure 3, and east-looking six element receive aperture was formed by the addition of two portable elements to four fixed elements of the existing Wide Aperture Research Facility (WARF) located in Los Banos, CA. The portable receive elements are relocateable and convey demodulated SFCW signals at baseband to the WARF control center by FM modulation of a UHF carrier. The fixed elements are wired directly to the WARF. This array is easily reconfigured for north-look measurements using four additional fixed elements and by moving the two portable receive elements, as shown in Figure 3. Each monopole element is a 5.5-m whip fed against a set of eight 15.2-m radial wires. The location of each whip was surveyed to a relative accuracy of ± 5 cm.

Assuming that the spatial statistics depend only on the relative positions of the elements and not on their absolute position (spatial stationarity), we generate correlations for 15 separations using six coherent receivers. Note, in figure 3, that the array was

designed to have some redundant spacings in order to verify the above assumption.

The measurement process includes data collection for three two-week periods throughout the year. Specifically, data were collected for an autumnal equinox (September 1989), a winter solstice (January 1990), and a summer solstice (June 1990). Only data recorded for the first two periods have been processed at the time of this writing. In each period, the first week is dedicated to east-look measurements, followed by a week of north-look measurements. A complete diurnal cycle is examined. Prior to data recording, a wide sweep (6-30 MHz) ionogram is recorded. This recording is a useful presentation of range or time delay versus frequency; it reveals the various ionospheric layers or modes that are present.

During the measurements, a ground wave calibrator (GWC) is situated approximately 5 km in front of the receive array. It transmits an SFCW signal and is received in parallel with a similar over-the-horizon (OTH) signal. The GWC signal is common to all array elements and is used as a coherent reference for the array.

Figure 4 shows the geographical locations of the WARF receiver and four remote OTH signal sites. For the east-look measurements, a transmitter in Lost Hill, CA excites either a transponder in White Sands Missile Range, NM, or

a transponder in Little Rock Air Force Base, AR. The ranges to the WARF are 1416 and 2585 km respectively. For the north-look measurements, a remote transmitter is situated in Langley, BC and Yellowknife NWT, both in Canada. The ranges to the WARF are 1336 and 2851 km respectively.

A 12.5 KHz bandwidth SFCW signal was used at each of the four remote sites providing a range resolution of 12 km. This resolution is quite adequate to separate the various time delayed multipath components that may exist.

Doppler resolution is achieved by Fourier transforming across 32 consecutive sweeps. A waveform repetition frequency of 20 Hz was selected. This implies 1.6 seconds of data are used to separate the GWC and OTH signals in a range-Doppler (RD) map. The GWC and OTH signals are offset in both time and frequency to allow easy detection in the RD map. Hanning weights are applied in both range and Doppler to suppress processing sidelobes. The amplitude and phase of the OTH and GWC signals are interpolated within the RD map for a better estimate of their values.

4. Results

The results presented here represent four snapshots of the two dimensional mutual coherence function during the winter solstice (January 1990), one snapshot

corresponding to each of the four remote sites. Each function was computed during nighttime conditions using an F_2 low ray propagation path. An average K_p index of 2 was reported at the time, which is indicative of relatively quiet ionospheric conditions.

Figures 5, 6, and 7 display measured mutual coherence functions for mid-latitude propagation paths, whereas figure 8 displays this function for an auroral path. Each of these curves are computed from a file containing approximately 13 minutes of data during the universal times indicated in the figures. The averaging was performed on an ensemble of wavefronts, each corrected for spherical curvature and slowly moving ionospheric tilts.

For each sampled wavefront a coherence factor was defined. This factor is the ratio of actual power that the six element array would receive to the maximum power if the errors were absent. Only the wavefronts that had a coherence factor greater than the median for the file were used to produce these curves. In this way, the malignant effects of Faraday rotation or low signal to noise ratio were removed form the results.

Most evident in the figures is that coherence degrades with range for both the north and east look directions. The coherence is reduced significantly when looking towards the long range north-look site, possibly due to

interaction with the auroral trough. There were several occasions when coherence from the Yellowknife site increased noticeably during the late afternoon.

The mutual coherence functions in figures 5 through 8 show the temporal properties of ionospheric errors as well. In general, temporal coherence appears unrelated to spatial coherence. Limitations on coherent integration time may be inferred. A comprehensive analysis of the seasonal and diurnal variation of the mutual coherence function and its effects on radar antenna performance will follow.

Acknowledgements

The authors would like to thank Dr. Erik Simpson, Mr. Kevin Reeds, Mr. James Gaddie, Mr. Dennis Gaydos, and Mr. James Binnion of SRI International for their technical contributions. Also, we would like to thank Dr. Gerard Nourry of the Communications Research Center in Ottawa, the Department of Communications in Canada, the Royal Canadian Mounted Police in Yellowknife NWT, the Science Institute of the Northwest Territories, the personnel of White Sands Missile Range NM, and the personnel of Little Rock Air Force Base, AR for their cooperation and support. Discussions with Drs. Peter Franchi and Leon Poirier of Rome Air Development Center are also appreciated.

References

1. Schell, A.C. (1967) A technique for the determination of the radiation pattern of a partially coherent aperture, IEEE Trans. on Antennas and Propagation, January:187-188.

2. Altshuler, E.E., et. al. (1990) The effects of an ionospherically induced partially coherent wavefront on the performance of a thinned random array, to be published in the IEEE Trans. on Antennas and Propagation.

3. Mitchell, R.L. (1966) Antenna Radiation Characteristics with partially coherent illumination, IEEE Trans. on Antennas and Propagation, (AP-14, No.3):324-329.

4. Born, M. and Wolf, E. (1980) Principles of Optics, Pergamon Press, sixth edition.

5. Ko H.C. (1967) Coherence theory of radio astronomical measurements, IEEE Trans. on Antennas and Propagation, (AP-15, No.1):10-20.

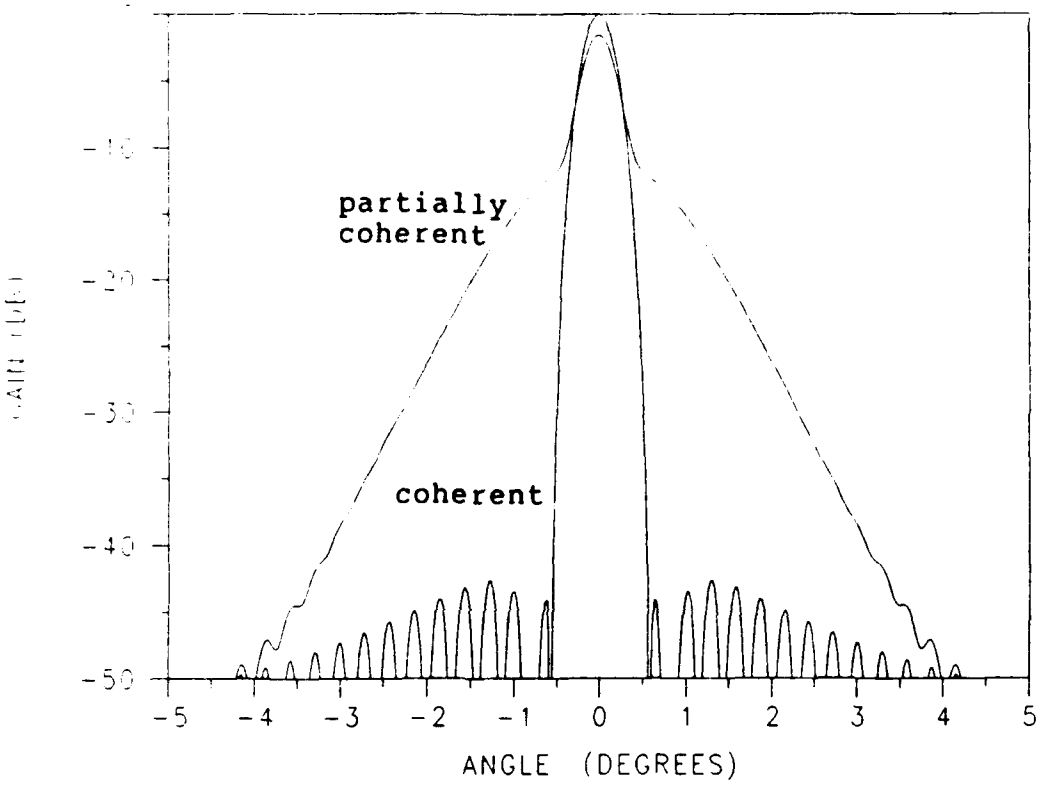

Figure 1. Comparison between coherent and partially coherent antenna patterns for a 100 element 10 km linear array.

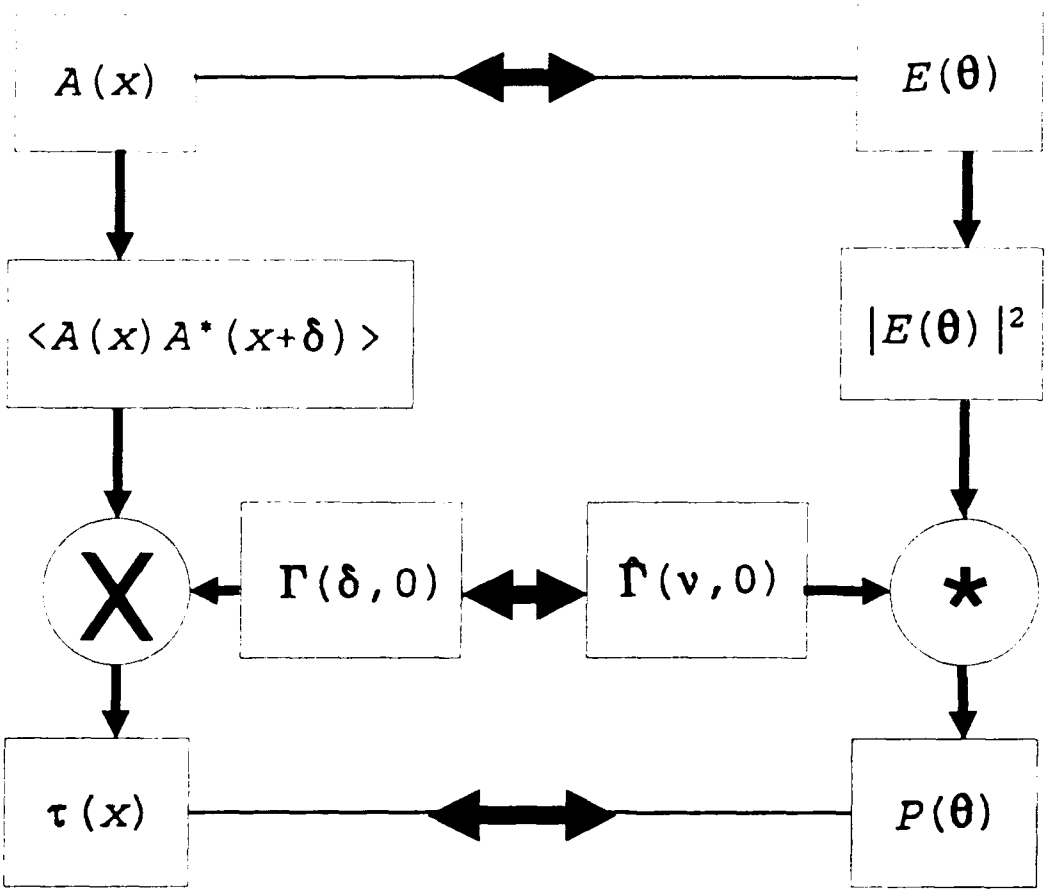

Aperture Field, $A(x)$

Voltage Pattern, $E(\theta)$

Autocorrelation, $\langle A(x)A^*(x+\delta)\rangle$

Power Pattern, $|E(\theta)|^2$

Lateral Coherence Function, $\Gamma(\delta,0)$

Effective Transfer Function, $\tau(x)$

Average Power Pattern, $P(\theta)$

Figure 2. Relationships between various parameters

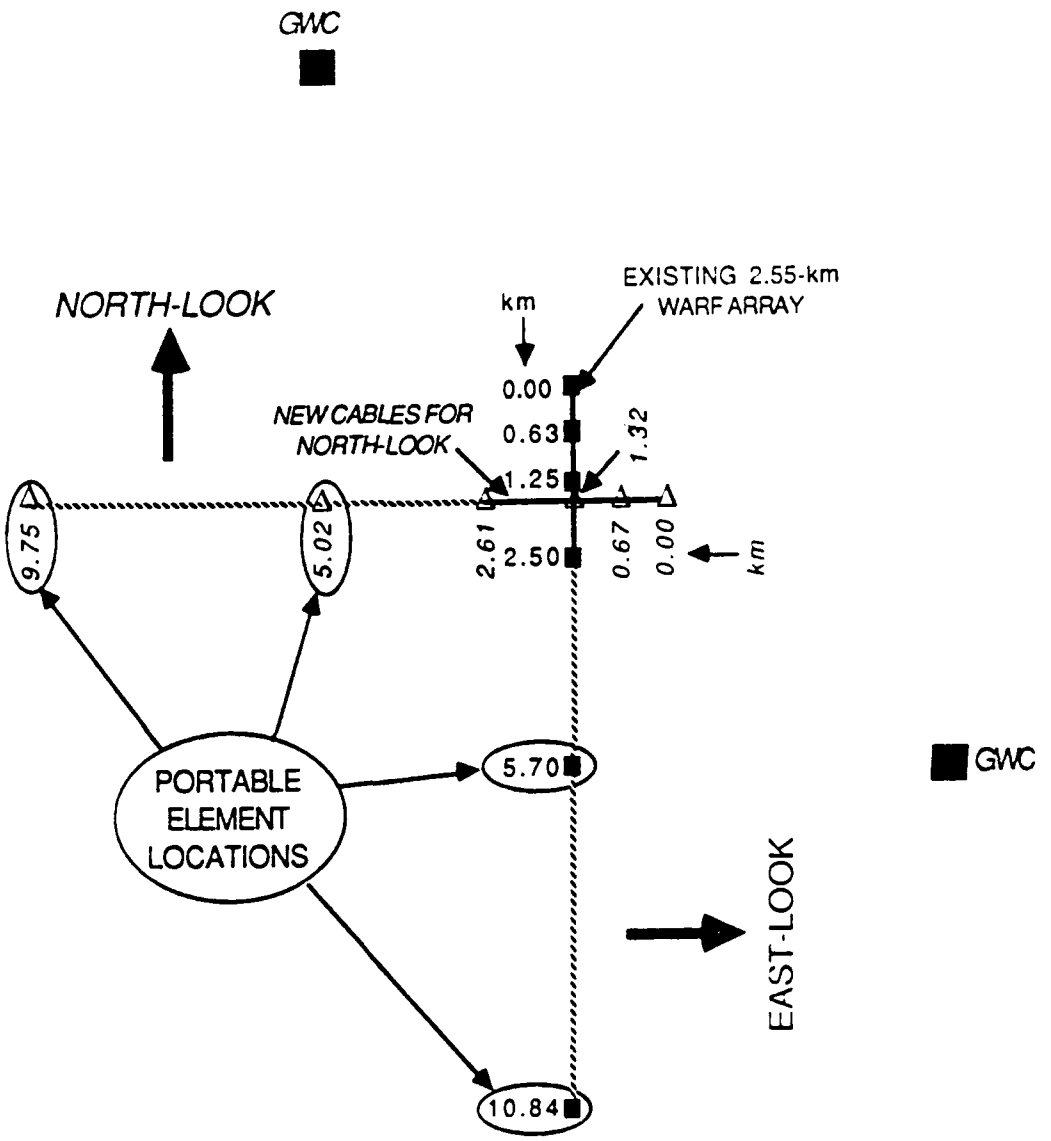

Figure 3. Receive element and ground wave calibrator locations.

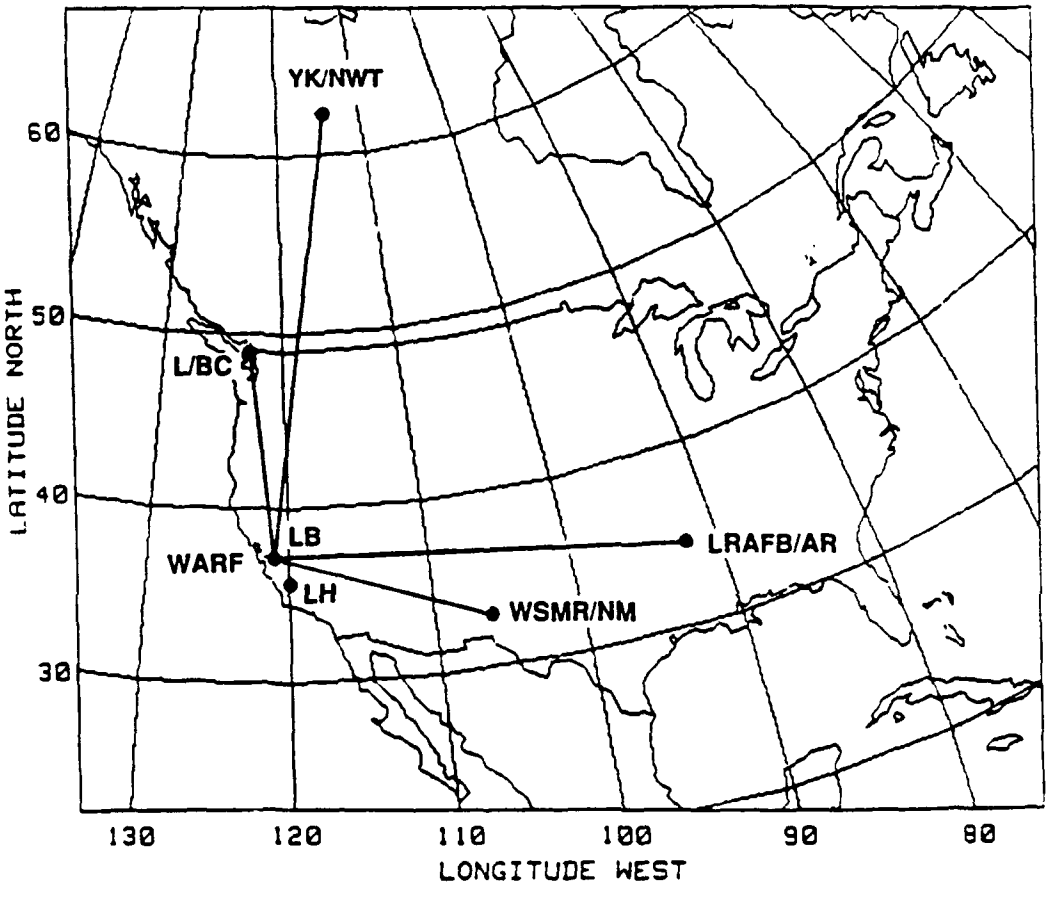

Figure 4. Geographical locations of WARF receiver and remote sites.

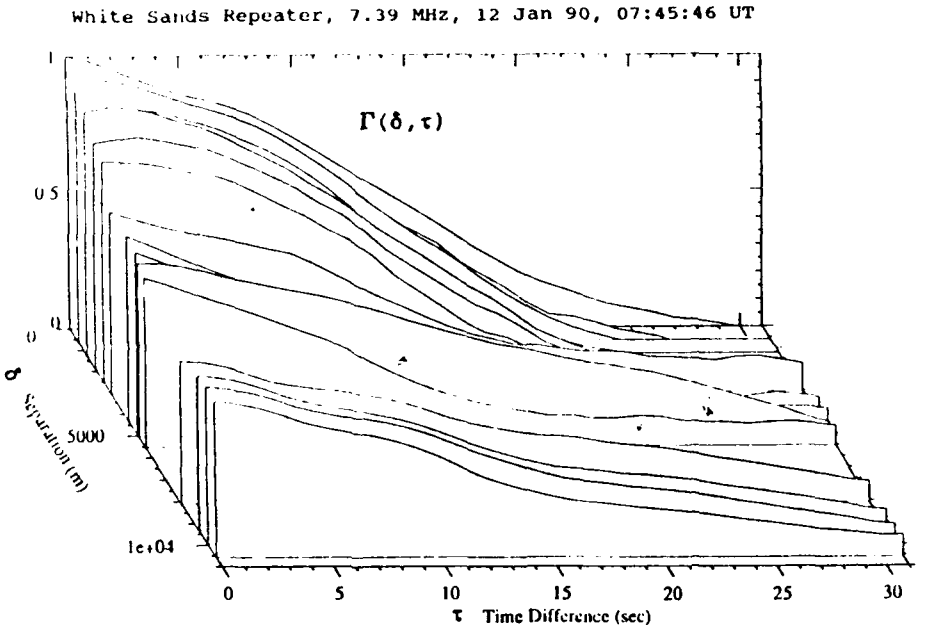

Figure 5. Mutual coherence function computed from signal transmitted via White Sands Missile Range, NM.

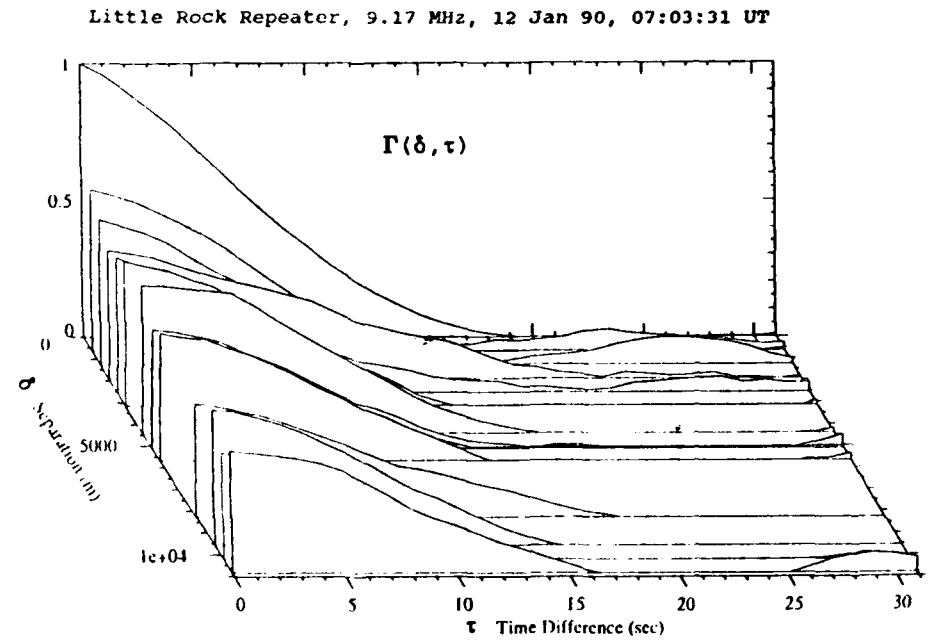

Figure 6. Mutual coherence function computed from signal transmitted via Little Rock Air Force Base, AR.

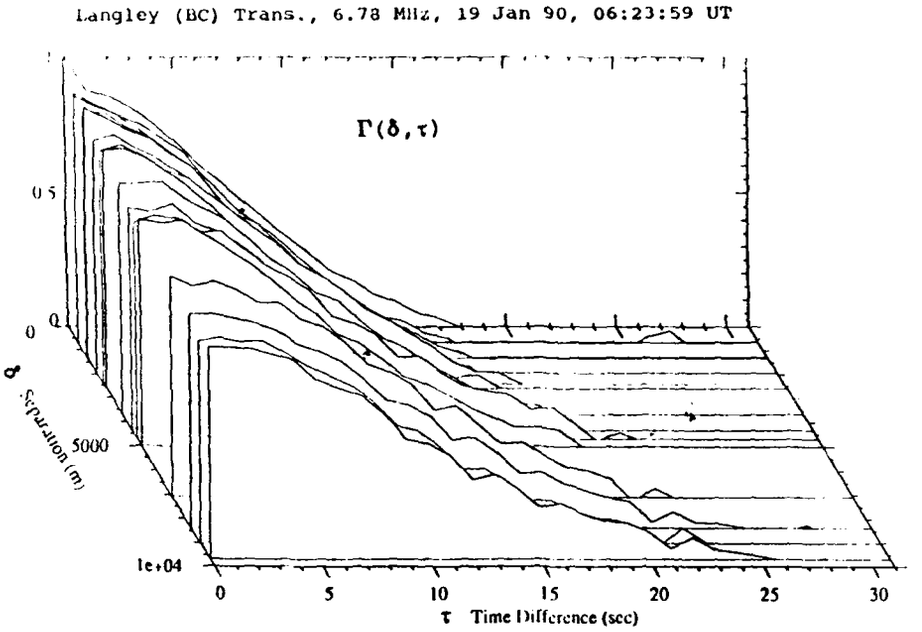

Figure 7. Mutual coherence function computed from signal transmitted via Langley, BC.

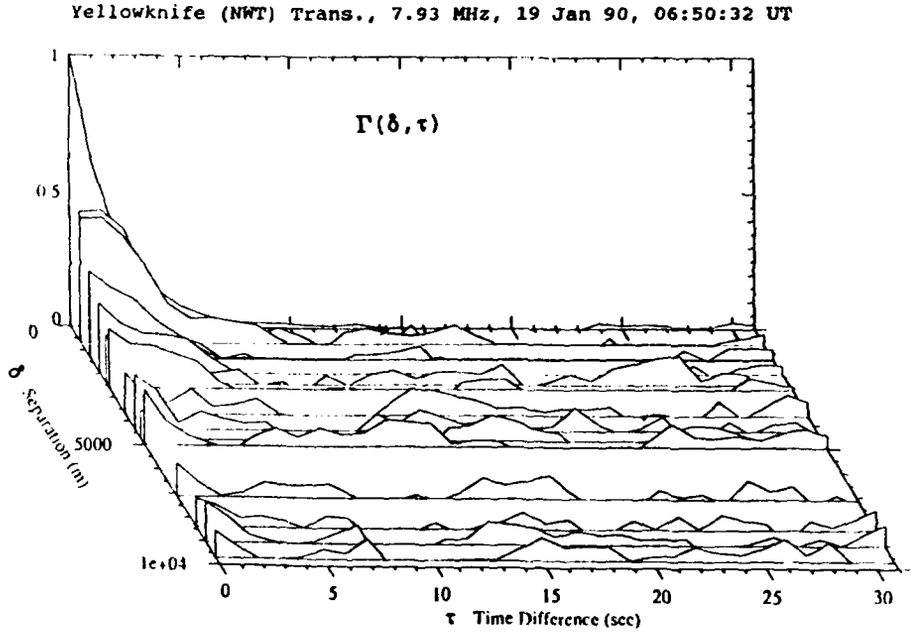

Figure 8. Mutual coherence function computed from signal transmitted via Yellowknife, NWT site.

ADAPTIVE NULLING OF TRANSIENT ATMOSPHERIC NOISE RECEIVED BY AN HF ANTENNA ARRAY

Dean O. Carhoun
The MITRE Corporation
Bedford, MA 01730

Summary

Impulsive noise transients at HF, presumably caused by atmospheric lightning discharge, can be a severe source of interference that limits the sensitivity of an HF receiver array that may be used in direction-finding or radar applications. To the extent that such energy subtends a small angle at the receiving array aperture and is received in the sidelobe region, it would be useful to suppress this source of noise by adaptive spatial nulling. We have recently examined records of elemental signals recorded from a linear HF antenna array in which the occurrence of transient atmospheric noise is evident. Closer examination of some of the stronger transients reveals that they are highly directional and provide a naturally occurring source of energy that is essentially phase-coherent across the array. These observations are based on the use of a very simple, iterative, retrodirective beamforming algorithm that calculates an estimate of the phase steering vector corresponding to the angular direction of the observed transient. This simple technique is useful not only for establishing the array weight vector to be used for nulling the interference, but also for checking the phase coherence and possibly compensating the array for calibration or propagation path phase perturbations. Results of application of this technique to the recorded field test data will be presented and the performance of the retrodirective nulling technique will be compared with an optimal baseline established by the computationally more costly method of adaptive sidelobe cancellation using a constrained least-squares algorithm employing reduced-rank principal components analysis. Results will be compared in terms of the amount of suppression of the transient noise and by the impact on the adapted array pattern.

This work was supported by the United States Air Force, Electronic Systems Division, under Contract F19628-89-C-001 with the MITRE Corporation.

ADAPTIVE NULLING OF TRANSIENT ATMOSPHERIC NOISE RECEIVED BY AN HF ANTENNA ARRAY

Dean O. Carhoun
The MITRE Corporation
Bedford, MA 01730

Abstract

Impulsive noise transients at HF, presumably caused by atmospheric lightning discharge, can be a severe source of interference that limits the sensitivity of an HF receiver array that may be used in direction-finding or radar applications. To the extent that such energy subtends a small angle at the receiving array aperture and is received in the sidelobe region, it would be useful to suppress this source of noise by adaptive spatial nulling. We have recently examined records of elemental signals recorded from a linear HF antenna array in which the occurrence of transient atmospheric noise is evident. Closer examination of some of the stronger transients reveals that they are highly directional and provide a naturally occurring source of energy that is essentially phase-coherent across the array. These observations are based on the use of a very simple, iterative, retrodirective beamforming algorithm that calculates an estimate of the phase steering vector corresponding to the angular direction of the observed transient. This simple technique is useful not only for establishing the array weight vector to be used for nulling the interference, but also for checking the phase coherence and possibly compensating the array for calibration or propagation path phase perturbations. Results of application of this technique to the recorded field test data will be presented in terms of the amount of suppression of the transient noise and the performance of the retrodirective nulling technique will be compared with an optimal baseline established by the computationally more costly method of adaptive sidelobe cancellation using a constrained least-squares algorithm employing reduced-rank principal components analysis.

1.0 Adaptive Nulling Fundamentals

Assume a linear array of N equally spaced omnidirectional antenna elements, with one-half wavelength element spacing, that is used to form a narrow beam in a designated direction. Assume that T complex digital samples, representing an analytic signal, are recorded from each array element and let X denote a $T \times N$ matrix of elemental array data in which the j^{th} column, x_j, consists of T samples recorded from the j^{th} element of the array. Denote by w_q the $N \times 1$ quiescent weight vector used to form and point a beam in the desired direction. Assume that $M < N$ array elements are used as the auxiliary elements of an adaptive sidelobe canceller used for adaptive nulling. Denote the auxiliary array data matrix by A and its adaptive weight vector, to be determined, as w. Denoting the mainbeam signal as $y = Xw_q$, the sidelobe canceller output, z, is expressed as $z = y - Aw$ where w is obtained by minimizing $z^H z$ (H denotes conjugate transpose). The adaptive weight vector is determined as (see [1])

$$w = (A^H A)^{-1} A^H y \tag{1}$$

from which it follows that the adapted output is

$$z = y - A(A^H A)^{-1} A^H y = P_A^{\perp} y. \tag{2}$$

$P_A^{\perp} = I - A(A^H A)^{-1} A^H$ is a projection operator that projects the mainbeam vector y onto the orthogonal complement of the vector subspace spanned by the columns of A to produce the adapted output z. By assumption, the auxiliary array elements receive negligible desired-signal energy and are dominated by the interference. The adaptive sidelobe canceller output can be viewed geometrically as the projection of

the array output onto a subspace that is orthogonal to the subspace determined by the interference. When the weak signal assumption is violated, the adaptive weight vector may need to be modified in accordance with linear constraints imposed to prevent desired-signal suppression [2].

In order to preserve the main features desired from the antenna pattern, while maximizing the signal-to-interference-plus-noise ratio (SINR) when there are more auxiliary elements than interfering sources, we have found it useful to use only the dominant principal components obtained from a singular value decomposition (SVD) of A in order to determine the adaptive weight vector [3]. Let A = USV be the singular value decomposition of A and assume there are p principal components distinguishing the p-dimensional interference subspace from the M–p dimensional noise subspace, as determined from analysis of the singular values [3,4]. Then the adapted output may be expressed as

$$z = (I - UU^H)y \tag{3}$$

or as

$$z_p = (I - U_p U_p^H)y \tag{4}$$

if the principal components method is used, where U_p denotes the first p columns of the matrix of left singular vectors, U, corresponding to the p dominant principal components.

It follows directly from (1) and the SVD of A that the adapted auxiliary weight vector can be determined as the projection of the quiescent weight vector onto the

vector subspace spanned by the columns of V, which are determined principally by the interference. Mathematically,

$$w = VV^H w_o \tag{5}$$

where w_o is the vector of quiescent auxiliary weights, or if the principal components method is used,

$$w_p = (V_p V_p^H) w_o \tag{6}$$

where V_p denotes the first p columns of the matrix of *right singular vectors* V (the eigenvectors of the sample covariance matrix $(A^H A)/T$), corresponding to the p dominant principal components.

Observe that the principal components method allows us to remove the distinction between an adaptive sidelobe canceller and a fully adaptive array. We may use all the array elements for adaptation, using the phase information obtained from all the elements, and choose the correct number of degrees of freedom as determined by the observed number of dominant principal components. In this case we may equate $A = X$ and $w_o = w_q$ and we see that the adapted output can be expressed as

$$z_p = X(I - V_p V_p^H) w_q. \tag{7}$$

This allows us to interpret the projection operator, $(I - V_p V_p^H)$, not only as an operator used to modify the quiescent weight vector, but also as a spatial filter that

could be applied to the array data matrix X to remove the interference components prior to beamforming. It is possible, therefore, to observe the effect of the adaptive spatial filter on the elemental signals.

2.0 The Complex Coherence Function

In the data analysis described later we have applied the principal components method of adaptation to a fully adaptive array, operating at HF, for the purpose of suppressing observed transients. While this provides an optimum performance baseline, we are also interested in simplifying the computations. We will describe a computationally simple algorithm that, in effect, extracts the largest principal component and we will show that it is effective in suppressing large transients of short duration. This algorithm is based on determining a normalized retrodirective steering vector v_S from a measurement of the complex coherence function of the received energy across the array, and using the measured vector in a projection operator $v_S v_S^H$ that can be used to project onto a one dimensional subspace or its orthogonal complement using the operator $(I - v_S v_S^H)$.

Fundamental to all adaptive phased array processing is the measurement of the phase distribution across the array resulting from one or more incident wavefronts. While this phase information is contained in the eigenvectors (or right singular vectors) that we employ in the principal components method, it can also be measured directly, particularly from a computation of the complex coherence function [5]. Let one of the array elements be used as a reference and let its analytic signal vector be denoted as $x_r = a_r e^{j\varphi_r}$ where x_r and a_r are complex vectors of T samples and $e^{j\varphi_r}$ is a scalar constant dependent on the spatial phase of the wavefront measured at the reference sensor. In our notation the phasor $e^{j\varphi_r}$, which we assume to be constant for the duration of T samples, multiplies each component of the complex vector a_r which contains the amplitude and temporal phase variation. Similarly $x_k = a_k e^{j\varphi_k}$ denotes the analytic signal sampled at the k^{th} element. If we

form the zero-lag cross-correlation between the reference signal and each of the other elemental signals we obtain the complex coherence function

$$x_r^H x_k = a_r^H a_k e^{j(\varphi_k - \varphi_r)} \qquad k = 1,..., N \tag{8}$$

The real part of (8), $2a_r^H a_k \cos(\varphi_k - \varphi_r)$, measures the mutual coherence across the array and the complex exponential $e^{j(\varphi_k - \varphi_r)}$ describes the phase distribution across the array. Notice that the measurement is taken over T samples of the data to reduce the effects of background noise that is essentially uncorrelated, or phase incoherent, from one sensor to another. In our analysis we have ignored the noise contribution since we are concerned with nulling interference that exhibits, by implication, a high per-element interference-to-noise ratio.

The complex phasor $e^{j(\varphi_r - \varphi_k)}$ can be used as a retrodirective steering vector to focus the array to match, or cancel, the phase of the impinging wave fronts. When there is only one incident wavefront, the phasor is the steering vector estimate for that source. A better estimate of the incident phase can be obtained by forming a retrodirective beam and using the beamformed output as the reference in a second measurement of the complex coherence function intended to improve the phase estimate. The process can be iterated several times if necessary. Finally, the steering vector estimated after several iterations can be used in a one-dimensional orthogonal projection operator for adaptive nulling or spatial filtering of the array data. The method is somewhat equivalent to extracting the largest principal component of the array data, but without the necessity of computing a singular value decomposition.

When more than a single degree of freedom is required because of multiple sources incident from distinctly different directions the simple algorithm described will not be adequate, although it may suppress a clearly dominant source of

interference. The technique can be useful in suppressing short transient bursts of interference when only one source is clearly dominant in the observation interval.

3.0 Adaptive Nulling of Transient Interference

Figure 1 shows an 8.5 second record (16,384 complex samples) of the envelope of the analytic signal recorded from a single element (number 41) of an 82-element narrowband linear HF antenna array tuned to the 30-meter band. Transient noise just before 2 seconds and between 6 and 7 seconds is clearly evident. The behavior is suggestive of that observed from atmospheric lightning discharge [6], but there is no corroborating evidence to firmly establish that these transients are due to lightning discharge. Further analysis will show, however, that the largest spikes are spatially coherent and can be adaptively nulled by the procedures described above.

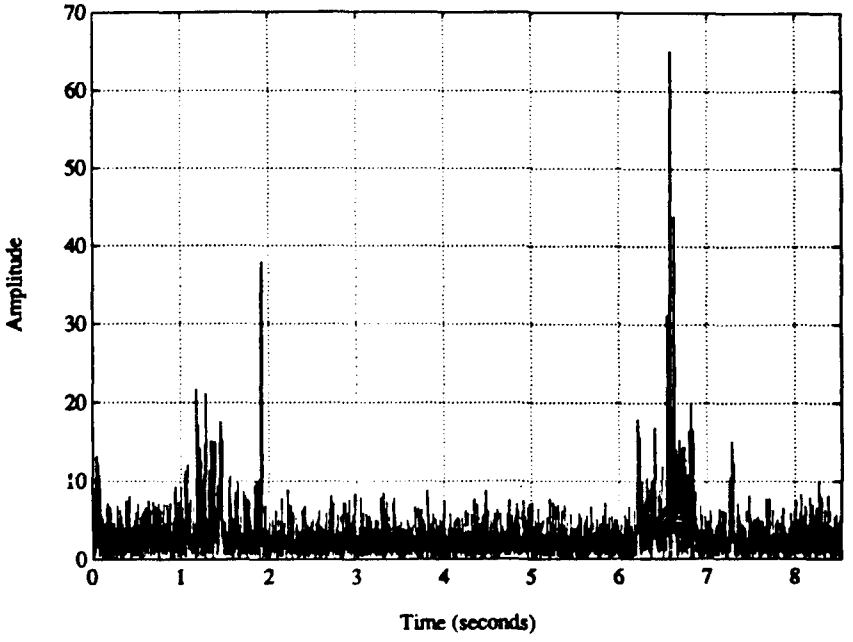

Figure 1. Detected Output from Element 41

We analyzed a 64-sample record containing the large transient at 1.9 seconds. Figure 2 shows the mutual coherence measured across the array using element 41 as a reference. It is evident that the mutual coherence falls gradually across the array and the low spatial frequency suggests a small angle of incidence with respect to boresight. Figure 3 shows the phase variation across the array (modulo 2π) calculated from the complex coherence function after one iteration. The dashed line plots the ideal phase distribution, calculated for a plane wave incident at 4.25 degrees, which closely matches the observed phase. In this measurement element 9 was inoperative, producing only receiver noise, accounting for the anomalous value at element 9.

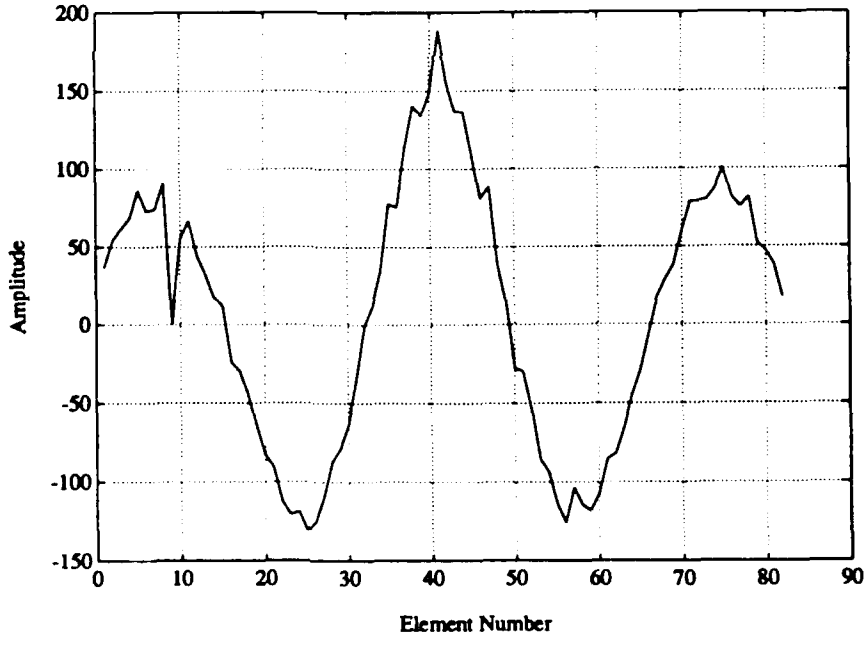

Figure 2. Mutual Coherence (4.25-Degree Transient)

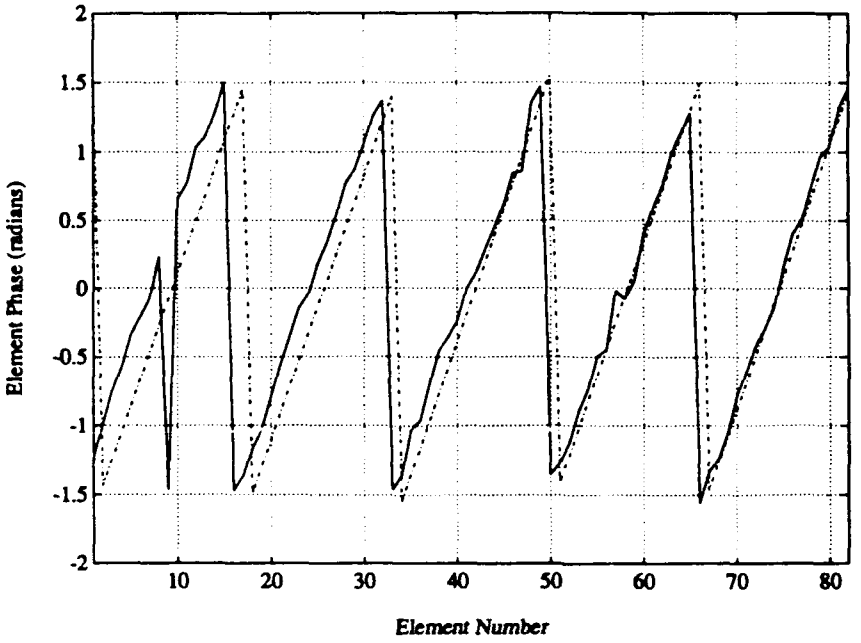

Figure 3. Element Phase Variation

Figure 4 shows the output envelope of the signal from a beam formed at 4.25 degrees, further supporting the conjecture that the transient is a spatially coherent source incident at 4.25 degrees. Closer analysis reveals that there are actually two, and perhaps three, distinct sources contained in the record. Figure 5 is a composite plot of the beam scans formed from the first three principal components of the array data; there appear to be distinct sources at 2.5 and 4 degrees and possibly a third source at 5 degrees.

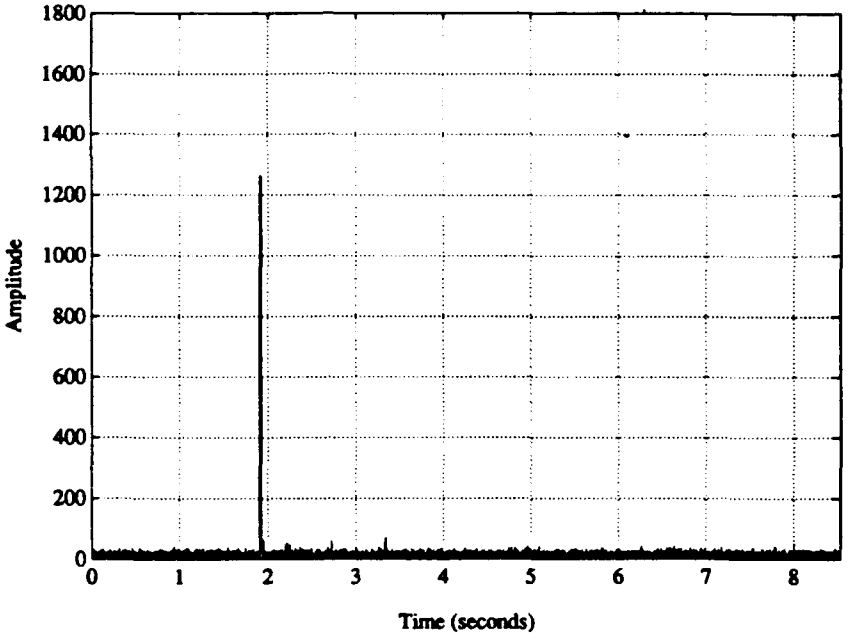

Figure 4. Receiver Output for Beam Formed at 4.25 Degrees

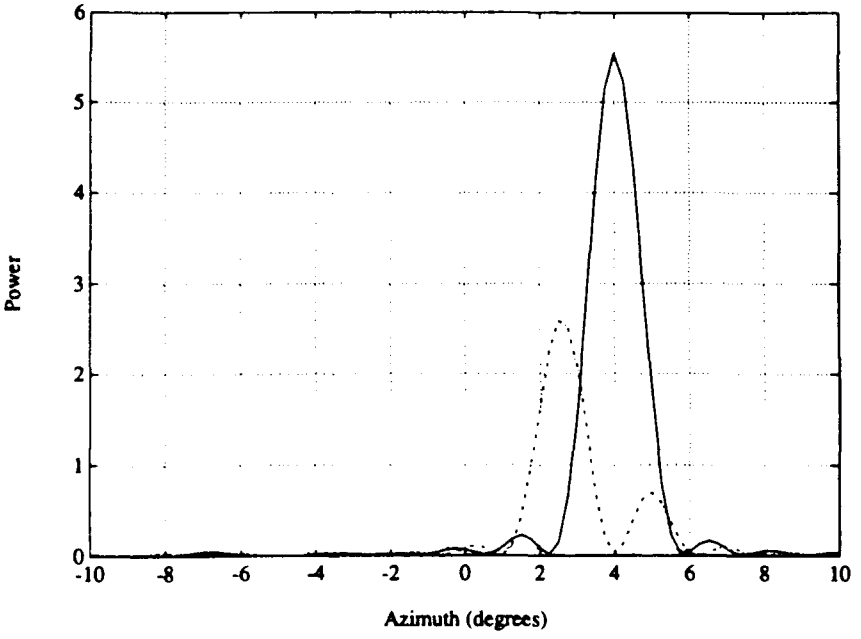

Figure 5. Beam Scan for First Three Principal Components

A similar analysis was performed using 64 samples enclosing the large transient at 6.5 seconds; the mutual coherence function is shown in figure 6. Again, spatial coherence is evident and the spatial frequency suggests a larger angle of incidence. Fine-grained principal components analysis revealed a strong transient at 49.25 degrees with an underlying narrow-band interferer at 46 degrees.

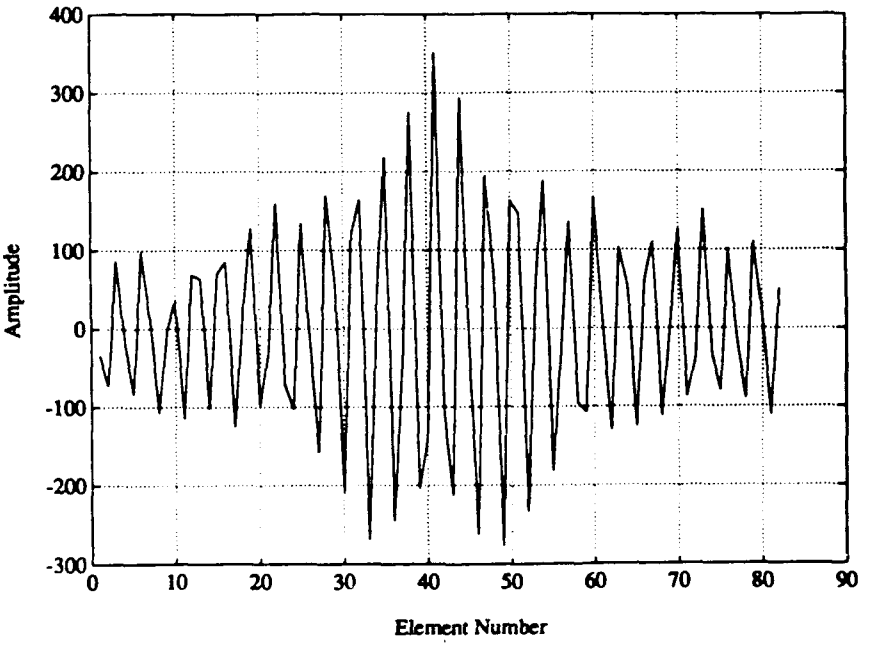

Figure 6. Mutual Coherence (49.25-Degree Transient)

Let the normalized retrodirective steering vector calculated for the 4-degree transient be denoted as v_4 and let the retrodirective vector for the 49-degree source be denoted as v_{49}. Then a product of orthogonal projections can be applied as a spatial filter to the array data matrix in order to suppress the transient events

$$X' = X(I - v_4 v_4^H)(I - v_{49} v_{49}^H). \tag{9}$$

Figure 7 shows the spatially filtered output for element 41. Although each of the components of the spatial filter were determined from 64 samples, the spatial filter was applied to all 16,384 samples of the array data. Suppression of the transient events is evident.

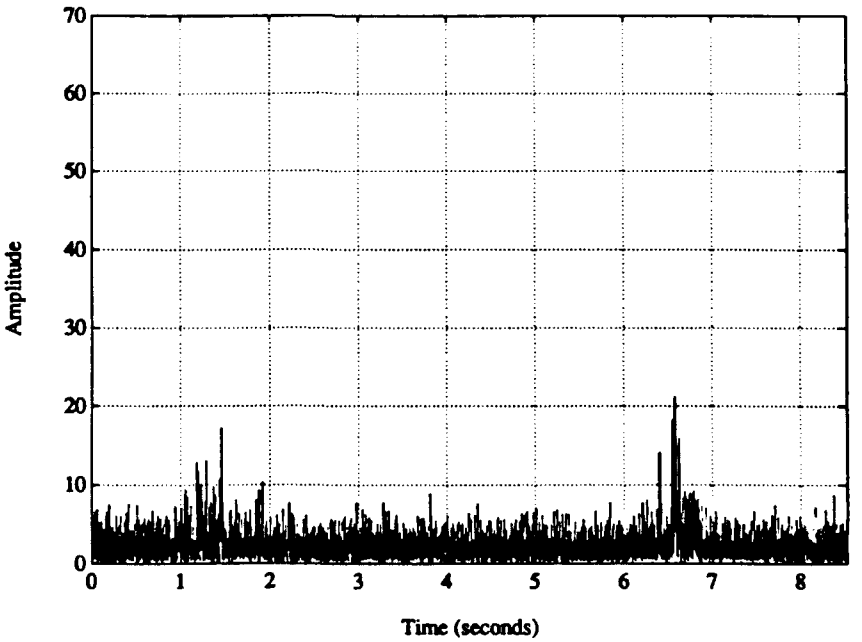

Figure 7. Spatially Filtered Output of Element 41
(Retrodirective Steering Vector Method)

Figure 8 shows the spatially filtered output of element 41 when the 64-sample records surrounding each transient are subjected to a principal components analysis, using a singular value decomposition of the data, in order to determine the adaptive spatial filter parameters. In this case five principal components were used in forming the orthogonal projection for each transient record. Comparison of figure 7 with figure 8 clearly shows that the simple algorithm based on estimating a retrodirective steering vector is suboptimum. It does, however, produce significant transient suppression and is computationally much less costly than the SVD-dependent method of principal components.

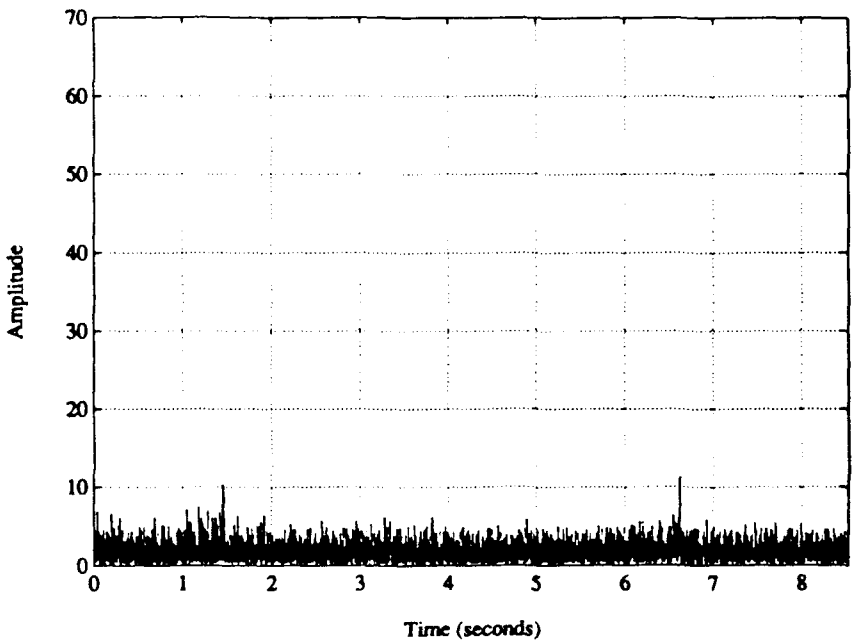

Figure 8. Spatially Filtered Output of Element 41
(Principal Components Method)

4.0 Conclusion

In this paper we have described a computationally simple algorithm, useful for adaptive nulling of spatially coherent transients received by a phased antenna array, based on measurement of the complex coherence function to extract the phase distribution from which a retrodirective steering vector is derived and used in an orthogonal projection. The effectiveness in suppressing transients was demonstrated by an actual example using data recorded from a narrowband linear HF array. The method was compared with an optimal procedure based on principal components analysis and found to be nearly optimal for the example used.

Acknowledgment

This work was supported by the United States Air Force, Electronic Systems Division, under Contract F19628-89-C-0001 with the MITRE Corporation.

References

1. Monzingo, R., and Miller, T. (1980) Introduction to Adaptive Arrays, Wiley, N. Y.

2. Griffiths, L. J. and Jim, C. W. (1982) An Alternative Approach to Linearly Constrained Adaptive Beamforming, IEEE Transactions on Antennas and Propagation, AP-30: 27-34.

3. Carhoun, D. O. and Williams, R. T. (1990) A Principal Components Sidelobe Cancellation Algorithm, Twenty-fourth Annual Asilomar Conference on Signals, Systems, and Computers, Monterey, CA.

4. Golub, G. H. and Van Loan, C. F. (1983) Matrix Computations, John Hopkins University Press, Baltimore.

5. Born, M. and Wolf, E. (1980) Principles of Optics, Pergamon Press, London.

6. Zavoli, W. B. (1977) Observed Characteristics of Ionospherically Propagated HF Atmospherics from Normal and Severe Thunderstorms, Stanford Research Institute Technical Report, Menlo Park, CA.

NEAR END FIRE EFFECTS IN A LARGE, PLANAR, RANDOM ARRAY OF MONOPOLES

R. J. RICHARDS
Electromagnetics Directorate
Rome Air Development Center
Hanscom Air Force Base, MA

Abstract

An experiment, is described, to determine the effects of mutual coupling, near end fire, on the array gain of a large, random, planar array of monopoles. An HF transmit antenna array 2.5 km in diameter with 4,000 randomly spaced elements is frequency scaled resulting in a 1.8 m diameter model antenna array. The mathematical technique and computer based numerical calculations used to approximate the expected array gain loss are presented. The approximate array gain loss is shown to be as much as 13 dB at 0° elevation angle. Calculation of the actual array gain is prohibited by the enormous amount of computer time and memory requirements, for example calculation of a single element pattern using a MicroVAX II takes approximately 47 hours of CPU time. Therefore, an experiment as described offers a practical approach to determine the array gain loss.

1. Introduction

A large, (approximately 2.5 km in diameter) circular, planar, transmit antenna array which operates in the High Frequency (HF) band (6-30 MHz) and consists of 4,000 randomly spaced sleeve dipoles with array element electrical spacing ranging from a half wavelength, at the lowest frequency (6 MHz), to 5/2 of a wavelength at the highest frequency (30 MHz) could be useful for Over-The-Horizon (OTH) radar applications. Such large planar arrays of closely spaced elements, present several significant technical problems, when phased to operate at low elevation angles (θ_{el}) near end fire. One problem is due to the mutual coupling between antenna elements that can cause a serious reduction in array gain. The coupling effects become especially critical at the low end of the HF operating band (for wideband arrays) and at very low elevation angles near end fire. The degree of mutual coupling increases as the electrical spacing of the elements decreases and when the elements are oriented such that the element's free-space pattern exhibits a maximum in the direction of its neighboring elements. The low HF frequency and very low elevation angle capability is extremely important for an OTH radar system. These systems must

operate at low elevation angle beam positions (5° to 30° or corresponding polar angles 85° to 60°), to detect targets at 3000 km ranges, and at low HF frequencies due to ionospheric propagation limitations, especially when looking north and during a significant portion of the winter night.

The coupling effect is maximum at the low HF frequency end of the radar system's operating frequency range where the transmit antenna elements are most closely spaced electrically. Because of this potential serious degradation in OTH radar system performance, it is important that mutual coupling effects, near end fire, for random planar arrays be identified and quantified.

2. Mathematical Analysis

2.1 Introduction

Mutual coupling is the result of the complex interaction between antenna elements in electrically close proximity. The interaction between elements changes the current distribution and thus the element pattern of an array element from that which it would have if it were isolated in free space. The element pattern of an isolated element will in general be quite different from the element pattern of an array element.

Furthermore, the element pattern of each element in a randomly spaced array will be unique. The element pattern is of interest because the superposition of all the array element patterns yields the active array radiation pattern. [1] [2]

The array under consideration consists of 4,000 identical, parallel, randomly located, matched-loaded, quarter wavelength monopoles on an infinite ground plane. This array is a good approximation to the 4,000 element sleeve dipole array described above. The analytical method used to analyze this array is a modification of the method of moments used by Fenn [3] to analyze periodic arrays of monopoles. The theory of images was used to replace the array of monopoles over an infinite ground plane by an array of dipoles in free space. The only factors that must then be accounted for are that the equivalent dipole has twice the input impedance and half the gain of the monopole. This dipole image approach was adopted because the mutual impedance between parallel dipoles in free space can be easily calculated using an equation given by Castello and Munk [4].

2.3 Mutual Coupling Calculations

Fenn of Lincoln Laboratories conducted a study to estimate the mutual coupling effect in large periodically spaced arrays [3]. Franchi (RADC) (private communication) using Fenn's data derived two empirical equations, one to estimate the depth of the gain null at zero degrees elevation angle as a function of the number of array elements and the element density and the other to estimate the 3 dB width of the null. The depth of the null is given by

$$f(N_e,p) = 1 \,/\, [1 + p\ (0.65\ \sqrt{N_e} - 1)] \qquad (1)$$

and the 3 dB width of the null is approximated by

$$w\ (N_e,p) = 126^\circ\ [4p/N_e]^{1/4} \qquad (2)$$

where p is the element density with respect to a unit cell size of $\lambda/2$ by $\lambda/2$ and N_e is the total number of elements. Predicted scan losses using this empirical formula for an array with N_e = 4,000 and p = 1/2 and w $(N_e,p) \approx 19^\circ$, at 6 MHz are 13.2 dB and 3 dB for elevation angles of 0° and 9.5° respectively. See Figure 1 for a plot of predicted scan loss as a function of elevation angle and frequency for a 4,000 element

periodically spaced antenna array using Equations (1) and (2). Note that the scan loss increases as the frequency and elevation angle decrease.

3. Computer Based Numerical Methods

3.1 Introduction

The usefulness of computer-based numerical methods, such as Moment Method, to determine the mutual coupling effect in a large array is limited by the amount of available processor (CPU) time and computer memory. Therefore, when an array is very large, on the order of a few thousand elements, an experiment is the only practical method to measure the expected reduction in array gain.

3.2 Numerical Method Limitations

Although calculation of all 4,000 element array gain patterns is prohibitive, it is useful to calculate several element patterns to approximate the mutual coupling effect on individual array elements and calculate an average element pattern. To calculate these element patterns, we must solve for the current vector (I) in Equation 3 either by directly inverting the previously calculated impedance matrix [Z] then multiplying it by the applied voltage vector (V) or by some other matrix solution technique.

$$(I) = [Z]^{-1} (V) \quad (3)$$

The matrix inversion method is itself time consuming; Fath and Terzuoli in 1978 [5] reported inverting an impedance matrix of (3752 by 3752) using the Electromagnetic Surface Patch (ESP) Code on a VAX-11/780. The inversion took 120 hours of CPU time. Rather than resorting to inverting the matrix to achieve a matrix solution, an iterative method, the Conjugate Gradient Method, was chosen. This method always converges to the solution in a finite number of iterations given an arbitrary initial guess, provided the matrix is nonsingular and round-off errors are kept negligible. Also, Conjugate Gradient Method requires much less memory ($\approx 5N$) than Moment Method ($\approx N^2$). In comparison to the matrix inversion method above the solution to Equation 3 where [Z] is a 4,000 by 4,000 array would only take approximately 35 hours of CPU time on a VAX-11/780 [6],[7]. Calculation of the mutual impedance matrix [Z], solving for the current vector (I) and computing a single phi cut element gain pattern for a 4,000 element random array such as the pattern shown in Figure 3 (a) takes approximately 46 CPU hours on a MicroVAX II.

3.3 Numerical Results

3.3.1 Element Gain Patterns

The element gain pattern of an isolated monopole on an infinite ground plane is shown in Figure 2 (a) and its 3-D equivalent plot is shown in Figure 2 (b). Since an isolated monopole pattern does not vary as a function of Φ, Figure 2 (b) is simply the revolution of Figure 2 (a) about its Z axis. Note in Figure 2 (a) that the polar angles (θ) between 90° to 70° and -90° to -70° correspond to the near end fire, elevation angles (θ_{el}) between 0° to 20°. Figu 3 (a) is the Φ=0 cut, element gain pattern for element # 1, located near the center of the full array of 4,000 elements. The gain pattern of an array element depends on the spacing between itself and its neighboring elements and since the element spacing is random, the gain pattern varies as a function of the azimuth angle Φ as well as the polar angle θ. This effect is illustrated in the 3-D display in Figure 3 (b). Further calculation showed that there is a significant difference between gain patterns of different array elements.

3.3.2 Array Gain Loss

The array gain loss is approximated by calculating

the difference between the isolated element gain pattern and the average element pattern of several elements located near the center of the array.

A close look at Figure 4 (a) will show the significant gain loss at the low elevation angles, between the isolated element shown in Figure 2 (a) and element # 1 shown in Figure 3 (a). Using the gain patterns of several elements located near the center of the array, an average element pattern was calculated and is shown in Figure 4 (b). Note that the average element pattern, unlike the individual element patterns, is not a strong function of Φ, therefore, the element pattern is completely described by the 2-D plot shown in Figure 4 (b). The array gain loss can be approximated by determining the difference between the average element pattern and the isolated element pattern. The comparison between the isolated and average element patterns is shown in Figure 5 (a) and the array gain loss as a function of elevation angle (θ_{el}) in Figure 5 (b). Since only relatively few element patterns were used to calculate the average element pattern the actual gain loss may be significantly different from that shown in Figure 5 (b). The approximation for the gain loss can be improved by using an average element pattern

based on a larger number of element patterns, however, calculating a large number of element patterns is impractical, therefore, an experiment to measure the actual array gain loss provides a practical approach.

4. Experiment Design

4.1 Background

The physical dimensions of the transmit array, described in the introduction, and the prohibitive use of computer time and memory requirements for calculating the predicted mutual coupling effects, led RADC to design and conduct an experiment using a frequency scaled model. As mentioned previously, the effects of mutual coupling are more serious at low HF frequencies, therefore, the model array is scaled in frequency from 6 MHz to 8 GHz. Measurements where taken at 8 GHz.

4.2 Antenna Array Model and Ground Screen

The antenna array model constructed is a 1.875 m diameter array with 4,000 randomly spaced monopole elements. This is scaled in frequency for a 2.5 km diameter array. The 4,000 monopole elements are specially manufactured Straight Bulkhead Jack Receptacle connectors with an extended center conductor equal to a quarter wavelength at 8 GHz as shown in Figure 6. The monopoles were installed in the array base plate and

match terminated in 50 Ω loads as shown in Figures 7 and 8 respectively.

It is a well documented fact that the element pattern of a single monopole over a ground plane of finite radius is affected by the size of the ground plane [8]. Since we wish to measure the array element gain patterns for near end fire, elevation angles θ_{el} from 5° to 20° the ground plane must be sufficiently large such that the isolated element gain pattern maximum occurs at polar angles $\theta_{max} \geq 85°$. Element gain patterns for a thin quarter wavelength monopole at the center of a circular ground plane of normalized radii (βa) were calculated and the angles of peak directivity plotted. A least square approximation was applied to the data to fit the curve

$$\theta_{max} = 90 - B\ (1/(\beta a)^{1/2}) \qquad (4)$$

where B is a constant. A plot of the polar angle of peak directivity versus βa for B = 118.505 is shown in Figure 9. Using the results illustrated in Figure 9 an approximate normalized ground plane radius of $\beta a \approx 2{,}500$ is required so that $\theta_{max} \approx 87.5°$. Therefore, the effects of the finite ground plane on the element pattern are negligible for $\theta < \theta_{max}$.

Since the element gain pattern measurements will be made for one azimuth angle, the ground plane does not need to be circular, however the ground plane length in the azimuthal direction of measurement must be approximately equal to the normalized radius of βa = 2,500 and the width sufficiently large so as to contain several Fresnel zones. Therefore, to minimize the effects of a finite ground plane the model array is placed on a 4.88 m X 23.16 m solid aluminum ground plane such that the center of the array is 17.07 m from the forward edge and 6.09 m from the rear edge. The ground plane, shown in Figure 10, is constructed from thirty eight, 1.22 m X 2.44 m sheets of 0.64 cm thick aluminum plates bolted together with countersunk bolts and mounted on top of 2.13 m high platform. Electrical continuity between each sheet is maintained by inserting an 0.64 cm X 0.32 cm aluminum knitted wire mesh with mesh core gasket between the plates and covering the seam with conductive adhesive aluminum tape. The ground plane was leveled to a tolerance of ± 0.32 cm at each of the 48 adjustment points using a transit.

4.3 Experiment Configuration

Far field measurements require that the transmit and receive antennas be separated by a minimum range of

$$R = 2\ D^2/\lambda \qquad (5)$$

where D is the diameter of the array and R is the range. For D equal to the diameter of the array and a wavelength of 2.5 cm at 12 GHz the range length (R) required equals 290 m An antenna range of this size is not readily available, therefore, an approximation for R was made. Since element patterns will be measured individually with all other elements match loaded the coupling between elements should become negligible within half the diameter of the array. For this case then D is equal to D/2 and the range R becomes R/4 or approximately 72 m. The elevation angles of interest were determined by using Figure 1 and noting that the scan loss becomes negligible at elevation angles greater than 16°. However, for completeness measurements should be made at as high an elevation angle as the antenna range permits. Using an existing RADC tower and locating the array 72 m from the tower, elevation angles up to 19° can be measured. Figure 11 is a sketch of the Experiment Configuration. Since the reciprocity theorem applies for antenna radiation patterns [9], the transmit antenna model and its ground plane is set up on the ground and operated in the receive mode while a transmit

antenna horn is moved up and down the tower. A standard gain monopole is mounted on the ground plane next to the array and 4,000 monopole element gain patterns are made by taking the difference in dB between the array test element and the standard gain element received signal levels.

4.4 Measurement Equipment Description

The equipment for this experiment consists of the transmit, receive and antenna positioning equipment controlled by a Hewlett Packard computer as shown in the block diagram illustrated in Figure 12.

4.4.1 Transmit Equipment

The transmit equipment consists of a Backward Wave Oscillator (BWO) source, 10 W Traveling Wave Tube (TWT) amplifier, 100 ft of low loss coaxial cable and X-Band horn antenna. The X-band horn antenna has elevation and azimuthal patterns such that the gain (towards the receive element under test) variation is less than 1 dB as the horn travels the height of the tower.

4.4.2 Receive Equipment

The receive equipment consists of an SA 1711 receiver, ratiometer, RF switch, and two mixers. The receive equipment is set up in the shared mixer mode configuration to provide synchronous switching in order

to time share the mixer between the standard gain monopole and the array test monopole element while maintaining phase lock of the RF signal through the Automatic Phase Control (APC) mixer. Receiver channel A is connected to the standard gain monopole and channel B to the array element under test. The ratiometer displays the difference in dB between these two channels. Ten samples are averaged per quarter degree of elevation angle and this average is recorded on disk for later processing. Signal averaging is used to minimize the local background environmental noise effects.

4.4.3 Antenna Positioning Equipment

The antenna positioning equipment consists of a controller card, microstep indexer card, driver card and stepper motor configured as shown in Figure 13. The system controller card is operated through the IEEE-488 bus by a program run on the HP computer. Signals from the controller are sent to a microstep indexer which provides the driver card with the correct number of properly sequenced phase control signals to accelerate, drive and decelerate the stepper motor as well as correct for backlash in the 10:1 gear reducer. The driver card supplies power to a 2-phase stepper motor to

turn a 10:1 gear reducer and drive the drum and cable assembly that is connected to the X-band horn cart. On command from the HP computer the stepper motor drives the transmitting X-band horn cart along the rail system attached to the tower with a positional accuracy of greater than 0.08 cm.

5. Element Gain Pattern Measurements

5.1 Reference Monopole Element Gain Pattern

The reference monopole element gain pattern was measured in the conventional way using a standard gain horn and the gain transfer measurement technique. The reference monopole element is identical to the 4,000 elements in the array and is mounted on the ground plane 1.73 m (46 wavelengths) away from the center of the array. The standard gain horn is located 0.5 m from the reference monopole element next to the ground plane and at the same distance from the transmitting horn as the reference element. The reference element and the standard gain horn are used in the receive mode with the transmitting horn located on the tower at an elevation angle of 10° with respect to the ground plane. Then a complete reference element pattern measurement is made from 0° to 19° at 1/4° increments. Transmitter power fluctuations due to the 10 Watt TWT output and cable

flexing as the transmitting horn travels up the tower are reduced by averaging 100 measurements at every 1/4° increment. Also, a correction is made to the reference element pattern measurement to account for the gain loss as the transmitting horn travels straight up the tower rather than at a constant distance from the reference element. The resulting rcference monopole element gain pattern is shown in Figure 11 (a) compared to the calculated monopole gain pattern of a monopole on an infinite ground plane. Notice the peak of the measured element pattern is below θ_{el} = 2.5°, therefore, measurements made at elevation angles greater than 2.5° are only effected by the ± 1/2 dB ripple on the element pattern. The reference monopole element pattern is not greatly effected by the finite size of the ground plane or the presence of the 4,000 element array.

5.2 Array Monopole Element Gain Patterns

The difference in dB between an array element and the reference element received signals are measured simultaneously and averaged over ten measurements for each 1/4° of elevation angle from 0° to 19°. Averaging is used to minimize the local background environment noise effects. Then, the difference must be added to the previously measured reference element gain pattern

to produce an array element gain pattern in dBi. The above procedure is repeated 4,000 times, manually switching elements between measurements. A comparison between the measured array element gain pattern for element # 1 located near the center of the array and calculated gain for element # 1 is shown in Figure 14 (b). The difference between the measured and the calculated pattern may be due to several approximations in the theory. Assuming a single sinusoidal current distribution on the wire is probably the largest contributor to the error, especially since the actual elements have a length to diameter ratio (l/d) of 7.38. The delta-gap voltage source model used for the feed region may also have some effect. Also, the ripple on the measured element pattern is due to the finite size ground plane where the theory assumes an infinite ground plane.

5.3 Array Gain Pattern

The array gain is calculated as the superposition of all 4,000 array element patterns. The array gain patterns calculated without mutual coupling, predicted with mutual coupling and measured with mutual coupling for $\Phi = 0°$ and $5° \leq \theta_{el} \leq 19°$ are shown in Figure 15. In this figure, the calculated array gain without mutual

coupling effects is the top curve. The middle curve is based on the predicted gain loss due to mutual coupling given by equations (1) and (2) for a periodically spaced array with Ne = 4,000 and p = 1/2. The bottom curve is the measured array gain pattern including mutual coupling. Note that the measured array gain (bottom curve) is lower than predicted for a periodically spaced array (middle curve). The array gain loss between the calculated without mutual coupling (top) curve and the measured with mutual coupling (bottom) curve at $\theta_{el} = 5°$ is approximately 8 dB and is still as much as 2 dB at $\theta_{el} = 19°$.

6. Summary

The analytical technique used to analyze the expected performance of a circular, randomly spaced array of monopoles over an infinite ground plane was presented. This analysis is valid for antenna elements with sinusiodal current distributions such as monopoles over an infinite ground plane. Excessive CPU time and memory requirements prohibited using this method to calculate the expected array gain based on 4,000 element patterns. However, an approximate array gain loss was calculated using an average element pattern based on several elements located near the center of the array.

Due to the computational difficulty of calculating the array gain and the physical dimensions of the proposed transmit antenna array, RADC designed an experiment using a scaled antenna array model. The antenna array model and ground plane were constructed at the RADC Hanscom AFB antenna test range. The measurement of all 4,000 transmit antenna array element patterns was completed and the array gain pattern calculated. The result of the measurements was compared to the predicted array gain and the calculated array gain without mutual coupling. The array gain loss between the calculated without mutual coupling and the measured with mutual coupling is approximately 8 dB at $\theta_{el} = 5°$ and 2 dB at $\theta_{el} = 19°$. Therefore the array gain loss, near end fire, due to mutual coupling must be taken into account when designing the transmit antenna array. Future efforts to reduce the gain loss at low elevation angles will include low coupling array element designs and terminating array elements with the impedance of an average element's input impedance when scanned near end fire.

REFERENCES

1. Warren L. Stutzman and Gary A. Thiele, Antenna Theory and Design, John Wiley & Sons, New York, 1981; pp. 154-155, 339-340.
2. R. C. Hansen, Microwave Scanning Antennas Volume II Array Theory and Practice, Academic Press, Inc., San Diego, CA, 1966; p.301
3. A. J. Fenn, "Theoretical and Experimental Study of Monopole Phased Array Antennas," IEEE Trans. on Antennas and Propagation, Vol. AP-33, pp. 1118-1126.
4. D. Castello and B. A. Munk, "Table of Mutual Impedance of Identical Dipoles in Echelon," Report 2382-1, October 1968, The Ohio State University ElectroScience Laboratory, Department of Electrical Engineering; prepared under Contract F33615-67-C-1507 for Air Force Avionics Laboratory, Wright-Patterson Air Force Base, Ohio. (AD 822013).
5. J. L. Fath and A. J. Terzuoli, "Large Matrix Problems in the Computation of Electromagnetic Fields." IEEE Atennas and Propagation Society, 1987 Symposium Digest, pp. 502-504.

6. Margret B. Woodworth, "Large Matrix Solution Techniques Applied to an Electromagnetic Scattering Problem," Interim Report RADC-TR-88-268, November 1988, ARCON Corporation; prepared under Contract F19628-86-C-0104 for the Rome Air Development Center (EECT) Hanscom Air Force Base, Massachusettes. pp. 8,26. ADA206917

7. Tapan K. Sarkar and Ercumant Arvas, "On a Class of Finite Step Iterative Methods (Conjugate Directions) for the Solution of an Operator Equation Arising in Electromagnetics," IEEE Trans. on Antennas and Propagation, Vol. AP-33, pp. 1058-1066.

8. Melvin M. Weiner, Stephen P. Cruze, Cho-Chou Li and Warren J. Wilson, Monopole Elements On Circular Ground Planes, Artech House, Inc., Norwood, MA, 1987; pp. 297-304.

9. Constantine A. Balanis, "Antenna Theory Analysis and Design,"Harper & Row, New York, 1982; pp. 94-99.

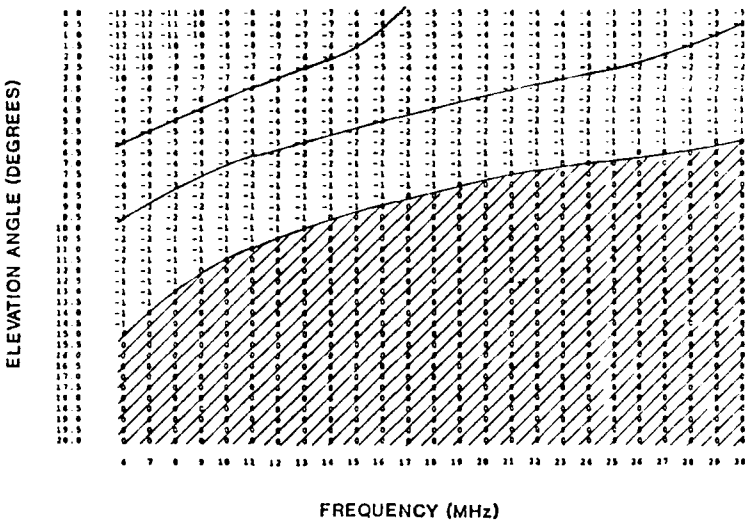

Figure 1. Predicted Scan Loss in dB for a 4,000 Element Periodically Spaced Array as a Function of Frequency and Elevation Angle.

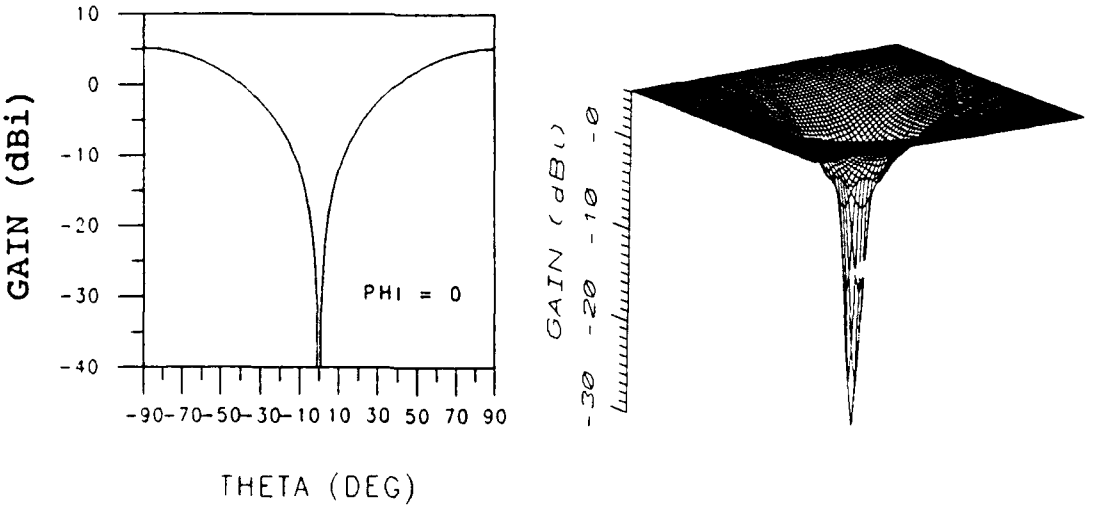

(a) (b)

Figure 2. (a) Element Gain Pattern for an Isolated Monopole on an Infinite Ground Plane. (b) 3-D view.

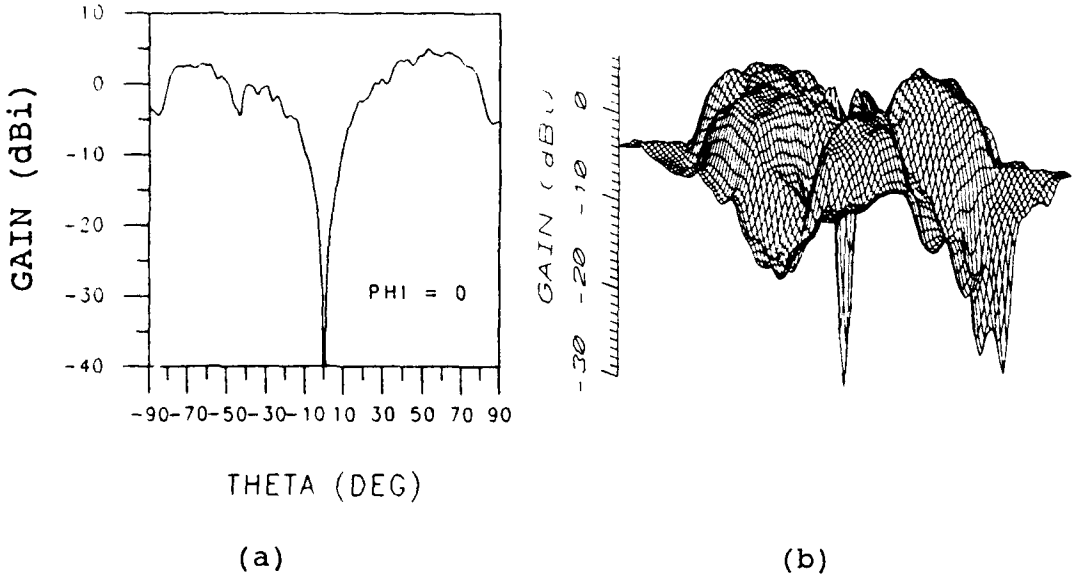

(a) (b)

Figure 3. (a) Gain Pattern for Element # 1 in the 4,000 Element Array Environment. (b) 3-D view.

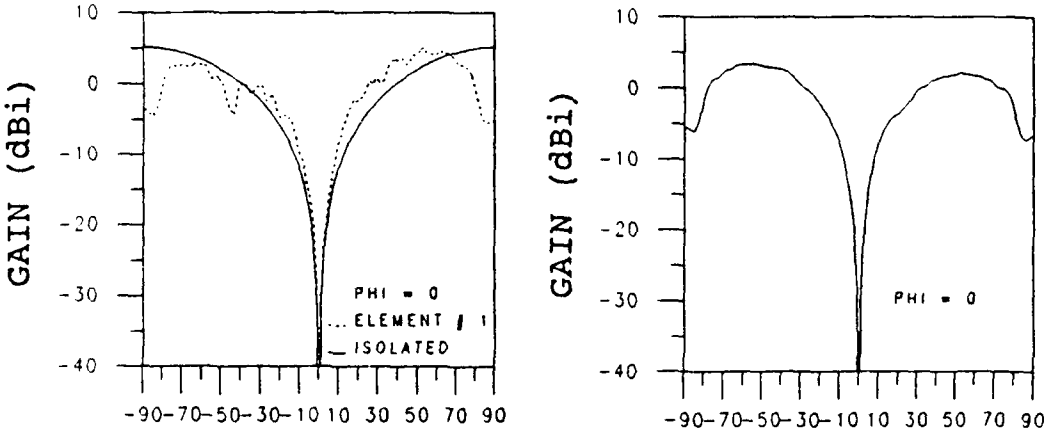

(a) (b)

Figure 4. (a) Gain Comparison Element Between an Isolated Monopole and a Monopole Near the Center of the Array. (b) Average Element Pattern.

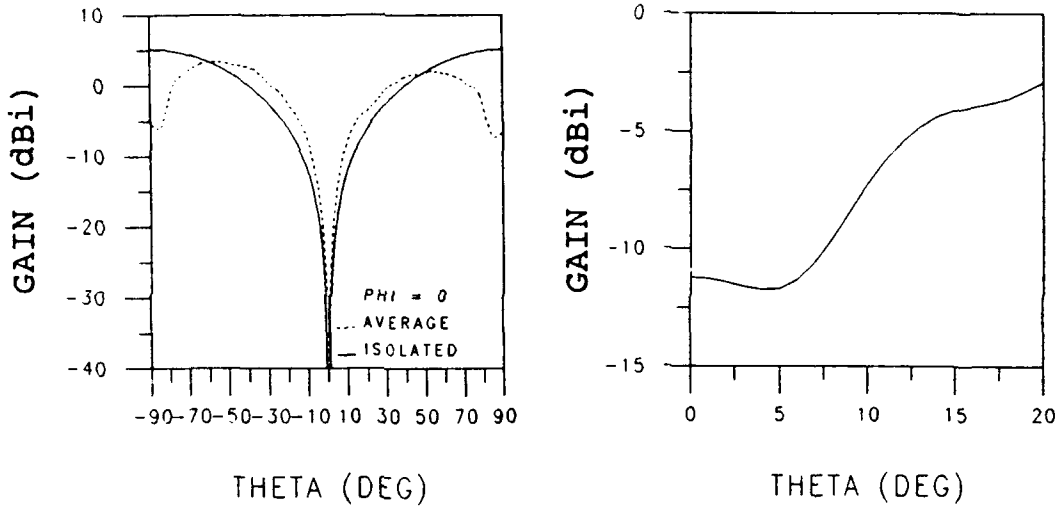

Figure 5. (a) Comparison Between Isolated Element Pattern and Average Element Pattern. (b) Array Gain Loss as a Function of Elevation Angle (θ_{el}).

Figure 6. Monopole Element.

Figure 7. Top View of AOTH Transmit Antenna Array Model with 4,000 Elements Installed.

Figure 8. Bottom View of the Transmit Antenna Array Model with 4,000 Loads Attached.

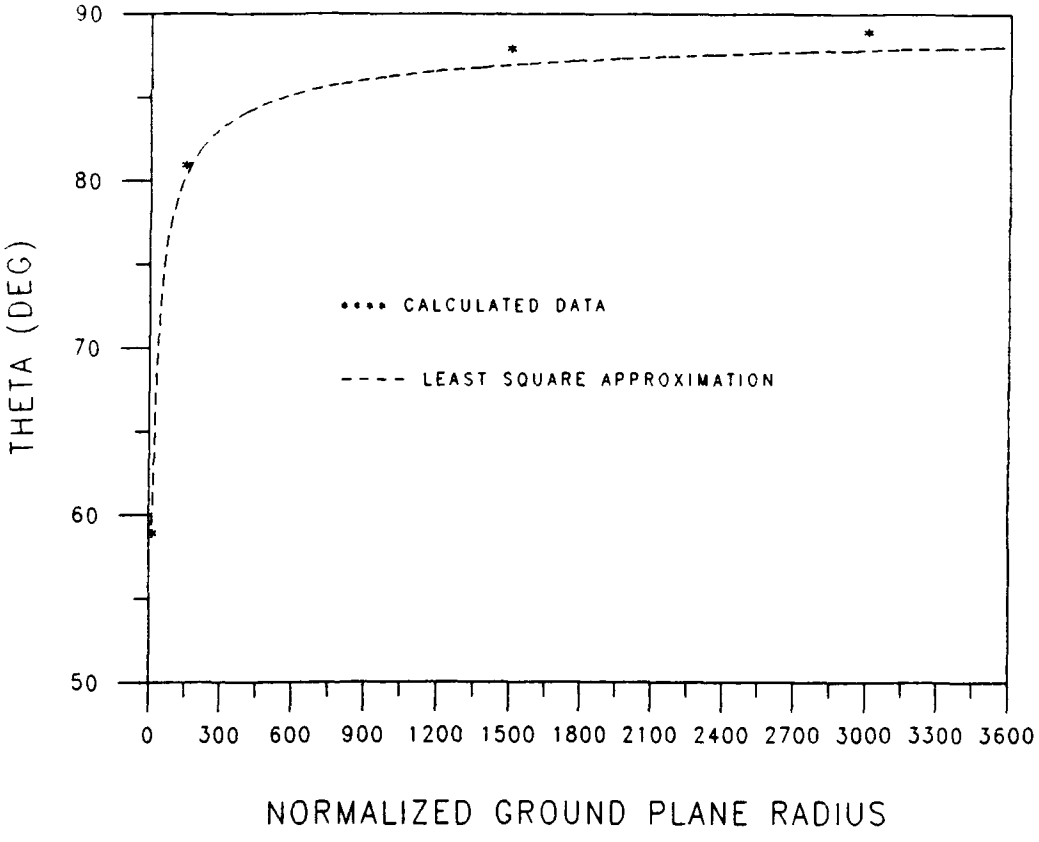

Figure 9. Least Square Approximation of Polar Angle of Peak Directivity Versus Normalized Ground Plane Radius for $15 \leq \beta a \leq 3600$.

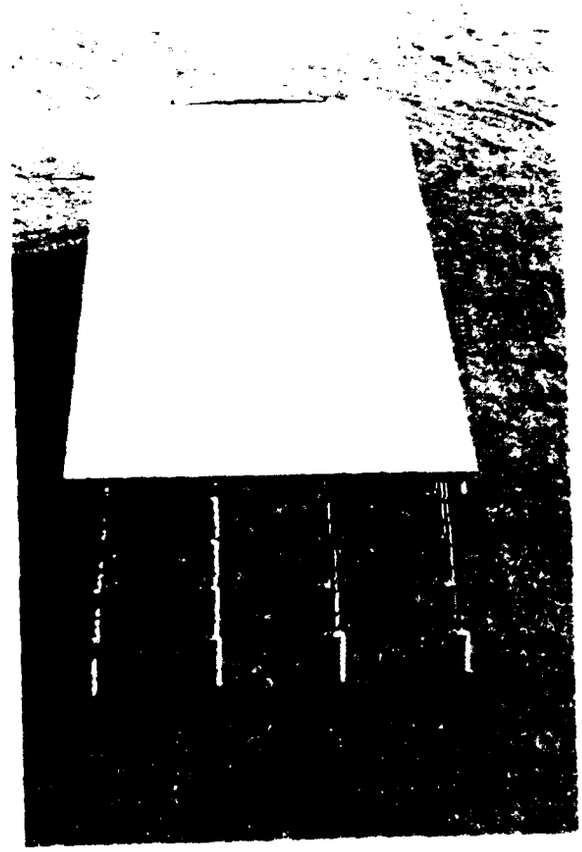

Figure 10. Ground Plane with the Model AOTH Transmit Antenna Array Installed.

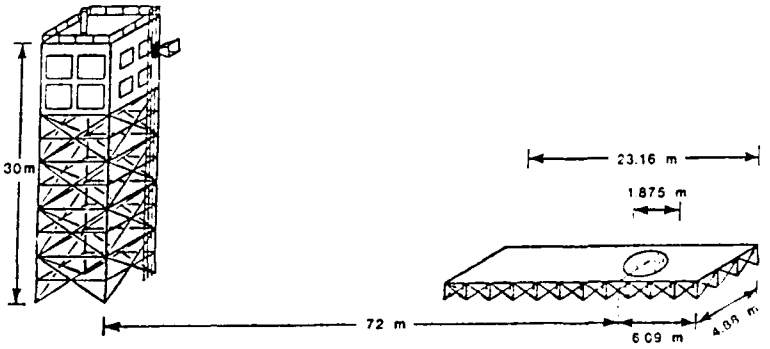

ANTENNA MODEL SPECIFICATIONS

DIAMETER	-	1.875 m
ELEMENTS	-	4000, 1/4 WAVELENGTH MONOPOLES
ELEMENT SPACING	-	RANDOM, 5/2 WAVELENGTH EXCLUSION ZONES
FREQUENCY RANGE	-	8 - 12 GHz (6 - 9 MHz)
GROUND PLANE	-	4.88 - 23.16 m

Figure 11. Experiment Configuration

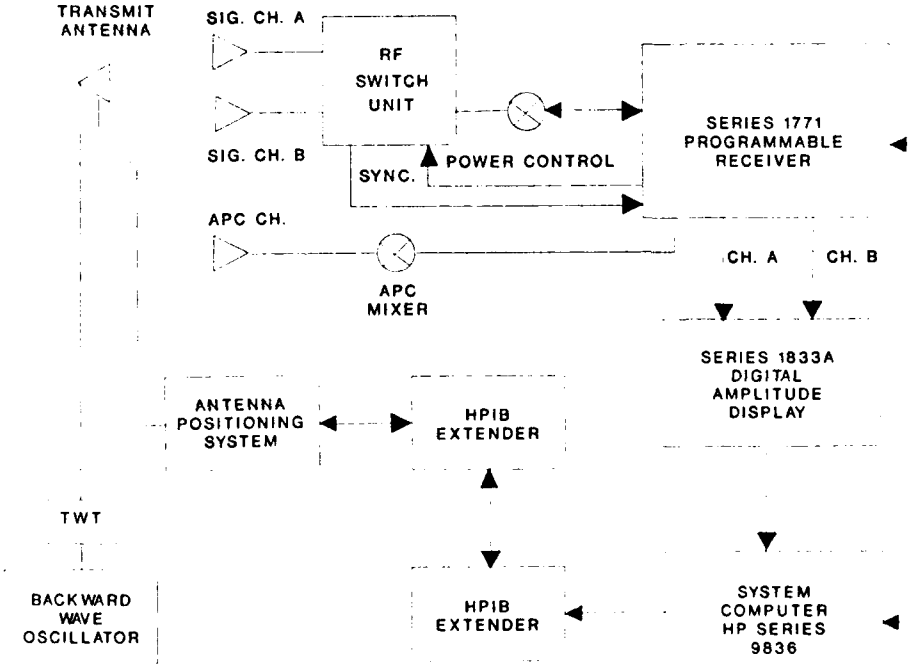

Figure 12. Block Diagram of the Measurement Equipment.

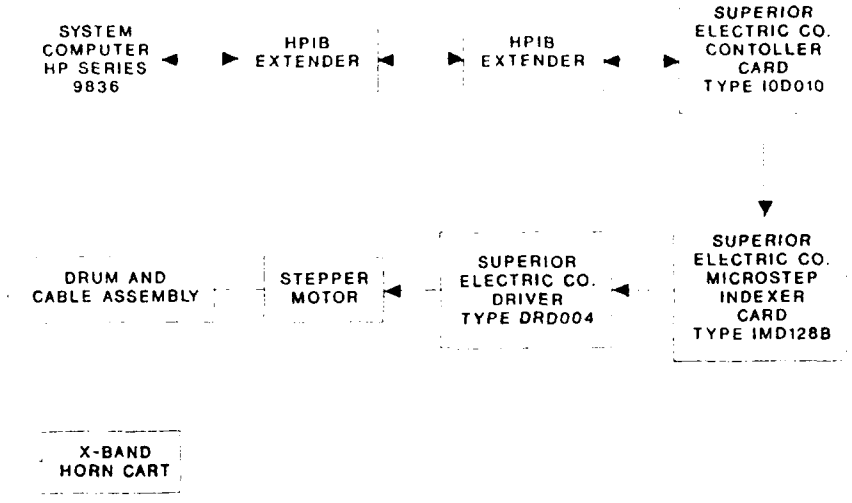

Figure 13. Antenna Positioning Equipment Block Diagram.

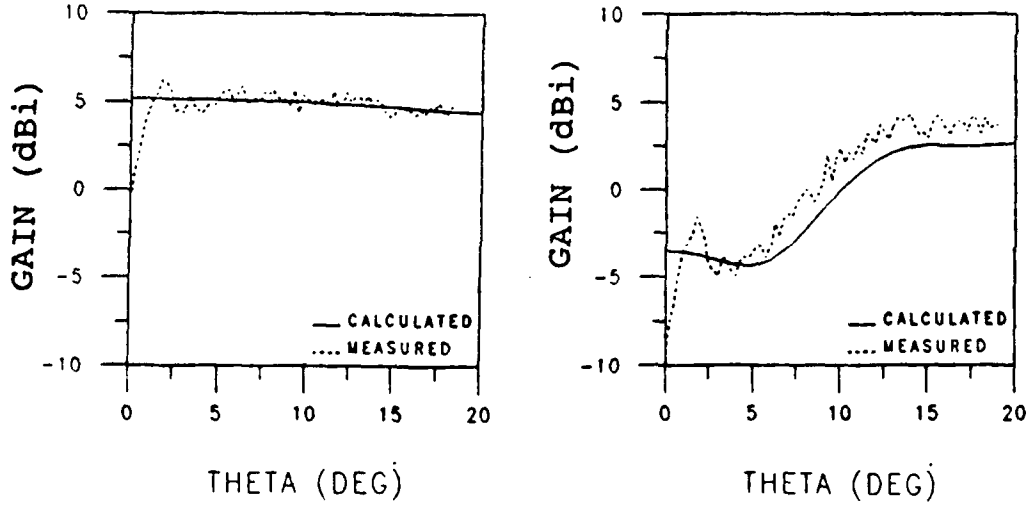

Figure 14. (a) Gain Comparison Between a Monopole on an Ifinite Ground Plane and the Reference Monopole. (b) Comparison Between the Measured and the Calculated Gain for Element # 1.

ANTENNA DESIGNS FOR THE AN/FPS-118 OTH RADAR

K. JOHN SCOTT
GENERAL ELECTRIC COMPANY
SYRACUSE, NEW YORK

ABSTRACT

The AN/FPS-118 Radar is a Frequency Modulation/ Continuous Wave (FM/CW) bi-static system having a transmit site, a receive site, and an operations site. The transmit and receive sites are generally separated by approximately 100 miles to provide sufficient isolation between the transmit and receive functions.

The transmit subsystem utilizes elemental transmitters and a low-level beamformer which has amplitude and phase control for each transmitter. The elemental transmitters drive a twelve-element dipole array for each of six bands with a backscreen and groundscreen reflector. A calibration coupler is provided at each transmitter output to sample amplitude and phase. An iterative calibration procedure is used to establish the aperture illumination needed for the desired beamwidth, scan angle, and frequency.

The receive subsystem utilizes elemental receivers and a digital beamformer. The elemental receivers are connected to a monopole array of 246 elements for three interleaved bands with a backscreen and groundscreen reflector. A test signal is inserted at each receiver input to provide amplitude and phase corrections for each receiver path.

An ionospheric backscatter sounder system provides the data needed to direct the operation of the radar. The sounder uses a transmit antenna having a beamwidth nominally equal to the 60-degree scan coverage of each radar segment. Eight narrow receive beams, spaced in 7.5-degree increments, are provided by an analog beamformer which utilizes a section of the radar receive antenna. This paper describes the transmit and receive antenna designs which evolved from the system performance requirements.

1.0. OVERVIEW

The site ground conditions and the surrounding terrain are integral parts of a High Frequency (HF) antenna design. At HF (long wavelengths), antennas are physically very large and site groundslope, blockage in the "look" direction, and soil characteristics (dielectric constant/conductivity) must be included in antenna performance tradeoffs. The choice of polarization is dictated by the elevation angle coverage requirements and antenna height constraints. The AN/FPS-118 antennas use primarily vertical polarization and long groundscreens to enhance pattern response at low elevation angles.

The CONUS OTH System will consist of an East Coast Radar (ECRS), A West Coast Radar (WCRS), an Alaskan Radar (ARS), and a Central Radar System (CRS). Figure 1 shows the total coverage of the CONUS OTH System.

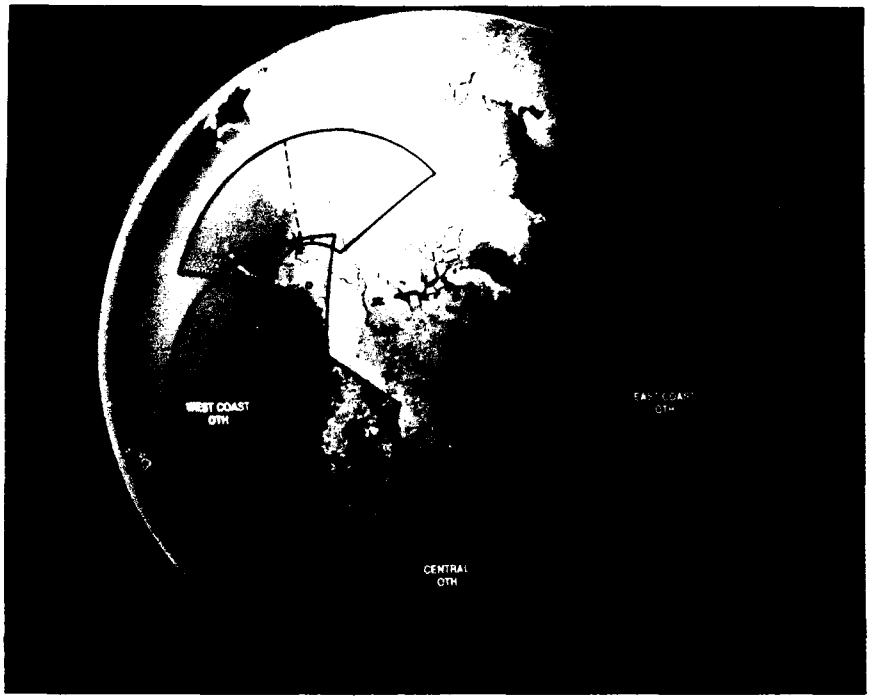

Figure 1. AN/FPS-118 Radar System Coverage

Six antennas are provided for the ECRS. Three broadside transmit arrays and three broadside receive arrays located in the state of Maine are used to provide 180-degree coverage along the Atlantic Coast of the North American continent. Figures 2 and 3 show the transmit and receive antennas, respectively. A transmit/receive antenna pair covers a 60-degree segment in eight sequential 7.5-degree increments. The transmit beam for any increment is overlaid with three 2.5-degree receive beams.

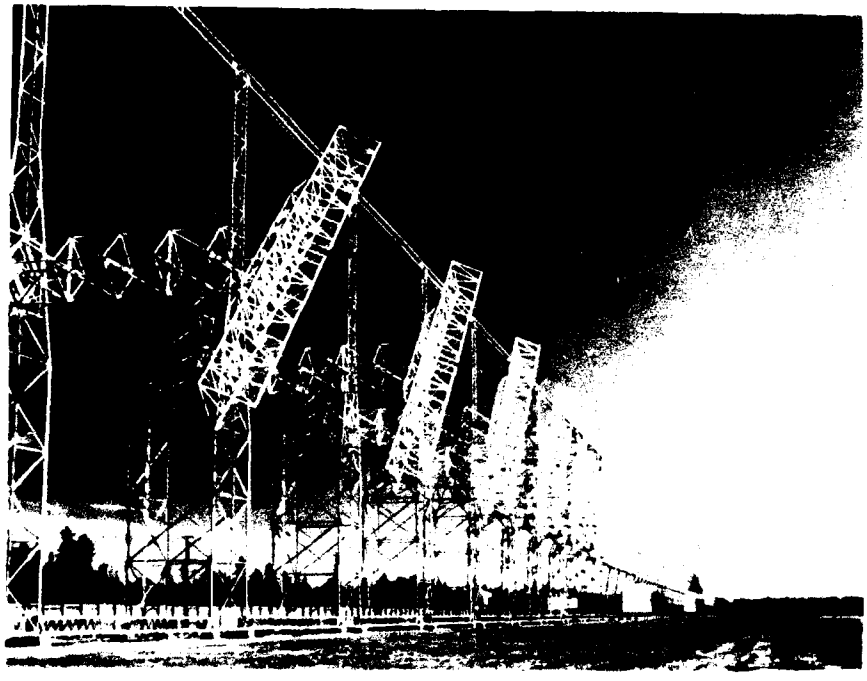

Figure 2. Transmit Antenna

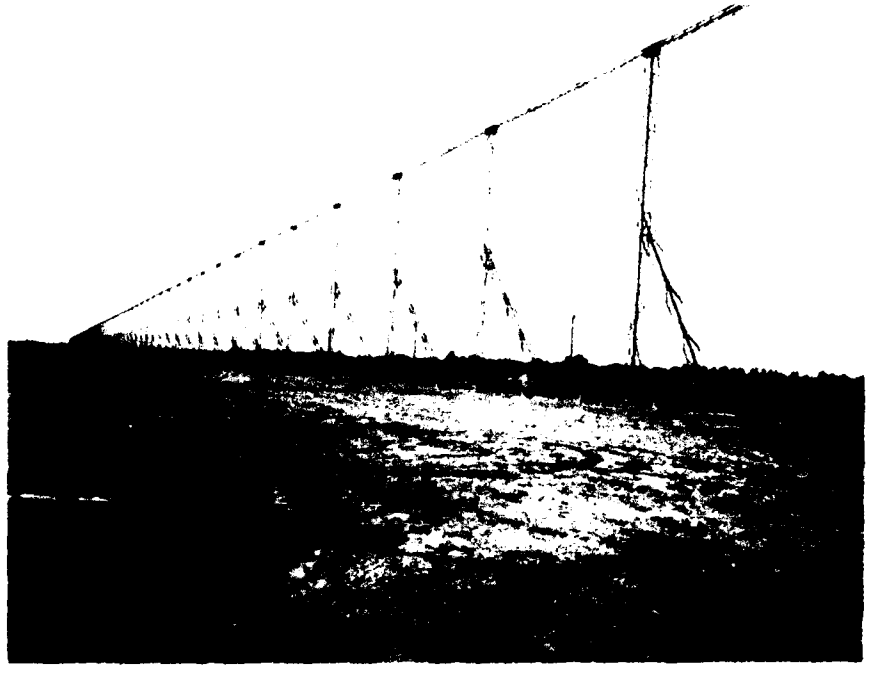

Figure 3. Receive Antenna

A transmit antenna array consists of six sub-bands designated A through F in ascending frequency order. Each sub-band is a 12-element broadside linear array of dipoles, mounted in front of a backscreen and above a groundplane. The frequency bandwidth ratio of each sub-band is 1.348, providing a 5-to 30-MHz total bandwidth.

Bands A through D have the radiating element canted at a 45- degree angle relative to the vertical. This angle is chosen to provide coverage at both high and low elevation angles using an elliptical polarization, which is primarily vertical at low angles and horizontal at high angles. Bands E & F use a vertically-oriented/polarized element to provide only low angle coverage. Subarray placement, element cant angle, and inter-subarray spacings are chosen to minimize coupling between subarrays and minimize transmission line loss. This results in a band A, C, E, D, F, B arrangement of subarrays.

The receive antenna is a broadside linear array of 246 equally spaced monopole elements placed in front of a backscreen and driven against a groundplane. Each of the 246 elements covers a 5- to 30-MHz frequency band. The antenna array is used in three bands designated as high, mid, and low band. Each band has 82 active elements, with the high band using the 82 contiguous centrally located elements; mid-band using the 82 centrally located, even numbered elements; and the low band utilizing every third element of the entire array. Table 1 shows the overall dimensions of the AN/FPS-118 Antennas and Figures 4 and 5 show detailed dimensions of the transmit and receive antennas, respectively.

TABLE 1.
ANTENNA CHARACTERISTICS

	Bands	Element	Elements Per Band	Total Elements	Antenna Length (ft)	Maximum Height (ft)	Ground-Screen Length (ft)
Transmit Antenna	6	Dipole	12	72	3,640	135	750
Receive Antenna	3	Monopole	82	246	4,980	65	750
In Cov Sounder Tx Ant	1	Log Periodic Monopole	2	2	318	140	750
In Cov Sounder Rcv Ant	3	Monopole	24	72	2,880	65	750
Out of Cov Sounder Tx Ant	1	Log Periodic Monopole	2	2	318	140	440
Out of Cov Sounder Rcv Ant	2	Monopole	10	20	625	65	60

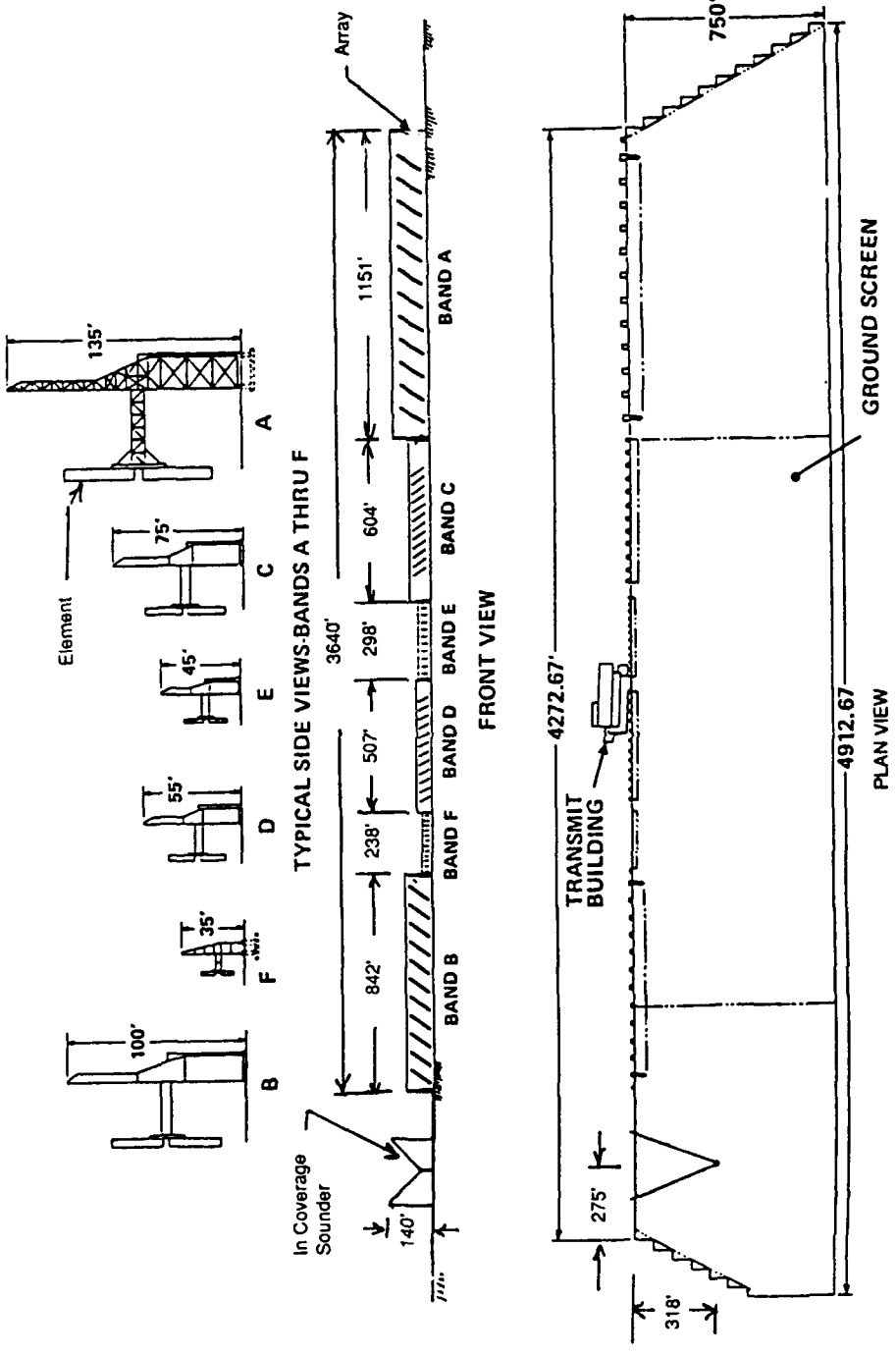

Figure 4. Transmit Antenna Dimensions

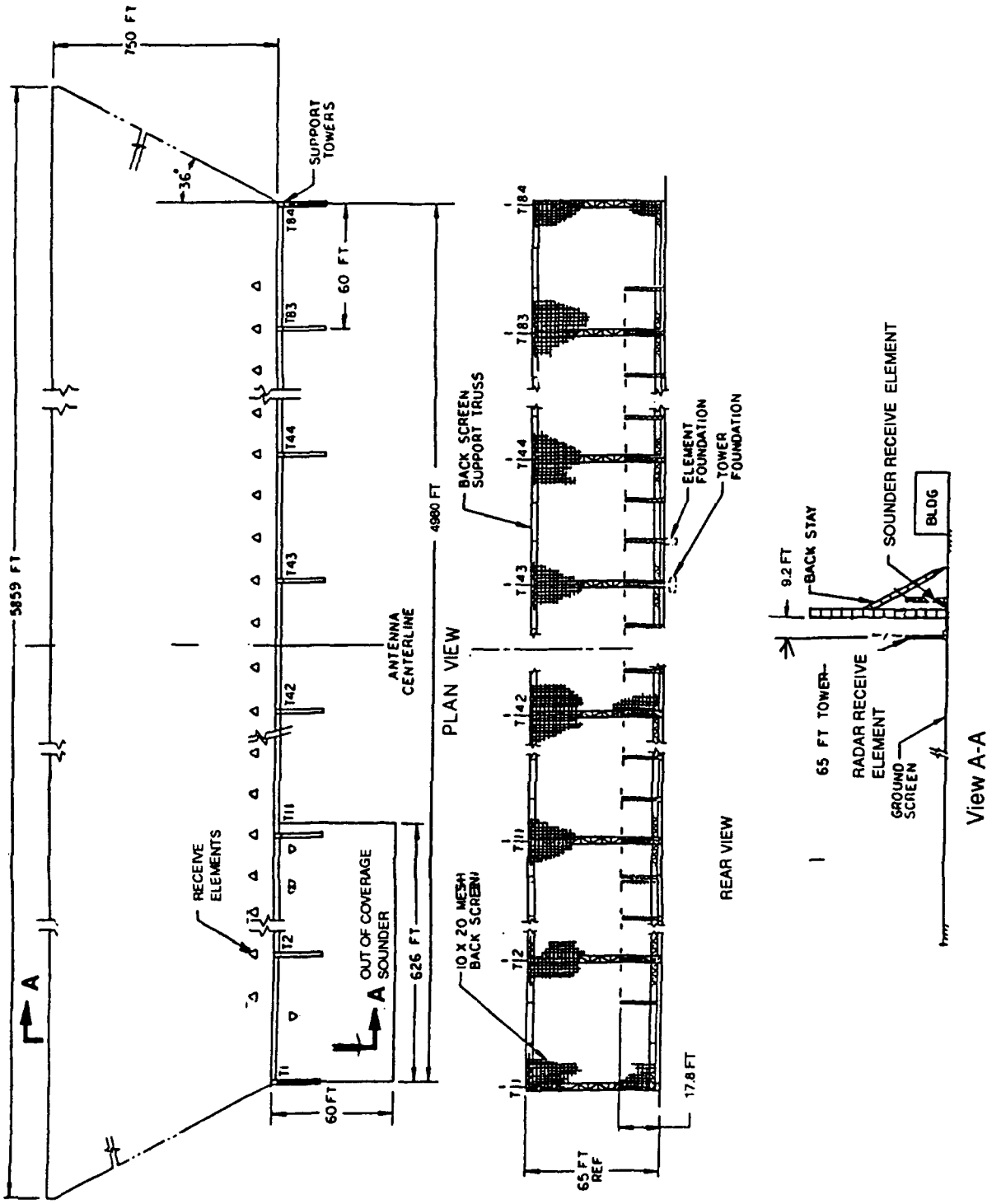

Figure 5. Receive Antenna Dimensions

Each segment has an in-coverage backscatter sounding antenna system. Two additional out-of-coverage sounder antennas are provided for the East Coast Radar. One is directed due west and the other pointed at geomagnetic north. The sounder transmit antenna is a two-element array of Log Periodic elements. The in-coverage antennas have a 750-foot long groundscreen and the out-of-coverage antennas have only enough groundscreen to stabilize the input impedance. The in-coverage receive sounding beams are formed using 24 high, 24 mid, and 24 low band radar elements. The element signals are obtained by a 3-dB power split after the first amplification stage in the receivers. An analog beamformer for each group of 24 elements provides eight beams steered in 7.5-degree increments to fixed angular positions which covers a 60-degree azimuth angle. Full time delay is used for steering to obtain frequency independent beam pointing directions. A switching matrix provides two simultaneous beams from any of the three bands which can be routed to two sounder receivers. An out-of-coverage sounder receive antenna can also be connected to one of the sounder receivers. Each of these antennas consists of a high and low band with each band having ten elements. The elements are positioned on the backside of the radar antenna backscreen and they use the radar backscreen as a reflector. An analog beamformer is used to collimate a beam in the desired direction, depending on the pointing direction of the companion radar antenna.

2.0. ARRAY DESIGN

The total 5- to 30-MHz frequency band is divided into six sub-bands for the transmit antenna. The frequency bandwidth ratio of each band is 1.348 (fh/fl) The azimuth element spacing is 0.62 λ at the high end of each band, and each band has twelve elements. This spacing is selected to place the azimuth grating lobe peak well into

imaginary space at a maximum scan of 27 degrees. This is necessary with a short aperture (wide grating lobe) to minimize the grating lobe impact on average sidelobe levels. The broadside azimuth beamwidth for uniform illumination varies from 7.0 to 9.6 degrees over the band. A maximum scan angle of 27 degrees is chosen to place the outer -3-dB point of the beam beyond the 30-degree coverage needed at the high band end of each subarray.

The element height above the groundplane for bands A through D is 0.41 λ at the high end of each band. The height for bands E & F is 0.44 λ at the high end of each band. These heights and the element orientation are selected to provide the required elevation angular coverage.

The receive antenna element spacing is 0.61 λ (20 feet) at 30 MHz and is selected to place the first null of the grating lobe at the edge of imaginary space for a maximum scan of 36 degrees. This maximum scan angle is chosen to permit depointing the receive antenna 6 degrees relative to the pointing angle of the transmit antenna, while still providing a 60-degree angular coverage from each antenna pair. The reasons for depointing the antennas are: 1) to correct for parallax arising due to the transmit and receive antenna physical separation and, 2) to ensure that the transmit and receive backlobes are never in alignment. This improves the round-trip backlobe level and provides backlobe auroral clutter suppression. The antenna has 246 total elements, of which only 82 are used at any given time. The high band uses 82 contiguous elements at the center of the array; in the mid band, 82 even-numbered central elements are employed and, in the low band, every third element is used. The frequency bands are 5.0 to 9.7 MHz, 9.7 to 15.0 MHz and 15.0 to 30.0 MHz. The azimuth beamwidth is held to 2.5 degrees across the frequency band (when not aperture limited) by adjusting the number of

elements used and the Taylor weighting on the aperture. At the lower end of the high and low bands the beamwidth increases to a maximum of 3 degrees. This weighting, along with the error sidelobes, provides the required sidelobe suppression to allow operation in an auroral environment. For higher azimuth resolution the aperture weight can be changed to provide a narrower beam.

3.0. BACKSCREEN AND GROUNDSCREEN DESIGN

The backscreen for the antennas is constructed of copper-coated steel wire. The wire diameter and spacing is selected to reduce the leakage through the screen to a level which is consistent with the required backlobe level. The backscreen height is chosen to control backlobe levels due to diffraction at the screen truncation edge. Connected mesh construction is used to control the vibrational characteristics of the backscreen rather than unconnected wires which vibrate at high frequencies and may affect the subclutter visibility of the radar. Three mesh openings are used for the transmit antenna. They are: 10" by 10" for band F; 14" by 14" for bands D and E; and 22" by 22" for bands A, B, and C. The receive antenna uses a 20" by 10" mesh opening with the 10" spacing in the horizontal direction. A galvanized steel structure consisting of towers and trusses supports the backscreen. The backscreen material is fabricated in rolls of various widths. The rolls of material are thermite-welded together at the site into panels. These are then tensioned and thermite-welded to the support structure.

The steel structures are fabricated into the largest fully welded sections which can be galvanized and shipped to site. During assembly, all metal-to-metal joints in the structure are coated with a conducting, anti-corrosive material to prevent any noise and/or spurious frequency generation from the joints over the life of the system. The structures

arc galvanized to minimize non-linear effects due to the iron content of the steel, and to prevent corrosion.

The groundscreen for the antennas is laid on the ground to provide a reflecting surface to control elevation beamshape and ground losses. The screen material is an aluminum-coated steel wire which is compatible with normal soils. The groundscreen is constructed of 14 gauge wire welded into a 6" by 6" mesh. The material is fabricated in 6-foot wide rolls, 380 feet in length. The rolls are installed in strips, normal to the antenna line. The strips are spaced 8" apart, and are spot-welded together every 4 feet for the transmit antenna and every 3 feet for the receive antenna.

A computer program was developed to calculate the elevation pattern performance of the antennas. The analysis includes the diffraction from the backscreen top edge, the groundscreen front edge, the leakage through the screen, and the effects of the ground surrounding the antenna. A flat earth is assumed for the analysis. Good correlation has been obtained between measured scale model patterns and patterns calculated for the scale model using the computer program. Measured azimuth patterns for the ECRS transmit antennas, taken at several elevation angles, show good correlation with calculated data. The program integrates the patterns to calculate the directive gain. Figures 6 through 8 show the transmit elevation coverage, receive elevation coverage, and the antenna directive gain, respectively.

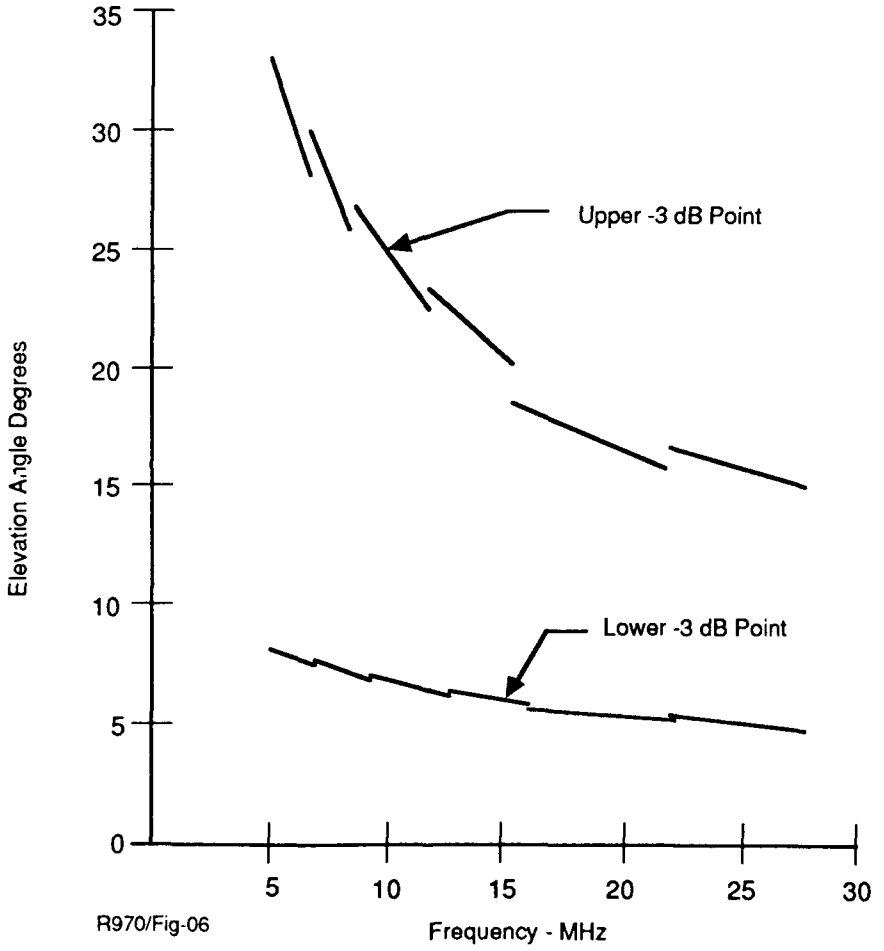

Figure 6. Transmit Antenna Elevation Coverage

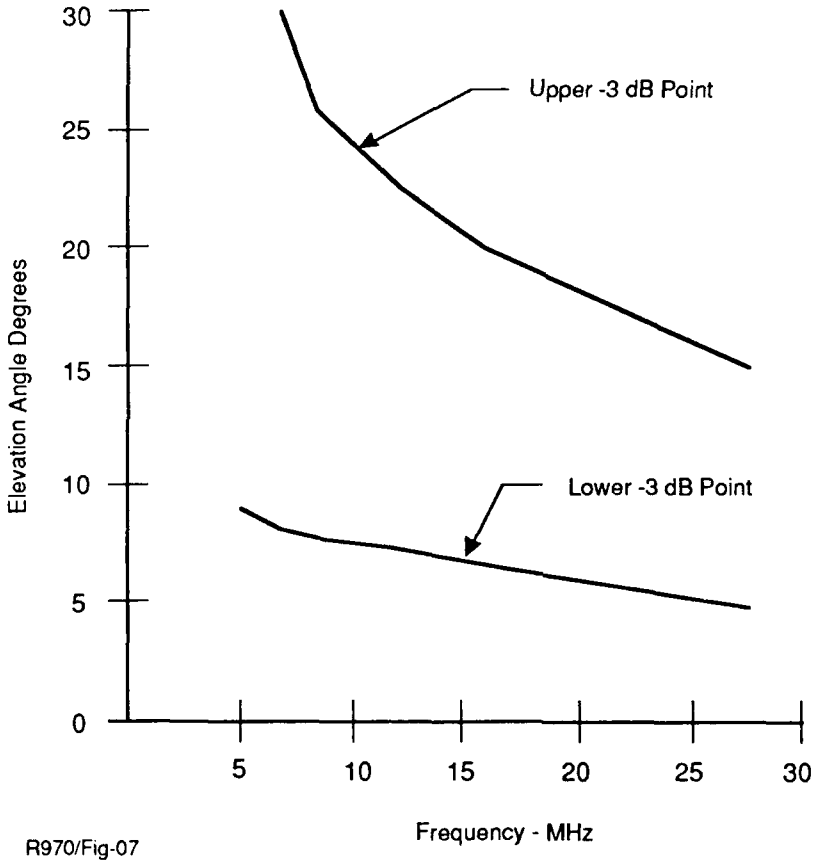

Figure 7. Receive Antenna Elevation Coverage

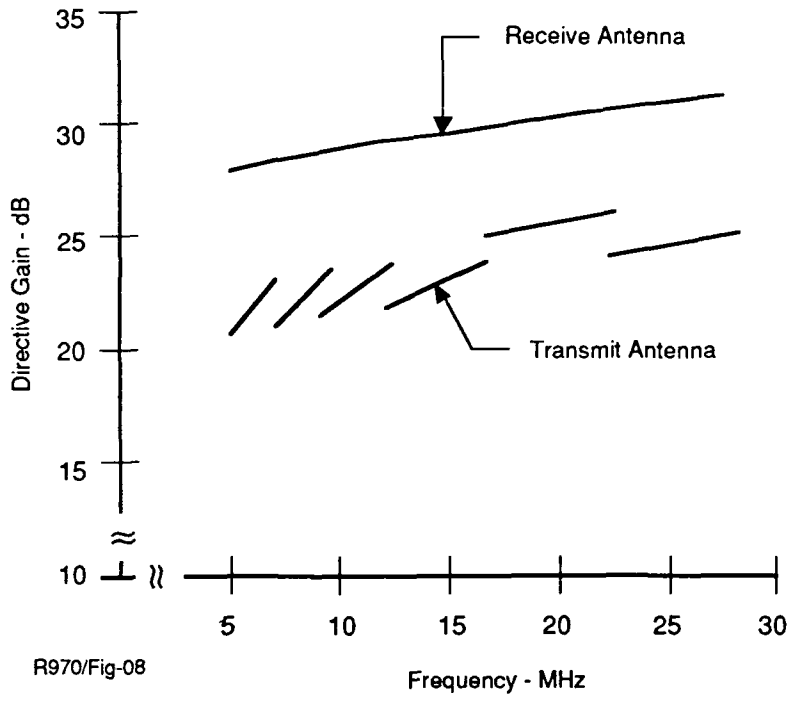

Figure 8. Antenna Directive Gain

4.0. ELEMENT DESIGN

The transmit element must provide a good impedance match (low VSWR) to the transmitter to obtain efficient power transfer to space. Each array element has a broadband transmitter which supplies 80 kW of power for VSWRs of less than 1.6. At a VSWR of 2.0, the power output falls to approximately 40 kW. To provide low VSWRs over the frequency band and scan angle, a broad band dipole is chosen for the transmit element.

The dipole design uses a bazooka balun to provide the transition from a 50 ohm, 6-1/8" diameter coaxial feed line to the balanced current on the dipole arms. A square aluminum truss structure provides the element support and also forms the $\lambda/4$ shorted line section for the balun. The radiating arms of the dipole are triangular aluminum truss

structures, which are isolated from the aluminum support by a dielectric structure. The 6-1/8" coaxial input line proceeds through the aluminum support to the element feed point. Each arm is fed through an open circuited 3-1/8" coaxial line located in the arm. This provides a series capacitance, which is used in conjunction with a two-section impedance transformer in the 6-1/8" input line, to match the active dipole impedance to 50 ohms. Figure 9 shows dimensional data and the configuration of the transmit elements.

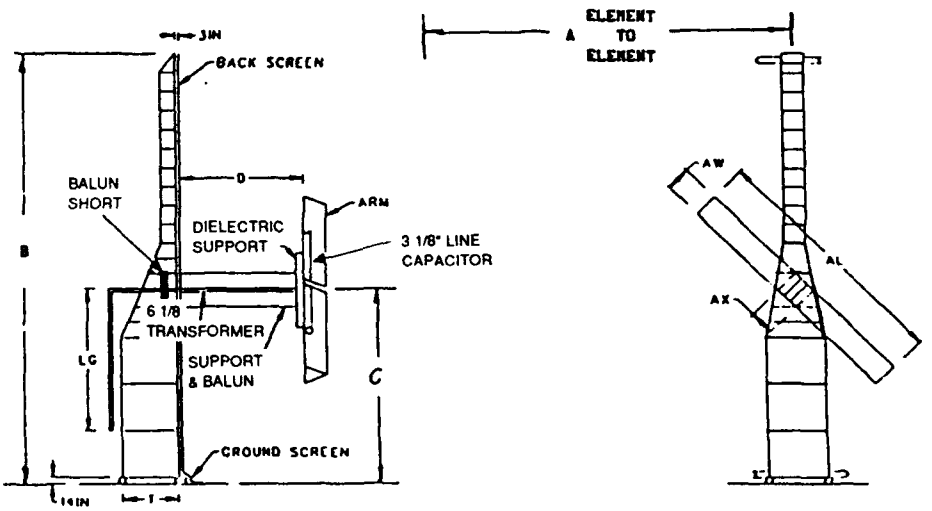

BAND	ORIENTATION	A(FT)	B(FT)	C(FT)	D(FT)	AL(FT)	AX(FT)	AW(FT)	LG(FT)	T(FT)
A	CANTED	90.0	135	60.0	45.1	79.4	7.6	7.8	53.5	18.0
B	CANTED	67.0	100	44.5	33.5	58.9	5.6	5.9	37.0	15.0
C	CANTED	49.7	75	33.0	24.8	44.7	4.2	4.5	25.5	12.0
D	CANTED	36.93	55	24.5	18.4	32.6	3.1	3.4	17.0	9.0
E	VERTICAL	27.40	45	19.5	13.6	24.7	3.8	2.6	12.0	7.0
F	VERTICAL	20.3*	35	14.5	10.1	18.4	2.8	1.8	7.0	6.0

R970/Fig-11

* Band F Tower Spacing is 61.0 Feet

Figure 9. Transmit Element Dimensional Data

Scale models of the elements were constructed without the impedance transformers to measure the single element feed point impedance. Seven element scale

models were constructed of bands C and E to measure the mutual coupling coefficients in the array environment for the two different polarizations. A computer program was developed to calculate from the measured data the active input impedance of each element versus scan angle and frequency. An impedance matching program, using an iterative procedure, calculates the parameters of a two-section transformer which minimizes the input VSWR for all scan angles, frequencies, and element positions in each subarray. The band F VSWR is optimized from 22.25 to 28 MHz due to operational frequency restrictions from 28 to 30 MHz. The scale model VSWR predictions are shown in Table 2. Full-scale VSWR measurements compare very well with the scale model predictions. Figure 10 shows a comparison of measured and calculated data at broadside scan and 10.6 MHz for the band C sub-array. Figure 11 shows the F band subarray and construction details of the transmit elements.

Each element in bands A through E is cantilevered from a backscreen support tower. For band F, three elements are cantilevered from a truss which is supported by towers. The element 6 1/8" transmission line is brought down the rear of the towers to approximately 7 feet from the ground. A bi-directional coupler is provided for monitoring element performance.

TABLE 2

TRANSMIT ANTENNA ACTIVE VSWR

Band	Frequency (MHz)	Average VSWR	Maximum VSWR
A	5.00 - 6.74	1.30	1.73
B	6.74 - 9.09	1.29	1.71
C	9.09 - 12.25	1.25	1.63
D	12.25 - 16.51	1.27	1.65
E	16.51 - 22.25	1.27	1.83
F	22.25 - 28.00	1.25	1.64

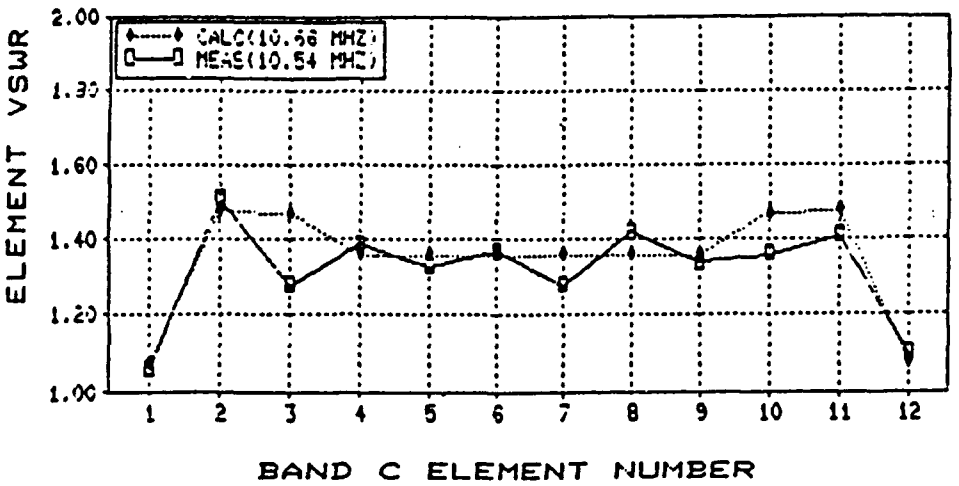

Figure 10. OTHB/ERS Transmit Array Performance Band C Broadside (Uniform Illumination)

Figure 11. Band F Transmit Elements

The receive antenna element is a 17.8-foot long monopole fabricated from galvanized steel. The element has an 18" by 18" by 18" triangular cross section and is isolated from the ground by three fiberglass dielectric insulators. The element is fed against the groundscreen using an end terminal assembly which has a "Type N" coaxial input connector. A surge protector is used to prevent receiver damage if lightning strikes the antenna structure. Figure 12 shows the receive element.

Figure 12. Receive Antenna Element

The receive element must operate over the total 5- to 30 MHz frequency band. The element length and distance from the backscreen are chosen to be as large as can be used without developing an appreciable reduction in the element gain in the broadside direction. This results in an electrical element height of 0.54 λ above the ground plane and a 0.28 λ (9.2 feet) electrical distance to the backscreen at 30 MHz. These dimensions provide an acceptable loss for operation at 5 MHz. The return loss of a typical element in a loaded array environment is shown in Figure 13. This variation in return loss and the resulting mismatch loss is compatible with the external noise characteristics at HF frequencies.

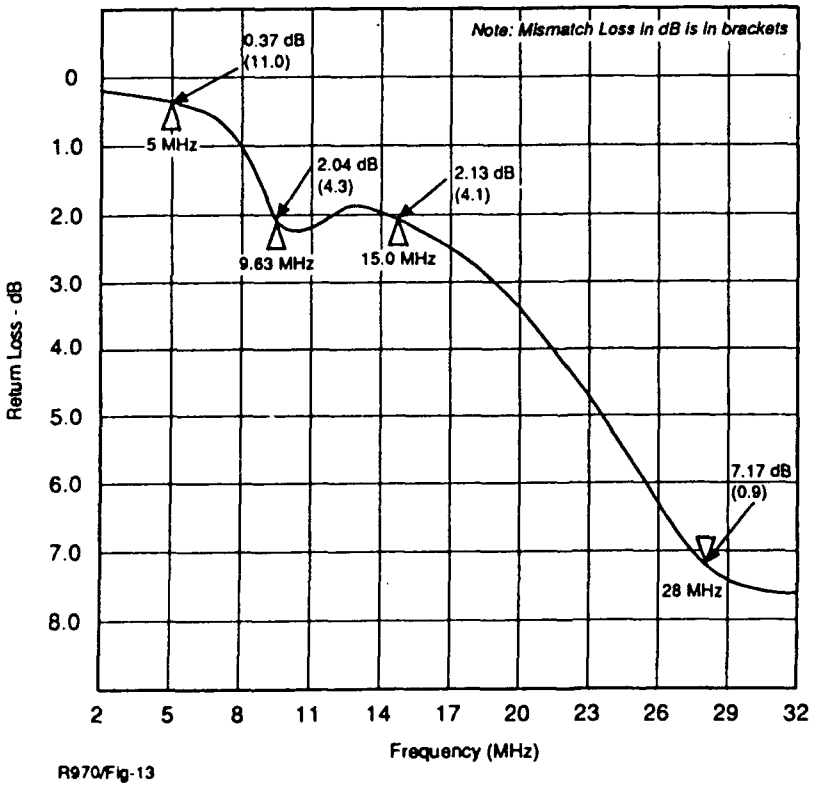

Figure 13. Receive Element Return Loss

The complete array is filled with elements to maintain impedance similarity for all elements in the three bands. Unused elements are terminated in 50-ohm loads. This is necessary to meet element similarity error requirements for sidelobe control.

5.0. FEED SYSTEM

The transmit antenna feed system is designed for an input power of 100 kW CW and a VSWR of 2 for each element. Semi-flexible 50-ohm coaxial transmission lines are used to connect the transmitter outputs to the element inputs. Bands A & B use 3" diameter line; bands C and D use 4" diameter line, while bands E & F use 5" diameter line. An adapter is used to interface with the 6-1/8" rigid line element input. A total of 61,000 feet of coaxial line is used for the transmit antenna. Each line is long enough to extend from the element to its transmitter terminal. The electrical length of the lines are measured during installation and the data used in a beamforming and steering algorithm to collimate the beam at the selected scan angle.

The receive feed lines are commercially available 0.412" diameter coaxial cables which are used in the cable T.V. industry. The cable characteristic impedance is 75 ohms and 164 cables are used to connect the active elements to the receivers. Equal length cables are used to all the active elements which are enclosed by the mid-band aperture. The outboard 14 low-band elements on each end of the antenna use just enough cable to connect the elements to the receiver. The cables are installed and buried in a trench, 5-foot deep, which provides a maximum temperature variation of 11 degrees C year round and limits phase changes versus temperature to an acceptable level. The cable lengths are measured and trimmed to a tolerance of 3.2 degrees. These measured phase differences are then used as a phase correction in the beamforming and steering algorithm in the

receive digital beamformer. A total of 316,000 feet of cable is used for the receive antenna.

6.0. Structural Design

The antennas are designed to survive a peak wind velocity of 90 knots at a 30-foot elevation without ice loading. With 2 inches of rime ice or 1.5 inches of clear ice on major support structures, the antennas must survive a 50-knot peak wind, acting at a 30-foot elevation. The backscreen and elements are not considered major support structures, and 0.5 inches of clear ice is used as the ice loading requirement on these structures.

A finite element model of the transmit antenna is created for each band using the ANSYS Engineering Analysis System. The structural members are represented as three-dimensional elastic beams. The beam elements are capable of developing tension, compression, and bending stresses. All of the joints in the structure are considered rigid. The loads are applied to the structure as nodal forces.

The wind force on the structure is calculated by taking the given wind velocity as the basic wind speed measured at 30 feet with the gust and importance factors included. A velocity pressure profile is then developed as a function of height using the appropriate exposure coefficient in accordance with American National Standards Institute (ANSI) A58.1 - 1982. The total static wind force on the structure is calculated as a function of the velocity pressure, the force coefficients for square towers, and the projected area of the structure. The wind is considered to be approaching from the front, rear, and quartering directions. The structure is designed to withstand the most severe of these cases.

The wind force on the backscreen is accounted for through the use of three-dimensional shell elements. The shells are stretched across the area of the structure where the backscreen is located. A pressure is then applied to the shells equal to the wind force

on the backscreen. The density of the shell elements is adjusted to account for the weight of the backscreen and the modulus of elasticity is set to near zero in order to avoid the backscreen contributing any stiffness to the structure.

The ice accumulation is taken into account by adjusting the density of the members to include the ice and by increasing the projected area of each member by twice the amount of radial ice present. The force coefficients are recalculated for the members because the members are considered to have rounded corners for iced conditions. New wind loads are then calculated based on the adjusted values for the projected areas and force coefficients of the members.

The stresses calculated are compared with the allowable stres. es prescribed in the American Institute of Steel Construction (AISC) Specification for the design of structural steel buildings. The calculated stress for any member is not allowed to exceed the allowable stress stated in the AISC Code for Tension, Compression, or Bending Stresses.

A structural dynamic analysis was performed to determine the mechanical resonant frequencies of the structures. A wind gust profile is assumed and used to excite the structures and determine their vibrational characteristics. A maximum vibration amplitude of 0.185 inches is allocated to the antenna from the Subclutter Visibility Budget for spectral noise density. This is in addition to the initial displacement due to wind velocities (including gusts) of 40 knots at 30 feet above ground level.

7.0 SUMMARY

Six transmit and receive antenna pairs have been fabricated and installed, three for the ECRS and three for the WCRS. The antennas have been integrated with the rest of the

radar equipment and are providing aircraft detection capabilities for ranges of 500 to 2000 nautical miles.

ACKNOWLEDGEMENT

The author wishes to acknowledge the contributions of all the people who have participated in the design, fabrication, installation, analysis, and test of the antennas. The design began in 1975 and involved a large number of people both at GE and the many subcontractors who supplied materials for the antennas.

PHASED ARRAY CALIBRATION BY ADAPTIVE NULLING

Herbert M. Aumann and Frank G. Willwerth
Massachusetts Institute of Technology, Lincoln Laboratory
Lexington, MA 02173

ABSTRACT

The limitations of phased array sidelobe performance were explored with a 32-element linear array operating at L-band. With conventional far-field calibrations, the average sidelobe level of the array was about -40 dB. Since the array contained T/R modules with 12-bit attenuators and 12-bit phase shifters, considerably lower sidelobe performance had been expected.

Initially, array performance was thought to be limited by inadequate calibrations. An examination of individual array element patterns showed a mirror symmetric ripple which could only be attributed to edge effects in a small array. Simulations indicated that more precise calibrations would not have significantly lowered the sidelobe level.

An adaptive calibration technique was developed which iteratively adjusted the attenuator and phaser commands to create nulls in the antenna pattern in the direction of the nulls of a theoretical antenna patterns. With adaptive calibrations, the average sidelobe level could be lowered to -60 dB. Array patterns with deep nulls in specified directions can also be implemented.

1.0 INTRODUCTION

A phased array antenna with low sidelobes has advantages for both clutter and interference suppression. However, besides of measurement range and multipath effects, a variety of causes may make it difficult to achieve low sidelobe performance.

Quantization effects are the most often claimed to limit array sidelobe performance. By using attenuator and phase shifters with 12-bits of control, quantization errors should become insignificant.

Obviously it would be desirable to build phased array components with sufficient tight tolerances to make further alignment unnecessary. In practice, amplitude and phase differences in the T/R modules and transmission lines of the beamforming network are almost unavoidable. Array calibrations can be used to compensate for these differences and relate digital commands to an actually applied excitation function.

Usually, array element patterns are assumed to be uniform. Mutual coupling and edge effects may distort array element patterns, thus compromising the array calibrations and excitation function calculations.

Rather than attempting to minimize the various error sources, the phased array calibration technique described in this paper concentrates on achieving the best array pattern under the given conditions.

2.0 ANTENNA RANGE AND PHASED ARRAY CHARACTERISTICS

2.1 Antenna Test Range

Phased array calibrations and antenna pattern measurements were made with the linear array in Figure 1 on a 100 ft. ground reflection antenna range. The range geometry is shown in Figure 2. Since this range did not meet the far-field criterion for the test array, focusing of the array was necessary.

2.2 Phased Array Characteristics

The experimental array operated at L-band and was about 15 ft. by 2 ft. in size. It contained 36 identical waveguide radiating elements. Two elements on either end of the array were terminated to reduce edge effects. The remaining 32 elements were connected to transmit/receive modules.

Half-height, open-ended waveguide radiating elements were chosen primarily because they were inexpensive and they had a broad, aspect angle insensitive pattern. Some typical elements patterns are shown in Figure 3. In the center of the array, the element patterns were nearly identical. However at the ends of the array, the element patterns exhibited a mirror symmetric ripple which was attributed to edge diffraction. Ordinary array calibrations cannot correct for this ripple.

Good sidelobe performance in a small array requires transmit/receive modules with very precise attenuation and phase control. Each of the modules used in the test array had 12-bits of amplitude and phase control. This was achieved by using voltage controlled devices operating at an intermediate frequency

[1]. Typical characteristics are shown in Figure 4 and Figure 5. A nominal quadratic approximation adequately described the attenuator the phaser characteristics. There is a weak attenuator and phaser interaction which is not easily accounted for by a closed-form calibration.

2.3 Array Performance with Standard Calibrations

Standard array calibrations were carried out with the array at broadside. That is, all elements, except the element under test, were terminated, and the characteristics of the element under test were determined. Using such calibrations, Figure 6 shows an antenna pattern of the test array with a 40 dB Chebychev taper. Although the measured average sidelobe level of -39 dB was considered quite good, with 12-bit quantization the average sidelobe level should have been -45 dB for a 40 dB Chebychev taper.

One way of determining the limits of array sidelobe performance is to measure the average sidelobe level as increasingly more severe array tapers are commanded. Figure 7 shows that the array sidelobe performance was limited to about -40 dB.

A simulation was carried out using actually measured element patterns, such as shown in Figure 3, and perfect calibrations. Of course, the measured element patterns included range multipath as well as small array effects. The resulting array sidelobe performance was only a few dB better than the performance measured on the antenna range. This indicates that the array performance with standard calibrations was about as good as could be expected.

3.0 ADAPTIVE CALIBRATION TECHNIQUE

A technique for calibrating a phased array from the far-field pattern has been has been described by Patton [2]. Actually, the process consisted of first calculating the far-field pattern of an array by Fourier transformation of planar near-field measurements. The array element excitations were then computed by inverse Fourier transformation of the far-field pattern back to the aperture plane.

The array calibration technique described here is based on iteratively forming nulls in the antenna pattern [3]. The calibrations are considered "adaptive" in that the measured antenna pattern is adjusted to match a theoretical model. When the specified nulls correspond to the nulls of an array with uniform illumination, the technique yields the insertion attenuation and phase of the array elements. By specifying other null directions, different array illumination functions can be implemented.

3.1. Theory

The excitation function of a phased array can be calculated from an observed far-field pattern by the direct matrix inversion method [4]. The pattern of a linear N-element array in the direction θ is given by

$$P(\theta) = \sum_{n=1}^{N} w_n z_n(\theta) \tag{1}$$

$$z_n(\theta) = \frac{E_n(\theta_n)}{R_n} \exp j\frac{2\pi}{\lambda}(R_n \, mod \, \lambda),$$

where w_n are the complex excitation coefficients and $E_n(\theta_n)$ are the element patterns. Usually it is assumed that all array elements are identical and the range geometry is such that

$$E_1(\theta_1) = E_2(\theta_2) = \cdots = E_n(\theta_n)\,. \tag{2}$$

By measuring the antenna pattern in N directions, a set of linear equations can be written and solved for the N excitation coefficients. These equations can be expressed in matrix form as

$$\boldsymbol{W} = \boldsymbol{Z}^{-1}\,\boldsymbol{P} \tag{3}$$

where

$$\boldsymbol{W} = \begin{bmatrix} w_1 \\ w_2 \\ \vdots \\ w_N \end{bmatrix}$$

$$\boldsymbol{Z} = \begin{bmatrix} z_1(\theta_1) & z_2(\theta_1) & \cdots & z_N(\theta_2) \\ z_1(\theta_2) & z_2(\theta_2) & \cdots & z_N(\theta_3) \\ \cdots & \cdots & \cdots & \cdots \\ z_1(\theta_N) & z_2(\theta_N) & \cdots & z_N(\theta_N) \end{bmatrix}$$

$$\boldsymbol{P} = \begin{bmatrix} P(\theta_1) \\ P(\theta_2) \\ \vdots \\ P(\theta_N) \end{bmatrix}.$$

In theory, measurements of the antenna pattern in any N directions could be chosen to determine the array excitation function. In practice, the quality of results obtained from a single "back transformation" has not been very satisfactory. The problem is that the assumption of identical element patterns is of limited validity and the range geometry is not sufficiently well known. However, an iterative solution, with careful selection of the measurement directions, has been successful.

3.2 Measurement Selection

Any measured antenna pattern will obviously be affected by the specific range geometry. Thus, Figure 2 should be used to carefully calculate the range to each element, particularly to include focusing corrections. Equation (1) also indicates that differences in the amplitude and phase of individual element patterns and errors in the excitation function have similar effects on the antenna pattern. This interaction can be minimized by making measurements in the directions of the pattern nulls.

For commonly used array tapers, the excitation function can be written in factored form. Consequently, the null locations of the far-field pattern are explicitly known [5]. In fact, the null locations were probably used to specify the array sidelobe level in the first place. For an N-element array, there can

be at most $N-1$ nulls in the antenna pattern. Ideally, if the main lobe is at θ_p and the nulls are at $\theta_1, \theta_2, \cdots, \theta_{N-1}$ then the normalized pattern values are

$$\begin{bmatrix} P(\theta_p) \\ P(\theta_1) \\ \vdots \\ P(\theta_{N-1}) \end{bmatrix} = \begin{bmatrix} 1 \\ 0 \\ \vdots \\ 0 \end{bmatrix}, \tag{4}$$

and the matrix inversion in Equation (3) will return the theoretical excitation function $\boldsymbol{W}_T$.

As a result of the assumption made in Equation (2), the nulls in the antenna pattern are entirely determined by the array factor. The above calculation will therefore not be affected by the shape of the element patterns.

Since the array under test and the measurement range are not perfect, the measured antenna response will not be zero at the null locations, that is

$$\begin{bmatrix} P(\theta_p) \\ P(\theta_1) \\ \vdots \\ P(\theta_{N-1}) \end{bmatrix} = \begin{bmatrix} 1 \\ \epsilon_1 \\ \vdots \\ \epsilon_{N-1} \end{bmatrix}. \tag{5}$$

However, Equation (5) and Equation (3) can be used to obtain an estimate $\boldsymbol{W}_E$ of the actually applied excitation function. In the following calibration procedure, attenuation and phase commands will be adjusted until differences between the estimated and theoretical excitation function are a minimum. When this is accomplished, the nulls of the measured and theoretical antenna pattern have been matched.

The nulls of an antenna pattern are usually of no particular interest. However, by forcing the antenna pattern to have nulls in the proper directions, a well formed antenna pattern is virtually assured.

It should be noted that the process is mathematically identical to adaptive nulling by sample matrix inversion [6]. That is the array is required to receive a desired signal from a given direction, and it is required to suppresses undesired signals in $N-1$ carefully specified other directions.

3.3 Calibration Procedure

Usually, the first step in the array calibrations is to correct for array element insertion attenuation and phase differences. Initially, an excitation function $\boldsymbol{W}_C$ is commanded without corrections to yield a uniform illumination $\boldsymbol{W}_T$

$$\boldsymbol{W}_C = \boldsymbol{W}_T = \begin{bmatrix} 1 \\ 1 \\ \vdots \\ 1 \end{bmatrix}. \tag{6}$$

For example, the resulting antenna pattern of the uncalibrated test array is shown in Figure 8. The amplitude and phase of the antenna pattern is measured at broadside and at the null locations corresponding to a uniform illumination. From Equation (3) an estimate of the actually applied excitation function $\boldsymbol{W}_E(i)$ is obtained. This estimate is then used to update the commanded excitation function on the next iteration as follows

$$\boldsymbol{W}_C(i+1) = \boldsymbol{W}_C(i)\left[\frac{\boldsymbol{W}_T}{\boldsymbol{W}_E(i)}\right]^k \tag{7}$$

where $k \leq 1$ is a gain constant. The actual commands have to be expressed in counts based on nominal attenuator and phaser characteristics. The above process is repeated until

$$\boldsymbol{W}_E(i) \approx \boldsymbol{W}_T, \tag{8}$$

and there is no further improvement in the null depths. For example, Figure 9 illustrates that after 4 iterations a nearly perfect pattern expected for an array with uniform illumination has been achieved.

Under the above conditions, the array element insertion attenuation and phase are given by the reciprocal of $\boldsymbol{W}_C$. Shown in Figure 10 and Figure 11 are the insertion attenuation and phase as determined by standard calibrations and as measured by adaptive calibrations. Standard array calibrations are usually carried out with a source at broadside. It was shown in Figure 3 that the element patterns are not entirely identical at all angles. Adaptive calibrations include element pattern differences and therefore yield slightly different calibration results.

As with any feedback algorithm, there is concern with convergence. For example, an instability may occur if the $\boldsymbol{Z}$-matrix does not adequately model the array and range geometry. Another cause for instability may be a lack of

monotonicity in the attenuator and phaser characteristics.

3.4 Array Performance with Adaptive Calibrations

3.4.1 Sidelobe Suppression by Chebychev Taper

The calibration technique is not limited to an array with uniform illumination. For example, shown in Figure 12 is the adaptively determined excitation function required to implement a 40 dB Chebychev taper. A parabolic phase distortion necessary to phase focusing is clearly evident. Although the differences between standard and adaptively determined excitation function are usually quite small, the resultant array pattern, in Figure 13, represents a considerable improvement over the corresponding pattern with standard calibrations shown in Figure 6.

With adaptive calibrations exceedingly low sidelobe performance could be demonstrated. Figure 14 shows an antenna pattern with a 60 dB Chebychev taper. At that level, the 40 dB dynamic range of the attenuators becomes the limiting factor.

Shown in Figure 15 is the sidelobe performance with adaptive calibrations. With adaptive calibrations, the array performance comes much closes to the theoretical array performance expected from an array with 12-bits of amplitude and phase control.

3.4.2 Sidelobe Suppression by Null Placement

In the above section the antenna pattern null directions were chosen to

correspond to standard Chebychev tapers. This resulted in very predictable array performance. However, uniformly low sidelobes may not be required in all applications. Rather than accepting the loss in efficiency and broadening of the mainlobe, selective null placement in the direction of a known interference source may be the preferred approach.

For example, shown in Figure 16 is an adaptively calibrated array pattern with a 30 dB Chebychev taper and an additional null at -30 degrees. Again, sidelobes in the direction of the interference have been suppressed by 60 dB.

4.0 SUMMARY

An adaptive calibration technique for a phased array was described. Since the algorithm derived array excitation function directly from the measured far-field pattern, no build-in test capability is required.

The technique is applicable not only to implement standard array tapers, but can also be used to implement antenna patterns with deep nulls in specified directions.

5.0 ACKNOWLEDGEMENT

This work was sponsored by the Department of the Air Force under Contract F19628-90-C-0002.

6.0 REFERENCES

1. Aumann, H. M. and Willwerth, F. G. (1988) Intermediate Frequency Transmit/Receive Modules for Low Sidelobe Phased Array Application,

IEEE National Radar Conference, Ann Arbor, Michigan

2. Patton, W. T. (1981) Phased Array Alignment with Planar Near-Field Scanning, or Determining Element Excitation from Planar Near-Field Data, Antenna Applications Symposium, Allerton Park, Illinois

3. Aumann, H. M. and Willwerth, F. G. (1989) Measurement of Phased Array Patterns by Near-Field Focusing, AMTA Conference, Monterey, California

4. Hoffman, M. (1961) The Utility of the Array Pattern Matrix for Linear Array Computations, IRE Trans. Ant. and Propag. AP-9:97-100

5. Elliot, R. S. (1981) Antenna Theory and Design Prentice-Hall, Englewood Cliffs, New Jersey, ch.5

6. Monzingo, R. A. and Miller, T. W. (1980) Introduction to Adaptive Arrays, Wiley, New York

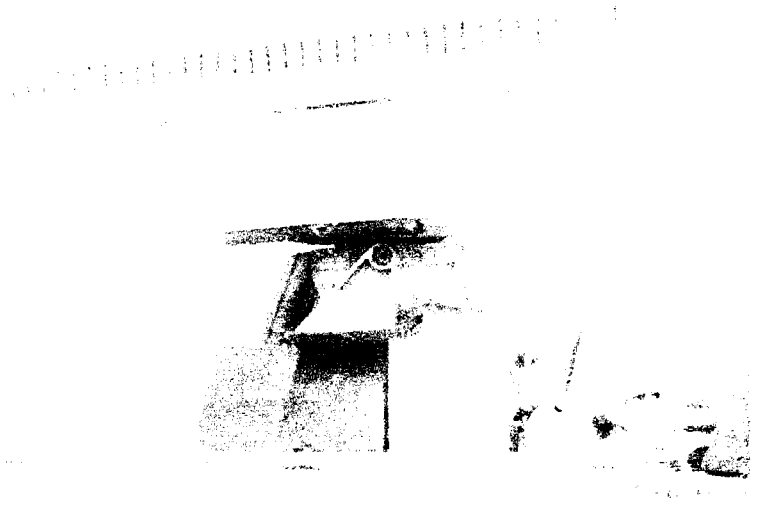

Figure 1: Experimental Phased Array

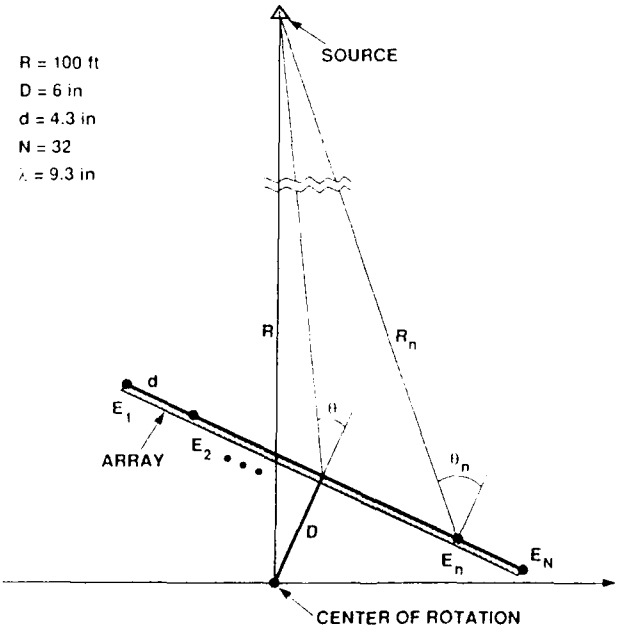

Figure 2: Antenna Test Range

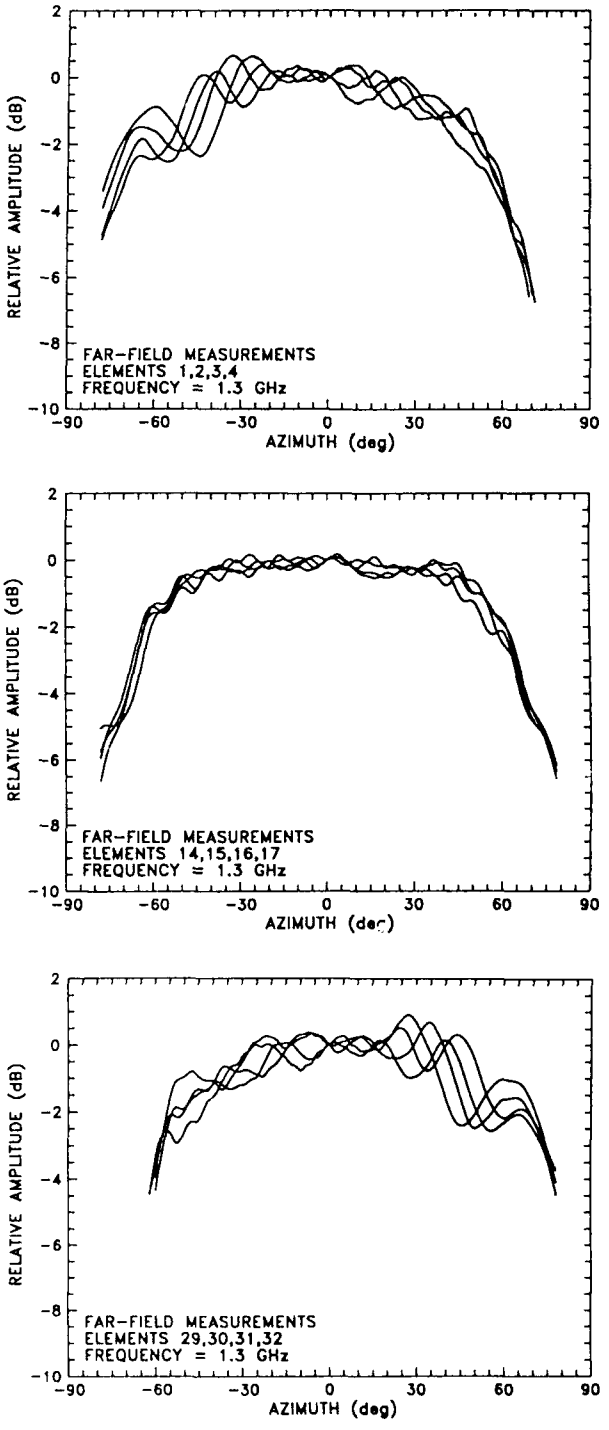

Figure 3: Typical Array Element Patterns

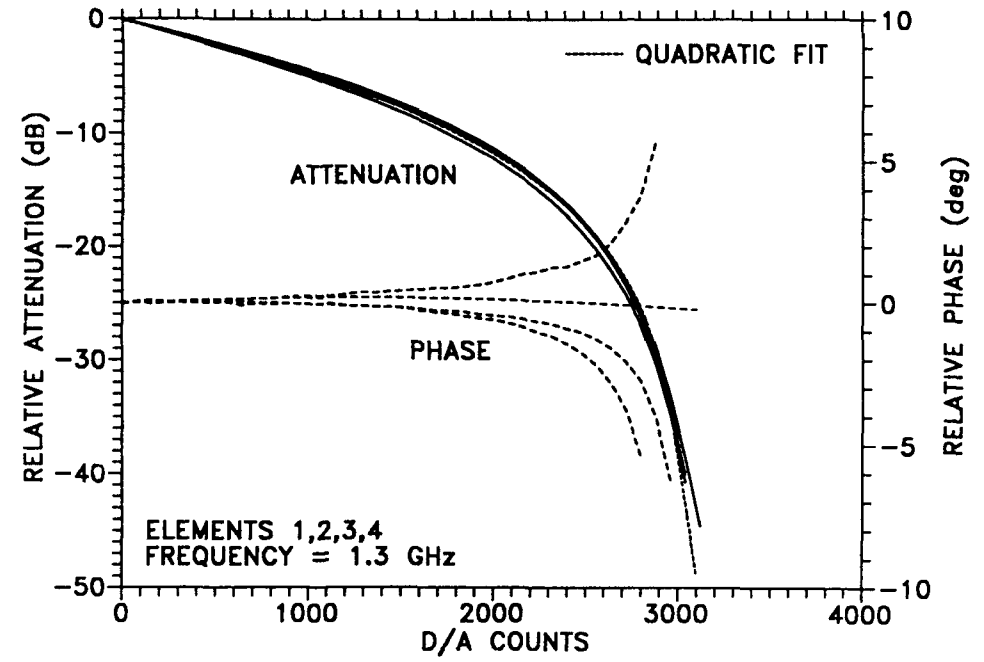

Figure 4: Typical AttenuatorCharacteristics

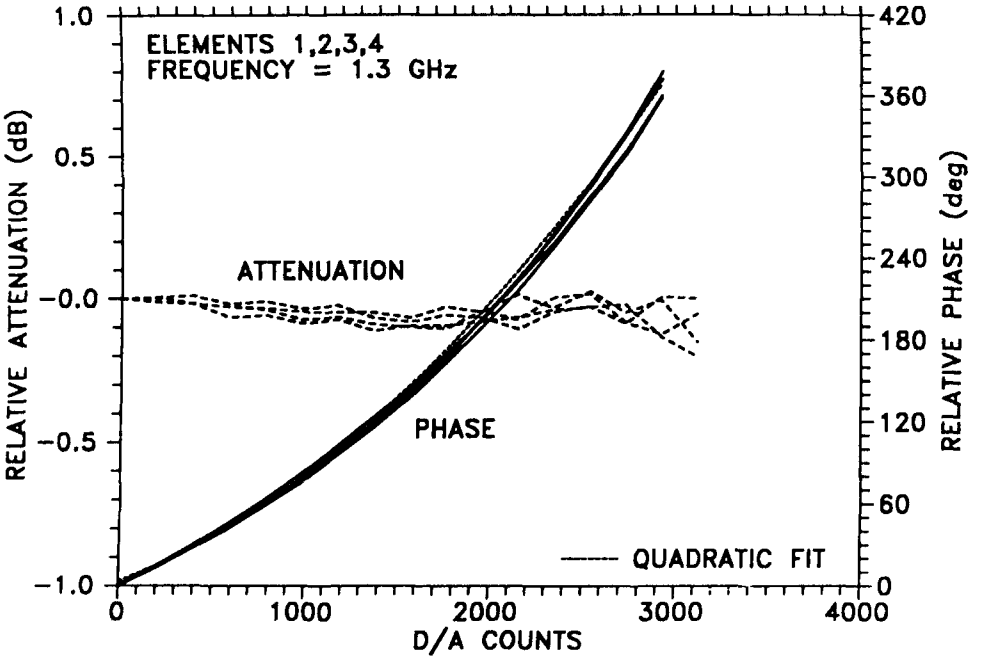

Figure 5: Typical Phaser Characteristics

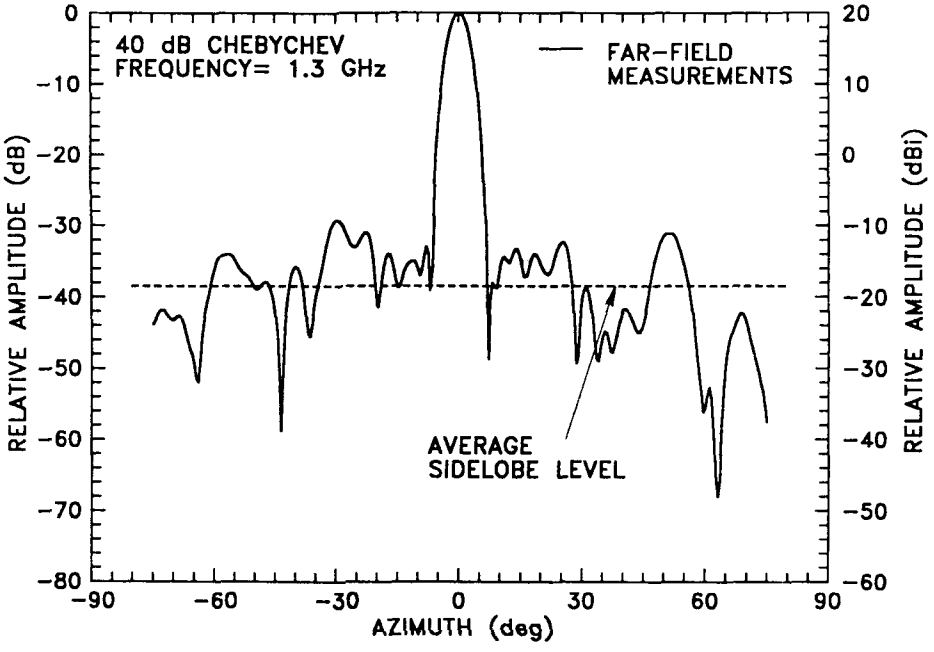

Figure 6: Antenna Pattern with Standard Calibrations

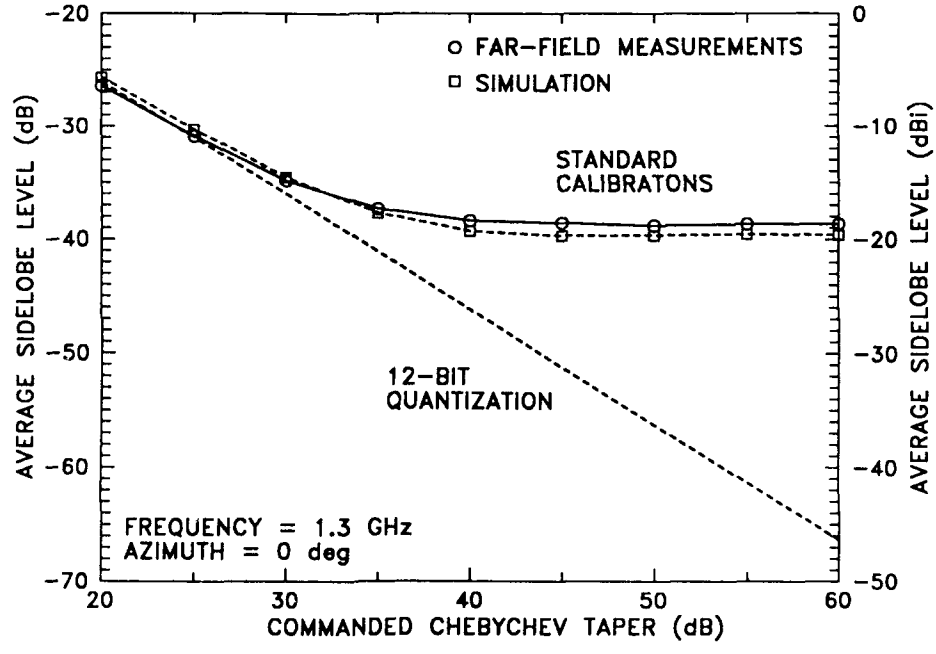

Figure 7: Array Sidelobe Performance with Standard Calibrations

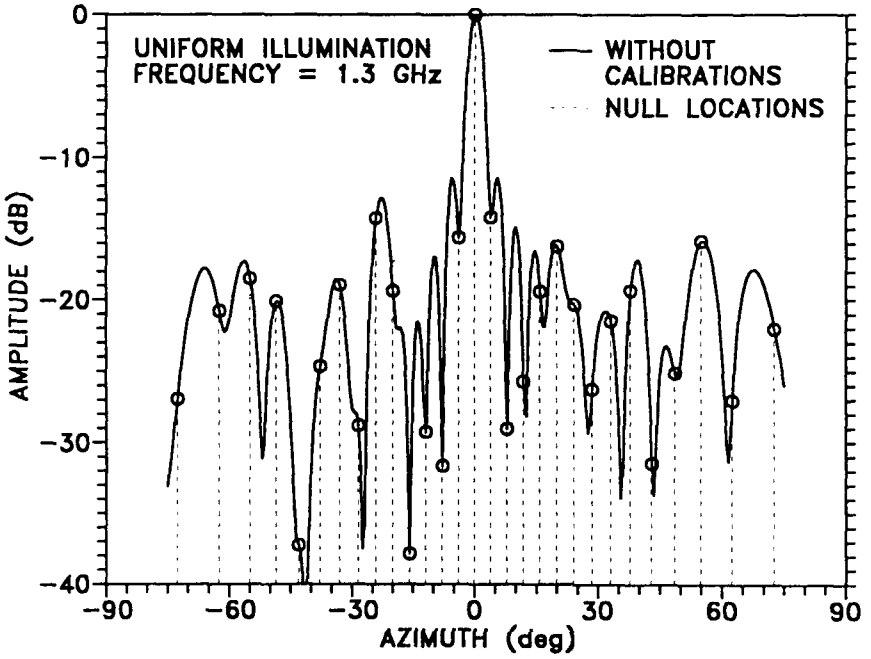

Figure 8: Uncalibrated Array Pattern

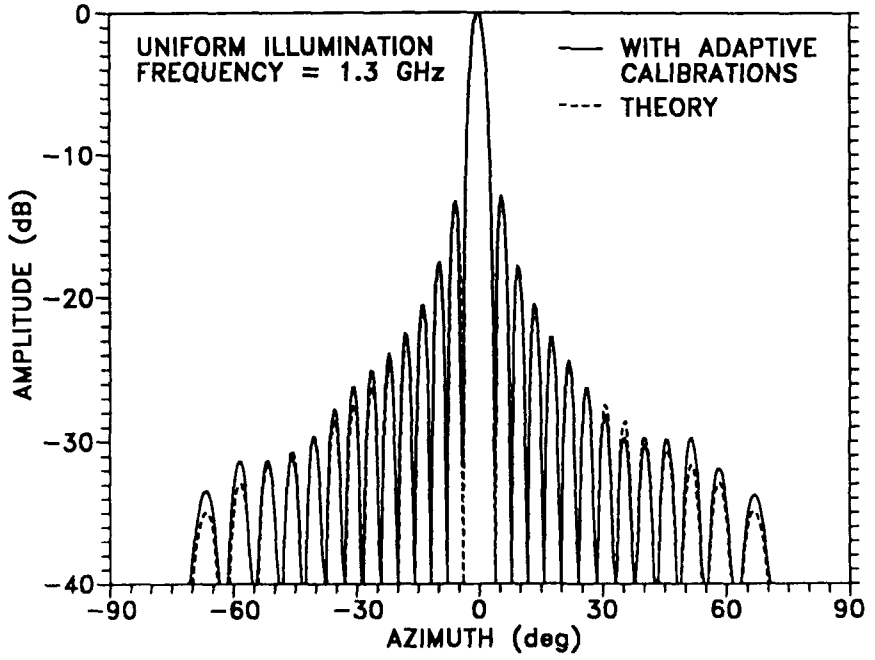

Figure 9: Array Pattern with Uniform Illumination

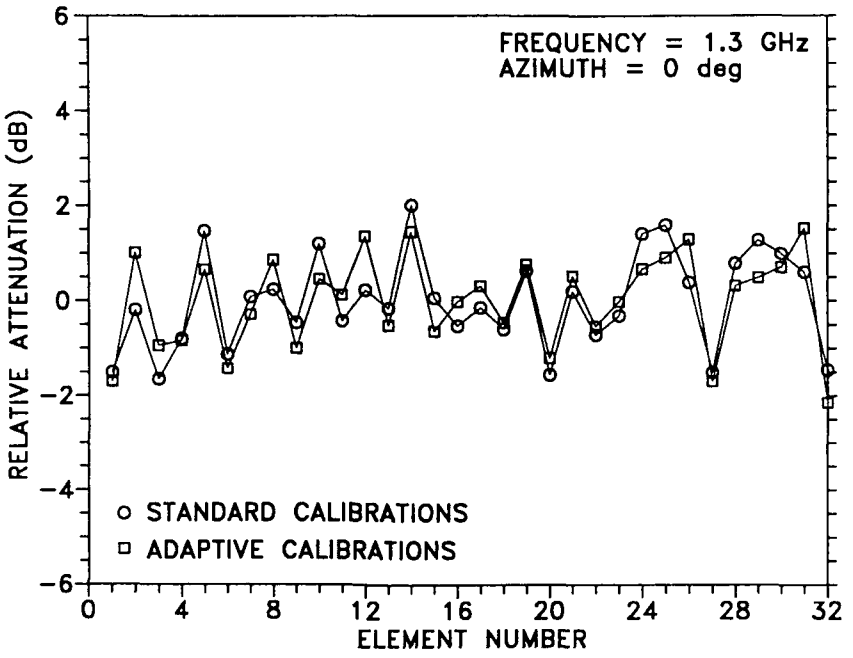

Figure 10: Comparison of Insertion Attenuation

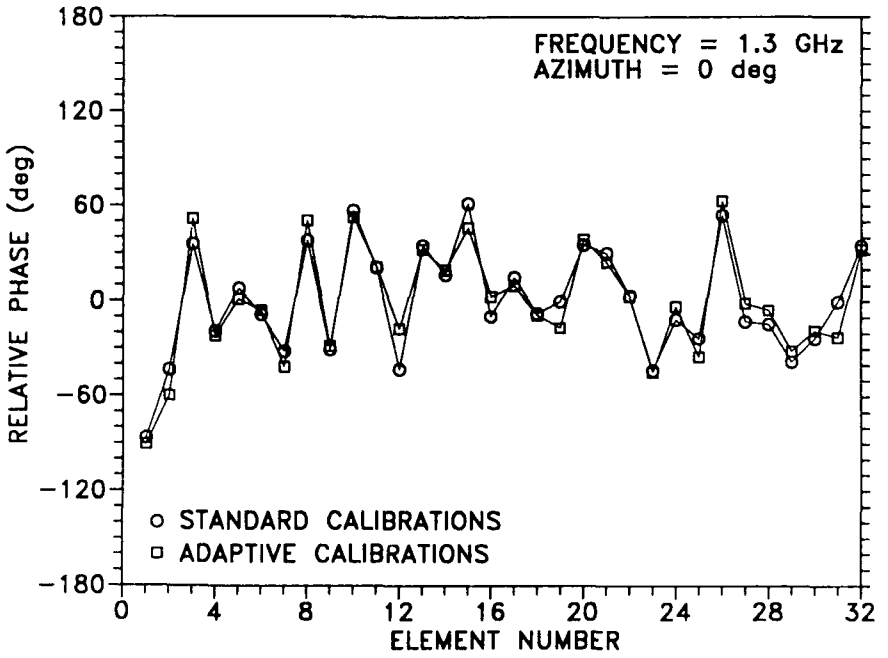

Figure 11: Comparison of Insertion Phase

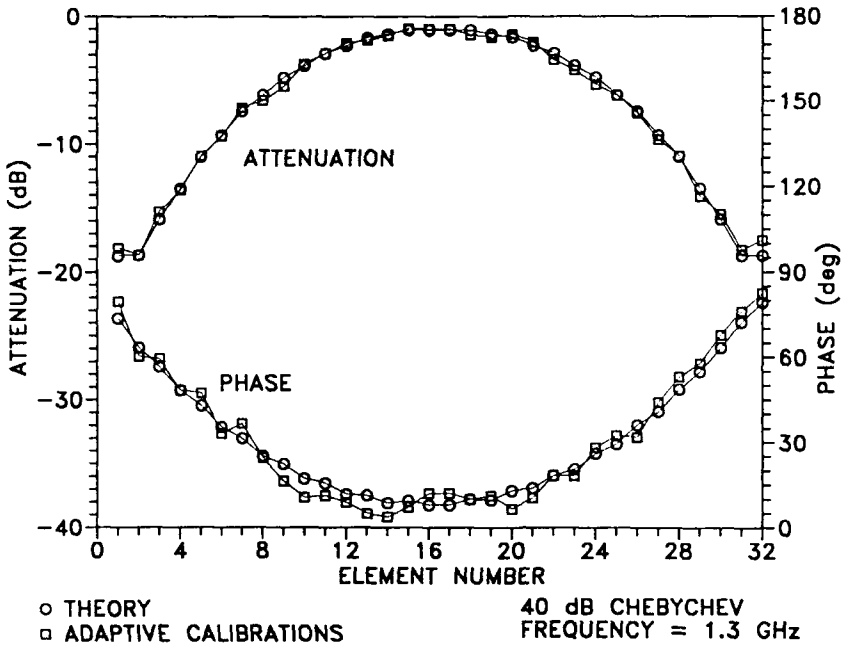

Figure 12: Excitation Function for a 40 dB Chebychev Taper

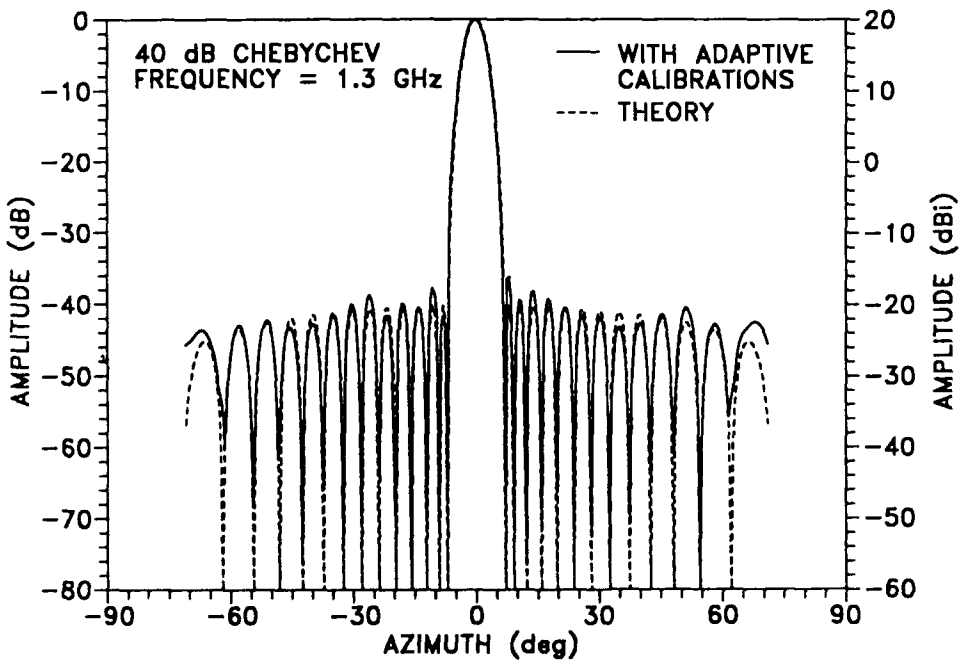

Figure 13: Array Pattern with 40 dB Chebychev Taper

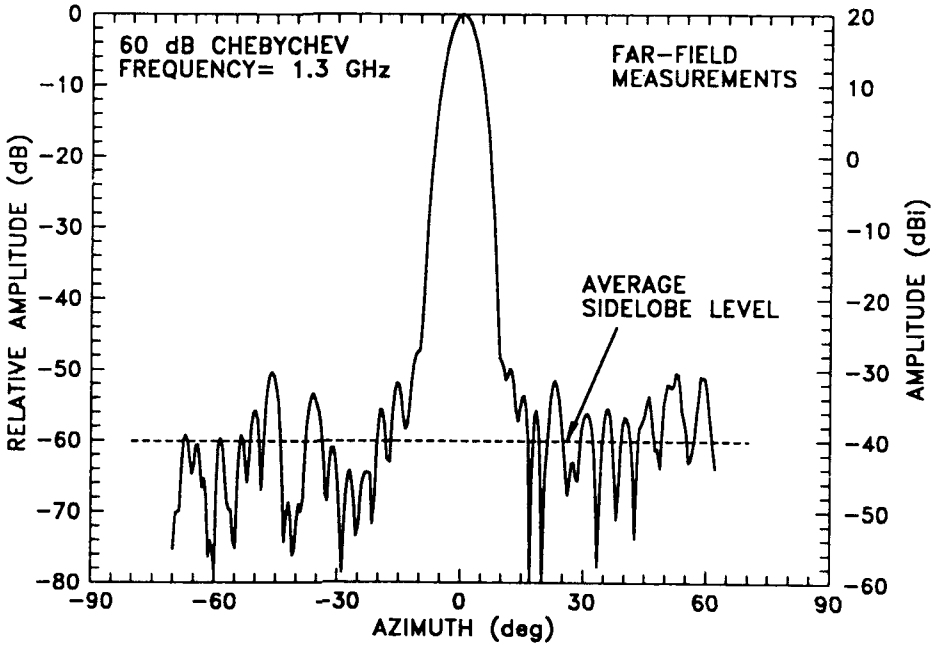

Figure 14: Array Pattern with 60 dB Chebychev Taper

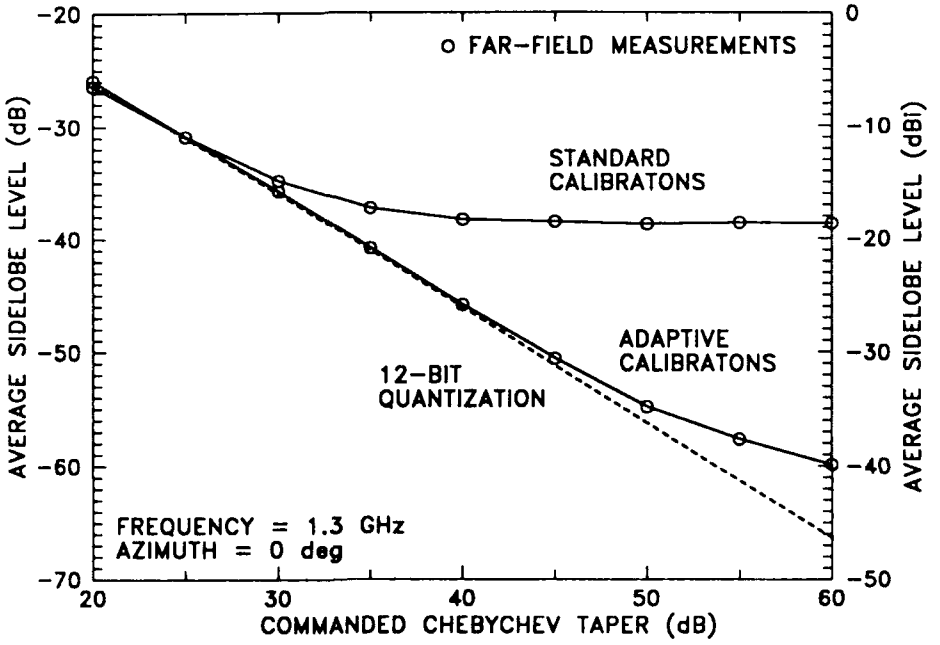

Figure 15: Array Sidelobe Performance with Adaptive Calibrations

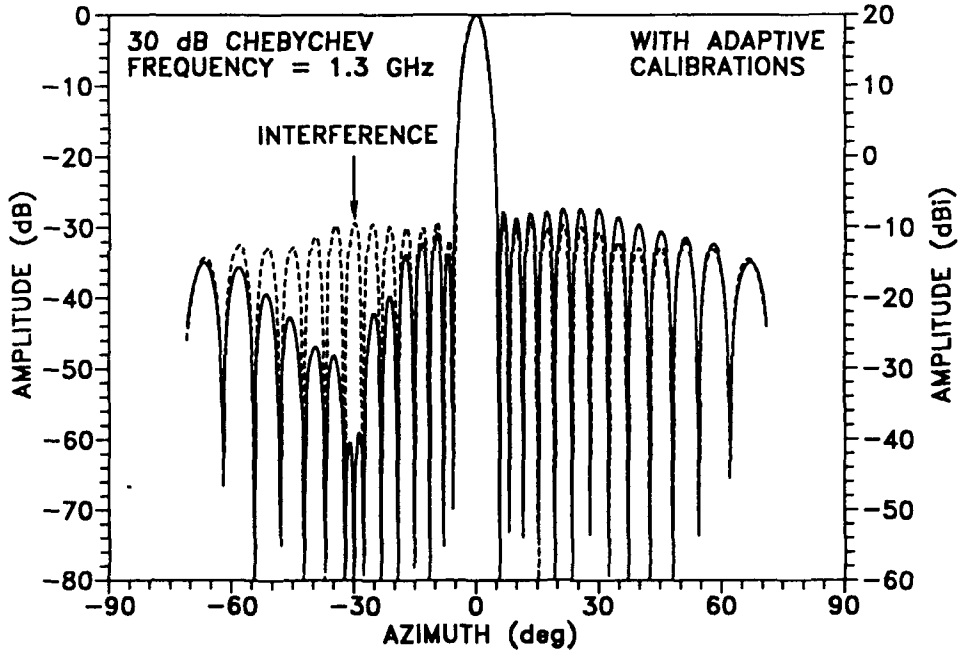

Figure 16: Adaptively Calibrated Antenna Pattern with Null

APPLICATIONS OF SELF-STEERED PHASED ARRAYS

Dean A. Paschen
Ball Communication Systems Division
Broomfield, CO 80038

ABSTRACT

Self-steered phased arrays were studied in the early 1960's to aid in communications with non-stationary low earth orbit satellites. Introduction and widespread use of geosynchronous satellites eliminated most of the necessity for tracking, and active transponders reduced the need for large earth stations. Consequently, interest in self-steered arrays declined. In spite of this decline, several uses for self-steered array techniques still remain. The beneficial applications range from lightweight, portable, quick erect antenna systems to fixed installation, ultra high gain ground stations. Antenna systems which operate in a disturbed atmosphere also benefit from the automatic phasing inherent in a self-steered array. The purpose of this paper is to discuss some of these applications along with methods of implementing the self-steered array.

1.0 INTRODUCTION AND HISTORY

Self-steered arrays were first investigated in the early 1960's for use with low-earth orbit satellites. Two types of self-steered arrays were studied for two different problems. Retrodirective or Van Atta arrays were studied for use in satellite communications to minimize the problems of achieving high transmit and receive gain at the satellite without tracking the received signal. The other use of self-steered array technology was the approach presented by Eberle[1]. Four 30 foot diameter reflector antennas were combined coherently to achieve the same performance as a 60 foot diameter single parabolic reflector. The array was designed for use with Echo I and Echo II passive satellites, and this configuration is shown in Figure 1-1. Combination of the signals provided maximum array gain in the direction of the signal source. Advantages of the approach were that combination of several smaller antennas was more cost effective than a single larger antenna, that the acquisition of the satellite was easier due to the larger beamwidth of the smaller antennas, and that the system compensated for phase variations due to atmospheric inhomogeneities.

The introduction of geosynchronous satellites using earth coverage antennas eliminated the need for tracking on the satellite, and the need for retrodirective arrays disappeared. The use of active transponders in these same satellites began to reduce the requirement for very large reflector antennas, and the study of self-steered arrays declined.

2.0 SELF-STEERED ARRAYS PROVIDE BENEFITS

The benefits which motivated the study of self-steered arrays in the past still exist for large antenna systems. Those benefits are lower cost, simplified acquisition and tracking due to a wider field-of-view (FOV), and compensation for atmospheric variations from element to element. Some additional uses which have been investigated more recently are highly portable satellite ground terminals, large baseline arrays where the source may not be in the far field, and arrays which are resistant to multipath fading.

The cost benefit of self-steered arrays is based on the property that very large reflector antennas have a cost versus area which is exponential[2]. A study by Potter et al. for deep space dishes found that cost was roughly proportional to area to the 1.4 power for constant surface tolerance[3]. Self-steering concepts

have a higher initial cost due to the electronics, but the increase with total aperture is linear. Figure 2-1 shows this relationship with the assumption that the electronics cost is equal to the cost of a single unit of aperture area. The cost benefit for large total aperture areas is obvious.

A self-steered array is made up of elements which are combined in the manner of a phased array. The elements may be any antenna type although parabolic reflectors, planar fixed beam arrays, and phased arrays have been the primary types considered. One advantage of self-steering is that since each element or subarray has a wider beamwidth than the composite array, the required pointing accuracy for each element is reduced. Also, the FOV of the system is actually the FOV of the individual elements, so that acquisition of the signal is simplified.

The benefit of compensation for atmospheric inhomogeneities which was mentioned in the earliest work is important for systems designed to operate in nuclear battlefields, as the atmospheric scintillation is a major concern for communications links. In this type of operation, phase variations may occur which cause the planar wavefront to be distorted such that standard antenna techniques suffer signal reductions.

Based on the statistics of the environment, a single aperture may be broken into pieces so that the phase variation across each piece is relatively small. The self-steering technique can then be used to compensate for the larger variations from aperture to aperture.

One of the major incentives for the investigation of self-steered phased arrays at Ball Communications Systems Division (BCSD) was the potential for use in highly portable satellite ground station antennas. Figure 2-2 shows a conceptual drawing of a self-steered array for use with the Defense Satellite Communications System (DSCS). The goal is to provide the equivalent performance of a 20 foot diameter reflector antenna and allow for storage in the aisle of a S-250 or larger shelter. Without self-steering, the panels which make up the antenna system would have to be positioned very accurately, and the cables, filters, amplifiers, and other components would require phase matched construction. All of these requirements are eliminated in a self-steered system, and as a result, the deployment time and cost of this type of antenna array are reduced significantly.

If a very large baseline array were constructed, the possibility would exist for a signal of interest to be in the near field region of the array. Under this

scenario, a self-steered array would continue to provide maximum gain by effectively compensating for the incident spherical phase front.

A common problem for antennas operating at low elevation angles or in urban environments is multipath fading. A self-steered antenna array will provide the best phase at each element for maximizing the total signal to the receiver. Brennan showed that the self-phased array is resistant to multipath fading, and that under certain conditions may achieve total gains which are higher than that obtained for the same array in an isolated environment[4]. A good example would be an array operated in the standard manner versus a self-phased array operated in front of a reflecting surface. Figure 2-3 shows how the capture of the energy from the surface may provide higher gain than for the array operated independently. One application which takes advantage of the multipath rejection benefit, especially in urban areas, is the one developed by Blaupunkt for use in high performance FM systems for automobiles[5]. The system uses four foil antennas in the corners of the car body and combines the antennas for maximum signal using self-steered array techniques.

3.0 SELF-STEERED ARRAY TECHNIQUES

The motivation for self-steering of phased arrays becomes apparent when some of the practical aspects are considered. A conventional phased array is shown in Figure 3-1. Here the phases are calculated under the assumption that the position of the elements are known, that the component insertion phases are also known, and that the incoming signal has a wavefront which is planar. Figure 3-2 shows a view of an array where all of these characteristics are violated. In this case, severe reductions in the signal level to the receiver may result. One type of processing technique which is analogous, is the code acquisition problem in spread-spectrum systems. Figure 3-3 shows how the autocorrelation of the spreading sequence with a replica changes with the time offset. Maximum autocorrelation indicates time alignment. The same process can be used in an antenna array by using signals from separate elements as the comparison signals. The signal at each element is identical in content with only displacement in phase (time). The autocorrelation of the two signals as shown in Figure 3-4 provides the necessary information to compensate for the phase difference using phase shifters.

All methods of self-steering must perform two basic functions. First, the relative phase between the elements must be measured, and second, the relative phase difference must be eliminated. Figure 3-5 shows one of the earliest methods of performing the phase alignment necessary for self-steering. Each element of the array performs a downconversion to intermediate frequency (IF) such that the IF is phase-locked to an internal reference frequency. The phase-locked loop performs both the measurement and phase difference elimination. Since the output phases of the IF outputs will all have phase relationship to the reference oscillator, the relative phase between the IF outputs will be zero. This approach also has the ability to compensate for differential frequency shifts between elements due to doppler shift variations. One potential disadvantage of this approach is that each element becomes a duplicate receiver front end with the combined output at the IF frequency. An alternative approach which provides a combined output at the radio frequency (RF) is shown in Figure 3-6. In this example, signal from each element is coupled to both sides of a phase detector or autocorrelator. One element is chosen as the reference, and each of the other elements is compared in sequence to determine the change in the phase shifter setting to provide coherent signal combination. The approach shown allows any

element to be the reference to minimize single point failures. Additionally, a single element can be fed simultaneously to both sides of the phase detector for calibration purposes.

A self-steered array built from aperture antenna elements will have radiation patterns which are dominated by the characteristics of the individual apertures. The sidelobes of the composite array will fall within the sidelobes of the aperture pattern, and grating lobe formation which may occur will fall within the main beam. The total antenna gain is independent of the composite pattern and depends only on the total aperture area which is combined. To illustrate this principle, Figure 3-7 shows an eight element subarray with 0.75 λ spacing. Figure 3-8 shows the array factor for eight of these subarrays with periodic spacing of 10 λ. Figure 3-9 shows the same array factor as Figure 3-8 with a normally distributed random error in the position having mean of zero and standard deviation of two wavelengths. Practical systems will be of the random type. Figure 3-10 and 3-11 show the product of the array factor and the subarray element factor with the element factor plotted for comparison. In both cases, the maximum composite pattern falls within the envelope of the subarray pattern. However, the randomly positioned array will always tend to provide

lower peak sidelobe and grating lobe levels due to the reduced gain of auxiliary peaks in the array factor for the subarray panels. Total energy in the sidelobe region is the same in either case; the random positioning of the panels simply reduces the peak levels.

CONCLUSION

Self-steered phased arrays have several benefits which should find renewed interest in certain applications. The potential for cost reduction in large antennas is certainly strong motivation in an era of ever tightening budgets. Simpler acquisition and tracking also offer cost reduction benefits. Interest in operation of large antennas in a disturbed atmosphere or in the near field encourage the study of self-phasing concepts. Portable operation is a major new area for the development and use of self-steered phased array techniques. Additionally, resistance to multipath fading encourages self-steered array use in low elevation or urban environments. In fact, the combination of auto-tracking with multipath rejection has already encouraged use in commercial mobile communications. The self-steered phased array provides increased flexibility in solving complex user requirements for many types of applications.

REFERENCES

1. Eberle, J. W. (1964) An adaptive phased, four-element array of thirty-foot parabolic reflectors for passive (Echo) communication systems, *IEEE Transactions on Antennas and Propagation* 12 (No. 2):169-176.

2. Hanson, R. C. (1981) Fundamental limitations in antennas, *Proceedings of the IEEE* 69 (No. 2):170-182.

3. Potter, P. D. et al. (1965) Large antenna apertures and arrays for deep space communications, JPL TR 32-848.

4. Brennan, P. V. (1989) An experimental and theoretical study of self-phased arrays in mobile satellite communications, *IEEE Transactions on Antennas and Propagation* 37 (No. 11):1370-1376.

5. Doherty, R. (1990) Four antennas are better than one, *Electronic Engineering Times*, March 5th, 29.

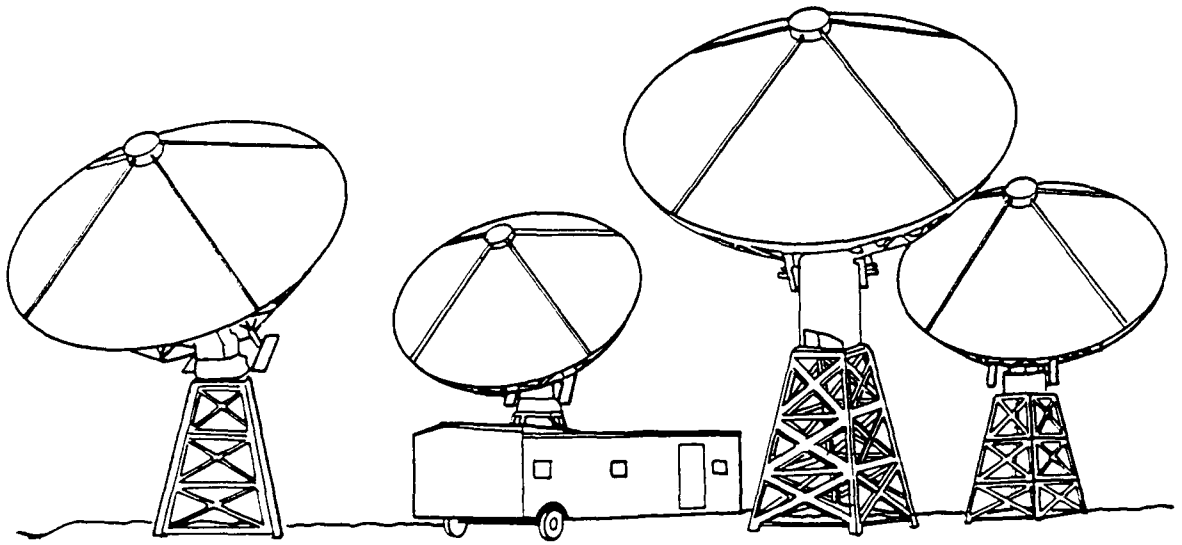

Figure 1-1. Four thirty-foot reflectors combine for Echo satellite communications.

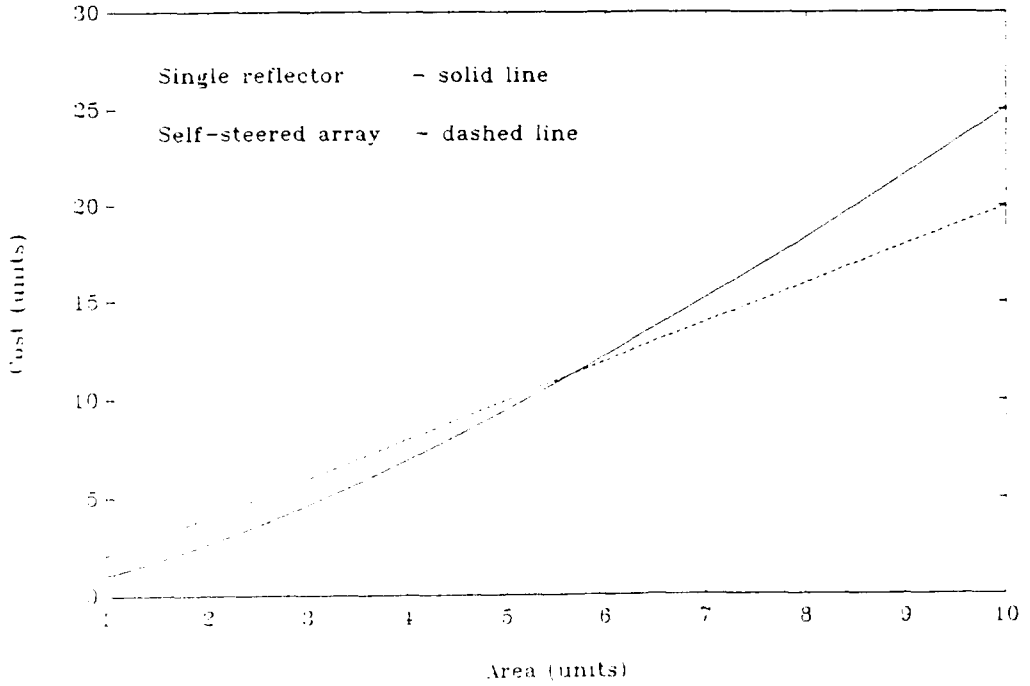

Figure 2-1. Reflector cost increases faster than the cost of self-steered phased arrays.

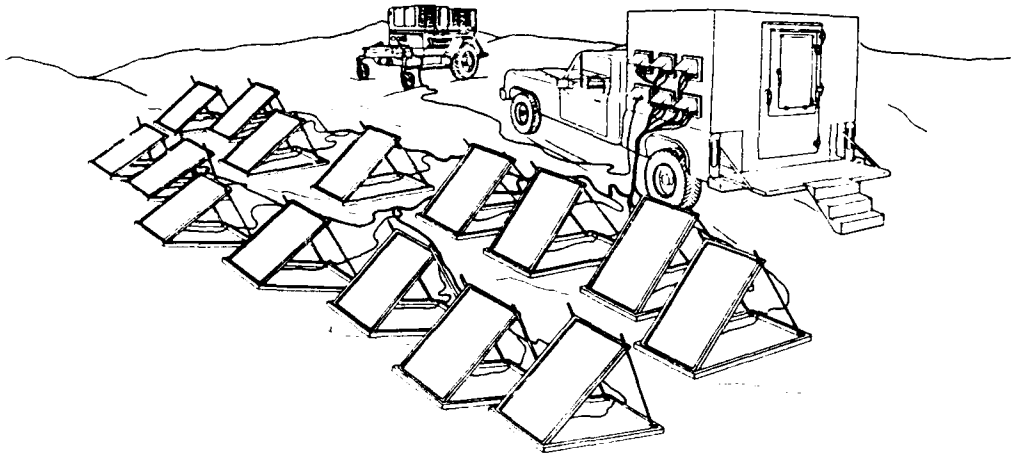

Figure 2-2. Self-steered array for DSCS provides increased mobility with lower volume.

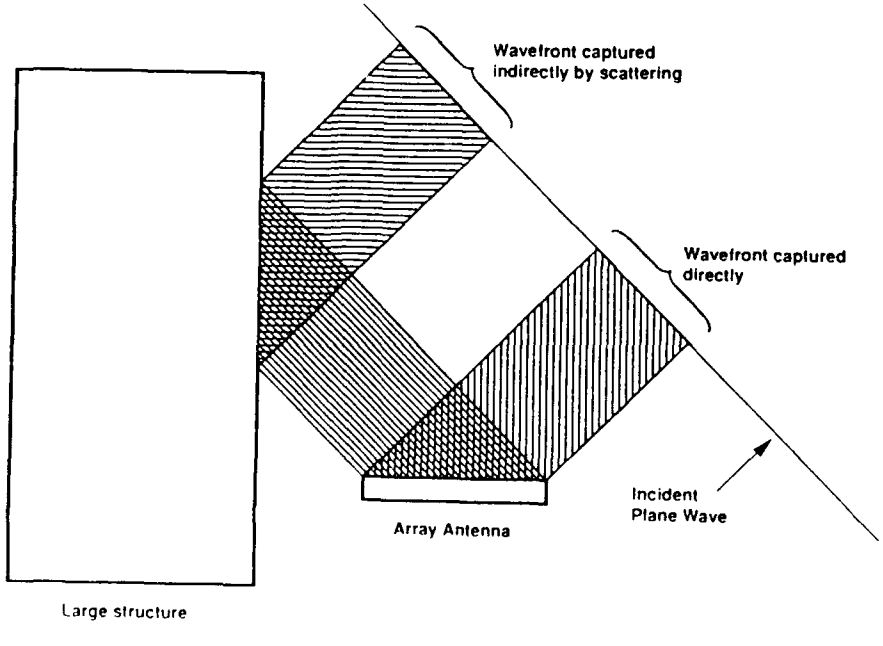

2400 38 053

Figure 2-3. Additional energy may be captured using self-steering concepts.

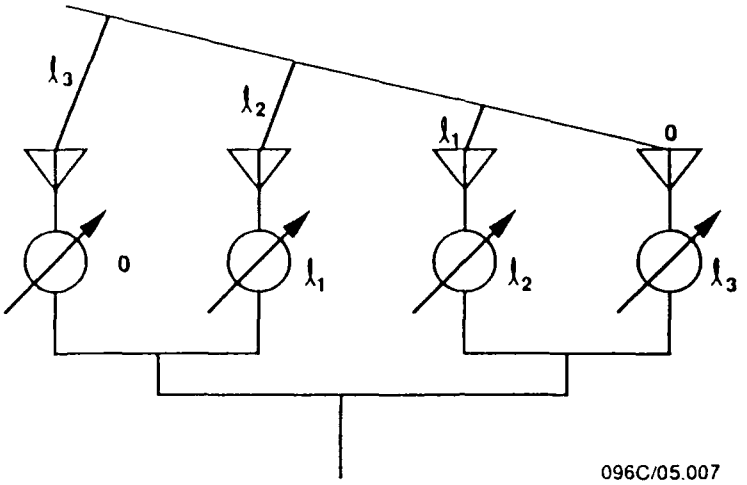

Figure 3-1. Conventional phased array requires knowledge of element positions.

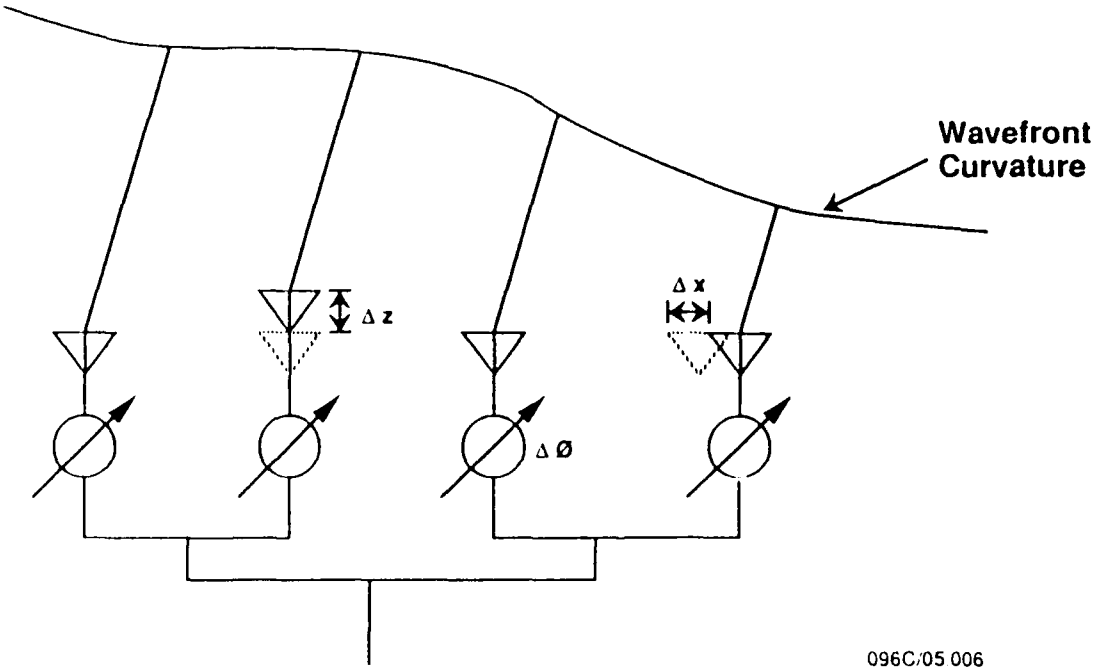

Figure 3-2. Errors cause gain reduction in conventional phased arrays.

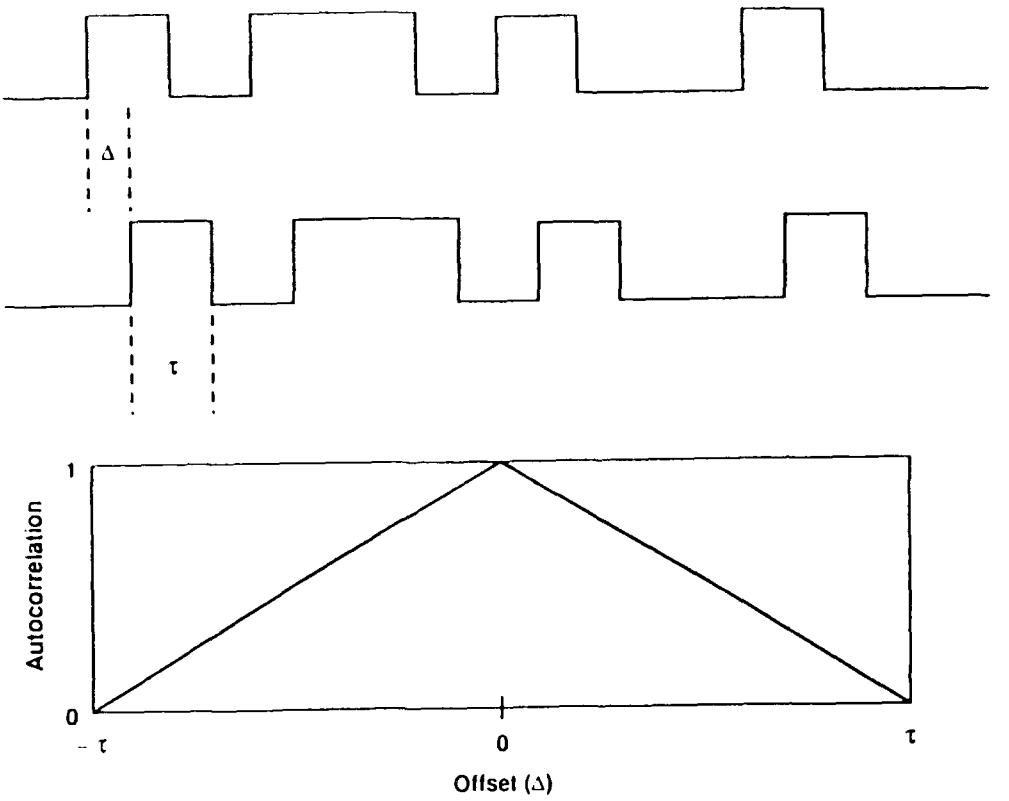

Figure 3-3. Autocorrelation allows determination of time offsets in spread-spectrum systems.

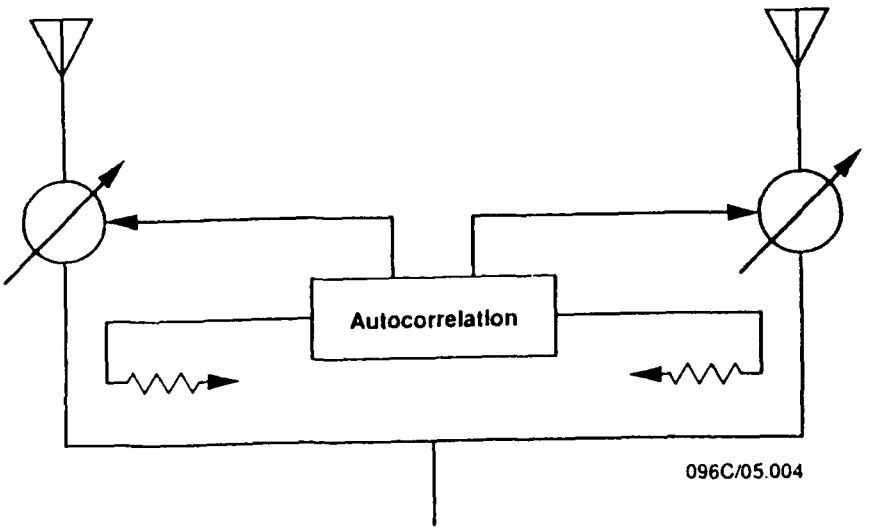

Figure 3-4. Comparison of element phases provides information to set phase shifters.

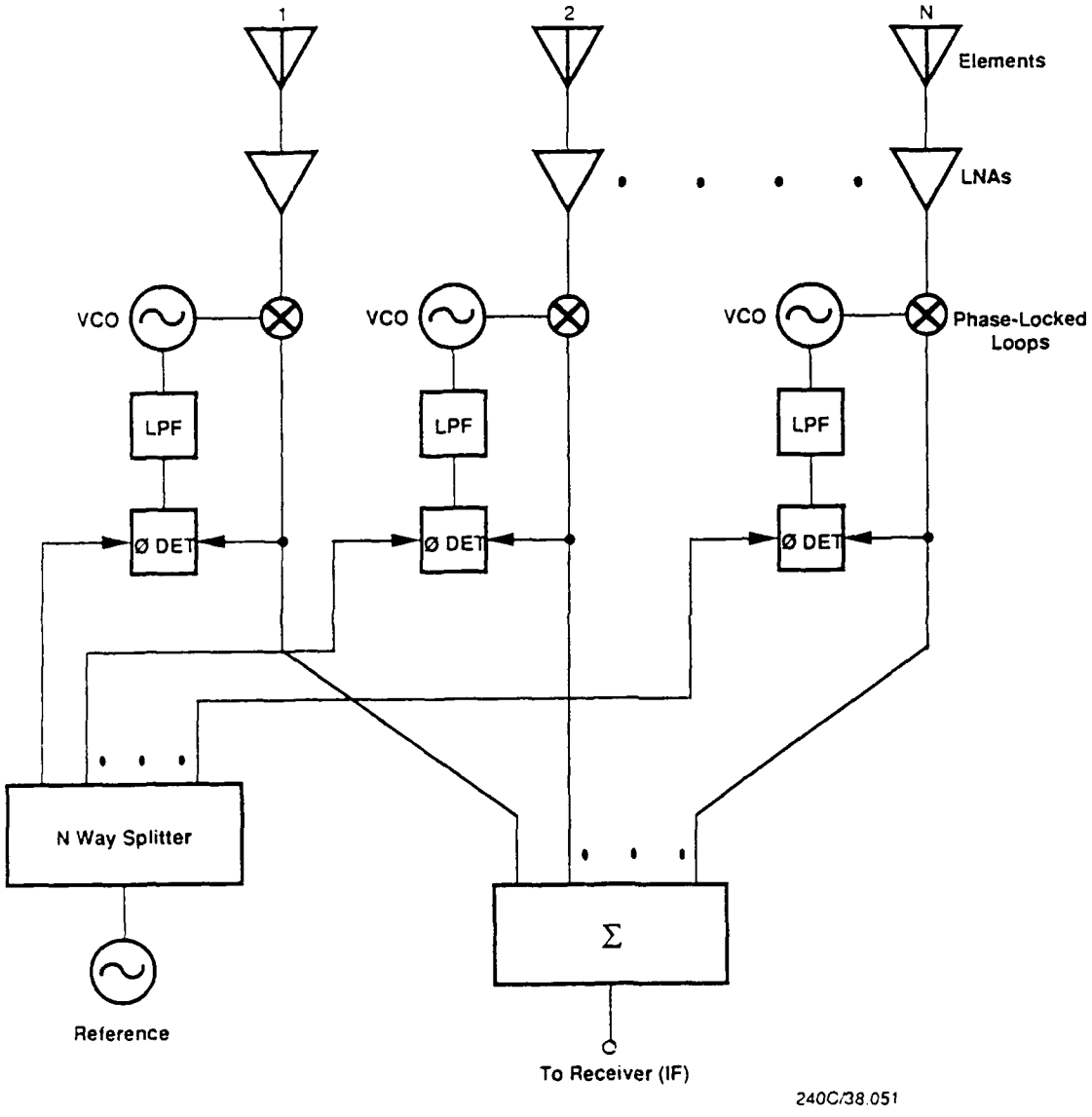

Figure 3-5. Phase-locked loops combine elements.

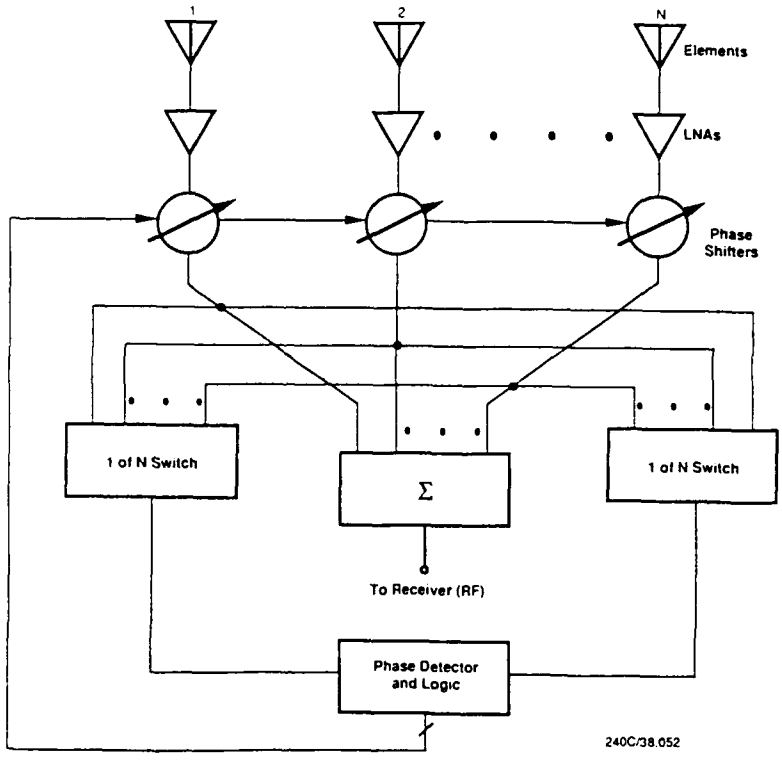

Figure 3-6. Alternate method sets phases at RF.

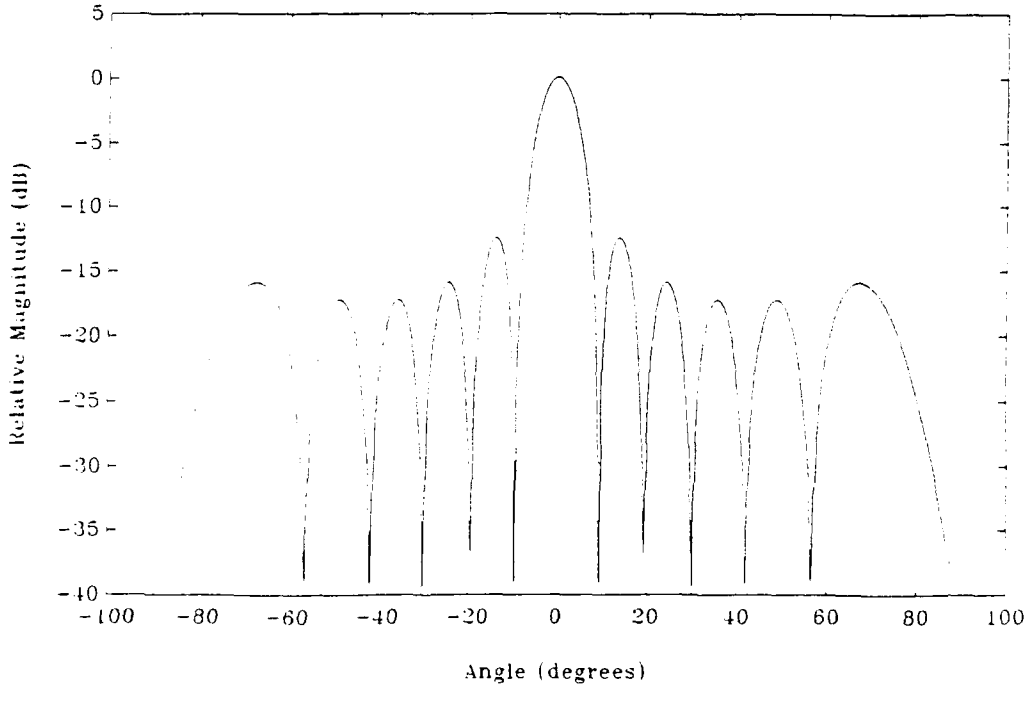

Figure 3-7. Subarray pattern provides an envelope for the composite array radiation pattern.

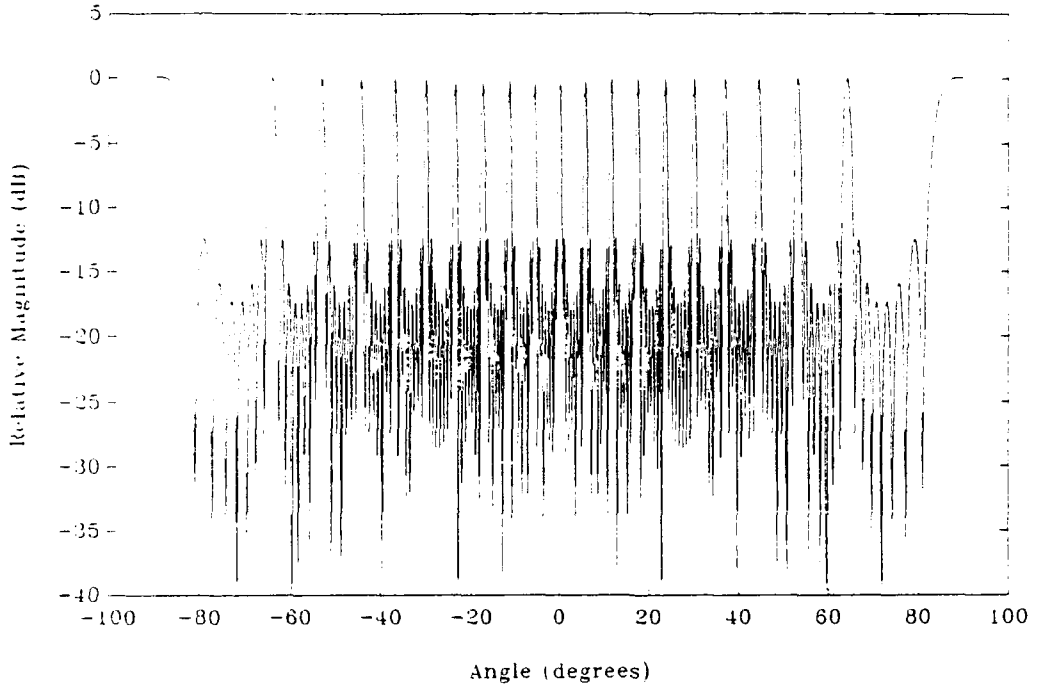

Figure 3-8. Array factcr of periodic spaced panels has full gain grating lobes.

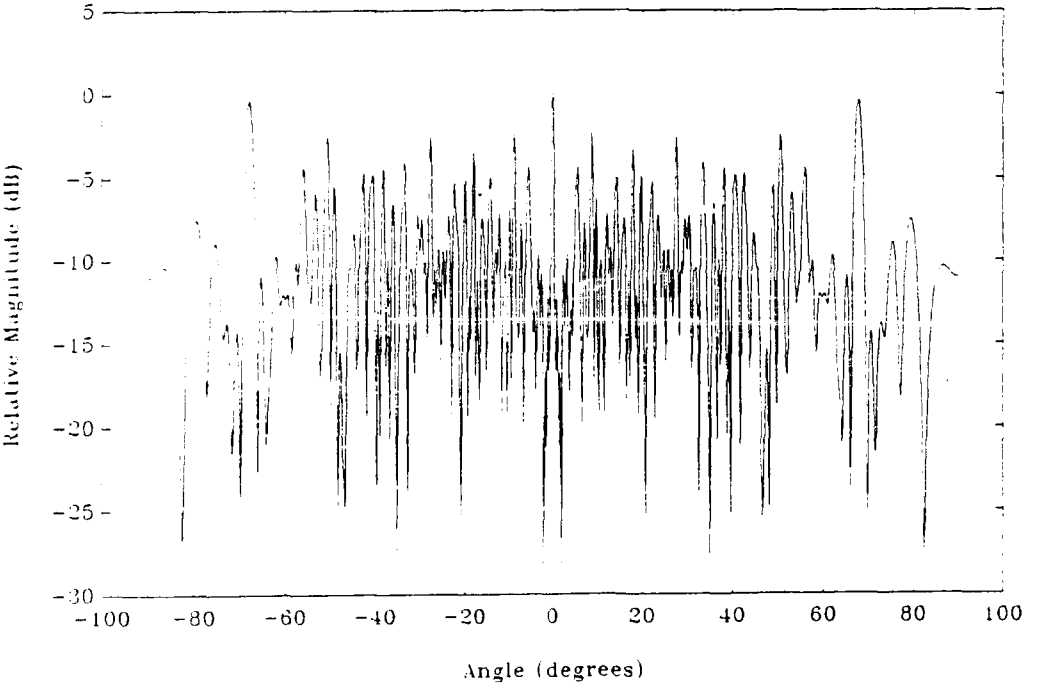

Figure 3-9. Random positioning reduces grating lobe peaks in the array factor.

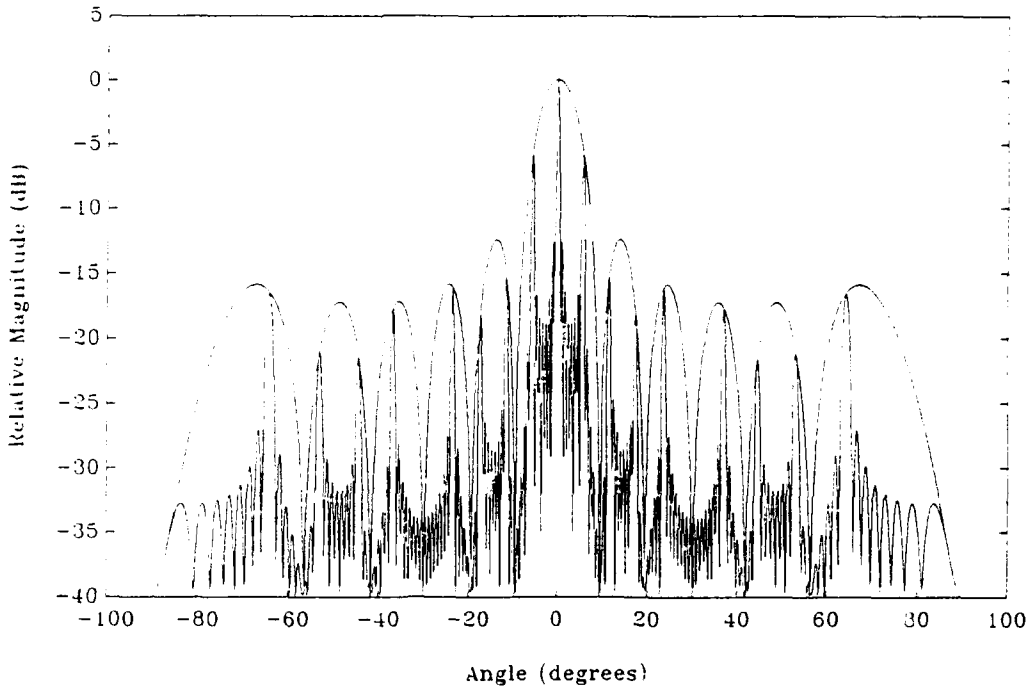

Figure 3-10. Composite pattern of periodic array is constrained by subarray pattern.

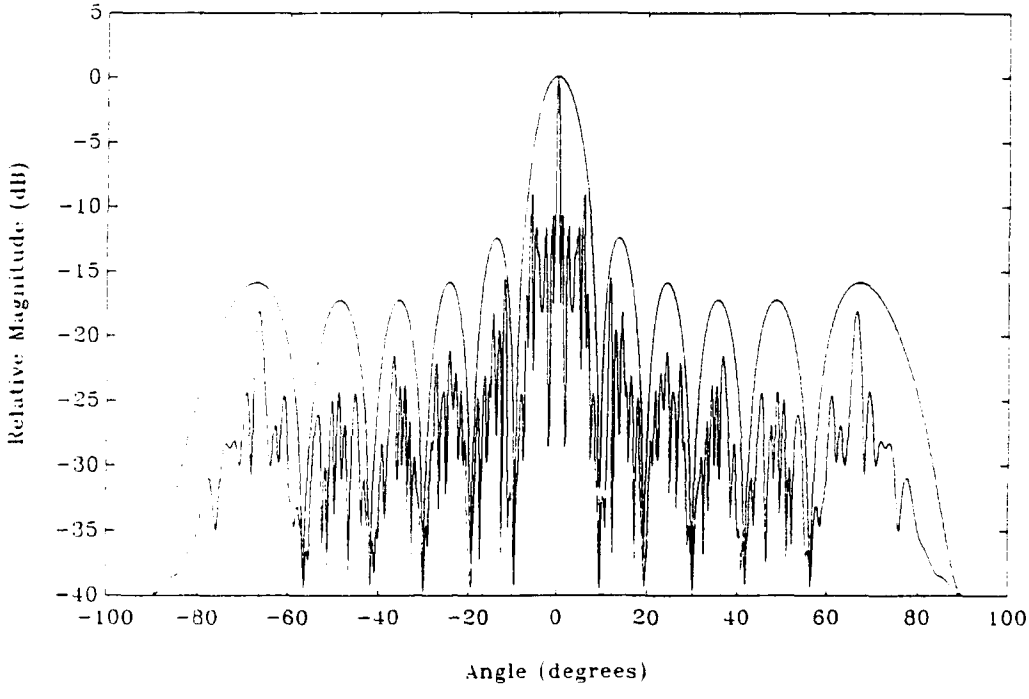

Figure 3-11. Random array reduces peak levels.

SEPTEMBER 1990

ARRAY THINNING USING THE IMAGE ELEMENT ANTENNA

PRESENTED AT THE 1990 SYMPOSIUM ON ANTENNA APPLICATIONS
ROBERT ALLERTON PARK, ILLINOIS

by

JOE KOBUS

ROBERT SHILLINGBURG

and

RON KIELMEYER

MOTOROLA INC.
TACTICAL ELECTRONICS DIVISION
GOVERNMENT ELECTRONICS GROUP
SCOTTSDALE, ARIZONA

ABSTRACT

Current image-antenna array technology is presented. The dielectric-slab image radiator, discovered by Von Trentini, was first incorporated into thinned slot arrays at Motorola's Government Electronics Group (U.S. Patent No. 3990078). This paper presents some previously unconsidered factors affecting image-array performance. An excessively high image-slab permittivity can, owing to enhanced inter-slot coupling, compromise the efficiency and bandwidth of even a highly thinned array. Optimum performance (maximum gain, minimum sidelobes, and maximum bandwidth) in general demands active impedance matching with Clavin-pin compensated slots. This is illustrated for a specific hardware application. A simple analytical extension of the pioneering work of Von Trentini [1] and Immell [2] is outlined for analysis. In addition, a field-theoretical solution is sketched which, although not yet fully exploited, should ultimately yield a sufficiently comprehensive analytical model for image arrays.

1. INTRODUCTION

Von Trentini [1] showed that the gain of a single radiating element could be increased to arbitrarily large values simply by placing the element between two reflecting planes, one of which is a semi-reflector and the other a perfect reflector. This configuration, using a slot as the radiating element and a dielectric slab as the semi-reflector, is displayed in Figure 1. Bellee et al [3] called it an Image Antenna since the gain enhancement can be explained in terms of image theory. Immell and Sasser [2] introduced directional impedances into Von Trentini's model in order to calculate the reflection coefficient of the partially reflecting dielectric sheet. Jackson [4] recently used a transmission line analogy to compute the gain enhancement of printed circuit antennas radiating through partially reflecting sheets.

Subsequent to the pioneering efforts [1] - [3], modifications to optical and transmission line analyses have been used as aids to image array design at Motorola (see for example [11]). While providing physical insights and first-order design relationships, they do not, however, yield adequate models for inter-element coupling. Mutual coupling becomes important in this type of gain enhancement scheme for thinned arrays when the permittivity of the partially reflecting dielectric screen becomes significantly large.

Section 2 gives an outline of the truncated image element model, useful as a simplified approach to array design. Section 3 sketches a field theoretical solution which will ultimately yield an adequate mutual coupling model. Performance of a specific hardware design is discussed in Section 4.

2. TRUNCATED IMAGE-ELEMENT MODEL

Figure 2 presents the geometry basic to understanding broadside array design. Fundamental theory dictates that no more gain can be realized from a finite aperture than

$$G_A = 4\pi A/\lambda^2 \quad , \qquad (1)$$

where A is the total area. If A is divided into N equal S x S sub-apertures, then

clearly for (1) to hold we must have

$$G_S = G_A / N \quad , \qquad (2)$$

for each sub-aperture. Attempts to design an array for which element gains are forced to be greater than G_s will be frustrated by mutual coupling. On the other hand, each gain must be nominally no less than that given by (2), else the composite array gain will fall short of (1), i.e., excessive power will be radiated into grating lobes.

Refer to Figure 1. The analysis of Von Trentini applies to dielectric slabs of infinite extent. Clearly this is not appropriate for arrays. An approach is to assume mutual coupling effectively truncates each sub-aperture in Figure 2 to an area S x S. Thus we need to establish a relationship for the gain enhancement G_I relative to its feed slot of an image antenna which is constrained to a finite aperture. This is done by limiting the number M of the equivalent "endfire images" in Von Trentini's model (Figure 1). Analysis yields

$$G_I = (1 - \rho^2)\rho^{M-1} F(\rho, \xi) \quad , \qquad (3)$$

where M (an integer) is the total number of sources,

$$F(\rho,\xi) = \frac{\mathrm{SINH}^2\left(\frac{M}{2} \mathrm{LN}\rho\right) + \mathrm{SIN}^2\left(\frac{M}{2}\xi\right)}{\mathrm{SINH}^2\left(\frac{1}{2} \mathrm{LN}\rho\right) + \mathrm{SIN}^2\left(\frac{1}{2}\xi\right)} \quad , \qquad (4)$$

and

$$\xi = -\left(\frac{4\pi S_p}{\lambda}\right)\cos\theta - \pi + \psi \quad , \qquad (5)$$

λ = free space wavelength

θ = angle off normal to dielectric slab

S_p = spacing of the slab from the groundplane

ρ = magnitude of the slab reflection coefficient

ψ = phase of the slab reflection coefficient.

If F_o is the band center frequency, then it can be shown [2] that maximum gain occurs at $\Theta = 0$ (Figure 1) when

$$S_p = \lambda_o / 2 \quad , \tag{6}$$

and the dielectric sheet thickness is

$$\tau = \lambda_o / 4\sqrt{\epsilon} \quad , \tag{7}$$

where ϵ is the dielectric constant. For any frequency F near F_o it then follows from an analysis of directional impedances that

$$\rho \cong \rho(F_o) = \frac{\epsilon - 1}{\epsilon + 1} \quad , \tag{8}$$

and

$$\psi \cong \pi \left[1 + \left(\frac{\sqrt{\epsilon}}{\epsilon + 1} \right) \left(1 - \frac{F}{F_o} \right) \right] \quad . \tag{9}$$

Clavin-compensated slots [5], [6], [7], [8], [9], are used to minimize radiation along the groundplane. They have been found to reduce inter-element coupling as well as Brewster-angle and grating-lobe radiation. For Clavin compensation it is easily shown that a slot has 7.8 dBI gain. Thus the total gain of an image radiator becomes

$$G_o = 10 \log_{10}(G_I) + 7.8 + 20 \log_{10}(\cos \Theta) \quad , \tag{10}$$

where G_I is given by (3).

Refer to Figure 3. Calculation of field radiation patterns for an array of N (here assumed identical) image antenna elements is made from

$$E = \sum_{n=1}^{N} E_e \, e^{j \psi(n)} \quad , \tag{11}$$

where

$$E_e = E_o(n) \sqrt{G_I} \, f(\Theta) \quad . \tag{12}$$

Here f(e) is the feed slot pattern sans dielectric, and G_t is given by (3); $E_o(n)$ are the amplitude weightings in the corporate (combiner) network. In terms of the Figure 3 coordinate system we also have

$$\Omega = \left[\frac{2\pi R(n)}{\lambda}\right] \sin\theta \cos(\phi - \phi(n))$$
$$= \left(\frac{2\pi}{\lambda}\right)\left[X(n)\cos\phi + Y(n)\sin\phi\right]\sin\theta \quad . \qquad (13)$$

Theoretical image antenna E-plane patterns are displayed in Figure 4. These patterns are computed at a frequency for which the image slab is $\lambda/4$ thick and spaced $\lambda/2$ from the ground plane. The slot illumination pattern is assumed to obey

$$f(\theta) = \cos\theta \quad , \qquad (14)$$

which requires Clavin pins. Observe that the untruncated patterns shown in Figure 4 display considerably more variation with ϵ than do the patterns truncated at M = 15, a value corresponding to typical image element-to-element spacings in practical broadside arrays. This variation is easily understood by referring again to Figure 1. The effective amplitudes of successive virtual images are given by

$$V(m) = E_o T \rho^m \quad . \qquad (15)$$

Thus, taking (8) into account, the V(m) are more rapidly attenuated for lower ϵ slabs. Consequently, the effect of removing images is more dramatic for higher dielectric constants than for lower. The physics of the situation is that less power is radiated per "bounce" from higher ϵ sheets than from lower. It is also why, given a fixed average spacing, inter-element coupling becomes a greater problem for higher ϵ slabs; more power remains to be coupled to neighbors in broadside arrays.

Comparison of E-plane patterns computed for a typical 24-element array are presented in Figure 5. Observe that patterns obtained with untruncated (incorrect) elements exhibit lower first (3dB) and second side lobes than do patterns for truncated elements. Recorded patterns of arrays larger than two image elements per quadrant commonly display higher sidelobes than those calculated using untruncated elements. Given Figure 4, these higher sidelobes

result from the broader truncated image element patterns.

In conjunction with the truncation model, Motorola has pursued an intensive laboratory effort to understand array thinning. The paramount techniques applied in this work were measurement and analysis of active element patterns, gain, and impedance. An isolated corporate feed network, Figure 6, with adjustable amplitude and phase weights was used as a measurement tool for verification of low-sidelobe image array designs of up to 28 elements. Standard array theory was used to calculate sum and difference patterns; first-order impact of coupling was approximated by truncation of individual element (sub) apertures. This model yields array gain in excellent agreement with measurement when the average element gain (2) is assumed to be equal to (10), but only for sufficiently low ϵ image slabs. The truncation model also yields patterns in reasonable agreement with those recorded for arrays, but only for a number ($M \backsim 15$) of image elements different from that ($M \backsim 8$) required for gain computations. Clearly this simplified approach is useful, but also incorrect, especially since, in any case, all elements in a small array hardly have identical patterns or gain. Consequently a field-theoretical solution to the problem of thinned arrays whose elements are modified with a dielectric sheet is desired. An effort in this direction is outlined in Section 3.

As an example, however, of the research findings in the context of the truncation model, consider the 24-element array of Figure 7. The gain calculation is superimposed on the Figure 8 recorded data for image element No. 1. Agreement is good if one recognizes that these data include impedance mismatch loss and stripline feed loss as functions of frequency whereas the computations do not. On the other hand, measurements for a dielectric sheet with relative permittivity of 37 fall considerably short of similar calculations. Evidently ϵ =37 is too high whereas ϵ =25 is probably close to optimum for the average element spacing in this particular array. Further data support the conclusion that a relative permittivity of 37 results in tighter slot-to-slot coupling (Figure 9) than does ϵ = 25. The truncation model clearly does not adequately account for mutual coupling.

Element gains for the two permittivities are presented in Figures 10-11. Embedded gain was recorded at an SMA coaxial connector near each slot radiator. Series stripline [10] is used to couple to each slot in the groundplane opposite an image slab supported by a hexagonal-cell honeycomb layer.

As expected, inner radiators display less gain than outer ones. Since they are virtually surrounded, inner elements are much more affected by coupling than are outer elements, exposing another shortcoming of the truncation model. Furthermore, these data constitute additional evidence in support of the conclusion that lowered permittivities yield less coupling.

Table 1 reveals the impact of image-slab permittivity on aperture efficiency. These values are computed with the aid of the basic array relationship

$$G = \left| \sum_n \sqrt{G_o(n)}\, E_o(n) \right|^2 \Big/ \sum_n |E_o(n)|^2 \quad , \qquad (16)$$

valid for generally dissimilar element gains $G_o(n)$. Observe that when all radiators are equally weighted, (16) yields

$$G = N^{-1} \left(\sum \sqrt{G_o(n)} \right)^2 \quad , \qquad (17)$$

which if all are identical reduces to (2). Recorded power (dBI) gains, given in Figures (10) and (11), respectively, were converted to voltage ratio gains $\sqrt{G_o(n)}$ and substituted into (17). Table 1 gains determined in this manner were also compared with corporate-fed gains recorded using the universal test arrangement of Figure 6. After correction for feed network insertion loss, the two independently determined array gains are virtually identical (typically within $\pm$ .3dB).

Figure 12 shows E-plane patterns recorded for a 24-element array in the Figure 6 universal feed network. Comparison with theoretical patterns obtained using (10)-(13) together with (3)-(5) is excellent.

3. FIELD THEORETICAL ANALYSIS

This section presents a field theoretical analysis of a single Clavin pin compensated slot in an infinite ground plane with M dielectric plates stacked in the **z** direction. The image antenna is a special case for which M=3. Normally, ε_{rM} would be air but the analysis which follows is kept general at this point. Figure 13 shows the specific case of M=3.

The single Clavin pin compensated slot solution is obtained by solving two seperate problems. The first problem is that of a single narrow slot enhanced with the dielectric slabs. For this problem a solution to the fields is found in terms of the assumed Electric field distribution in the slot. The second problem is that of a monopole antenna protruding into ε_{r1} in the z direction. A solution for the fields is found in terms of an assumed current distribution on the monopoles. A moment method solution is then applied to the problem to determine the current distribution along the monopoles in terms of the assumed Electric field distribution of the slot.

The solution to the first problem can be derived from the Magnetic (Π_h) and Electric (Π_e) Hertzian potentials [12] which have single components in the direction normal to the surface of the dielectric (i.e. the **z** direction). The equations which must be solved and their solutions are shown in Table 2, 3 and 4.

Table 2

Starting Equations for the Image Antenna Problem - Slot without Clavin Pins

$\nabla^2 \Pi_h + k^2 \Pi_h = 0$	$\nabla^2 \Pi_e + k^2 \Pi_e = 0$	(18)
$\mathbf{E} = -j\omega\mu \nabla X \Pi_h$	$\mathbf{E} = k^2 \Pi_e + \nabla\nabla\Pi_e$	(19)
$\mathbf{H} = k^2 \Pi_h + \nabla\nabla\Pi_h$	$\mathbf{H} = j\omega\varepsilon \nabla X \Pi_e$	(20)

$$\Pi(x,y,z) = [2\pi]^{-2} \int_{\Re} \int_{\Re} \mathbb{\Pi}(\alpha,\beta,z) e^{-j(\alpha x+\beta y)} \partial\alpha\partial\beta. \quad (21)$$

$$\mathbb{\Pi}(\alpha,\beta,z) = \int_{\Re} \int_{\Re} \Pi(x,y,z) e^{j(\alpha x+\beta y)} \partial x \partial y. \quad (22)$$

Table 3

Solution to the Equations in Regions $i \neq M$

$$\Pi_{hi} = A_i\{\cosh[\gamma_i(z-z_{i-1})]+\Psi_{hi}\sinh[\gamma_i(z-z_{i-1})]\}\} \quad (23)$$

$$\Pi_{ei} = B_i\{\Psi_{ei}\cosh[\gamma_i(z-z_{i-1}))]+\sinh[\gamma_i(z-z_{i-1})]\} \quad (24)$$

$$\gamma_i^2 = \alpha^2+\beta^2-k_i^2 \quad (25)$$

$$A_i = \{\mu_{i-1}/\mu_i\}\{C_{i-1}+\Psi_{hi-1}S_{i-1}\}A_{i-1} \quad (26)$$

$$B_i = \{\gamma_{i-1}/\gamma_i\}\{C_{i-1}+\Psi_{ei-1}S_{i-1}\}B_{i-1} \quad (27)$$

$$C_i = \cosh[\gamma_i(z_i-z_{i-1})] \quad (28)$$

$$S_i = \sinh[\gamma_i(z_i-z_{i-1})] \quad (29)$$

$$T_{i-1} = S_{i-1}/C_{i-1} \quad (30)$$

$$\Psi_{hi-1} = \{\Psi_{hi}-Z_{hi}T_{i-1}\}/\{Z_{hi}-T_{i-1}\Psi_{hi}\} \quad (31)$$

$$\Psi_{ei-1} = \{\Psi_{ei}-Z_{ei}T_{i-1}\}/\{Z_{ei}-T_{i-1}\Psi_{ei}\} \quad (32)$$

$$Z_{hi} = \{\mu_i/\mu_{i-1}\}\{\gamma_{i-1}/\gamma_i\} \quad (33)$$

$$Z_{ei} = \{\varepsilon_{i-1}/\varepsilon_i\}\{\gamma_i/\gamma_{i-1}\} \quad (34)$$

$$A_1 = \{(j\beta)\mathbb{E}_x(S_s)-j\alpha\mathbb{E}_y(S_s)\}/\{j\omega\mu_1(\alpha^2+\beta^2)\} \quad (35)$$

$$B_1 = -\{j\alpha\mathbb{E}_x(S_s)+j\beta\mathbb{E}_y(S_s)\}/\{\gamma_1(\alpha^2+\beta^2)\} \quad (36)$$

Table 4

Solution to the Equations in Regions $i=M$

$$\Pi_{hM} = A_M\exp[-\gamma_M z] \quad (37)$$

$$\Pi_{eM} = B_M\exp[-\gamma_M z] \quad (38)$$

$$A_M = \{\mu_{M-1}/\mu_M\}\{C_{M-1}+\Psi_{h(M-1)}S_{M-1}\}\exp[\gamma_M z_{M-1}]A_{M-1} \quad (39)$$

$$B_M = -\{\gamma_{M-1}/\gamma_M\}\{C_{M-1}+\Psi_{e(M-1)}S_{M-1}\}\exp[\gamma_M z_{M-1}]B_{M-1} \quad (40)$$

$$\Psi_{hM-1} = -\{T_{M-1}Z_{hM}+1\}/\{Z_{hM}+T_{(M-1)}\} \quad (41)$$

$$\Psi_{eM-1} = -\{T_{M-1}Z_{eM}+1\}/\{Z_{eM}+T_{(M-1)}\} \quad (42)$$

In the Tables above, $\int_{\Re}$ indicates integration over $\pm\infty$ and $\mathbb{E}_x(S_s)$ and $\mathbb{E}_y(S_s)$ are the Fourier transforms of the fields in the slot.

The far field patterns can be obtained from the total transformed electric field in the Mth dielectric region given by

$$E(x,y,z) = [2\pi]^{-2}\int_{\Re}\int_{\Re}\{\{-\beta\alpha(\Omega_h-\Omega_e)\}\mathbf{x}+\{\alpha^2\Omega_h+\beta^2\Omega_e\}\mathbf{y} + \{\alpha^2+\beta^2\}(j\beta)/\gamma_M\Omega_e\mathbf{z}\}\mathbb{E}_y(S_s)(\alpha^2+\beta^2)^{-1}e^{j(\alpha x+\beta y)}\partial\alpha\partial\beta. \quad (43)$$

$$\Omega_h=\prod\left[\{C_{i-1}+\Psi_{h(i-1)}S_{i-1}\}\right]\exp[\gamma_M z_{M-1}] \quad (44)$$

$$\Omega_e=\prod\left[\{C_{i-1}+\Psi_{e(i-1)}S_{i-1}\}\right]\exp[\gamma_M z_{M-1}] \quad (45)$$

The use of asymptotic techniques as **outlined** by Bleistein [13] to evaluate this integral provides an explicit formula for the far field pattern of the configuration. Inserting the standard conversions from rectangular to spherical coordinates into (43), an equation of the following form results

$$\mathbf{E}(\rho,\theta,\phi)|_{\rho\to\infty}=\pm jk_M\cos(\theta)[2\pi\rho]^{-1}\mathcal{g}(\alpha_o,\beta_o)\exp[j\rho\xi(\alpha o,\beta o)-j\pi/2] \quad (46)$$

where α_o and β_o are

$$\alpha_o=\pm k_M\sin(\theta)\cos(\phi) \quad (47)$$

$$\beta_o=\pm k_M\sin(\theta)\sin(\phi). \quad (48)$$

The function $\mathcal{g}(\alpha_o,\beta_o)$ is given by

$$\mathcal{g}(\alpha_o,\beta_o)=\mathbb{E}_y(S_s)\left\{\Omega_e\sin(\phi)/\cos(\theta)\theta+\cos(\phi)\Omega_h\phi\right\} \quad (49)$$

Inserting these results into (46) we obtain for the far field

$$\mathbf{E}(\rho,\theta,\phi)|_{\rho\to\infty}=-jk_M[2\pi\rho]^{-1}\mathbb{E}_y(S_s)$$
$$\left\{\Omega_e\sin(\phi)\theta+\cos(\phi)\cos(\theta)\Omega_h\phi\right\}\exp[-j\rho k_M]. \quad (50)$$

A similar route can be taken to obtain the field patterns of the monopole radiators when they are excited by a current distribution with a single component in the z direction. For this type of excitation $\Pi_h=0$ so only Π_e is considered. Table 5 shows the starting equations for the regions where the monopoles do exist.

Table 5
Starting Equations for the Image Antenna Problem - Monopole Radiators

$$\nabla^2 \Pi_e + k^2 \Pi_e = (1/j\omega\varepsilon_1)\mathbf{J} \tag{51}$$

$$\mathbb{H} = j\omega\varepsilon \{j\beta\Pi_e \mathbf{x} - j\alpha\Pi_e \mathbf{y}\} \tag{52}$$

$$\mathbb{E} = \{k^2 + \partial^2/\partial z^2\}\Pi_e \mathbf{z} + j\alpha\partial/\partial z \Pi_e \mathbf{x} + j\beta\partial/\partial z \Pi_e \mathbf{y}. \tag{53}$$

$$\Pi_{e1} = (-1/j\omega\varepsilon_1\gamma_1) \int_{o,h} \cosh[\gamma_1 z_<]\{\Psi_{e1}\cosh[\gamma_1 z_>] + \sinh[\gamma_1 z_>]\} J_z(z_o)dz_o \tag{54}$$

$$z_< = \min(z_o, z) \tag{55}$$

$$z_> = \max(z_o, z) \tag{56}$$

$$B_1 = (-1/j\omega\varepsilon_1\gamma_1) \int_{o,h} \cosh[\gamma_1 z_o] J_z(z_o)dz_o \tag{57}$$

$$B_i = \exp[\gamma_i z_{i-1}]/(j\omega\varepsilon_1\gamma_i) \prod [\{C_{i-1} + \Psi_{e(i-1)} S_{i-1}\}] \int_{o,h} \cosh[\gamma_1 z_o] J_z(z_o)dz_o \tag{58}$$

In Table 5, $\int_{o,h}$ indicates the integral from 0 to h . The B_1 in Table 5 can be used in (45) instead of (36).

In order complete the solution, the moment method must be applied to the system so that the sum of the fields from the slot and the scattered fields from the Clavin pins is zero on the surface of the pin. To this end we use basis functions of the form

$$J_{z1}(z_o) = f_{\alpha\beta 1} f_x(z) \tag{59}$$

where

$$J_{z2}(z_o) = f_{\alpha\beta 2} f_x(z) \tag{60}$$

$$f_x(z) = \sum_n A_{nx}\delta(z - z_{on}) \quad x = 1,2 \tag{61}$$

$$f_{\alpha\beta 1} = f_{\alpha\beta}\exp(j\beta d) \tag{62}$$

$$f_{\alpha\beta 2} = f_{\alpha\beta}\exp(-j\beta d). \tag{63}$$

$$f_{\alpha\beta} = (w_p/2)^2 \mathrm{sinc}(\beta w_p/2)\mathrm{sinc}(\alpha w_p/2) \tag{64}$$

Here d is the distance from the slot to the Clavin pin. Galerkin's method is used to reduce the integral equation to a matrix which in turn is solved for the amplitudes A_{nx}. Due to the shifting properties of the Fourier transform, this method can easily be extended to include all of the slots in an array and all of the Clavin pins, yielding a much bigger matrix, but all the coupling between the slots and Clavin pins would then be accounted for.

Figure 14 shows the gain enhancement in the E-plane as a function of angle for an uncompensated slot with an image plate dielectric constant of 25 along with the predicted sidelobe reduction due to the Clavin pins. Also shown in Figure 14 is a comparison between this theory and that of Immell and Sasser [2]. As can be seen from the figures, the two theories yield identical results.

Experimental evidence shows the existence of waveguide type propagation modes between the ground plane and the high dielectric constant image plate. In order for these modes to exist, the integral (21) has residuals at values of α and β which would be determined by the functions in (23)-(25) . The residuals could be obtained via graphical methods or some other numerical technique (however the authors have not yet completed this task). In order to meet the constraints imposed by the continuity of the tangential fields at the boundarys between each of the dielectric plates, α and β must be equal in all dielectric regions. Suppose that residual values for α and β were found such that $\alpha^2+\beta^2 = k^2_{res}$. Since we are integrating along the real axis, only real values of α and β are **expected.** Furthermore in order for the resulting solution to be physically meaningful, $k^2_{air}<k^2_{res}<k^2_{max}$ where k_{max} is the wavenumber of the highest dielectric constant in the system (ε_{r2} in Figure 13). Since the wavenumbers are inversely **proportional** to the wavelength $\lambda_{air}>\lambda_{res}>\lambda_{max}$. Therefore, if ε_{r1} in Figure 13 is equal to one, wavequide propagation in region 1 would be expected to occur, as it does experimentally.

4. DESIGN AND PERFORMANCE OF A SPECIFIC IMAGE ARRAY

A high gain, low sum and difference sidelobe, deep null antenna was needed for a Motorola seeker application. Analysis revealed this could be achieved with an optimum image array of 9 elements configured within a 5 wavelength diameter aperture. The antenna (Figure 15) consists of an image plate with a dielectric constant of 16, a honeycomb spacer, a metal ground plane and a triplate assembly containing the sum and difference channel stripline feed network. Fasteners (not shown) and bonding films were used to produce a rugged design. Coordination with the receiver and gimbal designers was required to obtain an assembly that functions properly within the limited volume available.

The number of slots and the dielectric constant were selected using the truncated image-element model discussed above. The antenna schematic is shown in Figure 16 and the stripline feed circuit in Figure 17. Signals intercepted at each radiating slot pass along a triplate section. The two slots in each quadrant are combined in an isolated power divider and these outputs are combined in a ring hybrid comparator to form sum, E-plane difference, and H-plane difference channels. The center slot is used only in the sum channel.

The reason why the center element is limited to the sum channel is explained by noting aperture amplitude (as well as phase) distributions for optimum sum patterns are considerably unlike those for optimum difference patterns [14]. For given minor-lobe requirements and a fixed aperture, an optimum sum-aperture distribution yields maximum gain, and an optimum difference-aperture distribution provides maximum tracking sensitivity. Now the analysis of Bayliss [14] is limited to line-source arrays. However, it can be generalized to circular apertures. The mathematics is somewhat complicated for image arrays. Near-optimum difference patterns can be realized by not using elements near the center of the array, while near-optimum sum patterns require a center element. The separable sum and difference channel aperture distributions provided by Motorola's design are thus its key performance advantage. Motorola has successfully incorporated this technique into several

image array designs.

Because of high mutual coupling among the elements, active matching is necessary to achieve the performance required. To illustrate the pattern distortion which can arise from electromagnetic coupling between the center and the outer elements, the array of nine described above was assembled with a separate waveguide-to-coax adapter feeding each slot. Waveguide was selected for simplicity of testing. The center element waveguide adapter was connected to a receiver while the outer element adapters were terminated in phase shifters and shorts. A pattern of the center slot was taken with all of the outer element phase shifters set to the same position; this was repeated for a total of 4 phase shifter positions. The results at a specific frequency are shown in Figure 18, which clearly demonstrates considerable variation in gain for the center element.

To achieve the required low sidelobes the center element is weighted heaviest. Consequently, substantial loss of array gain results if the center element gain is reduced by excessive coupling to the outer elements. Additional reduction to array gain can occur if this coupling also distorts element phase relationships. Furthermore, to achieve the required sidelobes in the presence of high coupling requires greater amplitude taper than without coupling. Thus active impedance matching is necessary to achieve the performance requirements.

Considerations for a good design are:

- Broadbanding demands active impedance matching at the radiators.
- Active impedance matching must take into account amplitude weighting of the elements.

Table 6 presents a performance summary of the specific image array.

TABLE 6
ANTENNA PERFORMANCE

PARAMETER		GOAL	TYPICAL	WORST
GAIN	CNTR FREQ	≥21.0 DBI	+22.0	+22.0
	FREQ BAND	≥21.0 DBI	+21.9	+21.8
SUM	E-PL	≥21 DB	23	22
SIDELOBES	H-PL	≥21 DB	24	22
DIFF	E-PL	≥22 DB	25	24
SIDELOBES	H-PL	≥22 DB	28	27
NULL DEPTH		≥27 DB	35	33

REFERENCES

[1] Giswalt VonTrentini, "Partially Reflecting Sheet Arrays," IRE Trans. on Antennas and Propagation, October 1956; pp. 666-671.

[2] Raymond G. Immell and Bill H. Sasser, "A Highly Thinned Array Using the Image Element Antenna," Third Annual Antenna Applications Symposium, Robert Allerton Park, Illinois, September 1979.

[3] E. Bellee, R. Breithaupt, D. Godwin and S. Walker, U.S. Patent No. 3990078, November 1976, assigned to Motorola, Inc.

[4] D. Jackson and N. Alexopoulos, "Gain Enhancement Methods for Printed Circuit Antennas", IEEE Trans. in Antennas and Propagation, Volume AP-33, No. 9, September 1985.

[5] Alvin Clavin, "A New Antenna Feed Having Equal E- and H- Planes", IEEE Trans. on Antennas and Propagation, Vol. AP-2, July 1954.

[6] Alvin Clavin, "A Multimode Antenna Having Equal E- and H- Planes", IEEE Trans. on Antennas and Propagation, September 1975, pp. 735-736.

[7] Alvin Clavin, "An Improved Element for Use in Array Antennas", IEEE Trans. on Antennas and Propagation, Vol. AP-22, July 1974, pp. 521-526.

[8] A.B. Papierz, S.M. Sanzgiri, and S.R. Laxpati, "Analysis of Antenna Structure with Equal E- and H- Plane Patterns", Proc. IEE, Vol. 124, January 1977, pp. 25-30.

[9] R.S. Elliott, "On the Mutual Admittance Between Clavin Elements", IEEE Trans. on Antennas and Propagation, Vol. AP-28, pp. 864-870.

[10] Rolf O.E. Lagerlof, "Design of Cavity Backed Slot Antennas and Some Other Related Microwave Components", Chalmers University of Technology TR No. 34, April 1973.

[11] Terry L. Gibbs, "Image Antenna Bandwidth Characteristics", Master of Science Engineering Thesis, Arizona State University, December 1984.

[12] R. Collin, "Field Theory of Guided Waves", McGraw-Hill, 1960

[13] N. Bleistein, "Mathematical Methods for Wave Phenomena.", N.Y., Academic Press, 1984

[14] E.T. Bayliss, "Design of Monopulse Difference Patterns with Low Sidelobes", Bell System Tech. J., May-June 1968, pp. 623-650.

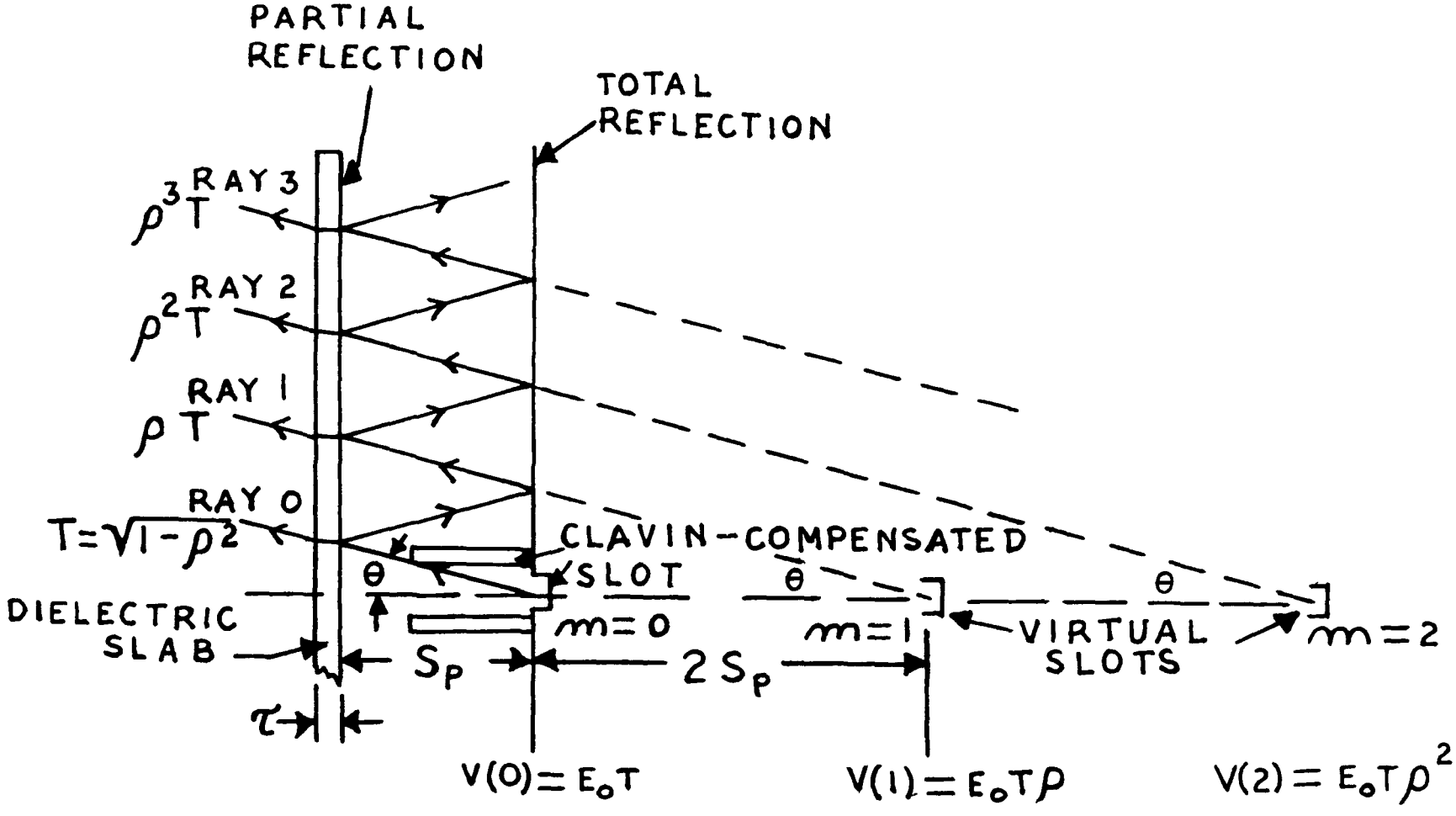

FIGURE 1. IMAGE ANTENNA CONCEPT

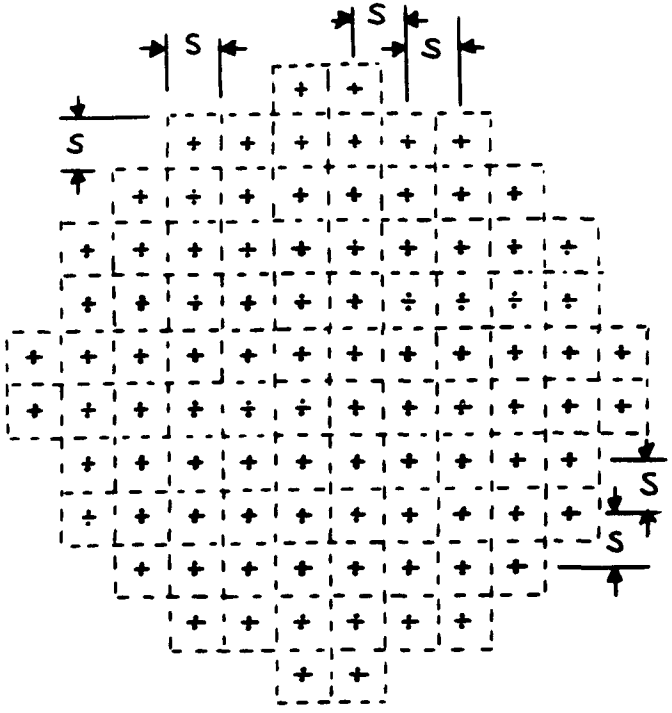

FIGURE 2. ARRAY COMPOSED OF N SXS SUB-APERTURES

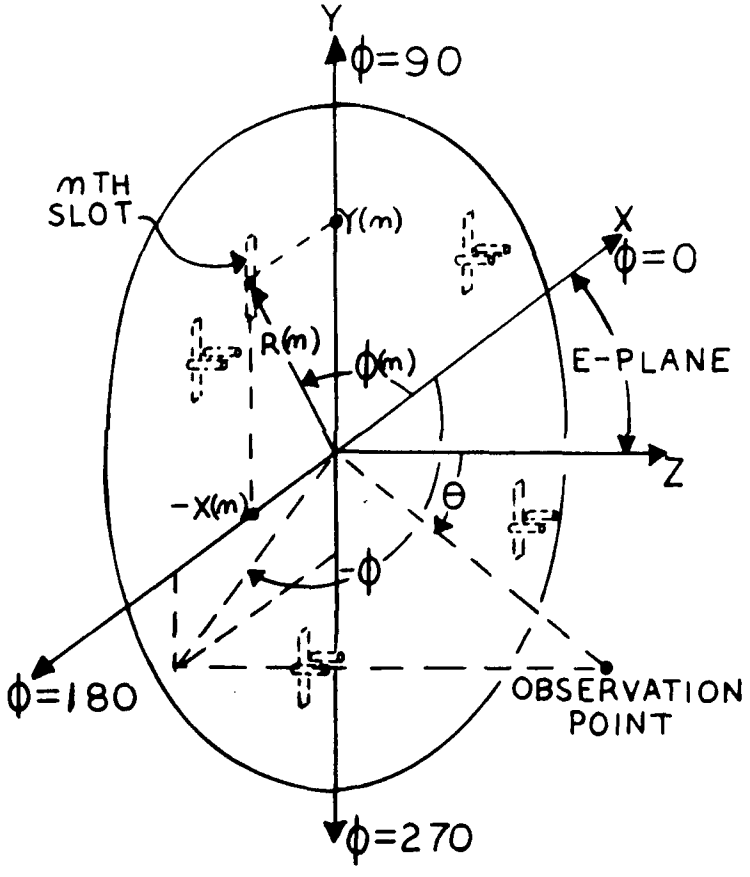

FIGURE 3. COORDINATE SYSTEM FOR PATTERN COMPUTATIONS

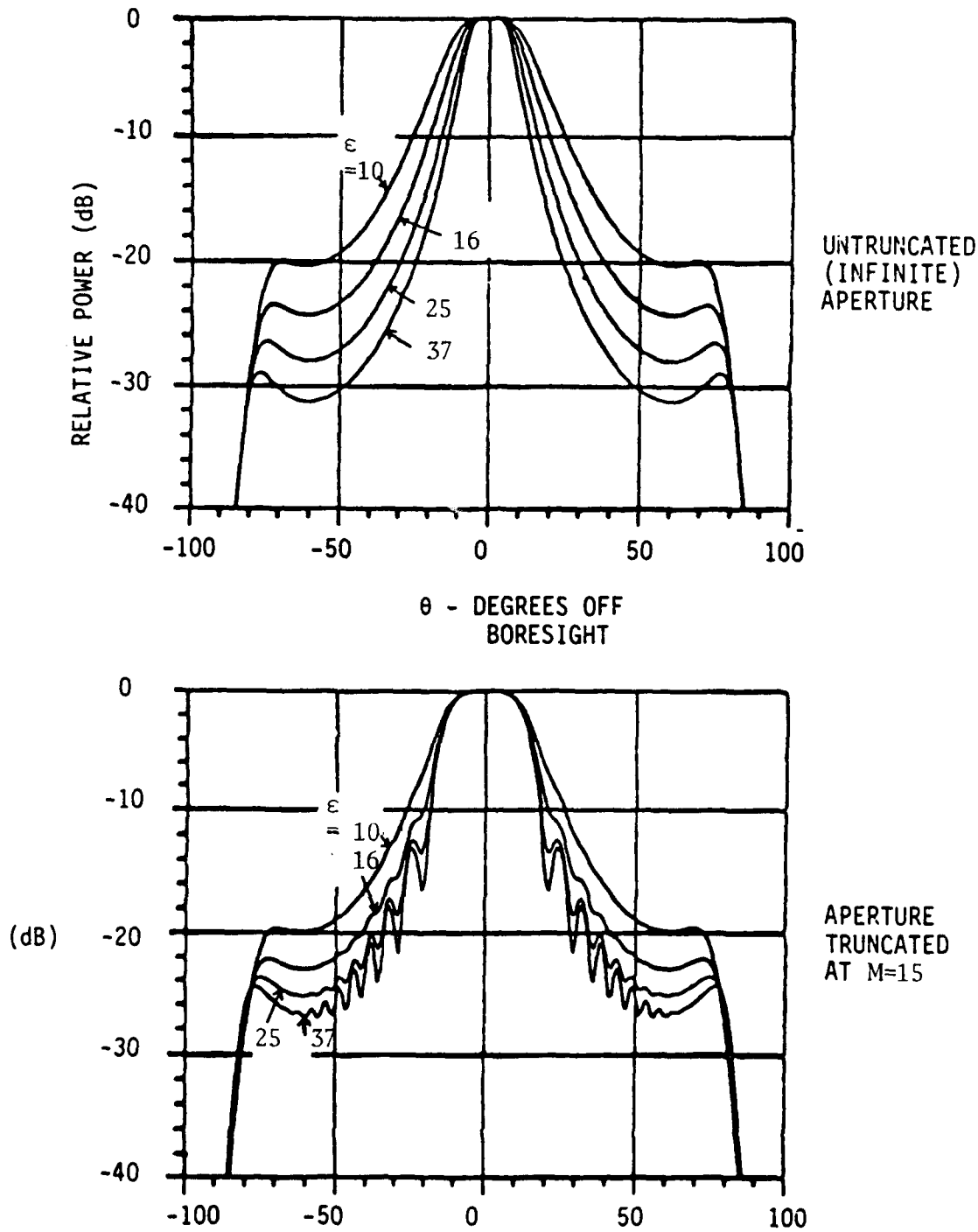

FIGURE 4. COMPUTED E-PLANE PATTERNS OF AN ISOLATED CLAVIN-COMPENSATED IMAGE-SLOT ANTENNA

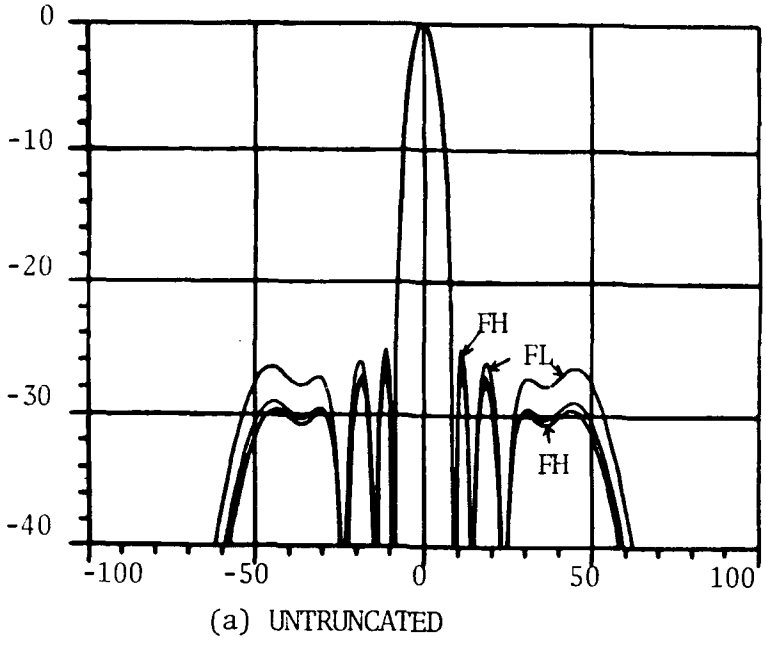

(a) UNTRUNCATED

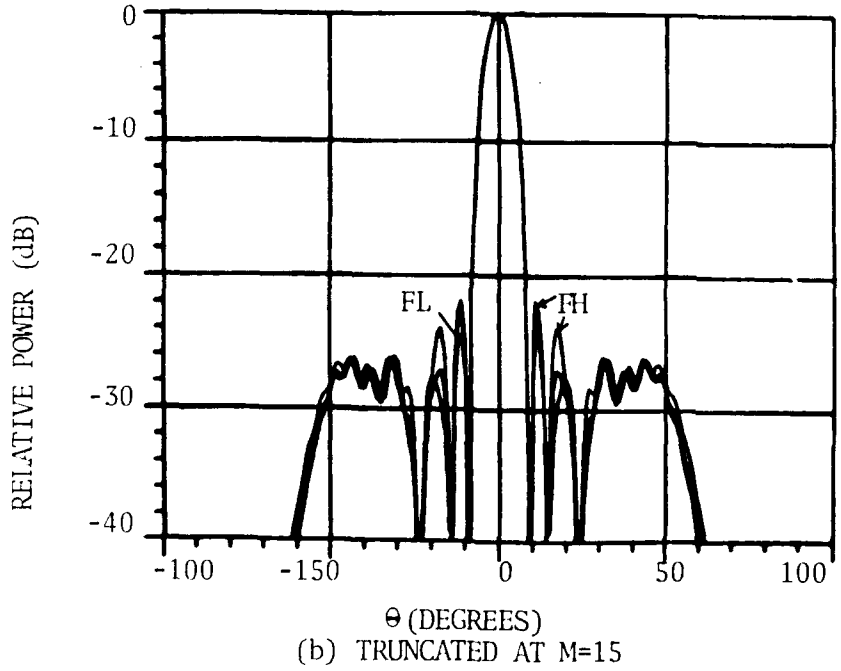

(b) TRUNCATED AT M=15

FIGURE 5. THEORETICAL E-PLANE PATTERNS OF ARRAY OF 24 UNIFORMLY WEIGHTED IDENTICAL IMAGE ELEMENTS WITH CLAVIN COMPENSATION

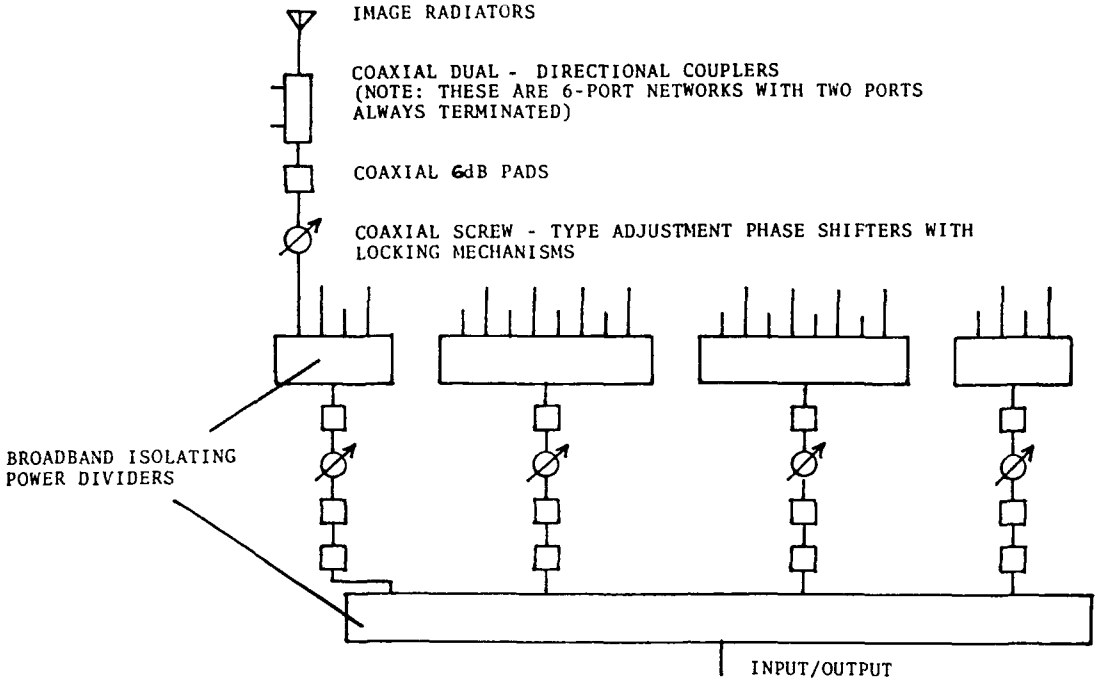

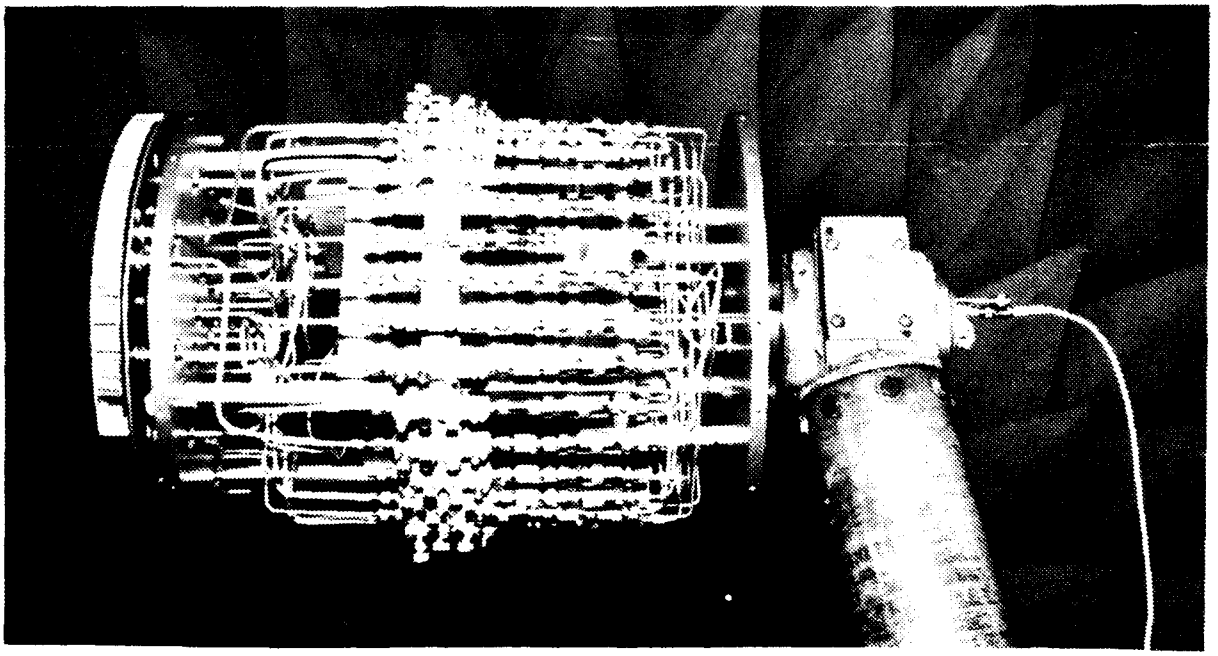

FIGURE 6. FIXTURE AND NETWORK SCHEMATIC FOR ACTIVE RETURN-LOSS AND PATTERN MEASUREMENTS OF 24-ELEMENT ARRAYS

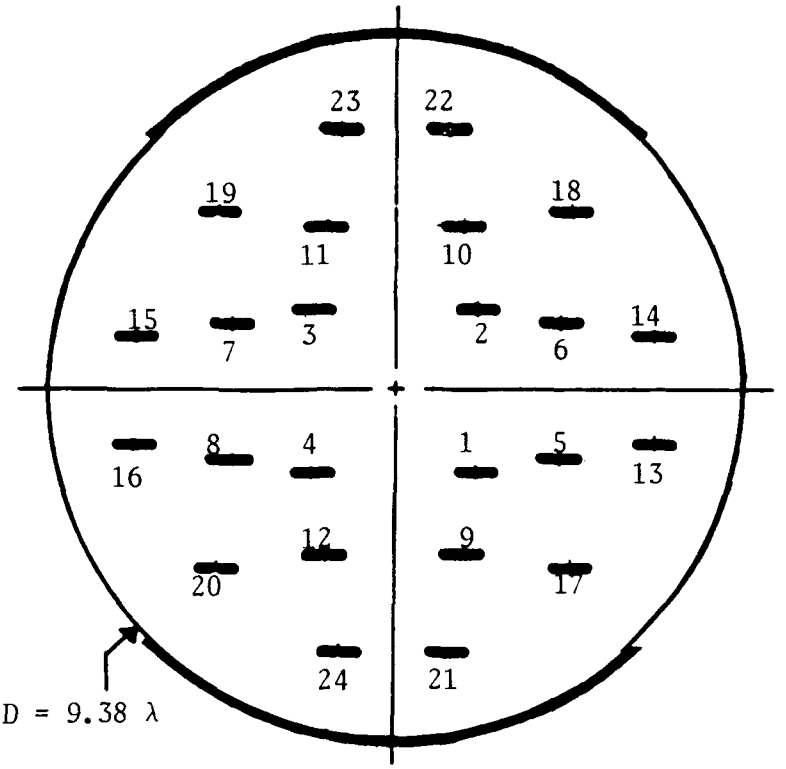

FIGURE 7. 24-ELEMENT IMAGE ARRAY SLOT LOCATIONS

TABLE 1. GAIN AND APERTURE EFFICIENCY OF 24-ELEMENT CLAVIN-COMPENSATED IMAGE ARRAY

FREQUENCY	GA $20 \log_{10}\left(\frac{\pi D}{\lambda}\right)$ (dBI)	ϵ = 25			ϵ = 37		
		G* (dBI)	G-GA (dBI)	EFF (%)	G* (dBI)	G-GA (dBI)	EFF (%)
FL	29.3	28.4	-.9	81	28.0	-1.3	74
FC	29.4	29.0	-.4	91	27.6	-1.8	66
FH	29.5	28.8	-.7	85	27.2	-2.3	59

* CALCULATED FROM (17) USING DATA OF FIGURES 10 AND 11.

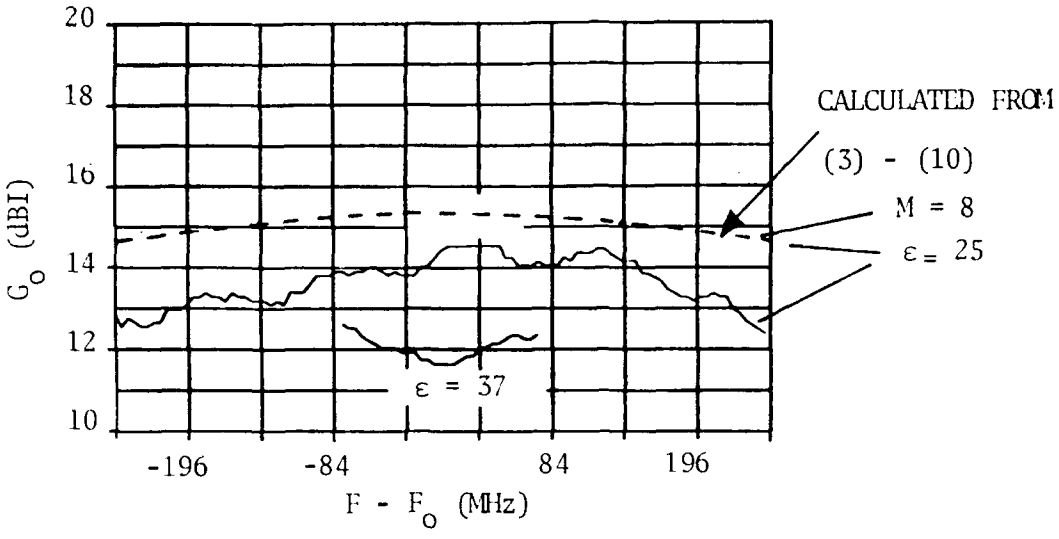

FIGURE 8. BORESIGHT GAIN OF IMAGE RADIATOR NO. 1 IN 24-ELEMENT ARRAY

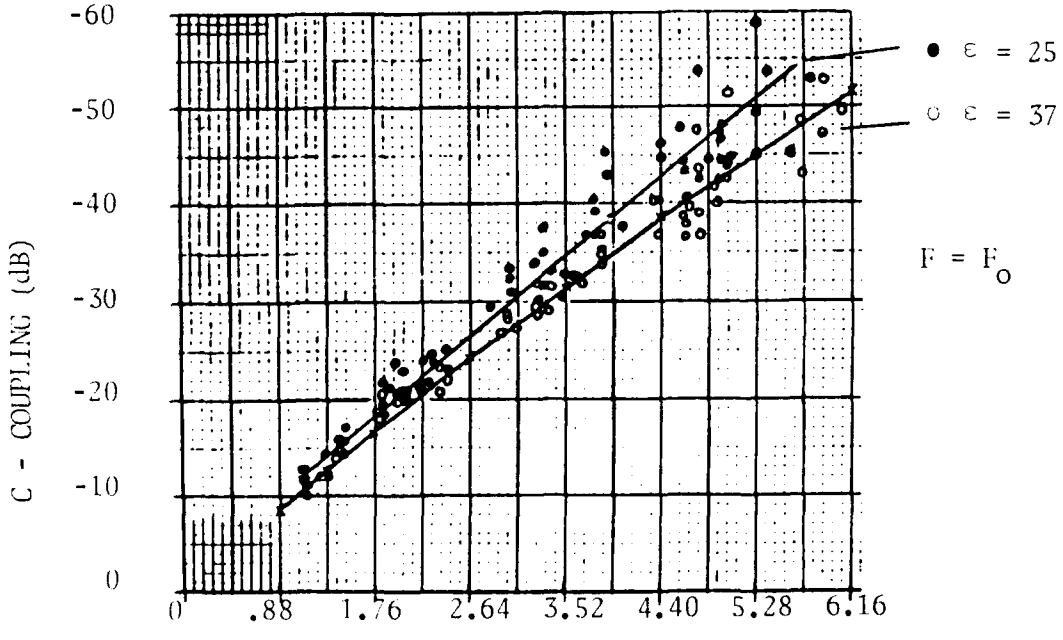

FIGURE 9. RECORDED COUPLING BETWEEN PAIRS OF IMAGE RADIATORS IN 24-ELEMENT ARRAY

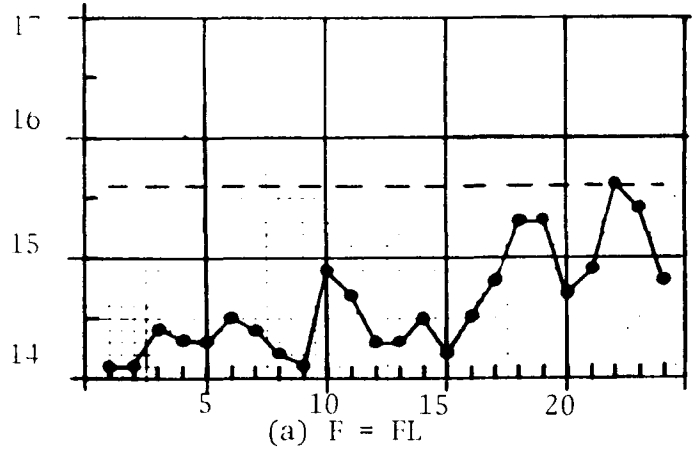

(a) F = FL

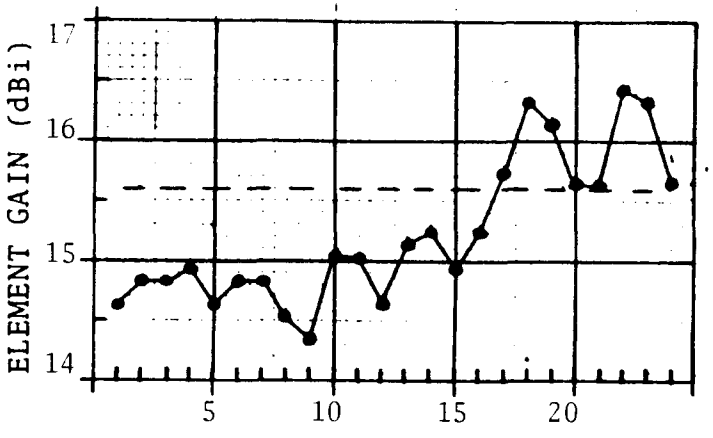

ELEMENT NUMBER

(b) F = FC

(All Gains Include Impedance Mismatch Losses)

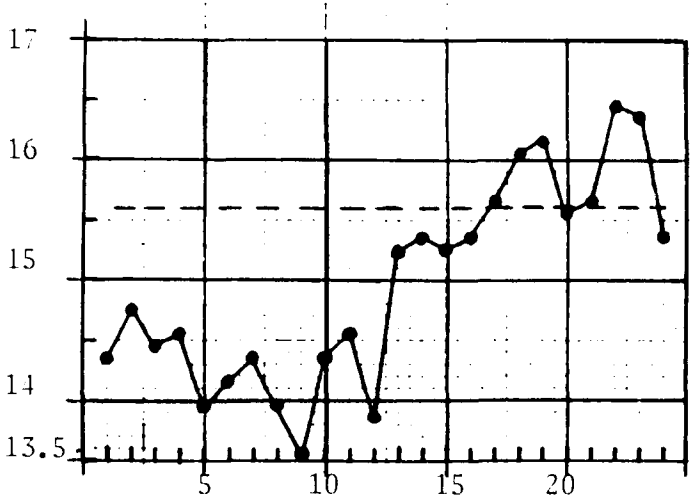

(c) F = FI

---THEORETICAL LIMIT FOR IDENTICAL ELEMENTS WITH NEIGHBORS ON ALL SIDES (ARRAY DIAMETER = 9.38 λ)

FIGURE 10. RECORDED GAIN FOR EACH RADIATOR OF 24-ELEMENT ARRAY WITH ε=25 IMAGE SLAB AND CLAVIN PINS

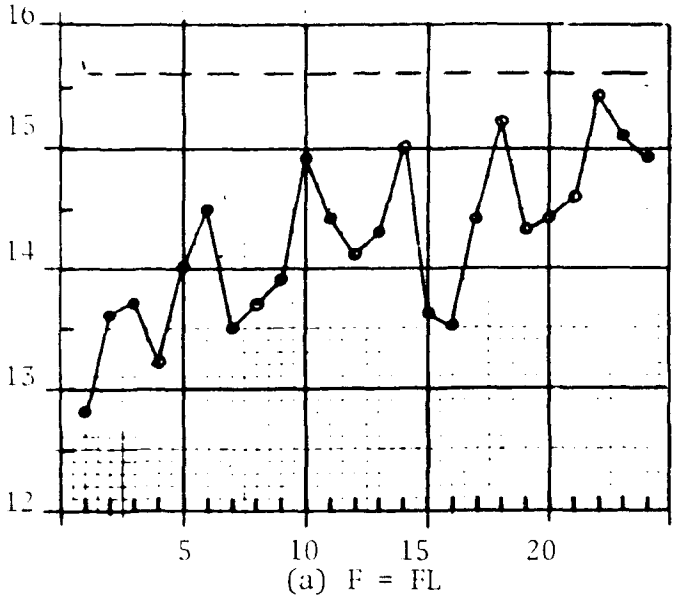

(a) F = FL

(All Gains Include Impedance Mismatch Losses)

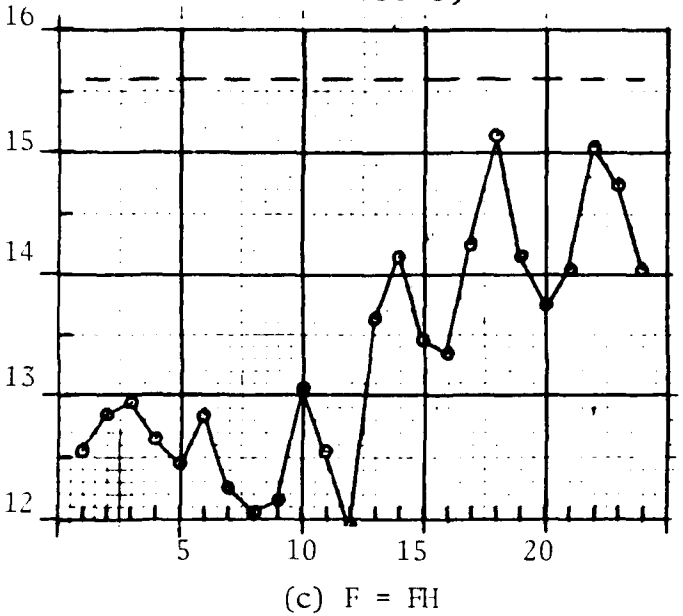

(c) F = FH

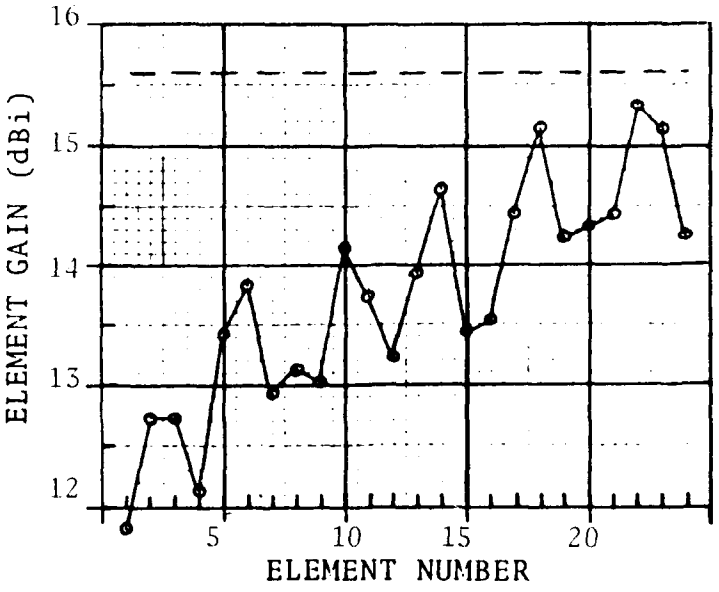

(b) F = FC

--- THEORETICAL LIMIT FOR IDENTICAL ELEMENTS WITH NEIGHBORS ON ALL SIDES (ARRAY DIAMETER = 9.38 λ)

FIGURE 11. RECORDED GAIN FOR EACH RADIATOR OF 24-ELEMENT ARRAY WITH ε=37 **IMAGE SLAB AND CLAVIN PINS**

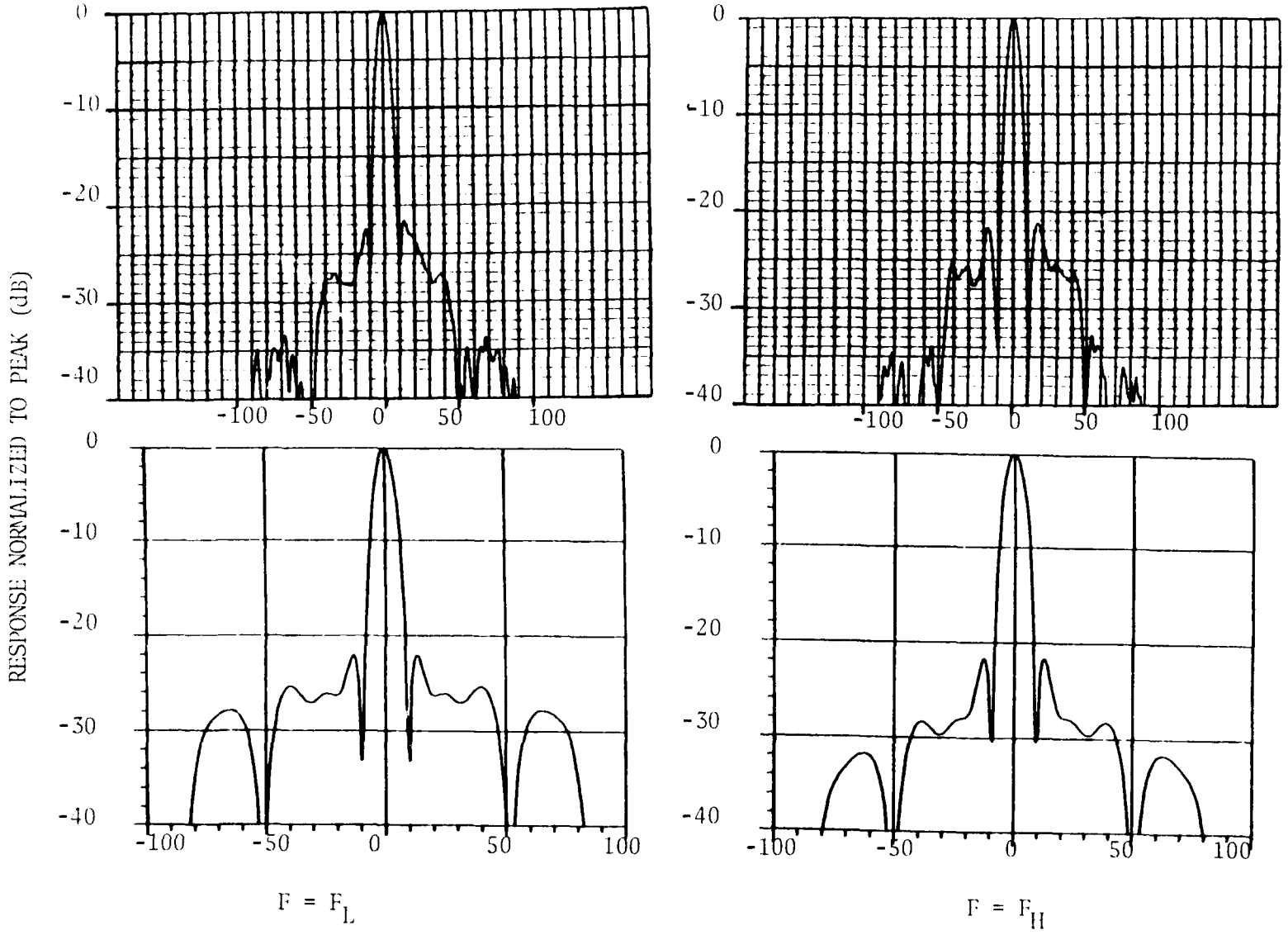

FIGURE 12. E-PLANE PATTERNS OF ARRAY OF 24 CLAVIN COMPENSATED IMAGE ELEMENTS

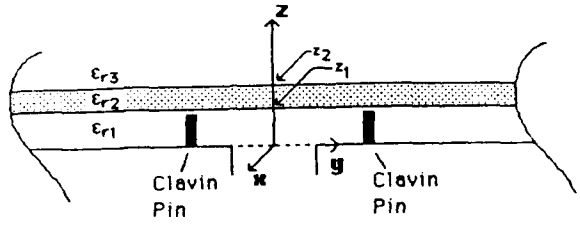

a) Side View

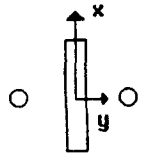

b) Top View of Slot and Clavin Pins

Figure 13. Illustration of the single Clavin pin compensated slot.

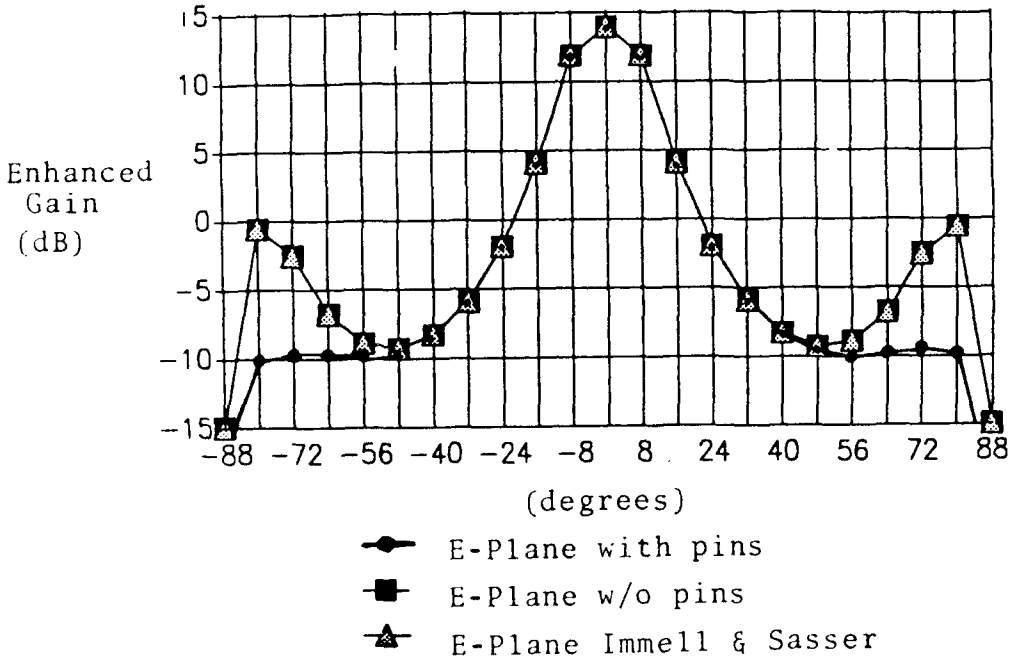

Figure 14. Predicted E-plane patterns with and without Clavin pins and comparison of this theory with that of Immell and Sasser.

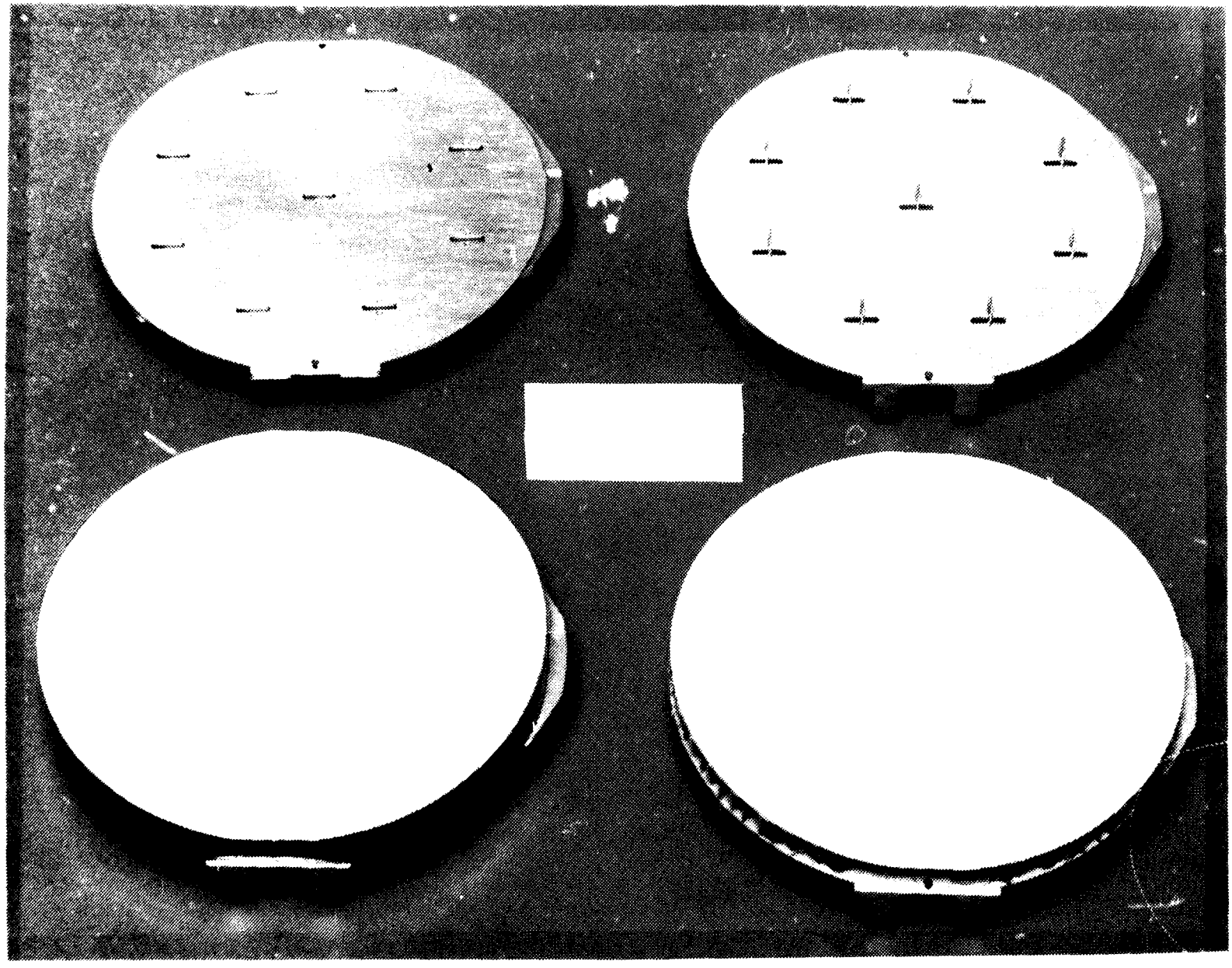

FIGURE 15. NINE-ELEMENT IMAGE ARRAY ASSEMBLY

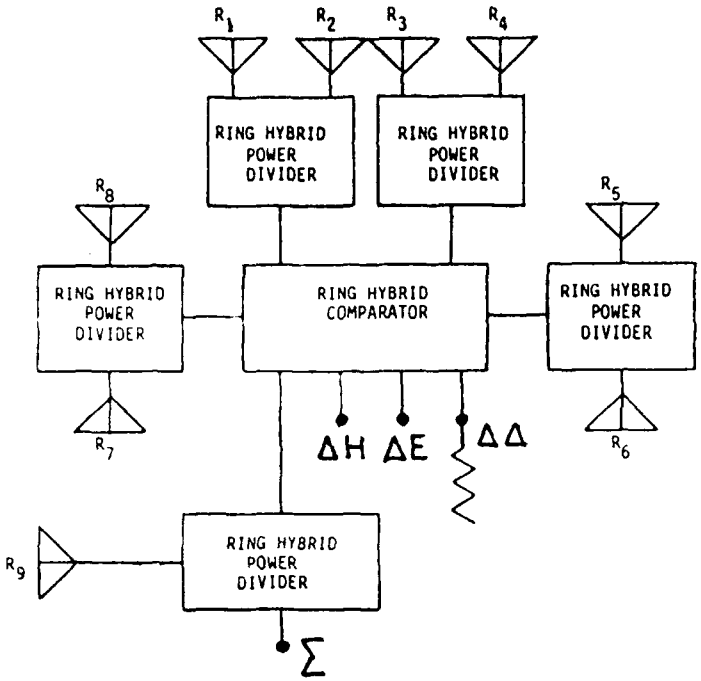

FIGURE 16. IMAGE ANTENNA ARRAY SCHEMATIC

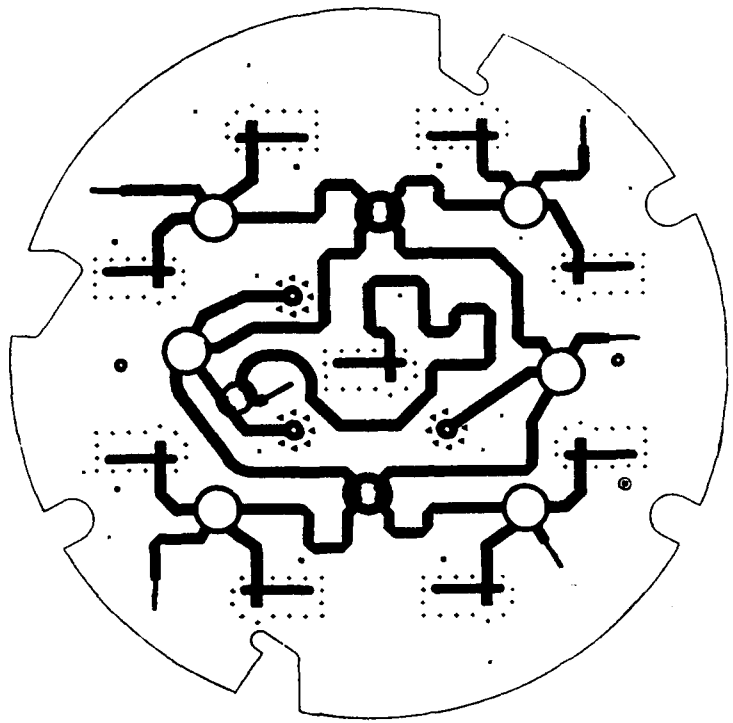

FIGURE 17. IMAGE ANTENNA FEED CIRCUIT

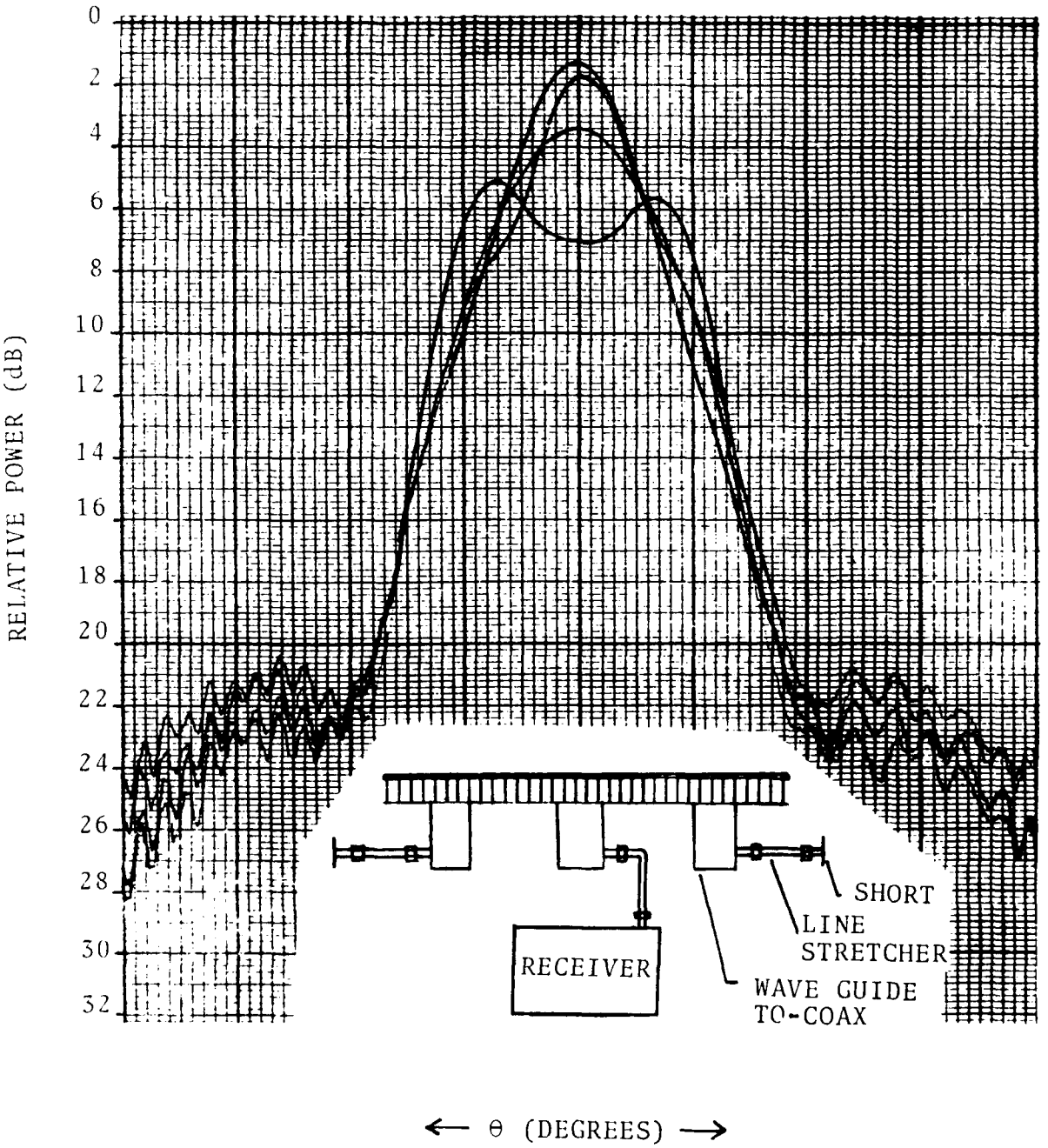

FIGURE 18. CENTER IMAGE - ELEMENT GAIN AS A FUNCTION OF OUTER ELEMENT TERMINATION

DISTRIBUTED BEAMSTEERING CONTROL OF MONOLITHIC PHASED ARRAYS

S.F. NATI, G.T. COKINOS, D.K. LEWIS

GENERAL ELECTRIC CO.

ELECTRONICS LABORATORY

P.O. BOX 4840

SYRACUSE, NEW YORK 13221

1.0 ABSTRACT

As satellite communication systems move to higher frequencies, a great deal of effort is being directed at monolithic phased arrays.[1] These arrays combine printed-circuit antenna technology with monolithic amplifiers and phase shifters. While significant advances in these areas are helping to make monolithic arrays a reality, array control still presents a challenge.

Phased arrays traditionally have been controlled by a single central computer that calculates a phase setting for each array element. This architecture has worked well for arrays operating at lower frequencies, having a small number of elements and modest update rates. Distributed control of phased arrays has been used for radar applications[2] and offers a solution to the problems of

array control for high frequency, monolithic arrays. Since each element, or small group of elements, has its own control, the bandwidth and number of connections to the central controller is reduced. In addition, the computation hardware is distributed, allowing the beamsteering calculations to occur in parallel, providing the means for higher update rates. Compensation for variation in element performance become possible with a distributed control scheme. Distributed control architectures also offer the potential for integration with the microwave components which would result in a truly monolithic array.

This paper will discuss the design of a distributed beamsteering controller (BSC) for high frequency phased array applications. The controller is designed using AT&T's digital GaAs HEMT technology. A review of the architecture and design for digital HEMT implementation will be presented. Areas of future development will also be discussed.

2.0 PROBLEM

The use of higher operating frequencies for satellite communications systems is reducing the area available for the antenna and related circuit elements such as amplifiers and phase shifters. Figures 1a and 1b show a block diagram of a typical

antenna element. Figure 1a shows a transmit element while Figure 1b shows a corresponding receive element.

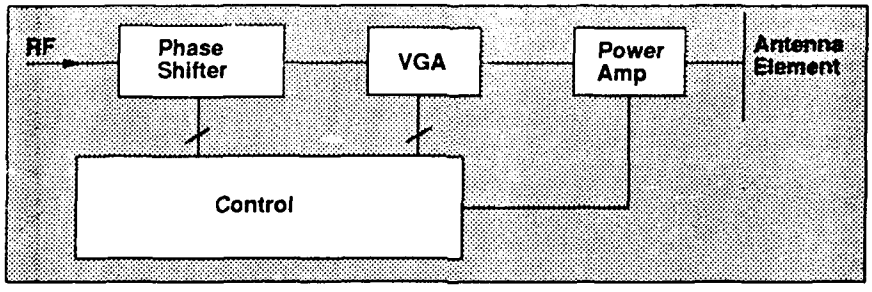

Figure 1a. Transmit Module

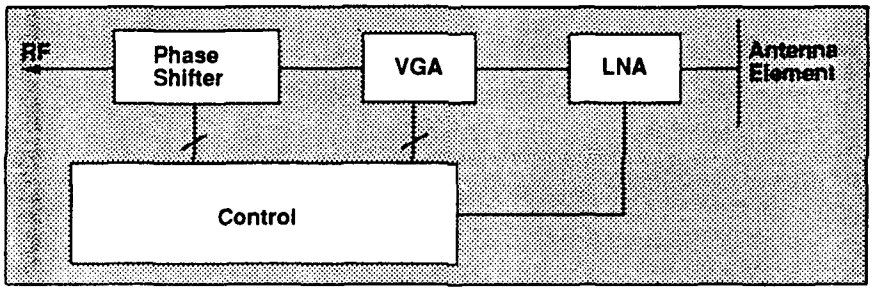

Figure 1b. Receive Module

Figure 2 shows the available area as a function of frequency, assuming a uniform element spacing of one half the wavelength. This decrease in element spacing, in addition to reducing circuit area, also limits the number of physical connections that can be made to the antenna element and its control circuitry. Connections must be provided for RF distribution, power, and control.

In addition to the smaller element spacing, the desire for increased array performance is causing the number of elements per array to increase. This combination has an effect on the number, speed and interconnect density of the required control signals. An architecture that minimizes the number of connections has a distinct advantage as operating frequencies increase.

The need for highly manueverable platforms to maintain communications results in a need to update the array beam pointing direction at higher rates. In addition, the use of techniques for improving security, such as spread spectrum communications, place even greater demands on the beamsteering control function.

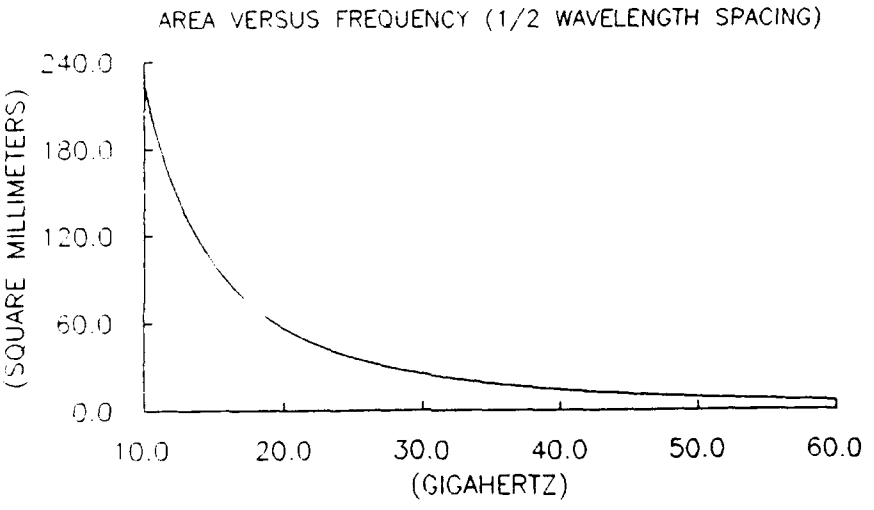

FIGURE 2

3.0 CONTROL ARCHITECTURES

There are several approaches to calculating and distributing the phase setting for each element in a phased array. The most simplistic approach is to compute the phase setting for each element in a central computer and apply the phase settings for the entire array simultaneously. This approach proves to be impractical due to the enormous amount of interconnect that would be needed for an array of any significant size. Additionally, the amount of time needed to perform the calculations for the entire array in a serial fashion would severely limit the update rate of the array.

An alternative approach is to compute the phase settings for each row and column and add the results at each element. This approach reduces the number of interconnects required but is restricted to arrays with uniform element spacing. The limiting factor in this approach is the time needed for calculation and distribution of each row and column phase setting. As the array size increases, the update rate will become limited. This approach also makes it difficult to provide compensation for element variations.

A fully distributed approach, where the beamsteering calculation is performed at the element or subarray level, has many desirable features. By broadcasting the desired antenna direction

cosines from a central array controller to a beamsteering controller located at each element, the number of interconnects can be reduced significantly. Each beamsteering controller will calculate the phase shifter settings in parallel, simultaneously, reducing the amount of time needed for computation. In this type of approach, the communication and computation time is basically independent of the number of elements in the array. Variations in element performance can be compensated by storing a correction memory in the beamsteering controller and applying these corrections on an element by element basis.

4.0 BSC ARCHITECTURE

The overall array control concept is shown in Figure 3. Each beamsteering controller controls a subarray of the entire array. The beamsteering controller receives commands from a central array controller and based on the command performs the required operations for each element in the subarray. These commands may be broadcast to all BSCs simultaneously, as in a pointing angle update, or may be addressed to an individual BSC, as in a modification to a compensation table entry. The BSC is also capable of performing a self test function and reporting it's status to the array controller.

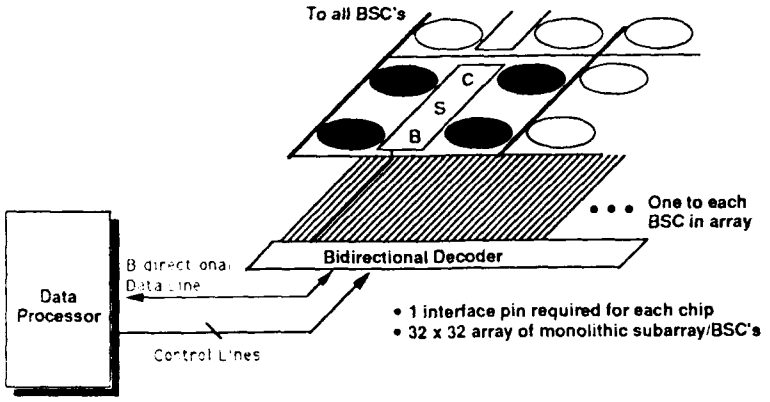

Figure 3. Control Concept

A timeline of a typical beam update sequence is shown in Figure 4. The sequence begins with the array controller broadcasting to each BSC the direction cosines of the overall array pointing angle. Upon receiving this command each BSC will calculate the required phase shifter settings for each element of its subarray. These settings will be stored within the BSC until an update command is received. Next, the array controller selects one BSC for testing. The selected BSC receives the test command and compares the results of the previously calculated phase shifter settings with those supplied by the array controller. The array controller then broadcasts the update command to all the BSCs and the new phase shifter settings are applied to each phase shifter in the array. The BSC that was selected for testing then transmits the test results to the array controller.

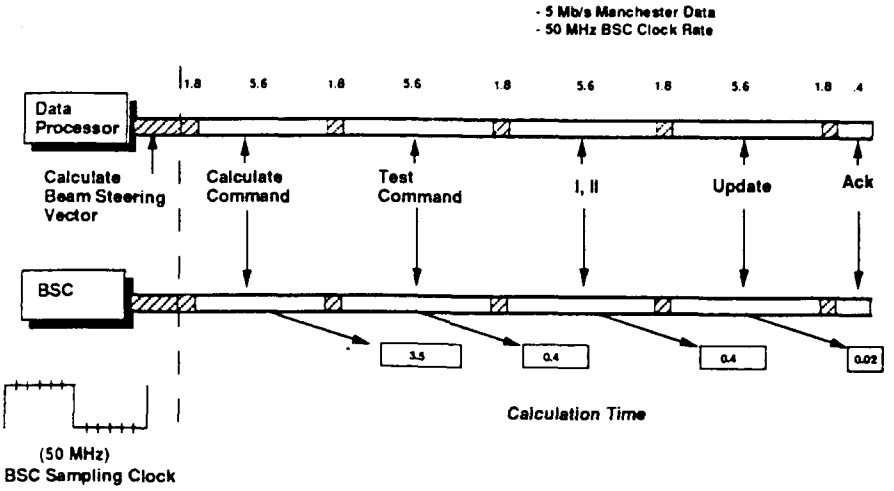

Figure 4. Beam Steering Timeline

Figure 5 shows a functional block diagram of the beamsteering controller. The main functions include a single wire interface to the main array computer, command decoding logic, beamsteeering calculation logic, a compensation table, built in test logic, and timing and control.

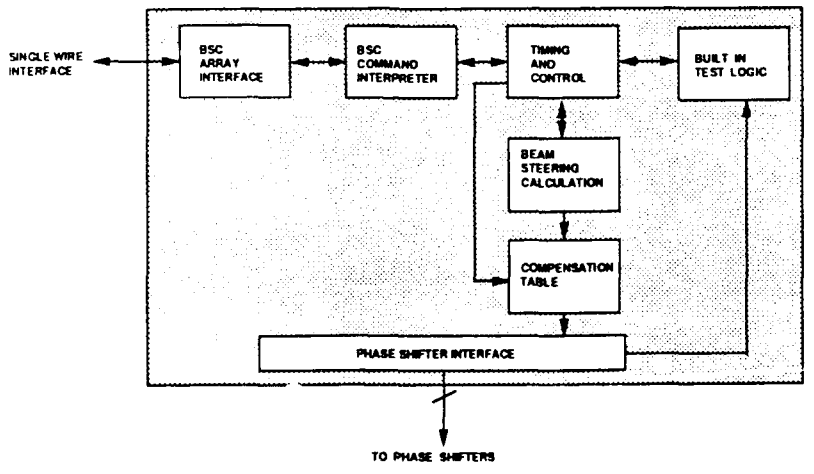

Figure 5. BSC Functional Block Diagram

5.0 BSC DEVELOPMENT

The number of elements that each BSC will control is based on tradeoffs with regard to the required system update rate, the processing capability of each BSC, along with area, power and interconnect considerations. It was decided, based on the above tradeoffs, to design the BSC to control up to sixteen elements.

The BSC receives its commands from the array controller over a single bidirectional interface. The bidirectional decoder that is used to interface between the array controller and the BSCs provides the capability for broadcast or individual addressing.

The BSC instruction set is shown in Figure 6. The CALCULATE, UPDATE, and TEST commands are used during each beam update, while the LOAD COMPENSATION TABLE, and the LOAD POSITION VECTOR commands are used during array initialization or when changes in parameters, such as temperature, require the values in the compensation table to be adjusted. Each instruction is a fixed length and is divided into a three bit command field and a twenty-four bit data field. A single bit is provided for parity.

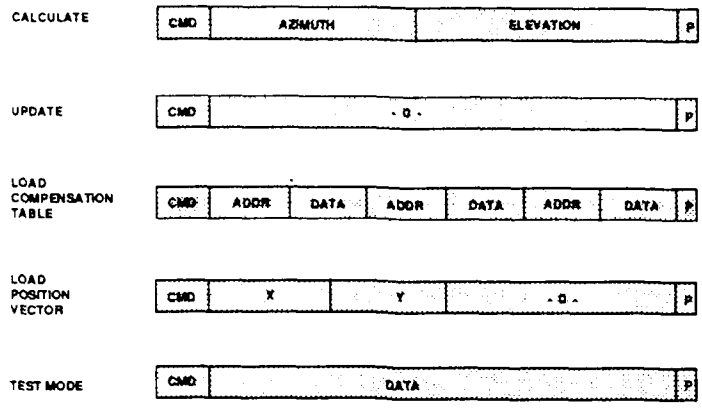

Figure 6. BSC Instruction Set

The CALCULATE command contains the direction cosines for the desired antenna pointing direction. This command is normally broadcast to each BSC simultaneously. The BSC calculates the phase shifter settings for its subarray based on these direction cosines and the position of the BSC in the array.

The UPDATE command is also normally a broadcast command. The BSC will update its phase shifter settings upon receipt of this command. The data that has been calculated during the previous CALCULATE command is transferred to the phase shifter control lines for each element in the subarray.

The TEST command is used to perform a functional test on one BSC during each beam update period. The data that has been computed as a result of the CALCULATE command is compared on a bit by bit basis with the data computed by the array controller for the designated BSC. The BSC will report the result of the comparison back to the array controller.

The LOAD COMPENSATION TABLE command contains the information to be loaded into the compensation table. This provides the ability to adjust the phase shifter settings for each subarray based on data obtained during an initial calibration sequence.

The LOAD POSITION VECTOR command gives each BSC its position within the array. This information is used during the CALCULATE command.

5.1 CALCULATIONS PERFORMED

The beamsteering calculation that is implemented in the BSC is shown in Figure 7. The BSC assumes that the array is planar and has uniform element spacing within the subarray. Although the BSC could be extended to the more general case, these assumptions allow the BSC to use two multiplies per beam update, minimizing the amount of time needed for computation. In addition, the internal logic for the beamsteering calculation is implemented using a pipelined bit serial approach.

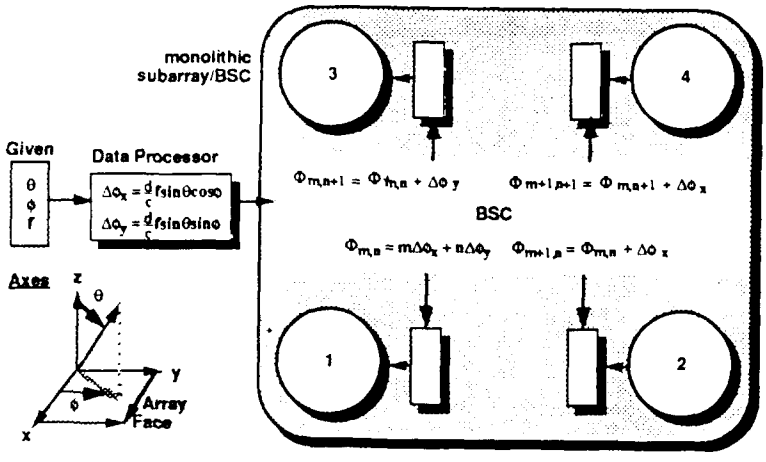

Figure 7. Phase Shift Command Calculation

This approach is highly efficient in area and power. A compensation table provides the ability to adjust to varying phase shifter performance between subarrays. Figure 8 shows an example of an imperfect phase shifter and the benefits that can be obtained through the use of the compensation table.

Without Compensation

Phase Setting	Desired Delay	Output Delay	Phase Error
000	0	31.4	31.4
001	45	82.1	37.1
010	90	146.3	56.3
011	135	198.9	63.9
100	180	249.1	69.1
101	225	301.5	76.5
110	270	354.8	84.8
111	315	401.6	86.6

With Compensation

Phase Setting	Table Entry	Output Delay	Phase Error
000	110	354.8	-6.2
001	111	401.6	-3.4
010	001	82.1	-7.9
011	010	146.3	11.3
100	011	198.9	18.9
101	100	249.1	24.1
110	100	249.1	-20.9
111	101	301.5	-13.5

Figure 8. Effects of Compensation

5.2 FAULT MONITORING

The approach that is used for fault monitoring at the subarray level is to test a single BSC during each beam update. This allows the entire array of BSCs to be tested in a round-robin fashion. A BSC is tested by comparing its calculated phase shifter data with data that has been calculated by the array controller for the same pointing angle. This will test a significant portion of the BSC, including the array interface, command decode logic, calculation logic, position registers, and compensation table. In addition, parity and message format checks are performed on the incoming command sequence. These errors, along with a test status are reported back to the array controller at the conclusion of the test sequence.

6.0 FUTURE DEVELOPMENT

The ultimate goal of incorporating the BSC with the phase shifters, amplifiers and antenna in a monolithic array requires that the BSC be capable of being integrated into a microwave compatible process. For analog components at EHF, it is anticipated that a gallium arsenide HEMT process will be used. With this in mind, the BSC was designed to be implemented in AT&T's digital GaAs HEMT process. This process, or similar processes,

although not intended for implementing analog components at EHF frequencies at the present time, could conceivably be modified to do so. A process using selective molecular beam epitaxy, would provide the capability to produce devices optimized for analog or digital functions on the same substrate. This would be the next step in producing a truly monolithic array.

7.0 ACKNOWLEDGEMENTS

The authors would like to acknowledge the efforts of Steve Taylor and Greg Barnett of the GE Advanced Technology Laboratories in Moorestown, NJ. in the development of the BSC architecture, and the efforts of Dr. Karl Wyatt and Dr. Perry Robertson of AT&T Bell Laboratories, Reading PA.

8.0 SPONSORSHIP

This work was sponsored by the Air Force Systems Command, Rome Air Development Center, RADC/EEAA, Hanscom AFB, MA., under contract F19628-89-C-0054. The contract monitor is Dr. Boris Tomasic.

REFERENCES

1. McIllvenna, J. F. (1988) "Monolithic Phased Arrays for EHF Communications Terminals," Microwave Journal, March 1988, p. 113-125.

2. Waldron, T. P. et al., (1986) "Distributed Beamsteering Control of Phased Array Radars," Microwave Journal, September 1986.

ANALYSIS OF EDGE EFFECTS IN FINITE PHASED ARRAY ANTENNAS

Steven M. Wright

Dept. of Electrical Engineering, Texas A&M University

College Station, Texas, 77843

ABSTRACT

An important concern in the design of phased array antennas is the effect of mutual coupling between elements on the array performance. For large periodic arrays, a common approach is to use an infinite array formulation. This approach does not include edge effects and is valid only for a uniform, periodic excitation of the array. Alternatively, the element-by-element approach can be used, but this may be impractical for large arrays. In this paper a method for the analysis of finite, periodic arrays of arbitrary size and excitation is discussed. The method is based upon an efficient solution of the extended infinite periodic array. In essence, the infinite array is excited with each of the coefficients of the discrete Fourier transform of the desired finite array excitation. The finite array behavior is then obtained by superposition. After initial characterization of the infinite array, finite arrays with arbitrary excitation and number of elements can be solved by simple FFT operations on the excitation and impedance matrices. Finally, by extracting an

approximate open-circuit impedance matrix for the array, the solution for free or forced voltage excitation is also obtained.

1.0 INTRODUCTION

An important criteria in the design of any phased array antenna is the behavior of the active element impedance as a function of beam scan angle. For large arrays with a single beam, this can often be sufficiently characterized either experimentally, by constructing a small section of the array, or theoretically, using infinite array theory [1].

This paper is concerned with the analysis of finite but periodic phased arrays of arbitrary size and excitation, as might be used for steering multiple beams and nulls. The analysis of this type of array is more difficult, particularly for relatively large arrays where the element-by-element approach can become impractical due to the large size of the impedance matrices.

The method presented here for the analysis of finite arrays is based upon an efficient solution for the active array impedance of the infinite array created by continuation of the finite periodic array. This approach allows arrays of essentially arbitrary size to be analyzed. Importantly, storage requirements are proportional to either the square of the number of basis functions on each element or the total number of elements squared (whichever is greater,) not the product of the two, as in the element by element approach.

The method is simple to implement because it requires only the computation of the impedance of an infinite array of the same elements. A matrix of infinite array scan impedances is computed over one period of scan (visible and invisible) space. This matrix is multiplied by the discrete Fourier transform of the desired current excitation to obtain the terminal voltages in the finite array, from which the active element impedances are obtained. In addition, the element impedances can be obtained for the case of voltage excitation, either free or forced [1].

A brief formulation of the method is given in Section 2. Computational efficiency is briefly discussed in Section 3, and some examples are considered in Section 4. Comparisons are made to element-by-element results for arrays in free space and microstrip dipole arrays.

2.0 THEORY

It is well known that the impedance of a single element can be obtained from integration of the impedance of an infinite array of the same elements [2]. Additionally, Ishimaru and co-workers have shown that the impedance of a finite array of current excited elements can be expressed as a convolution integral of the Fourier transform of the array aperture current distribution and the infinite array active impedance as a function of scan angle. A limitation in that work was slow numerical convergence in the convolution integrals. The formulation here is entirely discrete,

and may be more straightforward conceptually, but the concepts are very similar to those presented by Ishimaru [3]. The technique is founded in the basic principles of the array scanning method presented by Munk and Burrell [2]

Of particular interest here is a finite array of microstrip dipoles, a section of which is illustrated in Fig. 1. The array is periodic, represented by lattice vectors $\vec{S}_1$ and $\vec{S}_2$. The dipoles have width a and length b, and are printed on a substrate of thickness t and relative permittivity ε_r. For generality, the solution allows a superstrate layer of arbitrary thickness and relative permittivity, and loss tangents in both the superstrate and substrate. The method under consideration is based upon the formulation of the active array impedance for a infinite, periodic extension of such an array.

2.1 *Infinite Array Impedance vs. Scan angle:* $\tilde{Z}(\beta_0)$.

The active impedance of the infinite array can be found using well known methods [1,4,5,6]. In this work, a moment method solution was used which uses subsectional basis functions with a linear dependence (triangle) in the y direction (length) and an edge condition in the x direction (width). The edge condition is not necessary for very thin elements, but can give improved results for wide strips when no x directed basis functions are employed. The details of the moment method solution used here can be found elsewhere [5,6]

For purposes of discussion only, the form of the infinite array array impedance that obtains from a single mode approximation to the current is considered here:

$$\tilde{Z}_{in} = \frac{1}{A} \sum_{m} \sum_{n} \tilde{G}_{yy}(\vec{K}_{mn})\, \tilde{J}_{y}(\vec{K}_{mn}) \qquad (1)$$

A is the area of one unit cell in the array, $\tilde{G}_{yy}$ is the $\hat{y}\hat{y}$ component of the spectral-domain dyadic periodic Green's function for the problem under consideration, and $\tilde{J}_{y}$ is the Fourier transform of the single mode current approximation. The summations are from $-\infty$ to $+\infty$. Equation 1 is a summation of Floquet modes defined by the vector $\vec{K}_{mn}$.

$$\vec{K}_{mn} = \vec{\beta}_{mn} + \vec{\beta}_{0} \qquad (2a)$$

where:

$$\vec{\beta}_{mn} = m\vec{\beta}_{1} + n\vec{\beta}_{2} \quad \text{and} \quad \vec{\beta}_{0} = m_{0}\vec{\beta}_{1} + n_{0}\vec{\beta}_{2} \qquad (2b)$$

The vector $\vec{\beta}_{mn}$ represents the vector from the (0,0) Floquet mode to the (m,n) Floquet mode. $\vec{\beta}_{1}$ and $\vec{\beta}_{2}$ are lattice vectors for the reciprocal or periodic lattice, as shown in Fig. 2 for an arbitrary array periodicity. For a rectangular array, $\vec{\beta}_{1} = 2\pi/\vec{S}_{1}$ and $\vec{\beta}_{2} = 2\pi/\vec{S}_{2}$. $\vec{\beta}_{0}$ is an offset of each Floquet mode to allow beam scanning, as discussed below. As indicated by Eq. 1, the active array impedance is obtained by summing Floquet modes over the reciprocal lattice; hence the active array impedance is

periodic over the reciprocal lattice just as the array structure is periodic over the spatial lattice.

To scan the main beam of the array, the voltage source at element (m,n), denoted $V(\vec{S}_{mn})$ is adjusted to give $V(\vec{S}_{mn}) = V(\vec{S}_{00})e^{-j\vec{\beta}_0 \cdot (m\vec{S}_1 + n\vec{S}_2)}$. The constants m_0 and n_0 are essentially the direction cosines, which for a rectangular array become (following the conventions in [6]):

$$m_0 = -S_1 \sin\theta \cos\phi \tag{3a}$$

$$n_0 = -S_2 \sin\theta \sin\phi \tag{3b}$$

where $S_1 = |\vec{S}_1|$. One can alternatively excite element (m,n) with a current source $I(\vec{S}_{mn}) = I(\vec{S}_{00})e^{-j\vec{\beta}_0 \cdot (m\vec{S}_1 + n\vec{S}_2)}$. The active array impedance is the same in either case for an infinite array.

For notational convenience the active array impedance of the infinite array is denoted $\tilde{\tilde{Z}}(\vec{\beta}_0)$, to indicate that it is a function of $\vec{\beta}_0$, and that it can be considered a spectral domain quantity.

2.2 *Finite Array Impedance: Arbitrary Current Excitation.*

There are many applications where one would like to define excitation coefficients for each element of a finite array. For an N_x x N_y element array, this defines a discrete excitation function $I^{ex}(\vec{S}_{mn})$, which gives the excitation current at each of the $N_x N_y$ elements of the array, and where $\vec{S}_{mn} = m\vec{S}_1 + n\vec{S}_2$. Having defined an array geometry and the desired excitation currents, one can analyze the array using the standard element-by-element

approach. However, one can proceed in an alternative manner as follows. If the N_x x N_y array under consideration is periodic, one can consider the hypothetical extension of the array to an infinite structure. The goal is to synthesize the excitation of the finite array by a sum of appropriately weighted, uniform periodic excitations of the infinite structure. Those elements with zero current can be considered open-circuited. For resonant length elements, these elements have negligible effect, allowing the finite array to be approximately recovered. For elements for which open-circuiting does not render them negligible, the current would need to be forced to zero at additional points.

Unfortunately any finite array excitation is not band-limited, and cannot be synthesized exactly with a finite set of periodic excitations of the infinite array. However, one can obtain approximate results as follows. Given an excitation function for the finite array, one computes the discrete Fourier transform (DFT) using LK samples of the array excitation:

$$\tilde{I}^{ex}(\vec{\beta}_0^{mn}) = \text{DFT}\left\{I^{ex}(\vec{S}_{lk})\right\} \tag{4}$$

where the DFT pair for a discrete, periodic function defined by LxK samples on the 2-D lattice defined by $\vec{S}_{lk}$ given by [7]:

$$\tilde{f}(\vec{\beta}_0^{mn}) = \text{DFT}\left\{f(\vec{S}_{lk})\right\} = \sum_{l=0}^{L-1}\sum_{k=0}^{K-1} f(\vec{S}_{lk})\, e^{-j2\pi(ml/L + nk/K)} \quad (5a)$$

$$f(\vec{S}_{mn}) = \text{IDFT}\left\{f(\vec{\beta}_0^{mn})\right\} = \frac{1}{LK}\sum_{l=0}^{L-1}\sum_{k=0}^{K-1} f(\vec{\beta}_0^{mn})\, e^{j2\pi(ml/L + nk/K)} \quad (5b)$$

where

$$\vec{\beta}_0^{mn} = m\,\vec{\beta}_1/L + n\,\vec{\beta}_2/K \qquad 0 \le m \le L-1, \quad 0 \le n \le K-1 \quad (6)$$

and IDFT denotes inverse discrete Fourier transform. LK, the number of sampling points, will typically be much larger than $N_x N_y$, the number of elements in the array. Thus $I^{ex}(\vec{S}_{lk})$ will be zero for all of the LK samples except for the $N_x N_y$ which correspond to elements of the finite array.

Once the DFT of the excitation currents is calculated, the DFT of the terminal voltages in the finite array can be determined from:

$$\tilde{V}(\vec{\beta}_0^{mn}) = \tilde{I}^{ex}(\vec{\beta}_0^{mn})\; \tilde{Z}(\vec{\beta}_0^{mn}) \quad (7)$$

The element voltages for the N_x x N_y array, $V(\vec{S}_{mn})$, can be obtained by inverse DFT:

$$V(\vec{S}_{mn}) = \text{IDFT}\left\{\tilde{V}(\vec{\beta}_0^{mn})\right\} \quad (8)$$

This IDFT returns LK unique element voltages, which include the voltages for the original N_x x N_y array. All other coefficients

should be approximately zero. Finally, the input impedance of the element (m,n) in the finite array is obtained from:

$$Z(\vec{S}_{mn}) = \frac{V(\vec{S}_{mn})}{I^{ex}(\vec{S}_{mn})} \tag{9}$$

The approach described here can be viewed as a superposition technique. The DFT of the desired array excitation gives a finite set of uniform periodic excitations of the infinite array. One must keep in mind that the DFT of the excitation current is a periodic function, with periods $\vec{\beta}_1$ and $\vec{\beta}_2$. It is defined at the LK sample points defined by the vectors $\vec{\beta}_0^{mn}$. This set of LK excitations, when summed, recovers a periodic version of the desired excitation function, periodic over an array of LxK elements. In essence, it creates an "array of arrays"; an infinite, periodic array consisting of repetitions of the desired finite array. It is necessary that this second periodicity be large enough so that these repeated arrays would not affect the current distribution on the original N_x x N_y element array. This problem will be examined by comparison of results with the element-by-element approach.

2.3 *Open Circuit Impedance Matrix and Mutual Impedances.*

It is of interest to obtain the open circuit impedance matrix elements for the finite array. For an N_x x N_y array, element

(p,q) of the $N_x N_y$ by $N_x N_y$ open circuit impedance matrix of the array is as given by:

$$Z_{pq}^{oc} = \left. \frac{V_p}{I_q} \right|_{I_q = 0,\ q \neq p} \tag{10}$$

where p and q denote a single integer denumeration of the array elements. For elements which have essentially no current when open circuited, such as half-wave dipoles, one can obtain the open circuit matrix for a finite array by choosing an excitation matrix

$$I^{ex}(\vec{S}_{mn}) = \begin{cases} 1, & m = 0,\ n = 0 \\ 0, & \text{otherwise} \end{cases} \tag{11}$$

In this case, the response at the unexcited elements of the array are given by:

$$V^{oc}(S_{mn}) = \text{IDFT} \left\{ \tilde{Z}(\beta_0^{mn}) \right\} \tag{12}$$

The open circuit impedance matrix elements, (the mutual impedance between any two elements in the array with all other elements open circuited) can be obtained from Eq. 9,

$$Z_m(\vec{S}_{mn} - \vec{S}_{kl}) = V^{oc}(\vec{S}_{|m-k|,|n-l|}) \tag{13}$$

Note that there are only $N_x N_y$ unique values obtained by Eq. 13 for an N_x x N_y array. Equation 12 returns an approximation to the open circuit element voltage the finite array; the location in the array is not taken into account. Thus, while edge effects are

included in the excitation matrix, they are not included in the open circuit matrix. However, as stated earlier, this is a good approximation for many practical elements.

2.4 *Finite Array Impedance: Arbitrary Voltage Excitation.*

For a voltage excited array, direct application of the above formulation leads to impedance with all unexcited elements short circuited (or terminated in the generator impedance). However, the input impedance for the elements under voltage excitation with all unused elements open circuited can be obtained using this method by using the open-circuit impedance matrix. Once the open-circuit impedance matrix is found, the element currents under voltage excitation are determined by:

$$[I] = ([Z^{oc}] + [Z_T])^{-1}[V] \tag{14}$$

where $[Z_T]$ is a diagonal matrix which contains the generator impedances and any resonating elements. This gives the element currents under "free" excitation. Setting $[Z_T] = 0$ gives the "forced" voltage excitation, according to the definition in [1]. In general, the inverse of the Z matrix is not found, but the matrix equation is solved for the unknown currents. The input impedance of the m,nth element is obtained from

$$Z(\vec{S}_{mn}) = V_{mn}/I_{mn} - Z^{T}_{mn} \tag{16}$$

where the subscripts m,n indicate the dependence of all quantities on their location in the array, given by $\vec{S}_{mn}$.

3.0 NUMERICAL CONSIDERATIONS

Clearly the most time consuming aspect of the solution is the filling of the $Z(\vec{\beta}_0^{mn})$ matrix. Filling this matrix requires sampling the infinite array active impedance over one period of the spectral lattice. For a rectangular array of center fed dipole, symmetry reduces the number of samples by a factor of four. Even with symmetry, a 256x256 DFT requires the computation of 16,641 samples. Fortunately, the impedance matrix is filled only once for a given (infinite) array. Having filled the impedance matrix, the performance of any subset of the infinite array can be evaluated for arbitrary excitation using the methods of Sec. 2. Still, sampling the impedance matrix sufficiently to allow the analysis of microstrip arrays can be quite time consuming if not efficiently done. Two methods have been used to reduce the fill time significantly.

First, the time required to compute each sample of the impedance matrix can be reduced significantly by applying acceleration techniques to the summations of Floquet modes expansions. Many such summations can be required to compute the moment method solution for the array impedance at each scan angle. The method used here requires obtaining an asymptotic expansion for the generalized impedance matrix elements. The asymptotic form is subtracted from the original expression, leaving a rapidly convergent summation. The asymptotic terms can be directly accelerated using Poisson's summation formula. Details of the

method are given in [6].

The use of this method results in a rapidly convergent series, typically giving a reduction in computation time of approximately two orders of magnitude over a direct, unaccelerated summation. This has allowed the routine use of 256x256 or 512x512 impedance matrices. High sampling densities are needed for microstrip problems, where surface waves can lead to singularities in the impedance vs. scan angle surface.

Second, an adaptive sampling routine, similar to adaptive integration, combined with a birational interpolation technique, has been used to reduce the number of scan angles at which the array impedance is calculated. With this routine, the impedance surface is sampled over a grid of 17x17 points. Next, the impedance is calculated using a birational interpolation technique at the center of each of the 16x16 subsections defined by the initial gridding. If the interpolated result is sufficiently close to the actual computed value at that point, that subsection is designated as complete, and the remaining values filled by interpolation. If the interpolated value does not meet tolerance, that subsection is subdivided, and the testing procedure continued. A birational interpolation routine was chosen because of its performance near singularities [8]. This technique is continued over each of the 16x16 subsections, reducing the grid size in each subsection only as far as necessary to meet a predefined tolerance.

The time savings obtained by the adaptive filling algorithm could be improved by more sophisticated interpolation algorithms. The time savings is also highly dependent on the nature of the active array scan impedance. For arrays in free space or over ground planes, where the scan impedance is relatively smoothly varying, it can provide significant savings. For microstrip arrays, it can be less effective. Table 1 shows the number of impedance samples that were computed (as opposed to interpolated) and the relative time savings compared to computing each sample required to fill the impedance matrix for a microstrip dipole array. The array had element width a = $0.01\lambda_0$, length b = $0.39\lambda_0$, array spacing $S_1 = S_2 = 0.5\lambda_0$, substrate thickness t = $0.19\lambda_0$ and $\varepsilon_r = 2.55$. In addition, a loss tangent of $\delta = 0.005$ in the substrate was used to eliminate singularities. As would be expected, the effectiveness of the method improves with finer sample grids.

Using these methods, fill times of 5 minutes for a 256x256 DFT are typical on a DECstation 5000.

4.0 RESULTS AND DISCUSSION

The method has been tested by comparing to results in the literature and by comparing to results obtained using a standard spatial domain moment-method code employing subsectional sinusoidal basis and testing functions. Three examples will be considered.

TABLE 1

Reduction in computation time resulting from adaptive sampling. Savings is expressed as the ratio of the total sample points to the actual number of calls to the impedance evaluation routine as a function of the DFT resolution. Example is for a microstrip dipole array, with spacing of $0.5\lambda_0$ in x and y, element length b = $0.39\lambda_0$, width a = $0.01\lambda_0$, on a substrate with t = $0.19\lambda_0$, $\varepsilon_r = 2.55$, $\delta = 0.005$.

DFT Resolution	Total Sample Points	Actual No. Calls.	Savings Factor
64	1,089	455	2.4
128	4,225	1,067	4.0
256	16,641	2,419	6.7
512	66,049	5,098	13.0

4.1 *Mutual Impedance Calculations.*

The mutual impedance between parallel and collinear microstrip dipoles was computed using the present method and compared to results computed by Alexopolous and Rana [9]. The method described here is denoted the DFT method in the Figures. The impedances were computed for dipoles with length $l = 0.333\lambda_0$, $S_1 = S_2 = 0.5\ \lambda_0$, on a substrate with $\varepsilon_r = 3.25$ and thickness of $t = 0.1016\lambda_0$. No superstrate layer was included. A loss tangent of 0.005 was included in the substrate layer to eliminate the singularity in the impedance surface $\tilde{\tilde{Z}}(\beta_0)$. This small loss tangent was found to have little effect on the numerical results. Results for the mutual impedances are shown in Figs. 3a and 3b, with good agreement.

4.2 *Finite Arrays of Microstrip Dipoles with Voltage Excitation.*

Next, the impedance of a 19x19 array of microstrip dipoles was computed versus scan angle and compared to results calculated in [10]. For this case, $l = 0.39\lambda_0$, $S_1 = S_2 = 0.5\lambda_0$ and the substrate had $\varepsilon_r = 2.55$ and $t = 0.19\lambda_0$. Again, a loss tangent of 0.005 was included in the substrate layer, and a 256x256 point DFT was used. The results in [10] were calculated using the element-by-element approach, using a sinusoidal approximation to the current on each element (1 entire-domain mode was used on each element). The results from the present method, also using a single mode approximation to the element current, and the

element-by-element method approach are compared in Figs. 4a and 4b. The reflection coefficient of the center element in each row along the E-plane is shown for scan angles of 0 and 30 degrees (Fig. 4a) and 45 and 60 degrees (Fig. 4b).

It was found in [10] that little change in the reflection coefficient vs. scan angle was seen when additional modes were used to represent the current on the elements. This indicates that the behavior of the array versus scan angle is well represented using a single mode for the case of approximately resonant length dipoles. However, it should be noted the significant error in the actual impedance values can results from this approximation. Using a single mode the input impedance of a single isolated dipole was found in [10] to be $Z = 105 + j72\ \Omega$. This compares well to the value of $103 + j65\ \Omega$ found using the DFT method and a single mode. However, using 19 subsectional modes with the DFT method resulted in an impedance of $154 + j38\ \Omega$, which compares well to the result of $154 + j31\ \Omega$ obtained by Michalski and Zheng using a subsectional basis function moment method solution with 51 unknowns [11].

4.3 *19 Element Array with Two Beams.*

As a final example, a 19 element linear array of y directed 0.5λ dipoles in free space was considered. The dipole elements were spaced 0.5λ apart along the x axis. Initially, a Tschebyscheff distribution with 30 dB sidelobes was selected. To

demonstrate the ability to handle arbitrary excitation, two beams were created by superimposing on the original excitation the same distribution phased to produce a beam at 45 degrees. The required generator voltages needed to create the current excitations for this array pattern were determined using the methods of Section 2.4, with $Z_T = 50 + j0\ \Omega$ at each generator. The results are shown in Figs. 5-7. Figures 5a and 5b compare the active element impedances obtained with current generators using the present method (DFT) and using a standard element-by-element approach. In Figs. 6a and 6b, the active element impedances obtained with both methods using voltage excitation are compared. In both cases a generator impedance of $Z_T = 50 + j0\ \Omega$ was used. The results compare very well in both cases, demonstrating the ability of the method to handle both voltage and current excitations. Finally, the array patterns obtained using "uncorrected" and "corrected" voltage excitations are shown in Fig. 7. The"uncorrected feeds" simply used the desired current taper as the voltage excitation taper. This method gives relatively good results but the lobe at 45° is several dB below the ideal pattern. The "corrected feeds" were obtained by determining the terminal voltages obtained with a current generator excitation with the desired taper. These voltages were then used to excited the array. The ideal pattern, simply the array factor of the desired element currents is not shown, but it is indistinguishable from the pattern obtained using the "corrected feeds".

5.0 CONCLUSION

The infinite array approach for analyzing large arrays can be adapted to the efficient analysis of finite arrays with arbitrary excitation. An important feature of the method is that at least for the case of current excitation, the storage and computational effort numerical effort is essentially independent of the number of elements in the array. For voltage excitation, the method requires only the storage and solution of an array of order $(N_x x N_y)^2$, where N_x and N_y are the number of elements in the array. Fill time of the array is independent of the number of elements.

The method could find application in the design of large phased arrays with arbitrary excitation, where the active element impedance can vary significantly over the array, not just near the edges. Currently, the method has been applied with good results to arrays of microstrip dipoles. The method works for both free and forced excitation, and can give good approximations to the mutual impedance between array elements.

6.0 REFERENCES

[1] Hansen, R.C., Ed. (1966) *Microwave Scanning Antennas*. vol. II. New York: Academic Press.

[2] Munk, B.A. and Burrell, G.A. (1979) Plane wave expansion for arrays of arbitrarily oriented piecewise linear elements and its application in determining the impedance of a single linear antenna in a lossy half-space. *IEEE Trans. Antennas Propag.*, Vol AP-27, No. 3, pp. 331-343.

[3] Ishimaru, A., Coe, R.J., Miller, G.E. and Geren, W.P. (1985) Finite periodic structure approach to large scanning array problems. *IEEE Trans. Antennas Propag.*, Vol. AP-33, No. 11, pp. 1213-1220.

[4] Pozar, D.M. and Schaubert, D.H. (1984) Scan blindness in infinite phased arrays of printed dipoles. *IEEE Trans. Antennas Propagat.*, Vol., AP-32, pp. 602-610.

[5] Wright, S.M. and Lo, Y.T. (1983) Efficient analysis for Infinite Microstrip Dipole Array. *Electron. Lett.*, Vol. 19., No. 24, pp. 1043-1045.

[6] Lo, Y.T., Wright, S.M., and Davidovitz, M. (1989) Microstrip Antennas. in Chang, K. Ed., *Handbook of Microwave and Optical Components*, vol. I. New York: Wiley. Chpt. 13.

[7] Dudgeon, D.E. and Mersereau, R.M. (1984) *Multidimensional Digital Signal Processing.* New Jersey: Prentice-Hall.

[8] Press, W.H., Flannery, B.P., Teulkolsky, S.A., and Vertterling, W.T. (1988) *Numerical Recipes: The Art of Scientific Computing.* New York: Cambridge University Press.

[9] Alexopolous, N.G. and Rana, I.E. (1981) Mutual impedance computation between printed dipoles. *IEEE Trans. Antennas Propagat.*, Vol. AP-29, pp. 106-111.

[10] Pozar, D.M. (1985) Analysis of finite phased arrays of printed dipoles. *IEEE Trans. Ant. Propag.*, Vol AP-33, No. 10, pp. 1045-1053.

[11] Michalski, K.A. and Zheng, D., (1990) Personal Communication.

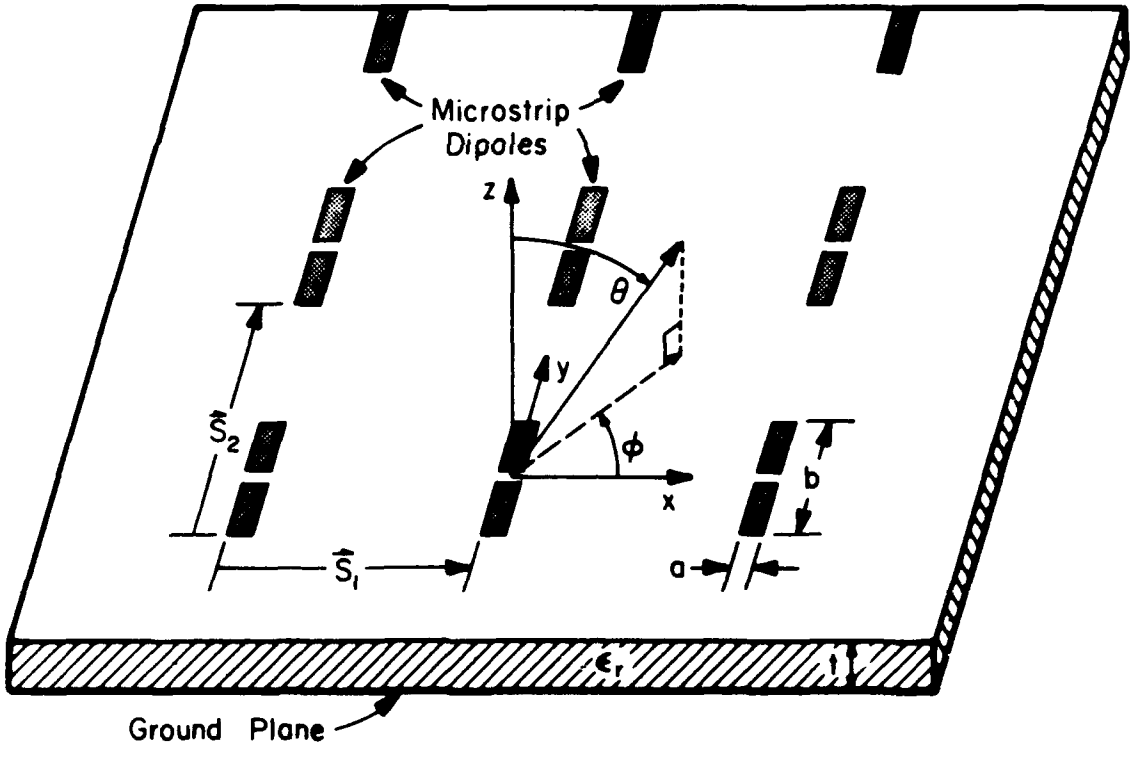

Figure 1. A section of a periodic array of microstrip antennas

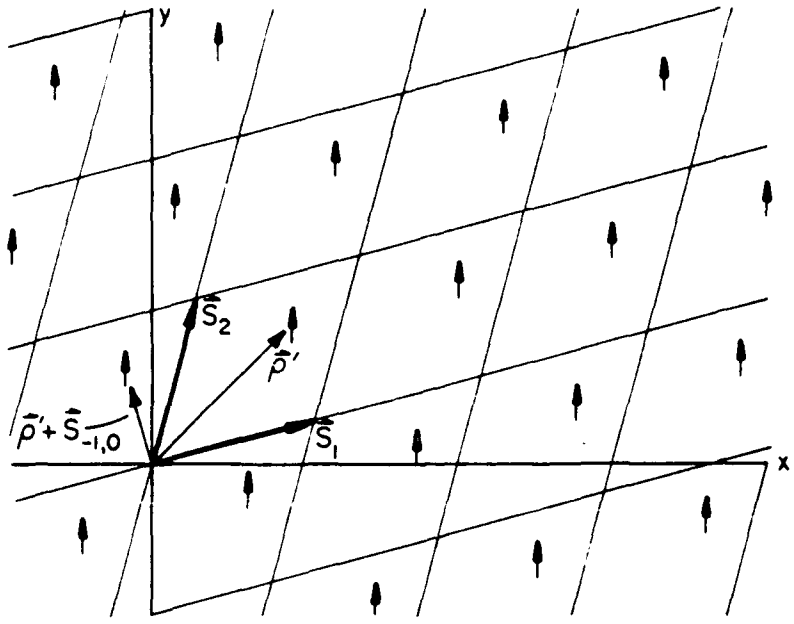

(a)

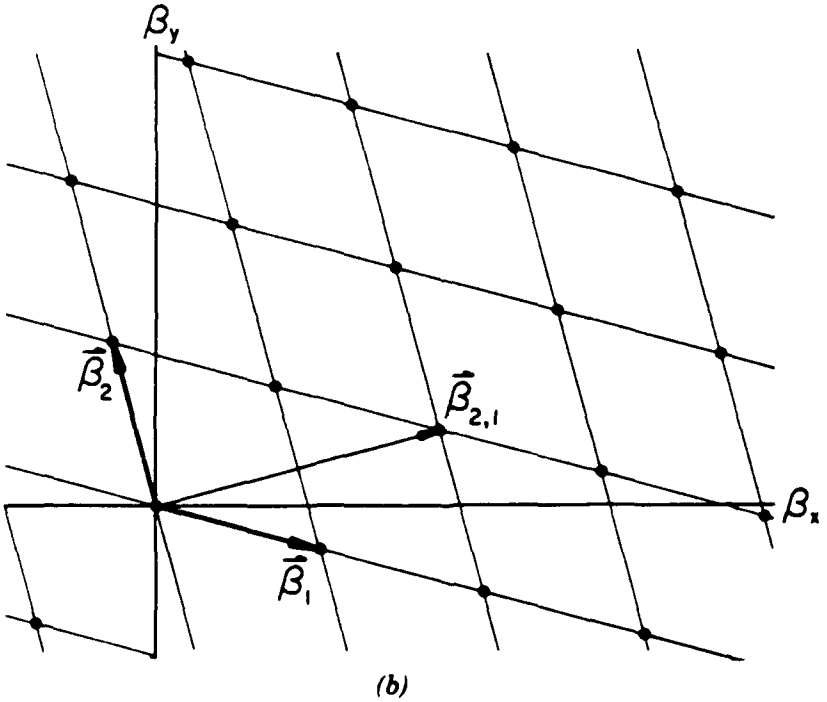

(b)

Figure 2. Periodic lattices in the spatial and spectral domains.

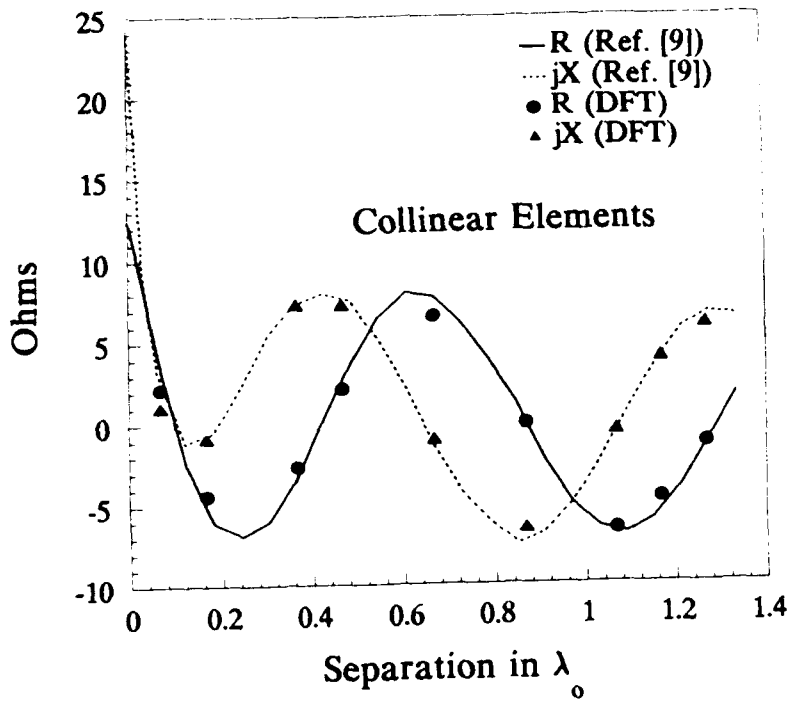

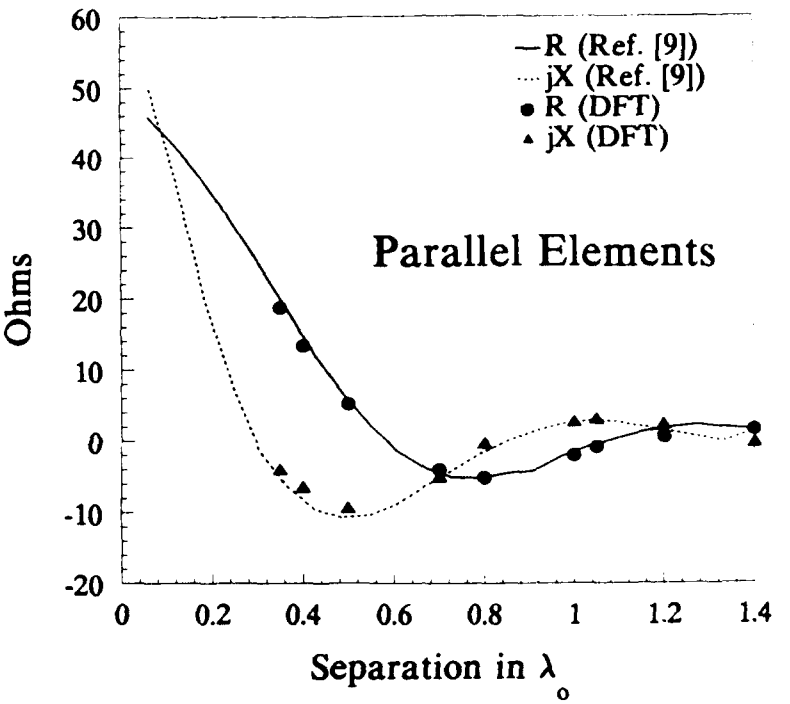

Figure 3. Mutual impedance between collinear microstrip dipoles. Comparison of results using DFT method and results in [9]. a) Dipoles collinear. b) Dipoles parallel.

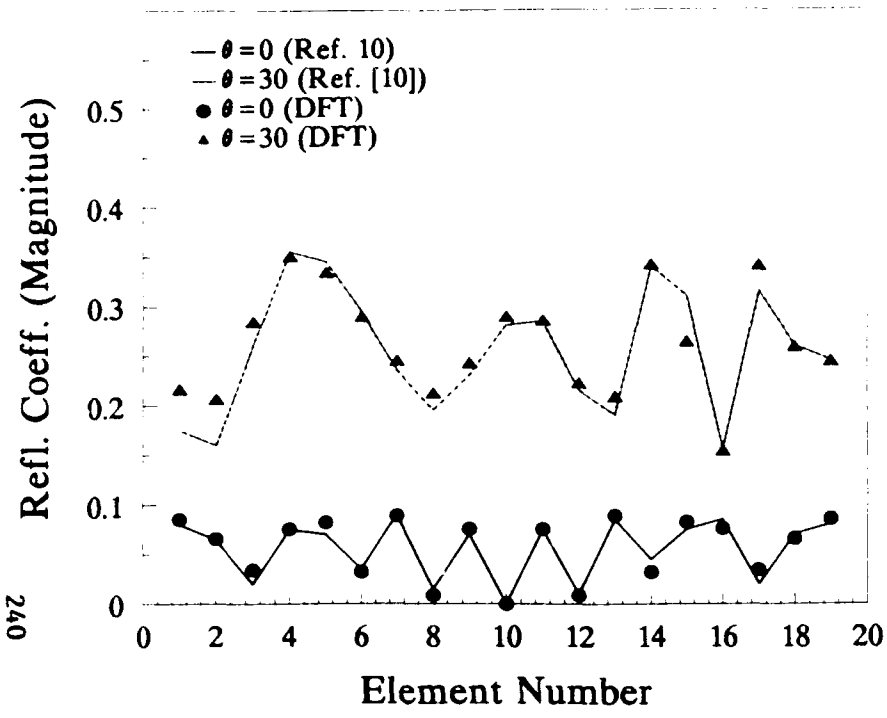

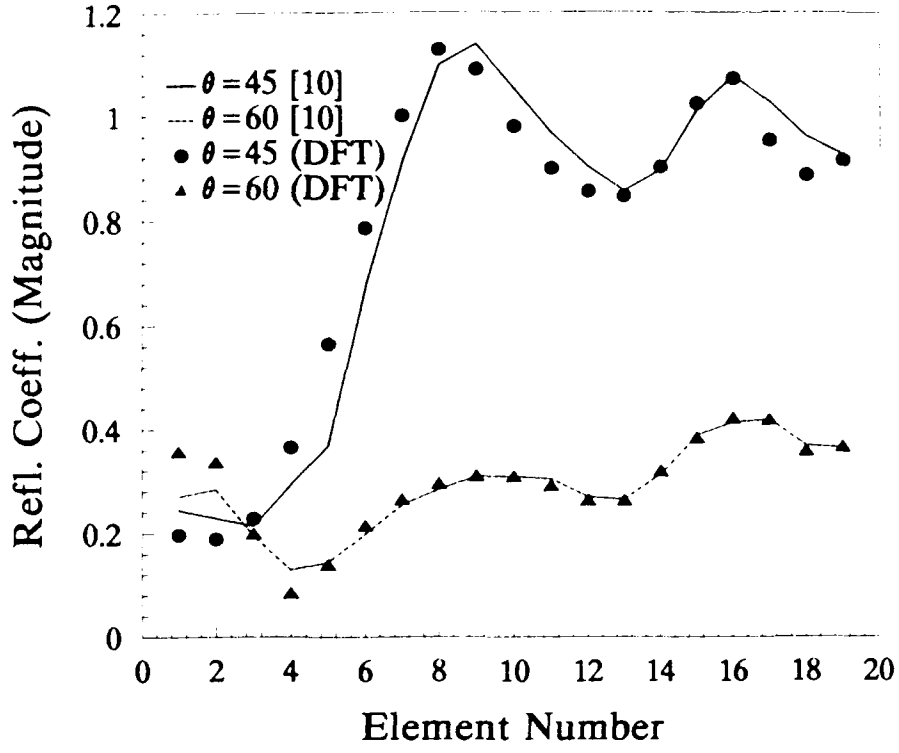

Figure 4. Reflection coefficient for center elements in E-Plane direction of a 19x19 element array of microstrip dipoles vs. scan angle in the E-plane direction. Comparison of DFT method to results from [10]. a) Scan angles = 0 and 30 degrees. b) Scan angles = 45 and 60 degrees.

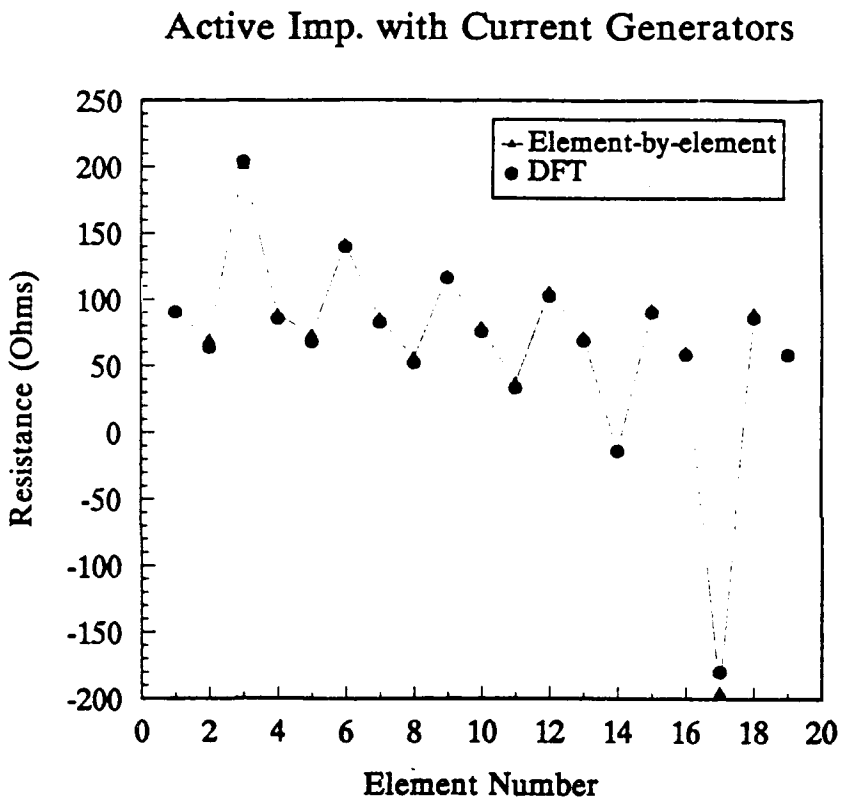

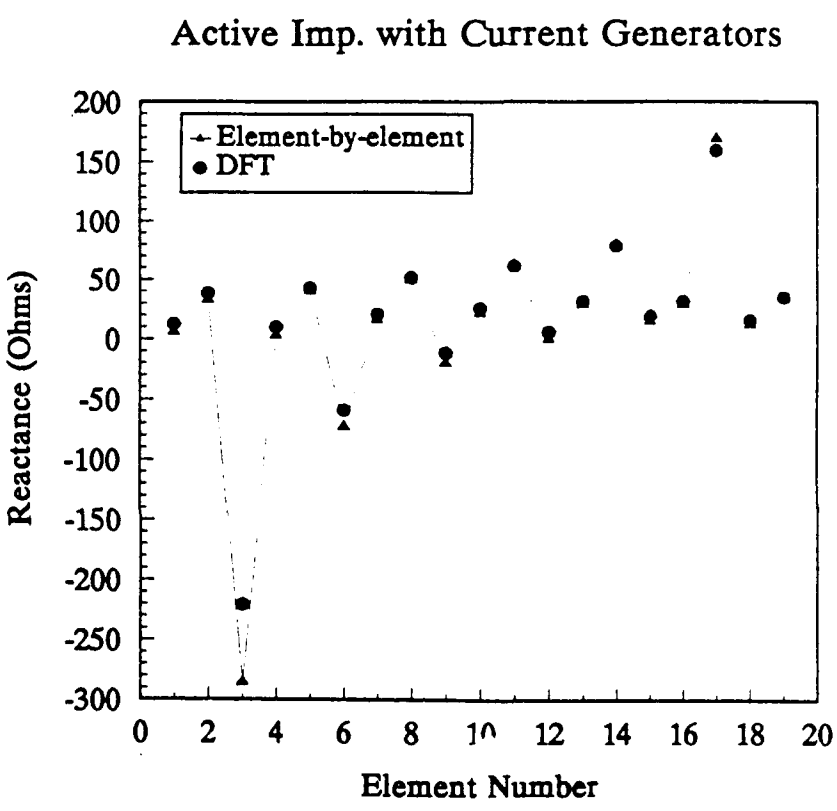

Figure 5. Active impedance for the elements in a 19 element array current generator excitation selected to form two beams, at 0 and 45 degrees. a) Resistance. b) Reactance.

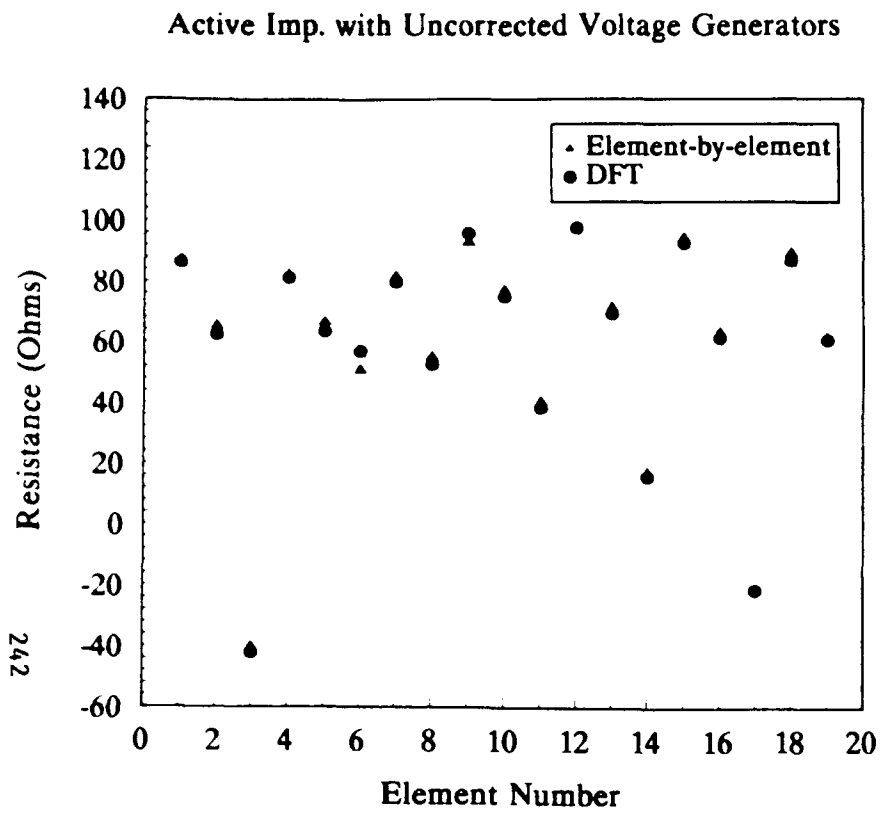

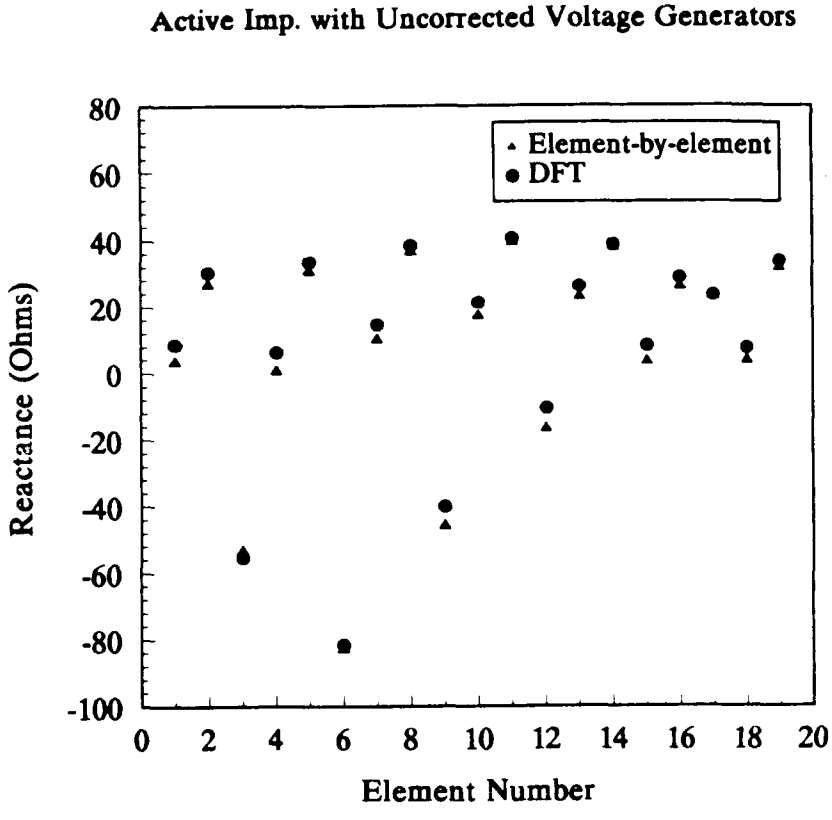

Figure 6. Active impedance for the elements in a 19 element array with voltage generator excitation. Excitation taper is the same as the taper in Figure 5, selected to form two beams, at 0 and 45 degrees. a) Resistance. b) Reactance.

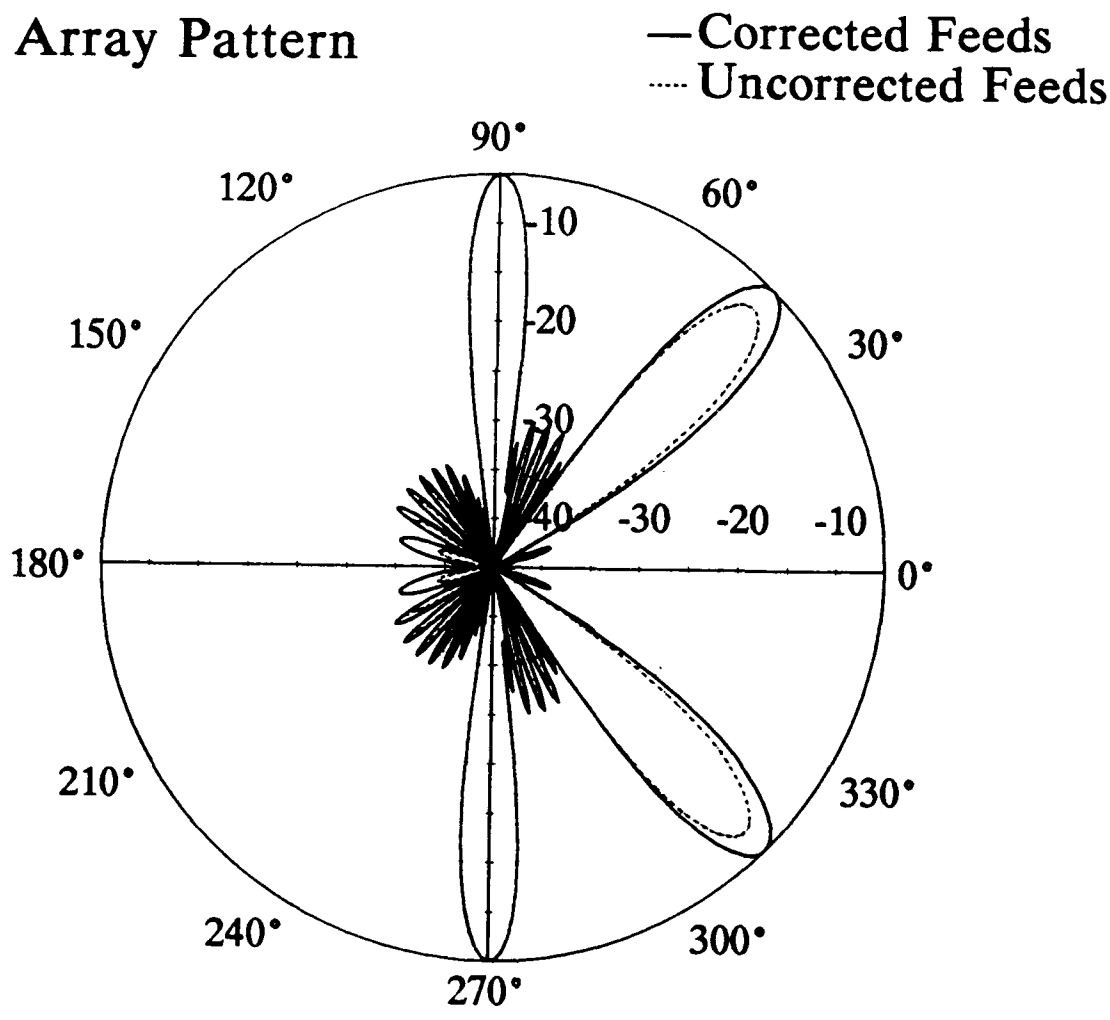

Figure 7. Array pattern for a 19 element array, with voltage generator excitation. Taper selected to form two beams, at 0 and 45 degrees. Uncorrected taper is identical to the desired currents, and causes errors in the realized pattern. Corrected taper is the excitation which gives the desired element currents. Generator impedance was 50 + j0 Ω.

MULTIMODE PERFORMANCE FROM A SINGLE SLOTTED ARRAY ANTENNA

by

John Cross, Don Collier and Len Goldstone
Norden Systems, Norwalk, Ct.

ABSTRACT:

Today's military aircraft must carry out various missions, some of them simultaneously. Consequently, antennas must be designed with the capability to function in a multiplicity of simultaneous as well as switchable modes. Slotted flat-plate arrays, with their unique ability to divide available aperture space among several antenna requirements, have become increasingly popular. Several recent design innovations have advanced the state of the art in attainable operational modes. Taking advantage of these approaches, one multimode antenna can now perform air-to-air pulse-doppler monopulse, ground mapping, terrain following, terrain clearance, terrain avoidance, weapons transponder tracking, and ground target tracking.

Three multimode antenna designs will be presented, ranging from the simplest and therefore least expensive, to the most complex, namely a flat-plate array design containing eight separate apertures and ten RF outputs. Measured performance data, including far-field patterns when operating in the various modes, will be shown.

1.0 THE LOW COST, MULTI-FUNCTION, FLATPLATE ARRAY ANTENNA

1.1 BACKGROUND: The Bandwidth Tradeoff

The slots on any flatplate antenna are excited by waveguide runs located behind the front plate of the antenna aperture. RF energy travels through these waveguides and is emitted from the slots whenever a component of H-field within the waveguide is parallel to the slot center line. The slots are precisely spaced to insure that the RF from each slot is in phase with that of its neighbor

[1]. The aperture is subdivided into resonant subarrays to simplify the feed network. This simplification limits the operational frequency band, however, and for this reason, antennas with good sidelobe characteristics at center frequency show higher sidelobes and VSWR at the band edges. This deterioration can be minimized by keeping the waveguide runs short. As energy travels down the guide from the RF feed port, the phase error of the RF increases as it reaches each successive slot. Therefore, if the antenna aperture were divided into small subarrays, and each subarray were fed by a separate RF feed port, the phase errors could be kept to a minimum. However, this method is expensive, as it requires a complex feed network attached to the back of the antenna.

Less expensive flatplate antennas must therefore be designed with fewer subarrays and longer resonant waveguide runs in each subarray. To compensate, a narrower frequency band and/or slightly higher sidelobe levels are tolerated.

1.2 DESIRED MODES OF OPERATION:

Three basic modes are required for a number of aircraft radar antenna applications; a pencil beam mode for long range target location; a Cosecant-Squared (CSC^2) mode for mapping and ground target identification; and an elevation monopulse mode for Terrain Following/Terrain Avoidance (TF/TA).

1.3 DESIGN:

Refer to Figure 1. In this "no-frills" economy design, a 12X14 element module was chosen. In the 28 slot elevation plane, there was sufficient space for two modules, and in the azimuth plane, space for four. This limited the required number of RF corporate feed ports to eight, and simplified the structure of the feed manifold on the back of the array. Equiphase summing the eight RF ports

with a corporate feed, in a manner similar to that described in Reference 2, accomplishes the pencil beam performance.

P. Smith of Norden Systems developed and patented a means to create a CSC^2 elevation beam from a flatplate aperture by 1) switching the power to only the upper half the radiating aperture and 2) introducing a fixed phase shift into the central row of the active aperture half.[3].

Power switching is accomplished by inclusion of an RF switch in the feed manifold as shown in Figure 2. In more complex array designs, especially in designs requiring low rms sidelobes in the pencil beam mode, the central row of slots has its own feed port, with a phase shift section that can be switched in or out as required. See Figure 8, for example.

In the simplified design (low cost array), a CSC^2 pattern is obtained by placing a fixed phase shift in the central row of aperture slots. See Figure 3. The resulting deterioration in rms sidelobe level in the pencil beam mode was accepted as a consequence. See Figure 4. The azimuth beam is unaffected, as can be observed in Figure 5.

The final mode, elevation monopulse for TF/TA operation, becomes possible with the inclusion of a magic tee at the RF input/output port. See Figure 2. The difference pattern is taken from the delta port, the pencil beam pattern from the sum port. Figure 6 shows the resultant sum and difference patterns superimposed.

2.0 A MORE COMPLEX MULTIMODE DESIGN :

The layout of this flatplate antenna is shown in Figure 7. The design contains not only an Az/El monopulse array, switchable to form a ground map antenna, but also 3 interferometers and a guard aperture. The guard array serves a sidelobe suppression function for both the interferometers and the monopulse array. In addition, this antenna includes two BIT (built in test)

circuits that permit a reference signal to be injected into the array to calibrate the waveguide runs during operation. The monopulse/ground map simplified diagram is shown in Figure 8. The ground map phase shifters and RF switch are shown as well as a T/R circulator. There are 8 waveguide ports (1 guard, 3 interferometer, receive sum, azimuth and elevation receive difference, and transmit sum), plus 2 coaxial RF injection (BIT) ports. The interferometer/guard BIT diagram is shown in Figure 9.

This more complex antenna is subdivided into smaller sized modules than the simplified array previously described, to achieve a wider frequency bandpass and lower pattern sidelobes. The modules are basically 4X4 slot layouts. The array diagram illustrating the module breakdown is shown in Figure 7. The monopulse array has 60 modules. Each interferometer has 10 modules. Each subarray or module is fed by a reactive power divider that is sensitive to module-to-module impedance mismatch. Module impedance thus becomes a critical design parameter if the desired sidelobes are to be achieved. Any mismatches between modules lead to aperture phase and amplitude errors which impact on the desired antenna patterns. Typical module impedances are shown in Figure 10.

The complete aperture is covered by a layer of Kaptan which protects the antenna face and holds waveguide pressure. The ability of the overall design to perform within specifications depends upon manufacturing tolerances, materials properties, and the quality of the bonding process. The array is fabricated largely as machined and dip brazed subassemblies and bonded or bolted in various manufacturing stages into one unit. In-process testing and quality control are vital to the attainment of performance goals. Final adjustment of the completed unit takes place on the antenna range, where the 8 monopulse sections are trimmed for equal phase, using shims in trombone

phase shifters. Pattern performance is "fine tuned" by adding thin layers of dielectric tape over the slots of selected modules, when required.

Finally, boresight is measured and the array mounting pads are machined to make the electrical boresight orthogonal to the mounting pads. Typical patterns are shown in Figure 11.

3.0 A COMPLEX MULTIMODE FLAT PLATE ARRAY:

This multimode flat-plate antenna was designed for a radar system which was to be integrated with a fighter-bomber aircraft. The projected aperture is approximated by a truncated ellipse 32" wide and 24" high. Contained within this area are 5 separate apertures; an azimuth and elevation monopulse, a 3-port azimuth interferometer, a 2-port elevation interferometer, a single port guard and a single port weapons uplink for a total of 10 RF outputs. All of the apertures operate over a 3% bandwidth at Ku band except for the uplink, which operates at X band and is used in transmit only. The only Ku band transmit channel is the monopulse sum, which has the capability of transmitting either a pencil beam or shaped beam pattern in elevation and a pencil beam in azimuth. The 9 receive channels, namely Sigma (shaped or pencil beam), Delta Az and Delta El (for monopulse), Left, Center and Right (for the azimuth interferometer), Up and Down (for the elevation interferometer) and Guard, are connected to 8 receivers (Delta Az and Delta El are time shared) mounted on the back of the array. Each microwave receiver consists of a transmit/receive limiter (TRL), a low noise amplifier (LNA) and a dual down-conversion module so that the array receive outputs are at the desired IF frequency. Also included in the array package are 7 RF injection ports for calibration and sensitivity checks, and an inertial measurement unit (IMU) for precise antenna orientation.

3.1 DESCRIPTION OF APERTURES AND FEED NETWORKS:

The outline of the monopulse, azimuth interferometer, elevation interferometer, guard and uplink apertures is detailed in the array face-plate drawing of Figure 12. The individual radiators of each of the 5 apertures are horizontally polarized resonant slots which are grouped into subarrays of resonant waveguide networks and fed by reactive 2-way power dividers. It was not possible to use 4-port power dividers, because of space and weight limitations.

The 4-quadrant monopulse is the most complicated antenna within the array, not only because of the large percentage area that it occupies, but also due to the complexity involved in the feed network to achieve either a pencil beam or shaped beam in elevation. The aperture is divided into 4 main quadrants with 16 subarrays each, combined by a reactive feed network and a comparator. The center rows just above and below the azimuth center line have a separate feed and comparator. The switching of the center rows provides elevation beam shape diversity. In the pencil beam mode, the entire aperture is illuminated with equal phase (Figure 14), while in the mapping mode, only the lower half of the aperture (PW 6 and PW 7 of Figure 15) and the 2 center rows are illuminated. Optimization of the shaped beam pattern is achieved by advancing the phase of the center rows relative to the lower quadrants. Transfer switches S2 and S3 in Figure 14 are used to switch in the appropriate phases through line lengths to the center rows. The predicted shaped beam elevation pattern and azimuth sum pattern with errors are shown in Figures 16 and 17.

The feed networks for the remaining apertures are similar to those of the monopulse antenna, but have no comparator assembly. Resonant waveguide

radiators are summed through a feed network to a single output for each of these arrays.

3.2 MODES OF OPERATION:

The monopulse aperture, azimuth and elevation interferometers and guard singly or in combination support all of the following radar modes. Air-to-ground modes including ground mapping (real beam, doppler beam sharpening and synthetic aperture), beacon and GMTI (pulse doppler and clutter suppression interferometry), air-to-sea modes including sea surveillance and ship classification, as well as air-to-air modes including air surveillance and air combat, terrain clearance including terrain following and terrain avoidance.

3.3 RF INJECTION:

RF injection is provided, mainly for in-flight calibration of the antenna system. As shown in the block diagram of Figure 13, monopulse calibration is achieved by single quadrant injection, while each of the azimuth and elevation channels as well as the guard have individual injection points. In addition, each interferometer injection line contains a variable phase trimmer for boresight alignment.

4.0 CONCLUSIONS:

Today's complex mission requirements make flexibility and multimode capability an operational imperative in modern radar systems. To support these needs, apertures with one basic antenna pattern are no longer viable. Until the long-awaited phased array becomes economically competitive, the best solution to date has been the multimode, slotted flat-plate array antenna. For cost-effective performance in a variety of scenarios, it is hard to beat.

5.0 ACKNOWLEDGEMENTS:

The authors wish to acknowledge the assistance of senior consultants Harold Shnitkin and Peter Smith in the preparation of this paper. They also wish to thank the respective Program Managers for facilitating the inclusion of previously unpublished technical material.

6.0 REFERENCES:

1) Yee, H.Y. and Richardson, P.N. (1982) Slotted Waveguide Antenna Arrays, IEEE Antennas and Propagation Society Newsletter.

2) Skolnik, M.I. (1970) Radar Handbook, McGraw-Hill, New York, pp. 21-13 to 21-21.

3) Smith, P.W. (1983) Multimode Array Antenna, U.S. Patent No. 4,376,281.

4) Moreno, T. (1948) Microwave Transmission Design Data, Dover, New York, pp. 111- 120.

5) Wolff, E.A. (1967) Antenna Analysis, John Wiley & Sons, New York, pp. 169- 178.

6) Silver, S. (1949) Microwave Antenna Theory and Design, Peter Peregrinus Ltd., London, pp. 286- 295.

7) Maxim, B.J. (July, 1960) Resonant Slots with Independent Control of Amplitude and Phase, IRE Transactions on Antennas and Propagation.

8) Oliner, A.A. (January, 1957) The Impedance Properties of Narrow Radiating Slots in the Broad Face of Rectangular Waveguide, IRE Transactions on Antennas and Propagation.

9) Collin, R.E. and Kucker, F.J. (1969) Antenna Theory, Part I, McGraw-Hill, New York, pp.587-617.

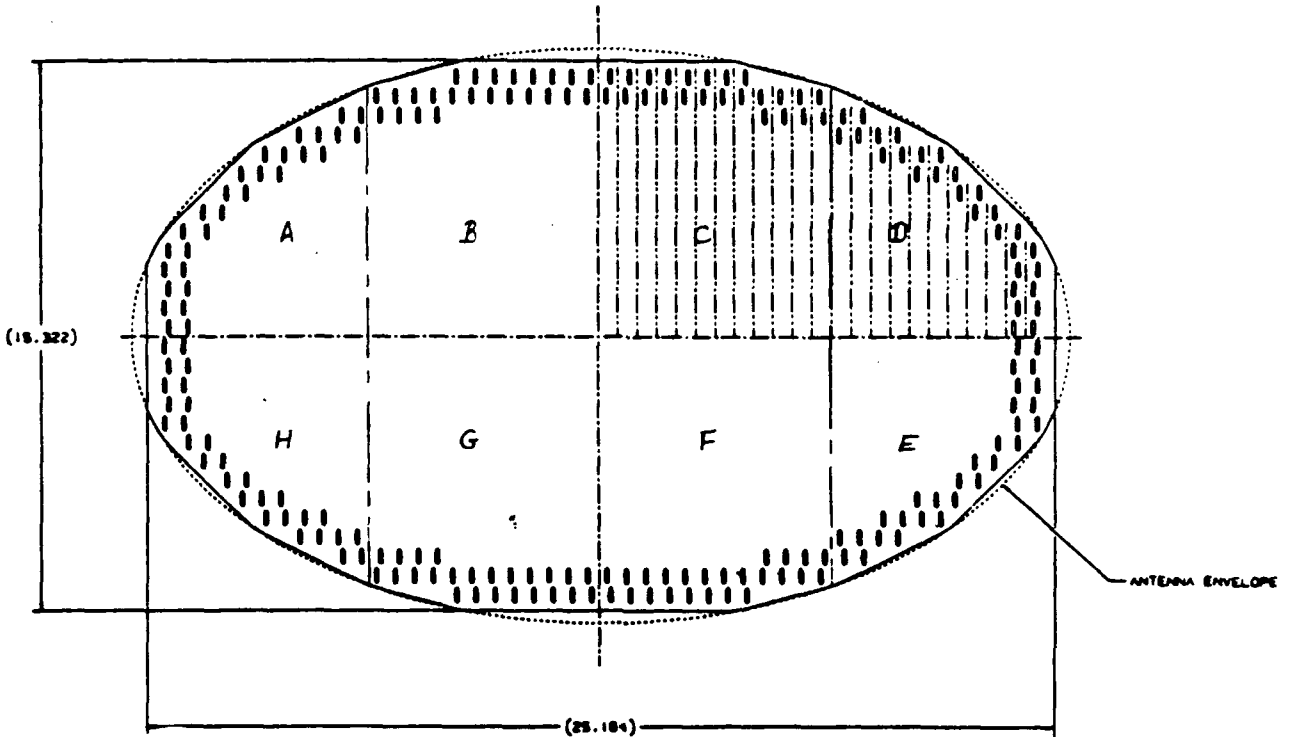

Figure 1. Front Face of Low-Cost Array Antenna.

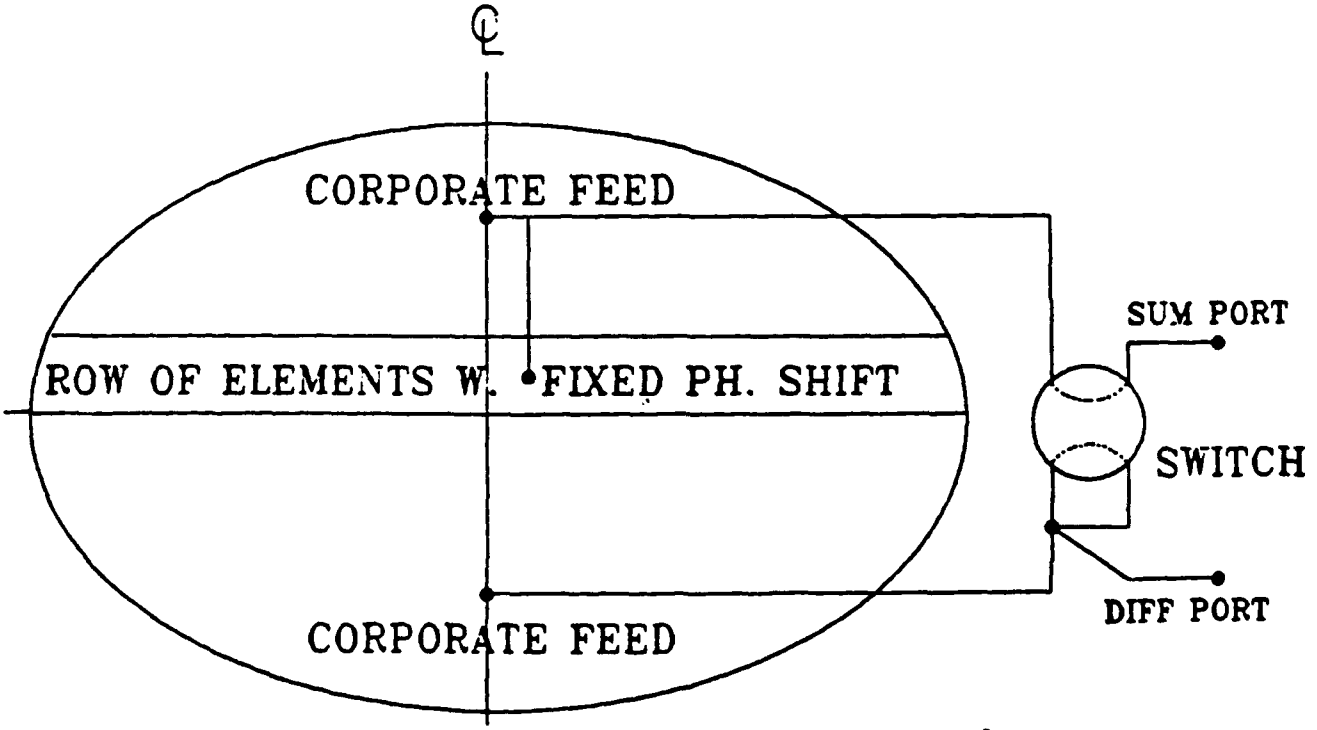

Figure 2. Simplified Schematic Showing RF Switch in CSC^2 Mode Position.

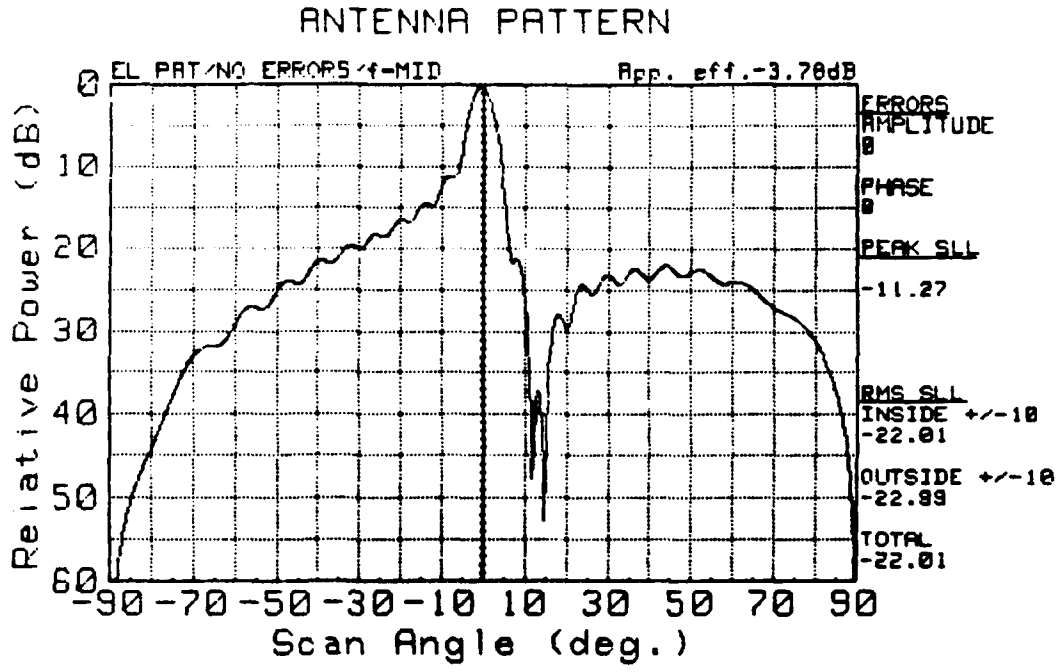

Figure 3. CSC² Antenna Pattern in Elevation Plane.

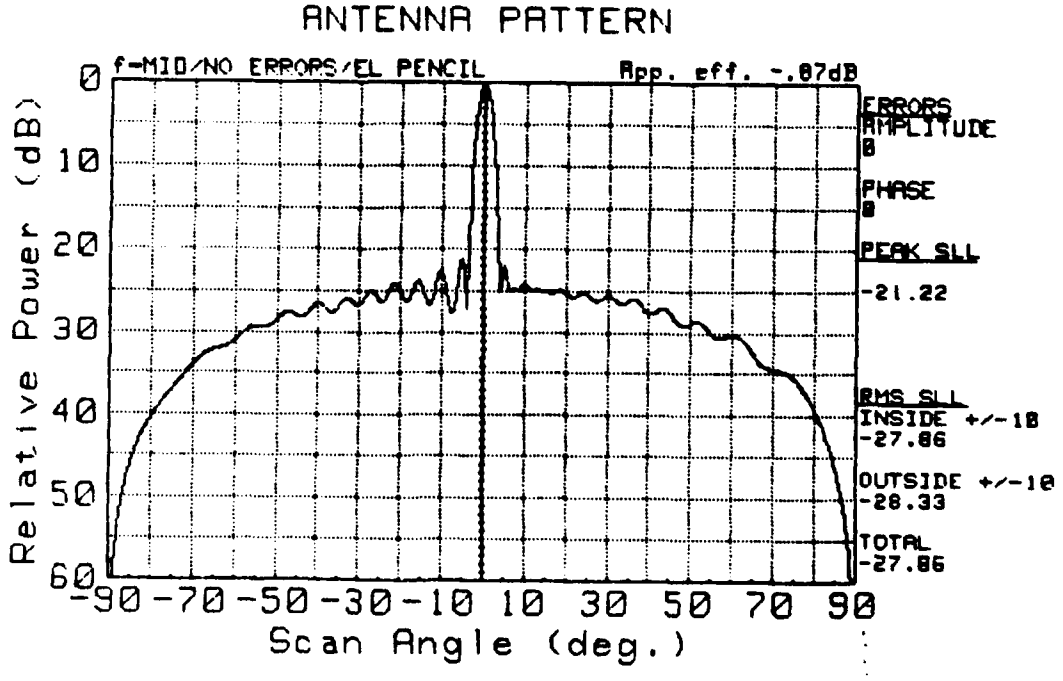

Figure 4. Pencil Beam Pattern in Elevation Plane.

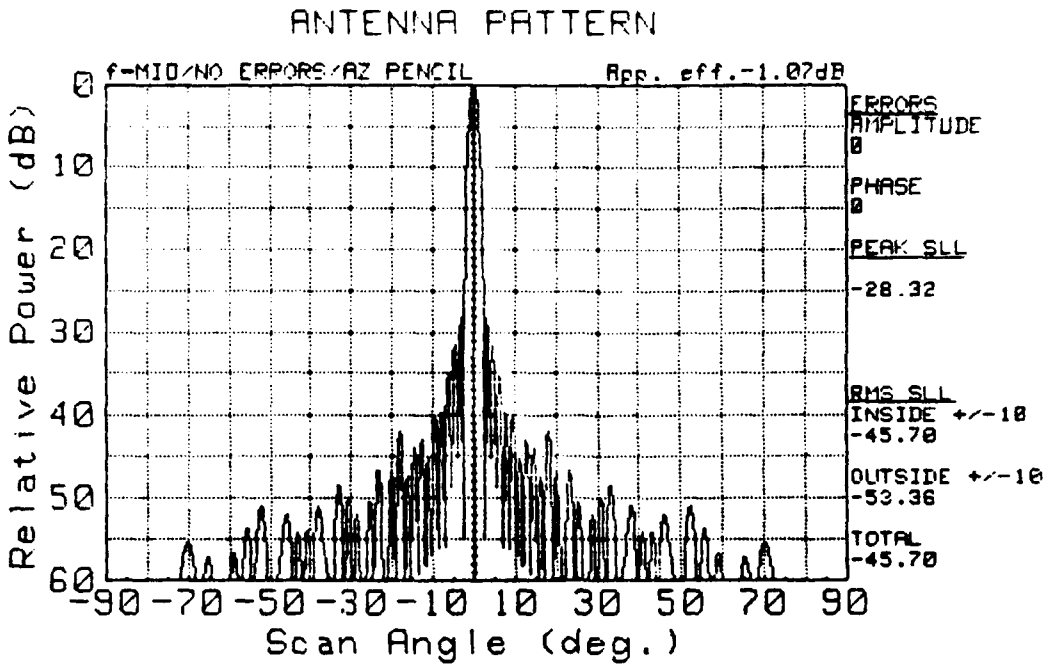

Figure 5. Azimuth Beam Pattern.

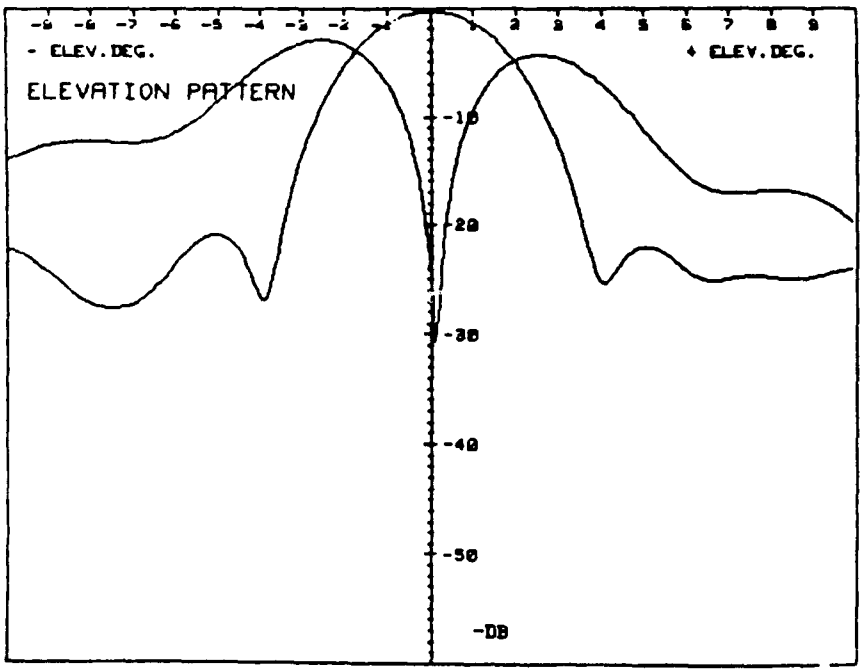

6. Elevation Sum and Difference Pattern.

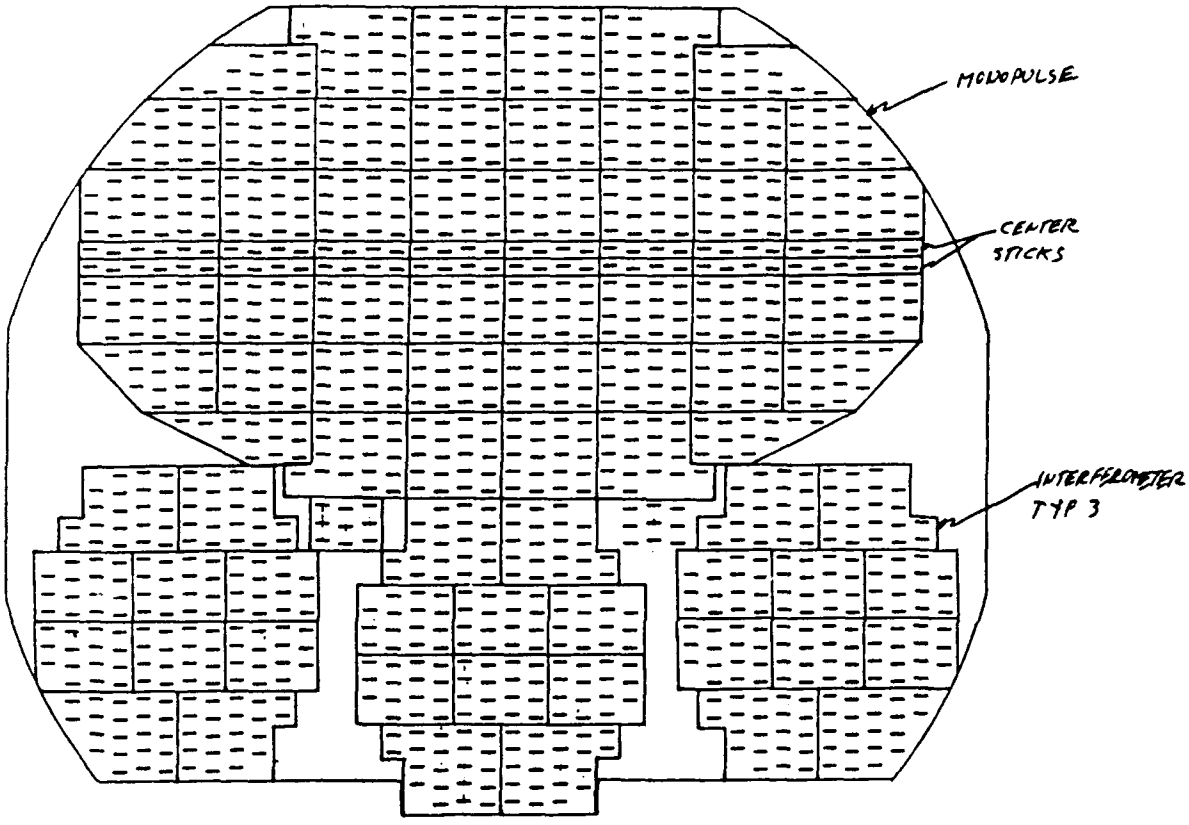

Figure 7. Front Face of Array Antenna.

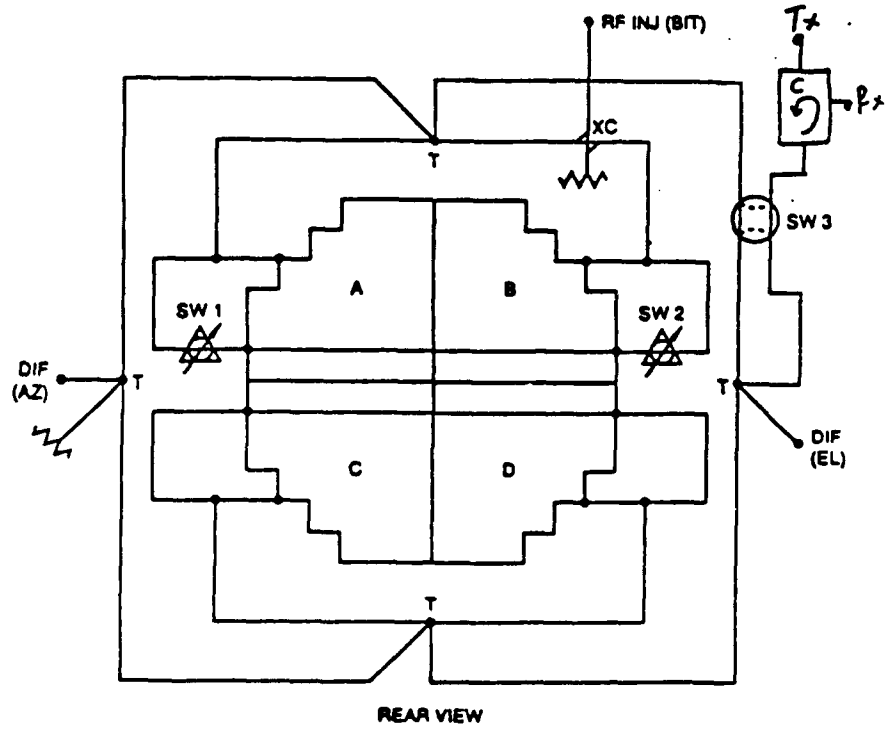

Figure 8. Simplified Diagram of Monopulse/Ground Map Array.

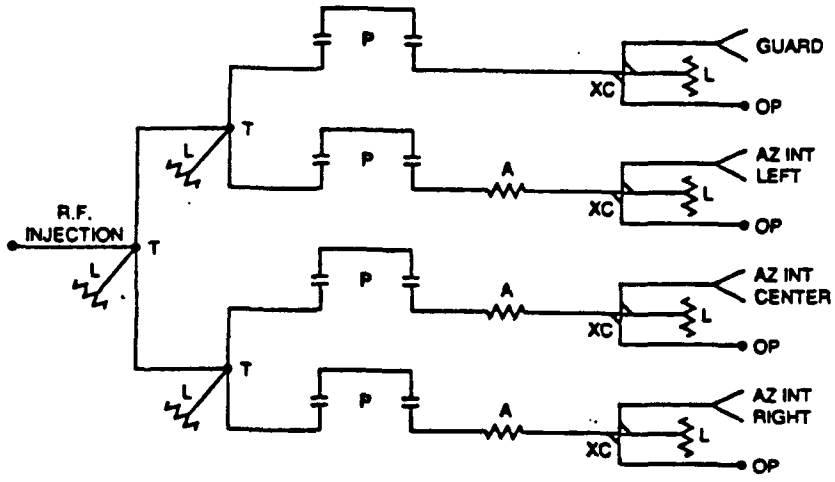

T = MAGIC TEE
P = TROMBONE SECTION
XC = CROSS GUIDE COUPLER
A = FIXED ATTENUATOR
L = DUMMY LOADS
OP = OUTPUT PORT

Figure 9. Interferometer/Guard BIT Schematic Diagram.

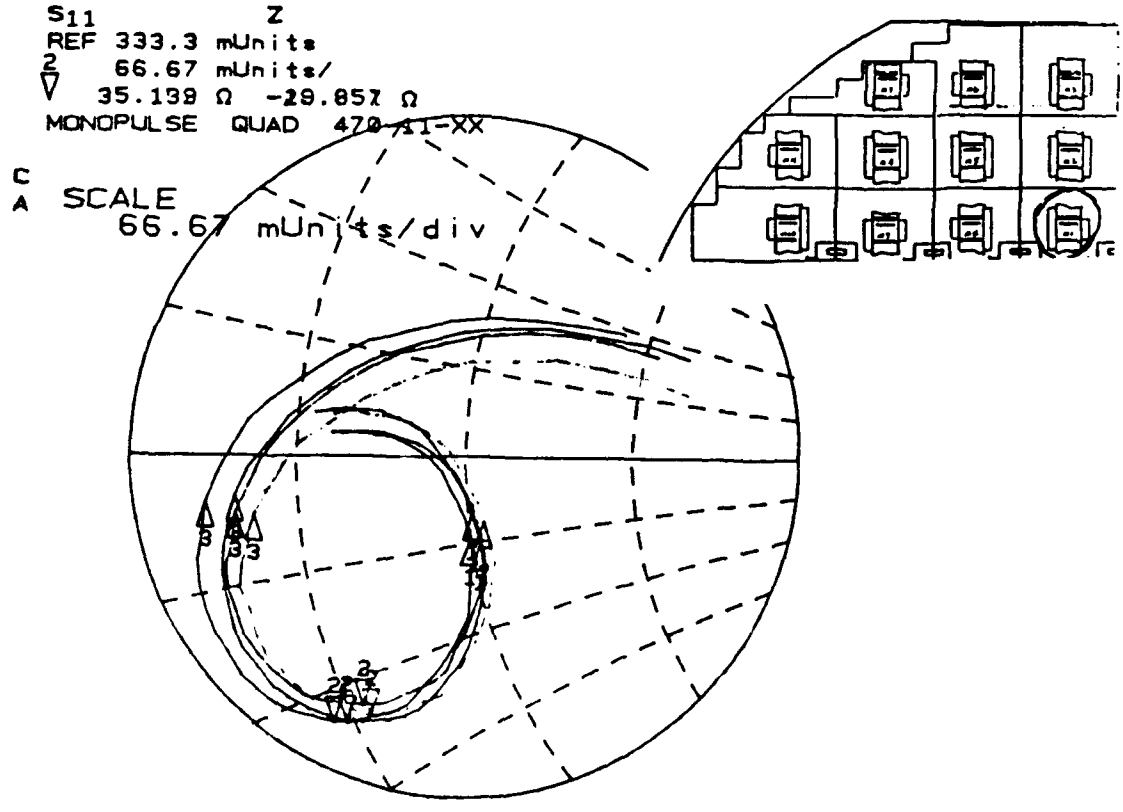

Figure 10. Four Typical Module Impedance Curves.

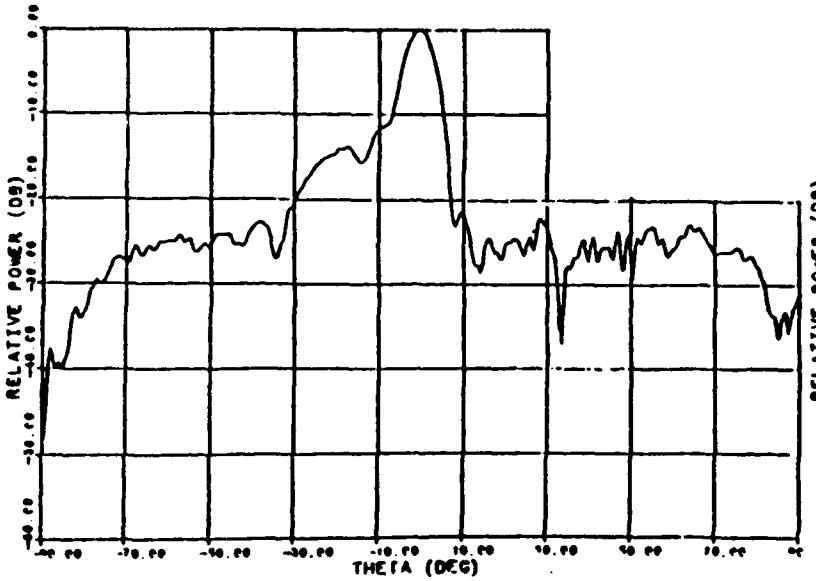

11a. CSC^2 Elevation Pattern

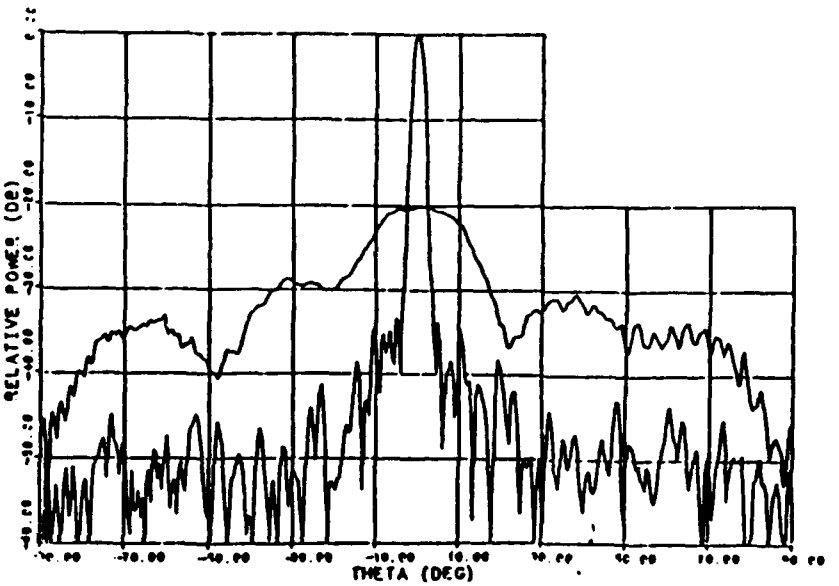

11b. Azimuth Pencil Beam plus Guard Pattern

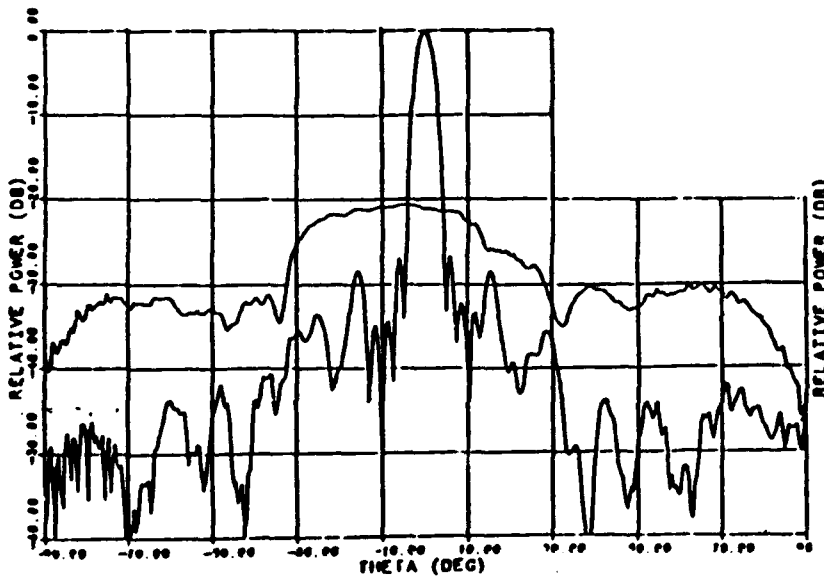

11c. Elevation Pencil Beam plus Guard Pattern

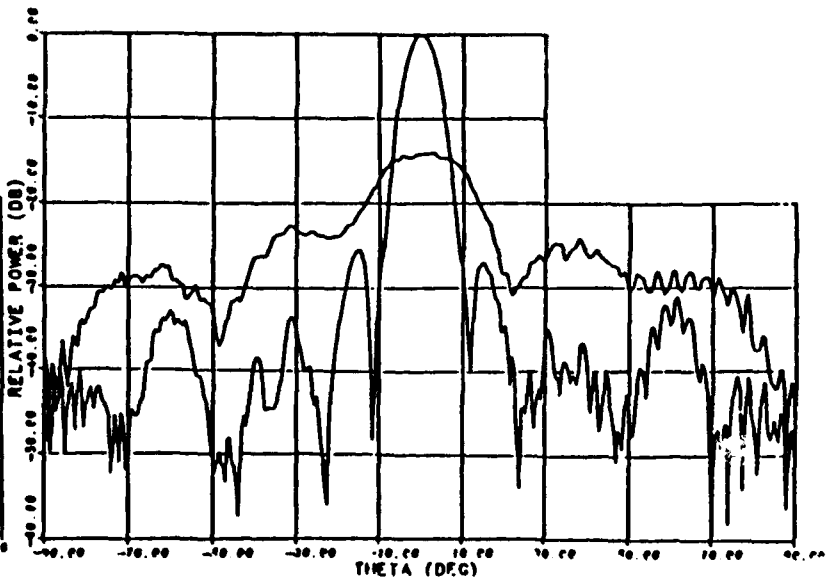

11d. Azimuth Interferometer plus Guard Pattern

Figure 11. Typical Measured Patterns.

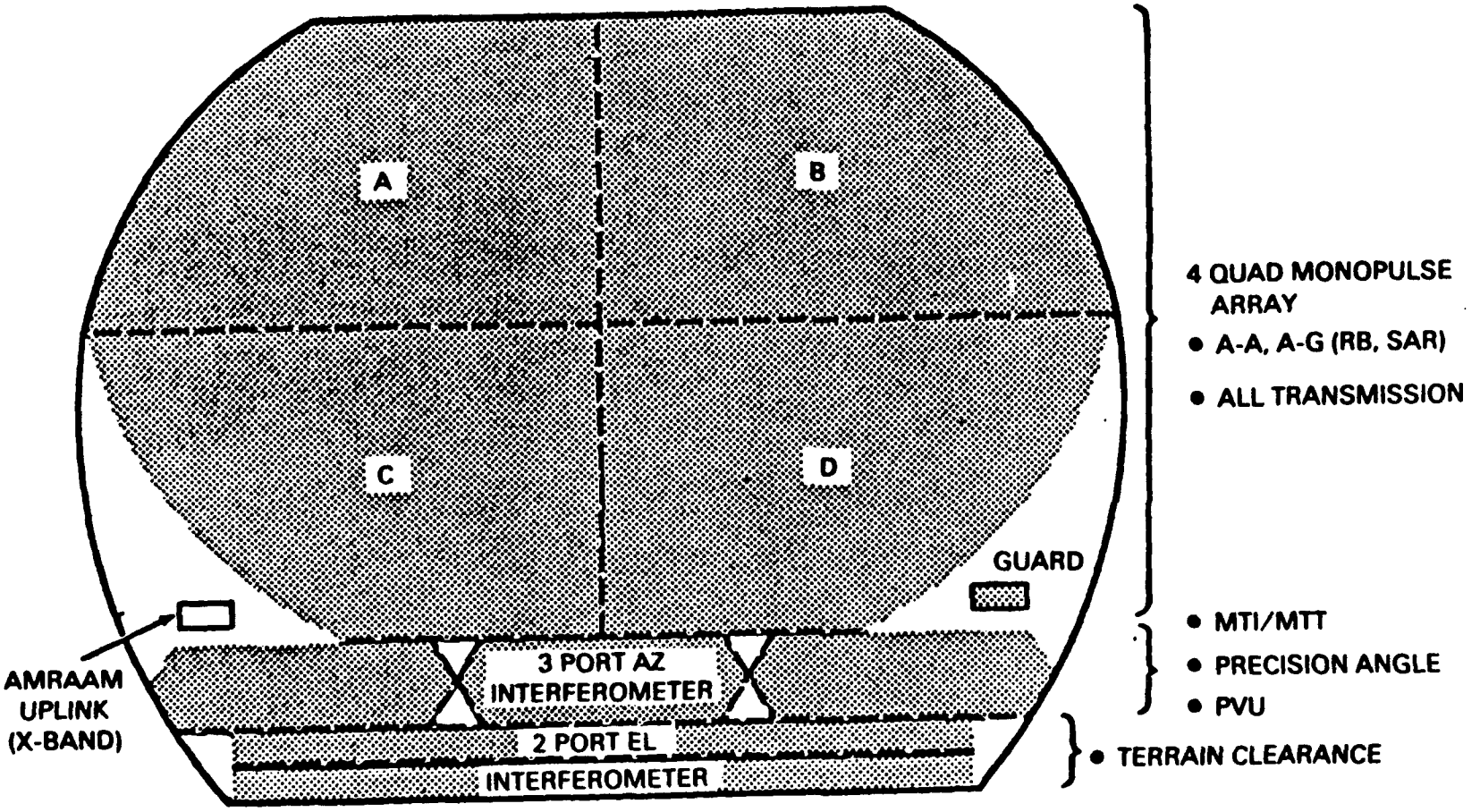

Figure 12. Complex Flatplate Array Front Face

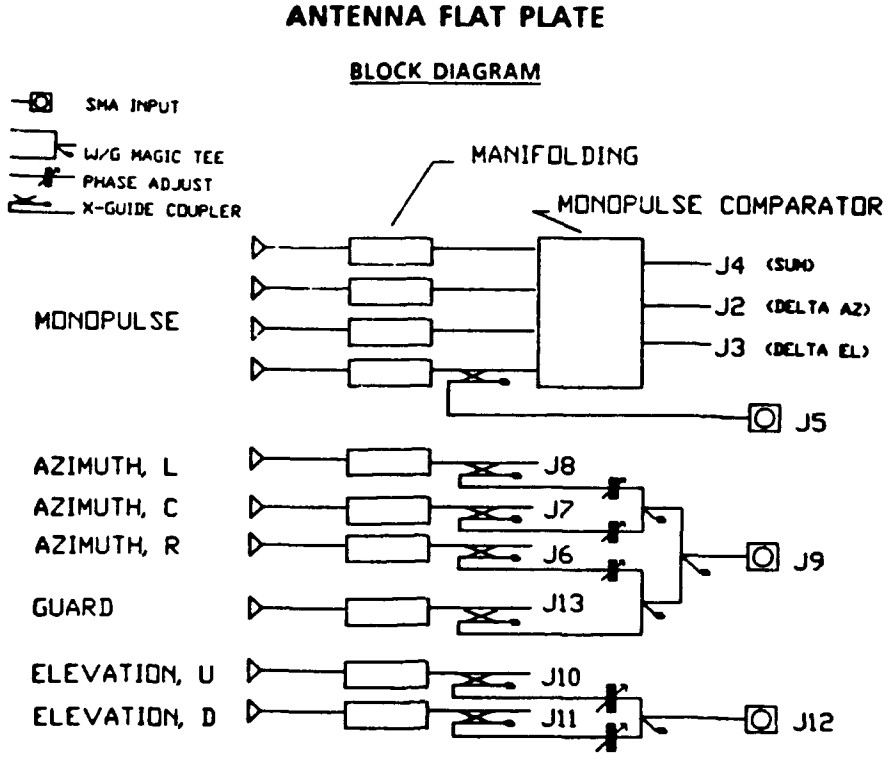

Figure 13. Functional Diagram of Array

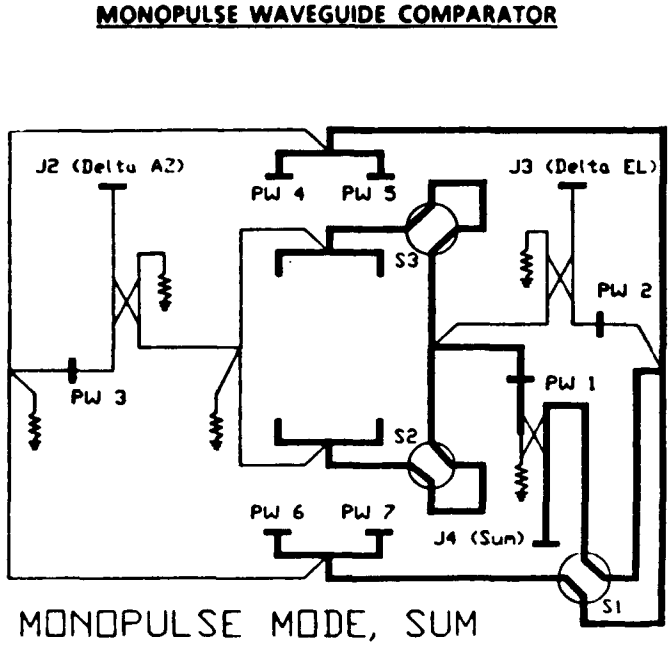

Figure 14.Monopulse Waveguide Compatator Schematic Shown in Monopulse Sum Mode.

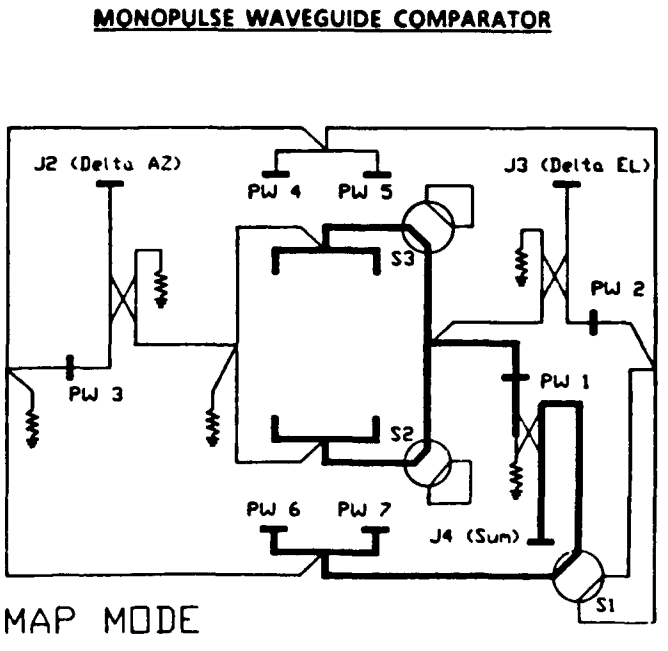

Figure 15.Monopulse Waveguide Comparator Schematic Shown in CSC^2 Mode.

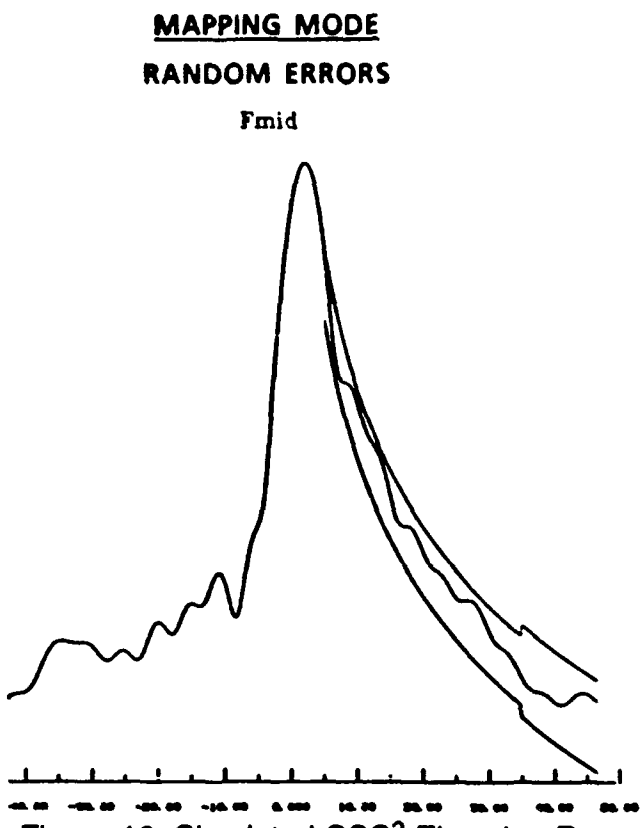

Figure 16. Simulated CSC^2 Elevation Pattern.

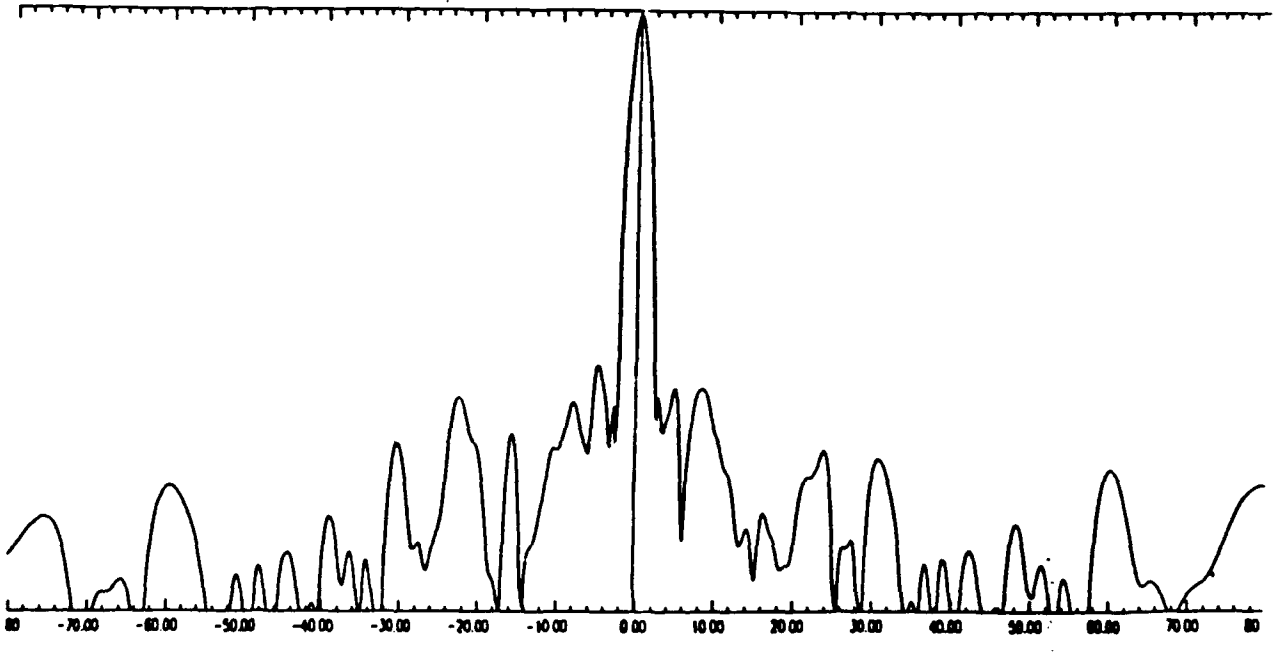

Figure 17. Simulated Azimuth Pencil Beam Pattern.

AN ADAPTIVE ARRAY USING REFERENCE SIGNAL EXTRACTION

Jian-Ren E. Wang and Donald R. Ucci
Department of Electrical and Computer Engineering
Illinios Institute of Technology
Chicago, IL 60616

ABSTRACT

This paper describes a new adaptive array which derives a reference signal from frequency and angle of arrival information. The array employs a Reference Acquisition Loop (RAL) consisting of an arbitrary filter and a nonlinear directional gain constraint to ensure proper operation. The array is more flexible since extremely accurate *a priori* information is not required. Simulation results are presented.

1. INTRODUCTION

Adaptive beamformers, which have been widely discussed and applied in radar and communication systems[1-4], use two major algorithms (i.e., the Least Mean Square (LMS)[5] and Applebaum algorithms[6]). For proper operation, an Applebaum array needs a precise steering vector to point the beamformer toward the desired signal source; the LMS algorithm requires a reference signal which is highly correlated with the information signal to distinguish the unwanted components from the desired signals.

To circumvent the dependency on *a priori* knowledge, several studies on self-generated reference techniques have been proposed. These studies can be separated into two categories: spread spectrum techniques[7-10] and "data-derived" techniques[11]. For both techniques, the required frequency bandwidth is increased

and an accurate desired signal characteristic is needed.

We propose an Autorecursive Nonlinear Adaptive Array (ARENA) using a Reference Acquisition Loop (RAL) to extract the reference signal. This array requires, *a priori*, the frequency and Angle Of arrival of the Desired signal (AOD). Thus, the proposed array is a more general system for most applications.

The general structure and the basic concept of the array are described in Section 2, while the operation is explained in the Section 3. Computer simulation results are presented in Section 4 and the Conclusion is in Section 5.

2. FORMULATION

Consider an m element half wavelength spaced LMS array with the self-generated reference signal as shown in Fig. 1. The array consists of two parts: the first is an m element LMS adaptive processor and the second is the RAL. Note that the reference signal is derived from the output of the array. The RAL must allow the desired signal component at the output of the array to pass through with only limited distortion (thus retaining correlation between the desired signal and the self-generated reference signal). Also, it must reduce the undesired signal component content.

We define the input signal vector, X(k), at discrete time k, to be

$$X(k) = X_d(k) + X_i(k) + N(k), \tag{1}$$

where $X_d(k)$, $X_i(k)$ and $N(k)$ represent the input desired signal, interference and thermal noise vectors, respectively. Assume $X_d(k)$ and $X_i(k)$ are not correlated to

each other. The thermal noise vector is a zero mean mutually independent random vector. The LMS algorithm is used to adjust the weight vector[5], $W(k)$,

$$W(k+1) = W(k) + \frac{1}{2}\kappa\nabla_W E[|\epsilon(k)|^2] = W(k) + \kappa E[\epsilon(k)X^*(k)] , \tag{2}$$

where κ is the gain constant of the adjustment loop, $E[\cdot]$ denotes the expected value and $(\cdot)^*$ denotes complex conjugation. $\epsilon(k)$ represents the system residual signal which is the difference between the self-generated reference signal and the system output, y(k), i.e., $\epsilon(k)=G[y(k)]-y(k)$, where $G[\cdot]$ denotes the function of the reference signal generator. ∇_W represents the gradient with respect to the weight vector. From Eq. (2), when the weight adjustment loop reaches steady state, $\epsilon(k)$ and the input signal are orthogonal to each other,

$$\begin{aligned} & E[\epsilon(k)X^*(k)] \\ &= E[(g_d(X_d(k)^T W_{ss}) - X_d^T(k) W_{ss})X^*(k) + (g_i^*(X_i(k)^T W_{ss}) - X_i^T(k) W_{ss})X^*(k) \\ &\quad + (g_n^*(N^T(k) W_{ss}) - N^T(k) W_{ss})X^*(k)] \\ &= 0 , \end{aligned} \tag{3}$$

where W_{ss} represents the steady state weight vector, $g_d(f)$, $g_i(f)$ and $g_n(f)$ are the RAL gains of the desired signal, interference and the thermal noise, respectively. The superscript $(\cdot)^T$ denotes the transposition. For simplicity, we assume that g_d, g_n and g_i are constant over the appropriate frequency band.

When both the desired signal and interference are zero mean and uncorrelated with each other, Eq. (3) can be further decomposed into

$$E[(g_d-1)X_d^T W_{ss} X_d^* + (g_i-1)X_i^T W_{ss} X_i^* + (g_n-1)N^T N^*] = 0 \ . \qquad (4)$$

To ensure that the steady state weight vector will converge and suppress the undesired signal component the RAL is designed to have unity gain for the desired signal but non-unity gain for the interference and thermal noise components. Therefore, Eq. (4) becomes

$$(g_i-1)E[X_i^* X_i^T]W_{ss} + (g_n-1)E[N^* N^T]W_{ss} = 0 \ . \qquad (5)$$

Obviously, when both g_i and g_n are not unity, a null weight vector is able to satisfy Eq. (5) which is a trivial solution. Therefore, a particular scheme is required in the RAL to avoid this while minimizing the undesired signal power. In particular, it is desirous to have g_n, $g_i<1$ so that the weight adjusting loop will have a faster convergent characteristic and better stability.

3. THE ARENA ARRAY

A type of adaptive array based on the general structure shown in Fig. 1 and a nonlinear direction constraint in the RAL is proposed as shown in Fig. 2. The RAL consists of a weight constraint, $C(k)$, and a filter, F. To determine the design of the weight constraint, first consider an output signal vector, $y(k)$,

$$y(k) = [X_d(k)+X_i(k)+N(k)]^T W(k) \ . \qquad (6)$$

Here

$$X_d(k) = a_d(k)S_d \ , \tag{7}$$

$$X_i(k) = \sum_{l=1}^{p} a_l(k)S_l \ , \tag{8}$$

and

$$N(k) = [n_1(k),\ n_2(k),\ \cdots,\ n_m(k)]^T \ , \tag{9}$$

with S_d and S_l (l= 1,2,...,p) the phase arrival vector of the desired and interference signals, respectively. $a_d(k)$ is the waveform of the desired narrowband signal. A continuous (non-impulsive) type wide band interference, $X_i(k)$, is represented by the sum of narrow band waveforms $a_l(k)$, $l = 1, ..., p$. $n_i(k)$, $i=1, 2, \cdots, m$ represents the thermal noise component at i-*th* element. Substituting Eqs. (7)-(9) into Eq. (6), the array output is given by

$$y(k) = a_d(k)S_d^T W(k)+\sum_{l=1}^{p} a_l(k)S_l^T W(k)+N^T(k)\, W(k) \ . \tag{10}$$

We define the output of the RAL, r(k), to be

$$\begin{aligned} r(k) &= C(k)F[y(k)] \ , \\ &= C(k)[g_d a_d(k)S_d^T W(k)+\sum_{l=1}^{p} g_l a_l(k))S_l^T W(k)+g_n N^T(k)\, W(k)] \ , \end{aligned} \tag{11}$$

where $F[\cdot]$ is a filter function, C(k) is a directional constraint, and g_l is the gain seen by a_l. Note that the output of the RAL is utilized as the reference signal and fed back to the weight adjusting loop. We define the system residue, $\epsilon(k)$, as

$$\begin{aligned}\epsilon(k) &= r(k) - y(k) \\ &= (g_d C(k)-1)a_d(k)S_d^T W(k)+\sum_{l=1}^{p}(g_l C(k)-1)a_l(k)S_l^T W(k)+(g_n C(k)-1)N^T(k)W(k) .\end{aligned} \tag{12}$$

In order to maintain a constant gain in the designated direction and also avoid the zero weight convergence, we have

$$C(k) = \frac{g}{g_d W^T(k) S_d} , \tag{13}$$

where g is a arbitrary gain constant. Note that C(k) is a nonlinear constraint and is inversely proportional to the gain of the weight vector in the AOD. Substituting Eq. (13) into Eq. (12), the system residue now becomes

$$\epsilon(k)=a_d(g-S_d^T(k)W)+\sum_{l=1}^{p}(\frac{g_l g}{g_d S_d^T W(k)}-1)a_l(k)S_l^T W(k)+(\frac{g_n g}{g_d S_d^T W(k)}-1)N^T(k)W(k). \tag{14}$$

3.1 Optimum Weight Vector

According to the complex LMS algorithm[12], the weight vector which yields the minimum $E[|\epsilon(k)|^2]$ can be obtained by solving

$$E[\epsilon(k)\nabla_W \epsilon(k)^*] = 0 \,. \tag{15}$$

After some manipulations, Eq. (15) can be rewritten as

$$\begin{aligned}
&E[\epsilon(k)\nabla_W \epsilon^*(k)] \\
&= \sigma_d^2 S_d^* (S_d^T W(k) - g) + \sum_{l=1}^{p} \sigma_l^2 [\frac{g \cdot g_l}{g_d (S_d^T W(k))^2} (S_l S_d^T - S_d S_l^T) W(k) - S_l]^* (\frac{g \cdot g_l}{g_d S_d^T W(k)} - 1) S_l^T W(k) \\
&+ \sigma_n^2 (\frac{g \cdot g_n}{g_d S_d^T W(k)} - 1) [(\frac{g \cdot g_n}{g_d (S_d^T W(k))^2})^* (S_d^\dagger W^*(k) W(k) - W^\dagger(k) W(k) S_d^*) - W(k)] \\
&= 0 \,,
\end{aligned} \tag{16}$$

where $(\cdot)^\dagger$ denotes complex conjugate transpose. Note that the first, second, and third terms in Eq.(16) correspond to the desired signal, interference, and noise contributions, respectively.

It can be shown that the solution for the weight vector of Eq. (16) when $g_l = g_n = 0$, for all l, and $g_d \neq 0$ is the optimal Wiener solution, i.e. $W = \Phi_u^{-1} S_d$ where Φ_u is the correlation matrix of the undesired signals. Otherwise, $W(k)$ will be a sub-optimal weight vector. However, both optimal and sub-optimal weight vectors tend to annihilate the undesired signal.

From the first term in Eq. (16) we see that $S_d^T W(k)=g$. This condition, drives the weight to form a gain g at the AOD. Combining this requirement with the constraint of Eq. (13), results in maintaining unity gain for the desired signal in the RAL. Consequently, this structure offers a more flexible design of the filter in the RAL and better system stability.

3.2 System Realization

To realize the ARENA structure, the gradient of the residual signal versus the weight vector is required. However, this is not generally available in practice. According to the orthogonality principle[13], in such situations, $\nabla_W \epsilon(k)$ is replaced by X(k). The weight adjusting equation, then, is written as

$$W(k+1) = W(k) + \kappa[\epsilon(k)X^*(k)] , \tag{17}$$

where κ is a step size constant. Comparing Eqs. (17) and (2) we see that the weight adjusting equation of the ARENA array is equivalent to the conventional LMS array. Thus, the steady state weight vector can be solved in the same manner, i.e.

$$\sigma_d^2(g-S_d^T W(k))S_d^* + \sum_{l=1}^{p} \sigma_l^2\left(\frac{g \cdot g_l}{g_d} - S_d^T W(k)\right)\frac{S_l^T W(k)}{S_d^T W(k)} S_l^* + \sigma_n\left(\frac{g_n g}{g_d S_d^T W(k)} - 1\right) W(k)$$

$$= 0 . \tag{18}$$

From Eq. (18) we find that this practical weight adjusting algorithm has a similar solution as Eq. (16) which minimizes the residual signal power by letting the weight vector approach $S_d^T W(k)=g$ and $S_I^T W(k)=0$. Note we must ensure that $g_I \neq g_d$ and $g_n \neq g_d$ since if $g_I=g_d$ it means the RAL has completely lost its ability to distinguish the interference and the desired signal or the interference has the same characteristic as the desired signal, the interference will be treated as the desired signal or vice versa. A matched filter can be used to accomplish this. For a wide band noise, a white noise cancelor[14] can be utilized in the RAL to decrease the RAL gain for noise and, consequently, avoid $g_n=g_d$.

4. SIMULATION RESULTS

In this section we look at several examples which illustrate the results derived above. We first examine a case with a desired signal and one narrow band interference signal. We use a 5 element half wavelength spaced ARENA array. The frequency of the desired signal is f_d and the interference is $1.258 f_d$. The input Signal-to-Noise Ratio (SNR) and Interference-to-Noise Ratio (INR) are 10 dB and 20 dB, the AOD and the Angle Of arrival of the Interference (AOI) are 15° and 30°, respectively. We assume the gain of the RAL for the desired signal is $g_d=0\ dB$. We consider two cases for the gain of the interferer, i.e. noise gain is assumed to be $g_n=-1dB$. In the computer simulations, the initial weight values are all set to zero except for the first element which is arbitrarily set to 0.01. The output SINR of the array is illustrated in Fig. 3 for both cases. We see that the weights converge as expected and drive the system to the optimal output performance; however, the case of weaker suppression of the undesired signal by the RAL filter results in the poorer output SINR performance as indicated by the slower convergence and greater jitter.

The major innovation of the proposed array is the employment of a Nonlinear Direction Constrainer (NDC) in the RAL. The NDC prevents the weight vector from converging to zero by constraining a constant gain in AOD. You may wonder if the AOD is known why we need the reference signal? With a precise estimation of the AOD an Applebaum array[6] can be used to achieve satisfactory performance. Previous study[15] has shown, however, that the Applebaum array is extremely sensitive to look direction error. The nonlinear direction constraint used in the RAL is a soft constraint which allows for some error without causing significant deterioration on the system performance. Because of this low sensitivity to steering vector error, the performance of the ARENA array is superior to the Applebaum array when a precise steering vector is not available. Simulations have been conducted to verify the results. Consider a 5 element ARENA array with half wavelength spacing at the center frequency, f_d, of the desired signal. The AOD is 15° and AOI is 30°. The frequency of the interferer is $1.258f_d$. The loop gains of the RAL are g_d=0 dB, g_l=−20 dB and g_n=−1 dB. The input SNR and INR are 10 dB and 20 dB, respectively. The output SINRs of the ARENA and Applebaum arrays with an estimated AOD equal of 25° are illustrated in Fig. 5. The simulation results indicate that the ARENA array is much less sensitive to the estimated error than the Applebaum array.

5. CONCLUSION

In this study we propose an adaptive array which employs a direction constrained Reference Acquisition Loop (RAL) to extract the reference signal from the array output without using spread spectrum or coding techniques. The *a priori* knowledge required for the proposed array is the AOD and the frequency band of the desired signal. It has been shown that the proposed array is less sensitive to the

estimation error of the AOD. The theoretical analysis and the computer results indicate that the proposed array successfully nulls the unwanted signal and maintains a constant gain in the arrival angle of the desired signal.

REFERENCES

[1] White, W. D., "Low-Angle Radar Tracking in the Presence of Multipath," *IEEE Trans. Aerosp. Electron. Syst.*, Vol. AES-10, No.6, pp. 835-852, November 1974.

[2] Gabriel, W. F., "Adaptive Arrays-An Introduction," *Proc. IEEE*, Vol. 64, No. 2, pp. 239-273, February 1976.

[3] White, W. D., "Angular Spectra in Radar Applications," *IEEE Tran. Aerosp. Electron. Syst.*, Vol. AES-15, pp. 891-895, November 1979.

[4] Evans, J. E., Johnson, J. R. and Sun, D. F., "High Resolution Angular Spectrum Estimation Techniques for Terrain Scattering Analysis and Angle of Arrival Estimation," *Proc. 1st ASSP Workshop Specturm Estimation*, Hamilton, Ontario, Canada, August 17-18, 1981.

[5] Widrow, B., Mantey, P.E., Griffiths, L. J. and Goode, B.B., "Adaptive Antenna Systems," *Proc. IEEE*, Vol. 55, No.12, pp. 2143-2158, December 1967.

[6] Applebaum, S. P., "Adaptive Arrays," *IEEE Trans. Antennas Propagat.*, Vol. AP-24, pp. 585-598, Spetember 1976.

[7] Compton, R. T. Jr., "An Adaptive Array in a Spread-Spectrum Communicat on System," *Proceedings of the IEEE*, Vol. 66, No.3, March 1978.

[8] Winters, J. H., "Spread Spectrum in a Four-Phase Communication System Employing Adaptive Antennas," *IEEE Tran. Commnications*, Vol. COM-30, No. 5, May 1982.

[9] Hudson, E. C., "Use of an Adaptive Array in a Frequency-Shift Keyed Communication System," Technical Report 712684-1, Ohio State University ElectroScience Laboratiory, Columbus, Ohio 43212; prepared under Contract N00019-80-C-0181 for Naval Air Systems Command, Ausust 1980.

[10] Ganz, M. W., "On the Performance of an Adaptive Array in a Frequency Shift Keyed Communication System," M.Sc. thesis, Department of Electrical Engineering, Ohio State University, August 1982.

[11] Compton, R. T. Jr., *Adaptive Antennas:Concepts and Performance*, New Jersey: Prentice-Hall 1988.

[12] B. Widrow, J. McCool, and M. Ball, "The Complex LMS Algorithm," *Proceedings of the IEEE*, Vol. 63, No.4, April 1975. (pp. 719)

[13] Papoulis, A., *Probability, Random Variables, and Stochastic Processes* 2nd Edition, McGraw-Hill Book Company 1984.

[14] Widrow, B. and Stearns, S.D., "*Adaptive Signal Processing*," New Jersey: Prentice-Hall 1985.

[15] Compton, R. T. Jr., "The Effect of Random Steering Vector Errors in the Applebaum Adaptive Array," *IEEE Trans. Aerosp. Electron. Syst.*, Vol. AES-18, pp. 392-400, September 1982.

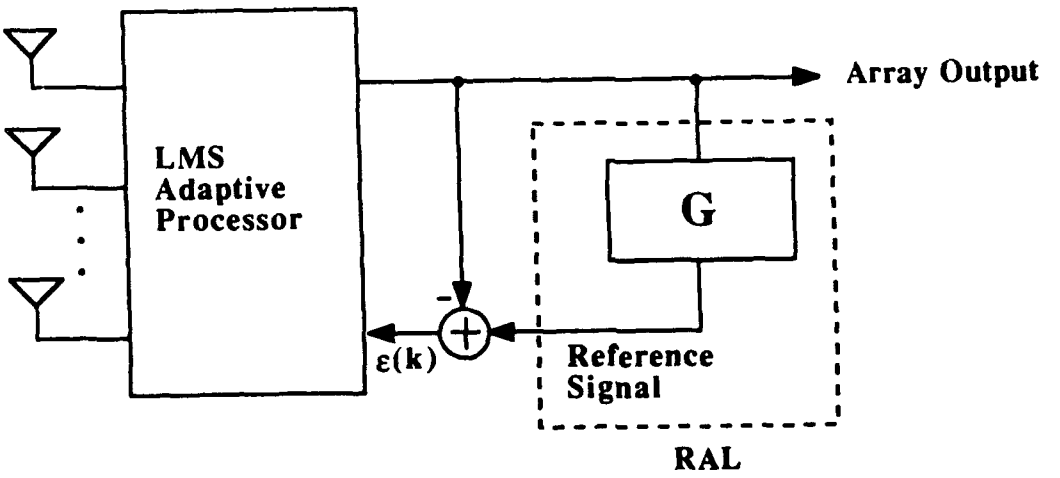

Fig. 1 General Struture of an LMS array with a self-generated reference signal

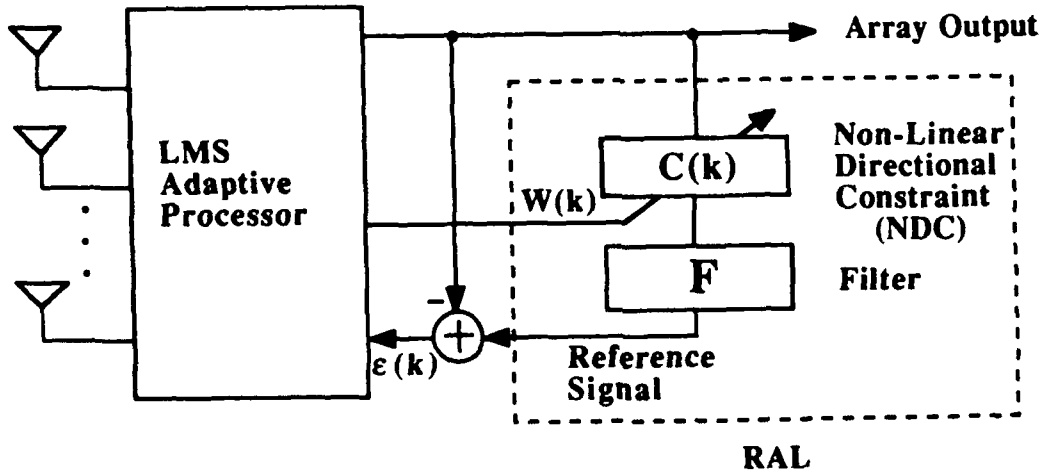

Fig. 2 Struture of the ARENA

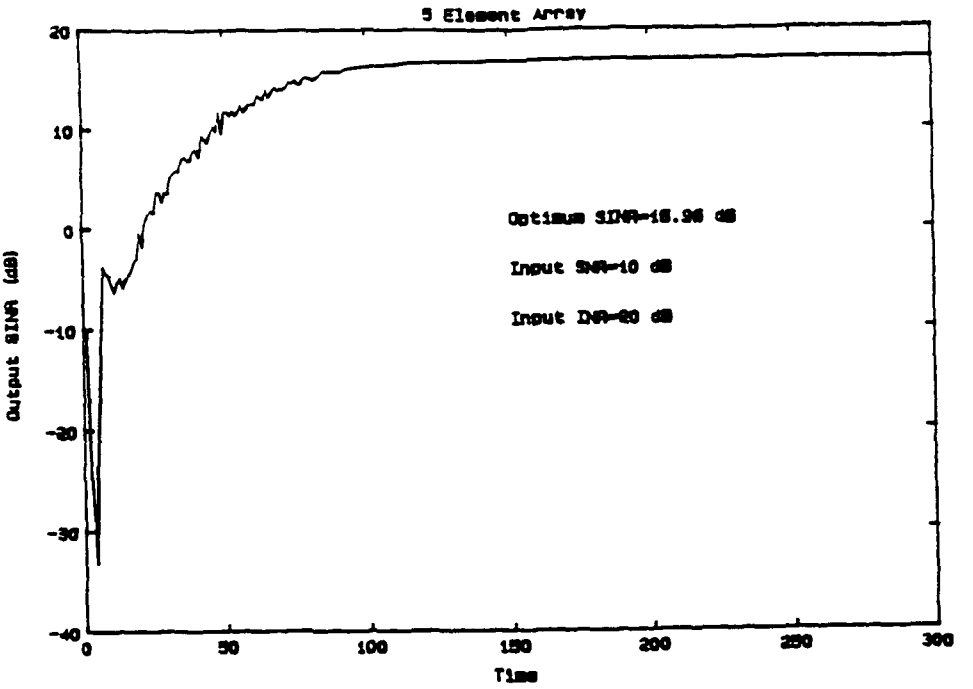

Fig. 3 The output SINR of the ARENA with g_d=0 dB, g_l=-20dB, g_n=-1dB, AOD=15° and AOI=30°

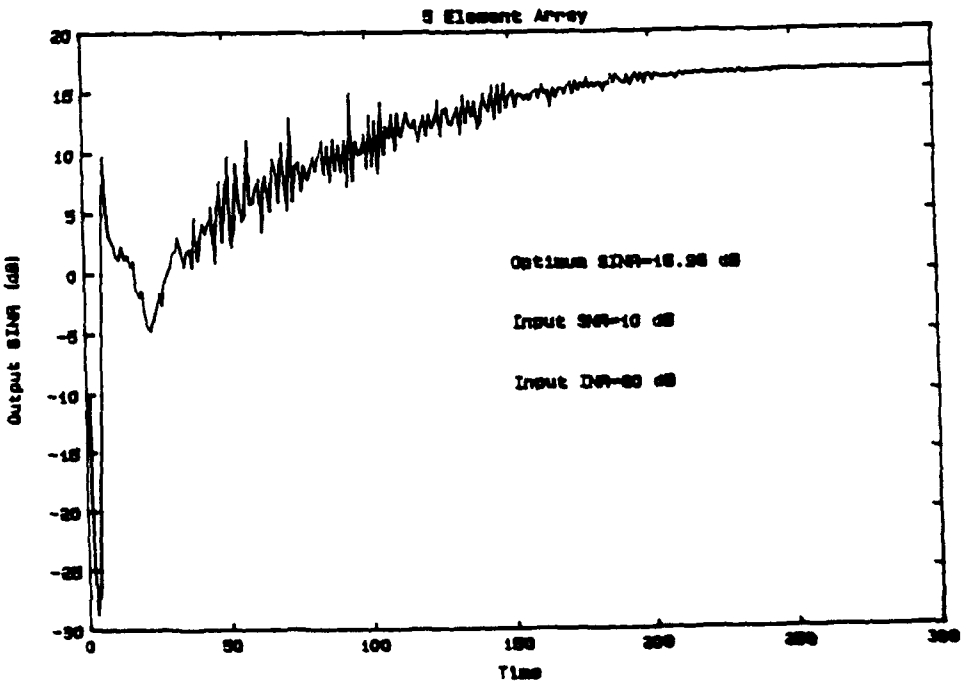

Fig. 4 The output SINR of the ARENA with g_d=0 dB, g_l=-5dB, g_n=-1dB, AOD=15° and AOI=30°

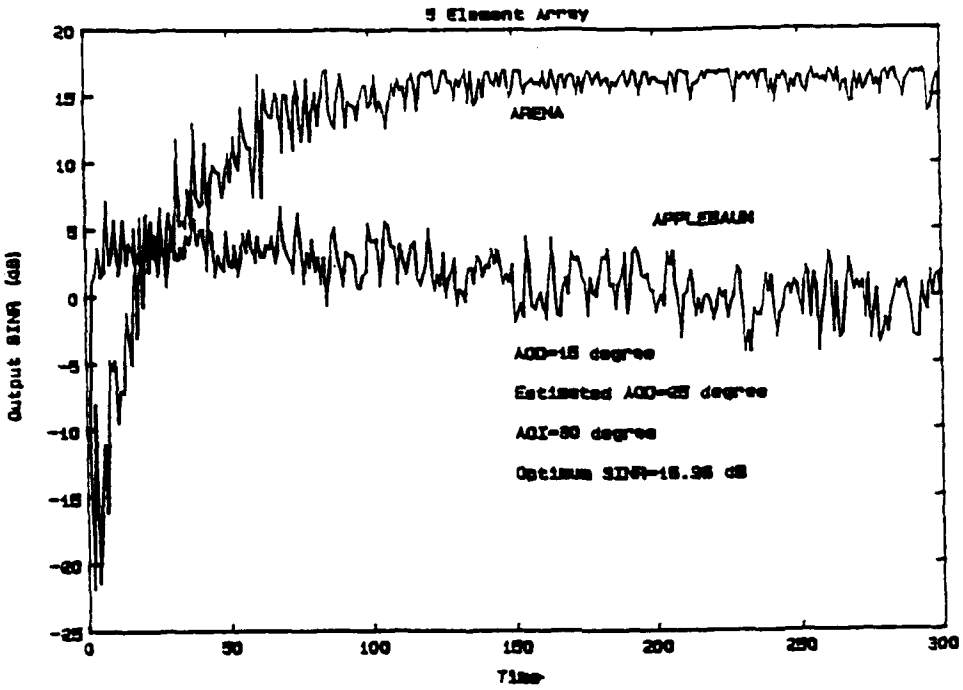

Fig. 5 The output SINR of the ARENA with g_d=0 dB, g_l=-20dB, g_n=-1dB, AOD=15°, AOI=30°, and estimated AOD=25°

OPTICALLY LINKED SHF ANTENNA ARRAY

Salvatore L. Carollo, Anthony M. Greci, Richard N. Smith

ROME AIR DEVELOPMENT CENTER

GRIFFISS AFB, NY 13441

1.0 ABSTRACT

This report covers the work done under Task 5 of Project 45194263, entitled, "Communications Adaptive Array Processor Evaluation".

Adaptive antenna technology has been an area of interest for many years. The progress to date can be characterized by extensive research on algorithms and processing architectures, development of a large number of prototype systems and fielding of a few systems.

Adaptive antenna systems normally consist of two or more antenna elements, two or more receivers, amplitude and phase weighting networks for one or more elements and a signal combiner. For some applications the size, weight, power consumption and cost of multiple receivers, antenna elements and associated radio frequency (RF) cabling can be limiting factors. In spite of these limitations, the impressive interference cancellation capabilities of adaptive antenna systems is highly desirable. Recent advances in photonics technology could provide solutions to the limitations described above. RF modulated lasers, optical cabling and optical detectors could reduce much of the size, weight, power consumption and cost of conventional

adaptive array systems.

Using the RADC/DC RF laboratory anechoic chamber and the "Flexible Adaptive Spatial Signal Processor" (FASSP) this effort was performed to established the feasibility of using optical technology to implement an adaptive antenna array system. This report covers the design, implementation and testing of an optically linked adaptive antenna array. The performance of the optically linked array is evaluated by comparison to a conventional adaptive array.

2.0 IN-HOUSE TEST FACILITIES

RADC/DC has an adaptive array processing test bed. The test bed shown in Figure 1 consists of a rectangular anechoic chamber, a flexible adaptive spatial signal processor (FASSP), a antenna pattern recorder, various types of jammer/desired signal sources and satellite communication simulation and analysis programs.

The test bed simulation/analysis computer programs are used to study and compare adaptive processing system concepts, techniques and algorithms. This provides a fast look approach to determine the merit and feasibility of a concept. If the results show promise the concept is further tested using real signals and adaptive

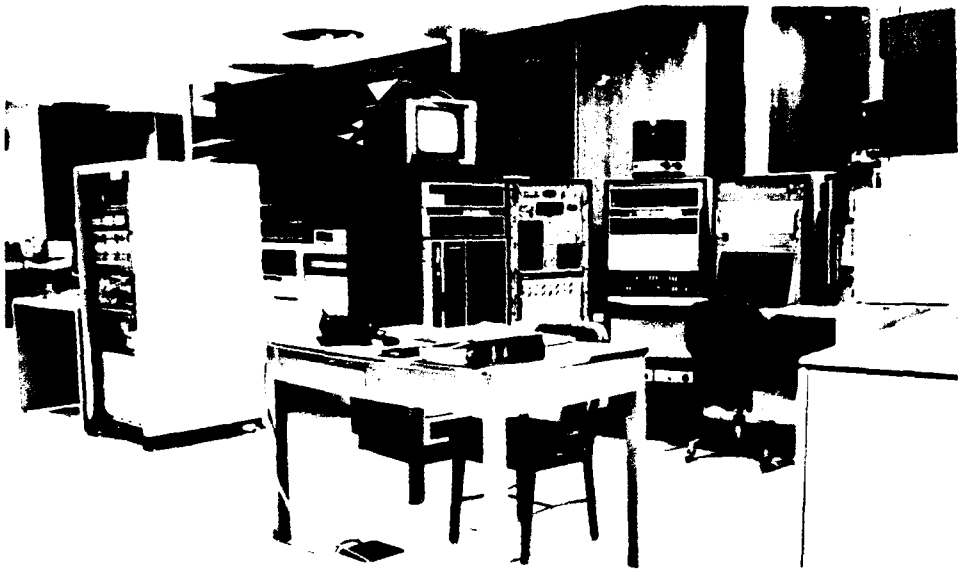

Figure 1. ADAPTIVE ARRAY PROCESSING TESTBED

processor hardware to determine the actual benefit attainable. The test bed is reconfigurable and functions as a tool to support the development of methodologies for comparing and evaluating new adaptive array processing algorithms, architectures and techniques suitable for meeting satellite communications requirements (such as those for the Defense Satellite Communications System [DSCS]).

2.1 ANECHOIC CHAMBER

The anechoic test chamber shown in Figure 2 is a rectangular structure 40 ft. long, 28 ft. wide and 18 ft. high[2]. The inner chamber is isolated from RF fields

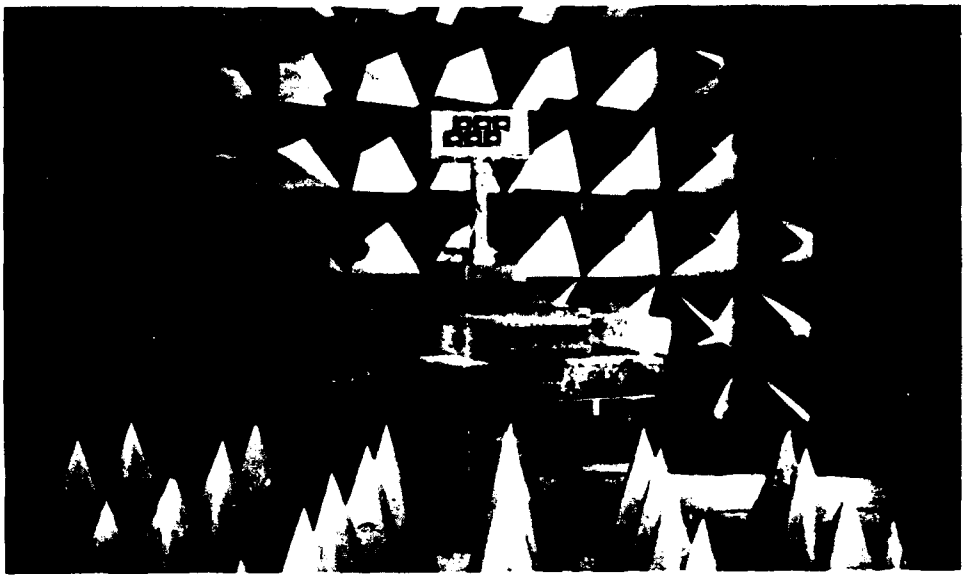

Figure 2. ANECHOIC CHAMBER

from 150 MHz to 18 GHz by at least 100 dB.

It has a six foot diameter spherical quiet zone located at its longitudinal axis. The center of the quiet zone is midway between the ceiling and the floor and about 50 inches from the tips of the absorber on the back wall. The receive element array is positioned in the center of the quite zone to minimize reception of all reflected signals. All chamber walls, ceilings and floors, except walkways, are covered completely with energy (RF) absorbing material. A Scientific Atlanta model 5315C-5 antenna positioner is installed in the chamber. The tip of the model tower (which supports the

array elements) is located in the center of the "quiet zone". The chamber is wide enough and has provisions so that several signal sources can be used simultaneously at the front wall opposite to the "quiet zone".

Six feet of the 40 ft. chamber is partitioned off and is used as an equipment room to house the signal sources and antenna positioner controls. Absorber panels are removable to allow access for mounting signal/jammer antennas. Signal and control connections between the chamber and the laboratory equipment (FASSP and Scientific Atlanta 2020 system) are provided through bulkhead feed through panels at each end of the chamber. All functions such as source power, frequency, mode and receiver antenna position (pedestal rotation) are controlled from outside of the chamber.

2.2 FLEXIBLE ADAPTIVE SPATIAL SIGNAL PROCESSOR (FASSP)

The FASSP[4] test bed is shown in Figure 3. All adaptive Spatial processing systems consist of three generic components:

1. An array of receiving elements (spatial array) to provide the degrees of freedom required to null out a number of directional jamming signals,

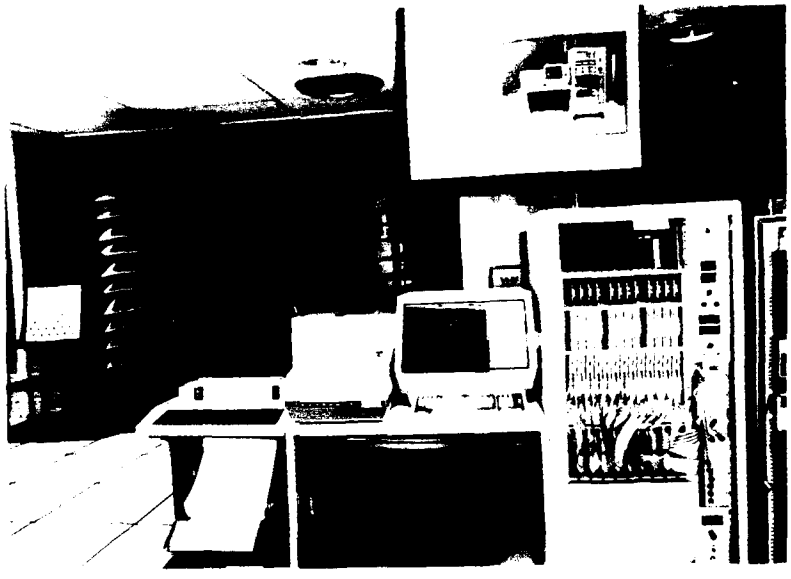

Figure 3. FLEXIBLE ADAPTIVE SPATIAL SIGNAL PROCESSOR

2. An adaptive processor that uses the signal samples from the array receive sensors to compute the adaptive weights that produce the resultant spatial response, and

3. Weighting networks that apply the adaptive weights to the signals from the individual input channels.

The design of adaptive spatial processing systems is very complicated because of the close interaction among these three basic components. Although computer simulations can be used to compare the performance of adaptive algorithms and techniques, the hardware

implementation effects cannot always be easily modeled.

With this in mind, RADC/DCCD conceived the ideas of a Flexible Adaptive Spatial Signal Processor (FASSP), which was designed and fabricated for RADC by Syracuse Research Corp. The FASSP is a general purpose flexible hardware adaptive array processor system that supports the integration/test of adaptive processing algorithms, architectures, techniques and real components.

The FASSP system was fabricated with high performance quality components and consists of 12 real RF receivers and weighting networks that are reconfigurable. The designer uses a computer based operating system to select the adaptive algorithms and hardware configuration and specify the necessary system parameters. Adaptive processor performance can then be evaluated against RF signal (desired) and jamming signals using an antenna array and an anechoic chamber.

3.0 CONVENTIONAL ADAPTIVE ARRAY

The conventional adaptive array processing system shown in Figure 4 was used as the baseline system configuration. The receiver antenna was a line array of four standard gain horns separated by 3/2 wavelength

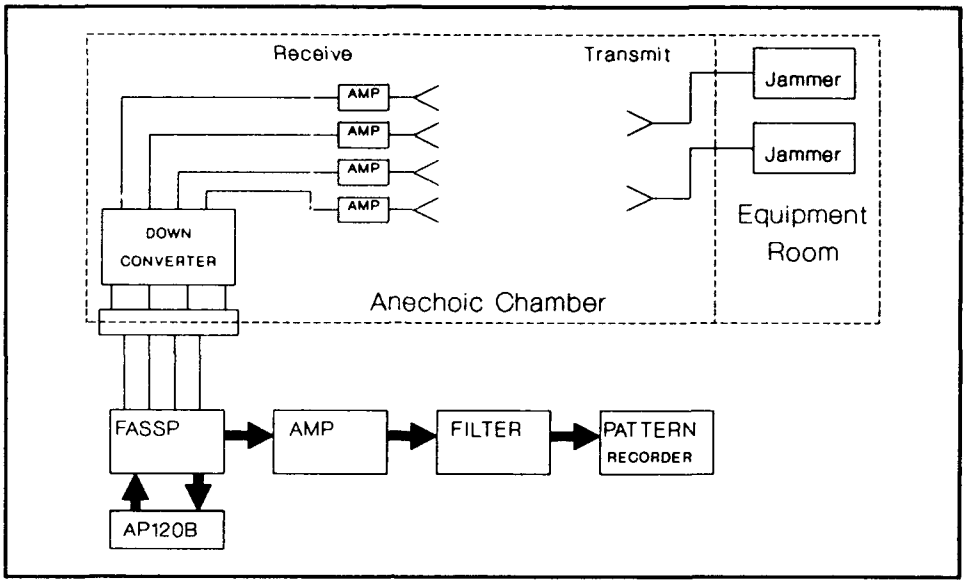

Figure 4. CONVENTIONAL ADAPTIVE ARRAY

spacing. The array was located on the positioner with the elements centered in the chamber quiet zone. The optically linked adaptive array configuration is shown in Figure 5 and is described in Section 4.

The CW and wide band noise jammer antennas were located at the opposite end of the chamber. One jammer transmitter element was positioned broadside/boresight (zero degrees azimuth, zero degrees elevation) to the array and a CW signal was applied. Figure 6 is a plot of the array steered to that CW source.

The array response plot shows that the main beam is centered at zero degrees azimuth and the sidelobes are

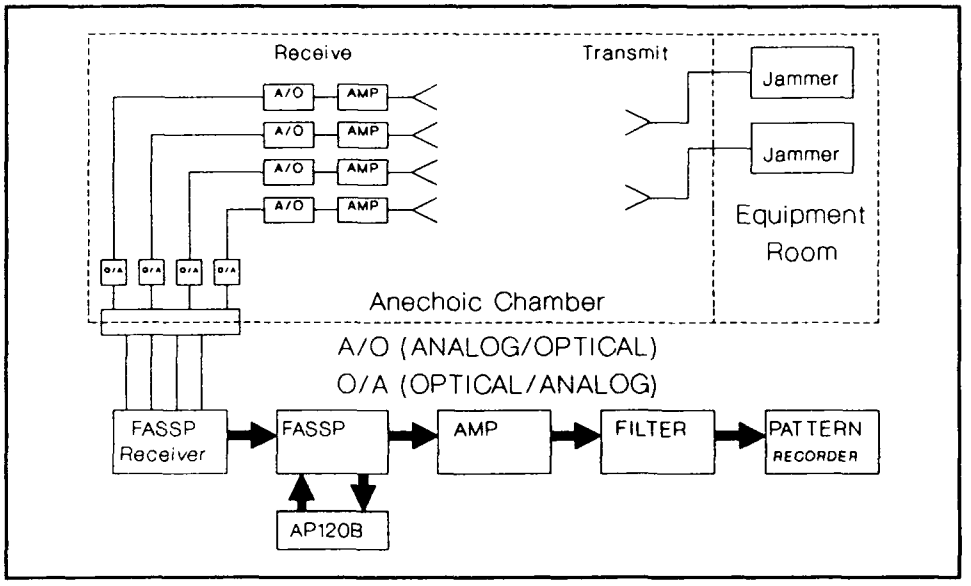

Figure 5. OPTICALLY LINKED ADAPTIVE ARRAY CONFIGURATION

located at plus or minus fourteen degrees azimuth. The second jammer transmit element was positioned at fourteen degrees centered on one of the side lobes.

Nulling tests were then performed using single jammers at each position.

3.1 BASELINE PERFORMANCE

The performance measure used to compare the performance of the optical implementation with that of the standard coaxial implementation was cancellation ration (CR)[3].

CR's for a given input jamming signal are measured by comparing the adaptive and conventional output power

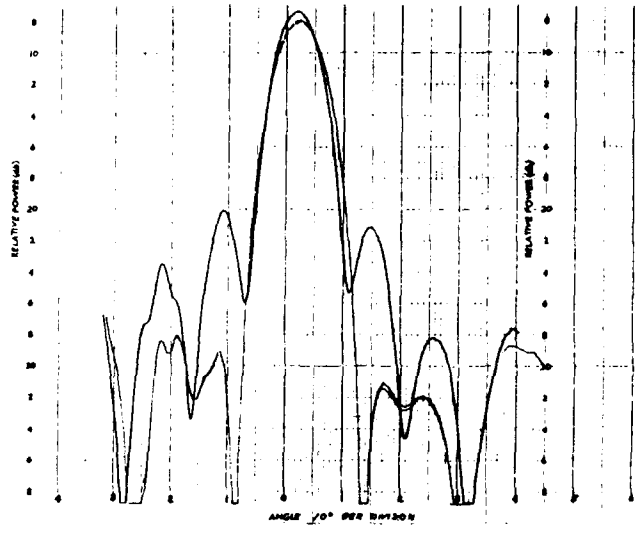

Figure 6. BEAMFORMED ARRAY PATTERN

of the adaptive processor. Usually, CR is used to characterize the performance of the adaptive processor against different jamming scenarios. It is a direct measure of the adaptive processor nulling capability and is shown in Equation (1) where Pa is the

$$CR(dB) = 10\log(Pa/Pc) \quad (1)$$

adaptive processor output power in the adaptive mode and Pc is the adaptive processor output power in the conventional or beamformed mode. Normally adaptive processor output is measured in dbm and, thus, Equation (2) is used to compute the CR ratio.

$$CR(dB) = Pa(dB) - Pc(dB) \quad (2)$$

4.0 THE OPTICALLY LINKED ARRAY

An adaptive array usually consists of a number of antenna elements, a receiver for each element and the RF/IF cabling and connectors necessary to connect the system together. One channel of such a system is shown in Figure 7. The block marked "Flexible Adaptive Spatial Signal Processor" (FASSP) indicates the equipment that performs the adaptive signal processing tasks. Because of the losses in the RF cabling, the SHF receivers are co-located with the antenna elements in the anechoic chamber. Along with the RF/IF cabling, the receivers

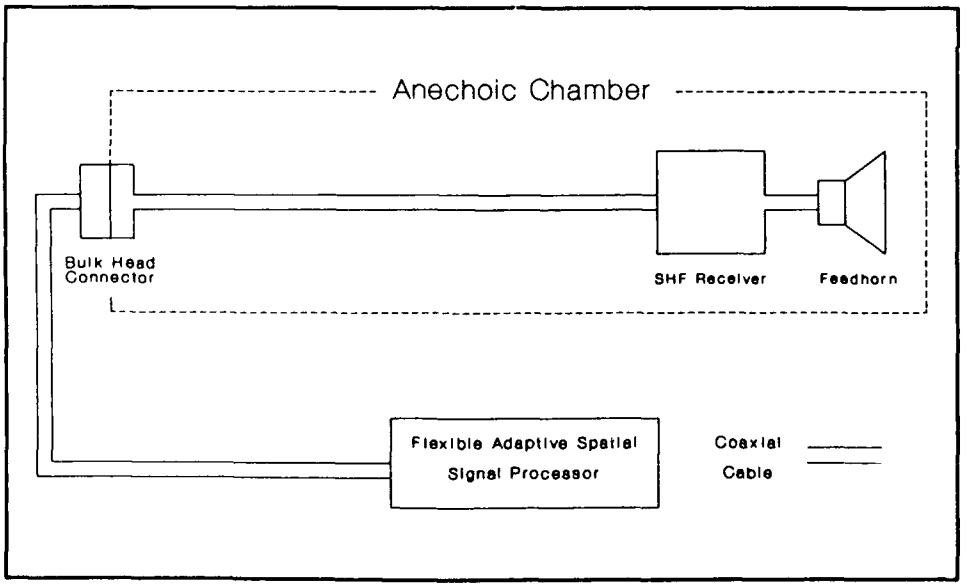

Figure 7. CONVENTIONAL ADAPTIVE ARRAY CONFIGURATION

introduce another source of unwanted RF/IF radiation.

Shown in Figure 8 is an optically linked/connected adaptive antenna array.

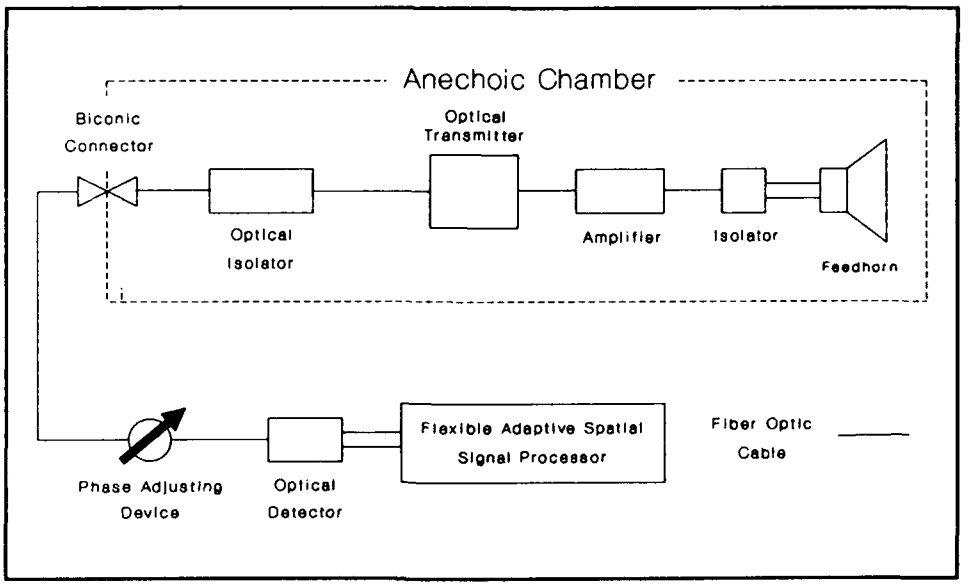

Figure 8. OPTICALLY LINKED ADAPTIVE ARRAY

Because of the very low losses in the optical fiber it is possible to remove the SHF receivers from the chamber and co-locate them with the FASSP. The optical linkage also eliminates the IF cabling from the chamber.

4.1 HARDWARE

Component selection was based on anechoic chamber and associated equipment interface requirements. Since the antenna system was designed to run at 8.41 GHz, the task of optical link selection was significantly simplified. The Ortel TSL-1000 optical transmitter and

the Ortel RSL-25 optical receiver were selected based on their frequency range of 10 kHz to 10 GHz.

The maximum received signal likely to be seen at the output of each antenna element (feedhorn) is less than -40 dBm. Therefore, 50 dBm gain, narrow band (centered at 8 GHz) Miteq amplifiers were selected to boost the signal. This will supply the Ortel transmitters with power near their maximum RF input level of 12 dBm and thereby allowing us to maximize the usable dynamic range of the links.

Other devices are incorporated in each elemental leg of the antenna system (see Figure 8). These include electrical and optical isolators to prevent impedance mismatch reflections from the feedhorn, and optical reflections to the laser, respectively, 50 meter lengths of fiber and phase adjusting mechanisms to time match the links are also integral parts of the system[1].

4.2 FUNCTIONAL DESCRIPTION

Each array link consists of the equipment described in Section 4.1. An adaptive array is composed of two or more links, usually one for each antenna element in the array. In terms of a single link the RF signal arrives at the array and is received by the antenna

element, in this case an SHF feedhorn. The low level signals are amplified to provide an appropriate signal level for the optical transmitters. The optical transmitters put out a single frequency of light the amplitude of which is modulated by the RF input signal. The light is then transmitted along an optical cable to the phase adjusting device where the electrical length of the optical cable can be adjusted so that all the links in the array can be time and phase matched[5]. The modulated and time and phase matched optical signal then travels along the optical cable to the optical detectors where the light is demodulated and the RF signal is output to the SHF receivers through conventional RF cabling.

5.2 TEST AND EVALUATION

The optically linked array was tested in a manner identical to the conventional/baseline array as described in Section 3.0. Data was collected to plot cancellation ratio for three separate sensors[3]. All of the figures indicated below are identical in form. The horizontal axis (Pe) is the ratio of signal plus noise to noise power as measured at the antenna element. On the vertical axis two quantities are plotted. The

quantity (Pc) is referred to as the conventional/unadapted output power as measured at the beamformer/residue output port of the adaptive processor. When measuring this quantity the array is beamformed to broadside and then the interference signal is activated and again the signal plus noise to noise ratio is measured. The quantity (Pa) is referred to as output power after the adaptive processor is allowed to adapt. Again the signal plus noise to noise ratio is measured at the residue output. Using these graphs the CR in dB can be read directly as the difference between the two plotted lines on the graphs.

Shown in Figure 9a is a plot of the conventional and adaptive response. Figure 9b is a plot of the optically linked conventional and adaptive response. Both Figures 9a and 9b are for a single continuous wave (CW) signal broadside to the array.

Shown in Figure 10a is a plot of the conventional and adaptive response. Figure 10b is a plot of the optically linked conventional and adaptive response. Both Figures 10a and 10b are for a single CW source in the first sidelobe which is 14 degrees from broadside for the antenna array in use.

Shown in Figure 11a is a plot of the conventional and adaptive response. Figure 11b a plot of the optically linked conventional and adaptive response. Both Figures 11a and 11b are for a wide band noise (WBN) source broadside to the array.

6.0 CONCLUSIONS AND RECOMMENDATIONS

Analysis of the data presented in Section 5.0 indicates that the performance of the optical linked array is as good as the baseline conventional array and is in some cases better. During the design and fabrication of the optically linked array it was apparent that optical technology would provide reduced size and weight over the conventionally linked array. The RF cabling associated with a conventional link is bulky and weighs about 15 - 20 lbs. as compared to the optical link which is far less bulky and weighs only a few pounds, including modulator and demodulator. These size and weight improvements are obtained with no loss in performance and, in some cases, with even better performance.

Further improvements are attainable by the following means. An increase in the dynamic range of the optical links could be obtained by using indirect modulation of

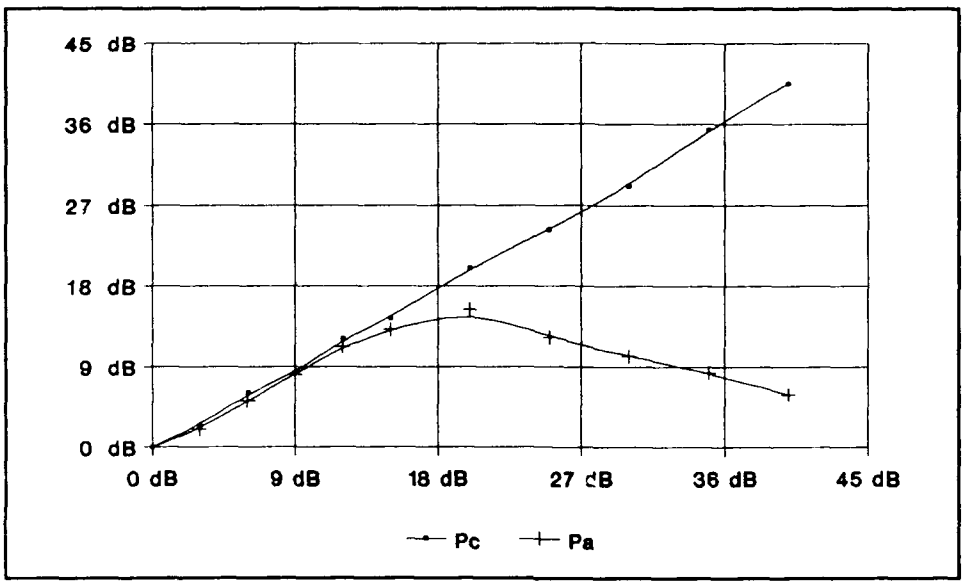

Figure 9a. CONVENTIONAL CW BROADSIDE CR

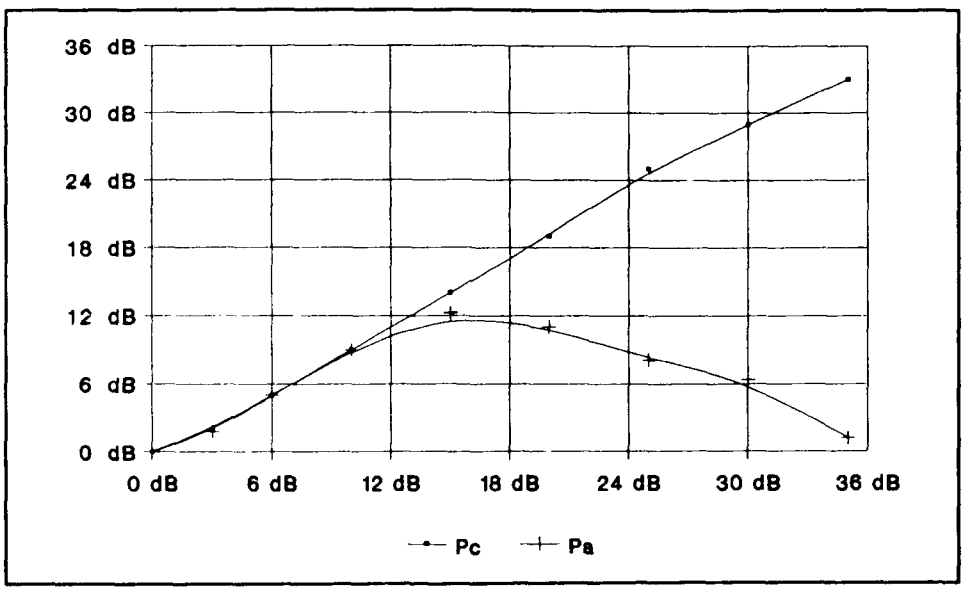

Figure 9b. OPTICAL CW BROADSIDE CR

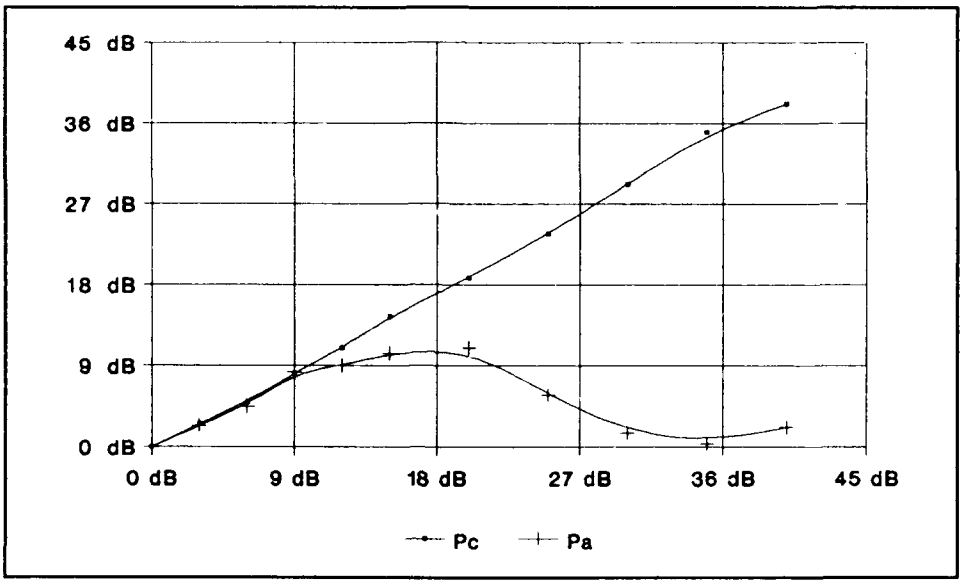

Figure 10a. CONVENTIONAL CW SIDELOBE CR

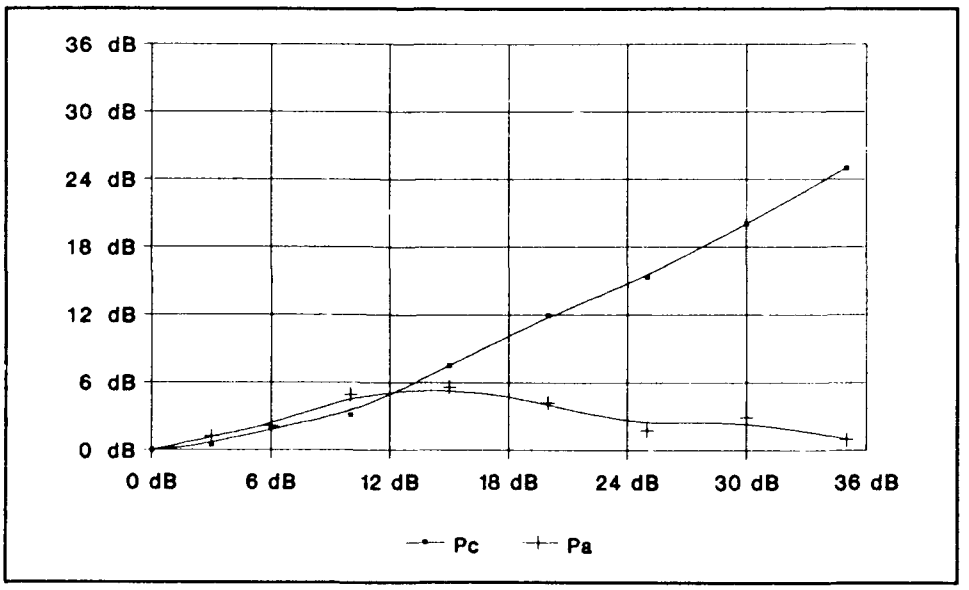

Figure 10b. OPTICAL CW SIDELOBE CR

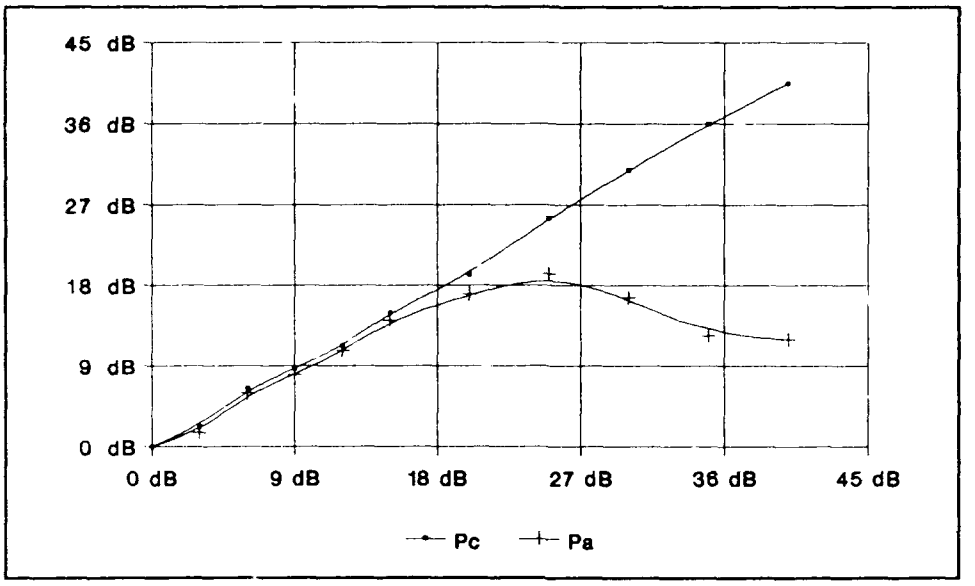

Figure 11a. CONVENTIONAL WBN BROADSIDE CR

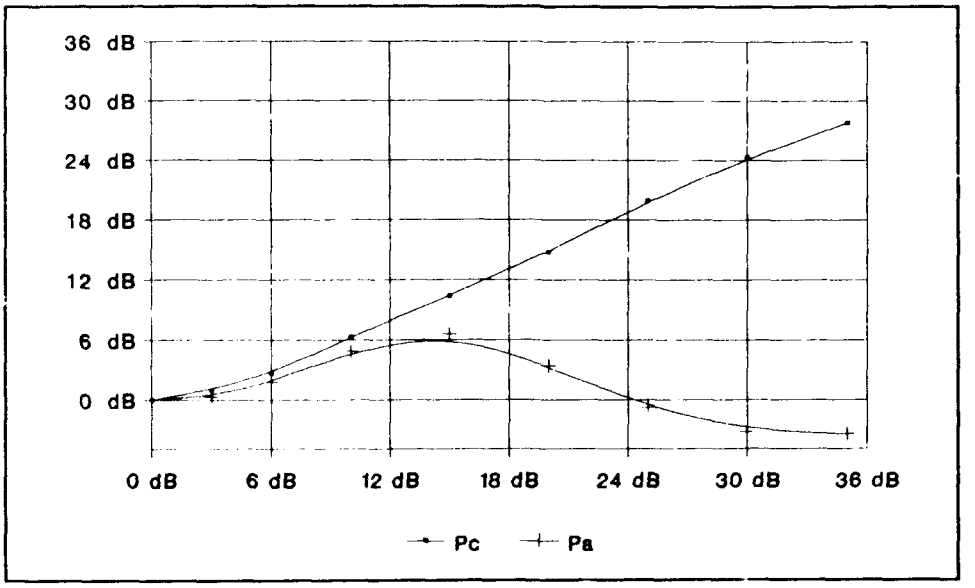

Figure 11b. OPTICAL WBN BROADSIDE CR

the lasers verses the direct modulation used for these tests. Single mode fiber optic cable should be used instead of multimode to prevent cable losses due to gradient effects when the fiber is bent or deformed in any way. Using a single laser with external modulators for each antenna element would ensure system coherence and make the system even more cost effective. The single laser technique would also allow all the elements to be multiplexed on to a single fiber that could then be demultiplexed at the adaptive processor. The detector(s) could be RF biased to provide down conversion, thereby eliminating the FASSP receivers. Elimination of the FASSP receivers will result in a reduction in size, weight and power of a complete adaptive antenna system. These means of improvement will be further investigated and verified in future in-house efforts. This RADC/DCCD in-house initial investigation of optical technology, as applied to adaptive antenna systems, indicates that evolving optical technology can and will provide important enhancements especially for mobile platform systems.

REFERENCES

1. Carollo, S. L.; Greci, Anthony M.; Jackson, D.; Smith, Richard N.; and Toughlian, Edward N. (1988). "THE FLEXIBLE ADAPTIVE SPATIAL SIGNAL PROCESSOR". Paper presented September 21, 1988 at the Antenna Applications Symposium.
2. Giangiulli, David (1978) TEST REPORT ON A RECTANGULAR ANECHOIC CHAMBER, RANTEC Doc. No. 15032-TR.
3. Greci, Anthony M.; Kulon, Frank T. (1988), PERFORMANCE MEASUREMENT OF A CASCADE ADAPTIVE ARRAY PROCESSOR AND SPEECH ENHANCEMENT UNIT IN THE PRESENCE OF INTERFERENCE, RADC-TM-88-7.
4. Hadley, Hugh W., FLEXIBLE ADAPTIVE SPATIAL SIGNAL PROCESSOR (FASSP), RADC-TR-84-255. ADB092024
5. Johns, Steven T.; Schmitt, Mark C.; Toughlian, Edward N. (1990), OPTICAL LINKS FOR MICROWAVE APPLICATIONS, RADC-TR-90-12. ADA220574

*U.S. GOVERNMENT PRINTING OFFICE: 1991-500-000/40006

MISSION

OF

ROME LABORATORY

Rome Laboratory plans and executes an interdisciplinary program in research, development, test, and technology transition in support of Air Force Command, Control, Communications and Intelligence (C^3I) activities for all Air Force platforms. It also executes selected acquisition programs in several areas of expertise. Technical and engineering support within areas of competence is provided to ESD Program Offices (POs) and other ESD elements to perform effective acquisition of C^3I systems. In addition, Rome Laboratory's technology supports other AFSC Product Divisions, the Air Force user community, and other DOD and non-DOD agencies. Rome Laboratory maintains technical competence and research programs in areas including, but not limited to, communications, command and control, battle management, intelligence information processing, computational sciences and software producibility, wide area surveillance/sensors, signal processing, solid state sciences, photonics, electromagnetic technology, superconductivity, and electronic reliability/maintainability and testability.